

THE FABRICATION OF NOVEL MICROFLUIDIC DEVICES FOR CHEMICAL  
SEPARATION AND CONCENTRATION ENRICHMENT OF AMINO ACIDS, PROTEINS,  
PEPTIDES, PARTICLES, AND CELLS

by

GREGORY T. ROMAN

B.A., Bard College, 2002

AN ABSTRACT OF A DISSERTATION

submitted in partial fulfillment of the requirements for the degree

DOCTOR OF PHILOSOPHY

Department of Chemistry  
College of Arts and Sciences

KANSAS STATE UNIVERSITY  
Manhattan, Kansas

2006

## Abstract

My doctoral dissertation consists of three fundamental studies: 1) synthesis of biocompatible materials that can be used as microfluidic substrates, 2) characterizing these materials with respect to properties important to microfluidic fabrication, biochemical separations and concentration enrichment, and 3) employing these novel devices for real world applications in bioanalytical chemistry.

The surface properties of a substrate will dramatically affect the resolution and efficiency that can be obtained for a specific CE separation. Thus, the ability to modify the surface is very useful in tailoring a microfluidic chip to a specific separation mode. The substrates we have synthesized for microfluidic devices include metal oxide modified poly(dimethylsiloxane) (PDMS), poly(ethyleneoxide)-PDMS (PEO-PDMS) coblock polymers, and surfactant coated PDMS. The metal oxide modified PDMS materials we synthesized include silica-PDMS, titania-PDMS, vanadia-PDMS and zirconia-PDMS. The surfaces of these materials were characterized using contact angle, X-ray photoelectron spectroscopy (XPS), Raman, transmission electron microscopy (TEM), scanning electron microscopy (SEM), atomic force microscopy (AFM) and electroosmotic mobility (EOM) measurements. All of the metal oxide modified PDMS surfaces were significantly more hydrophilic than native PDMS, suggesting potential application in separations of biopolymers. In addition to being more hydrophilic the EOF and zeta potential of the channels were stable and quite durable with aging. Well characterized silane chemistry was used to derivitize the surface of the PDMS metal oxide surfaces allowing a number of different functionalities to be placed on the surface. This method has the potential for wide applicability in many different fields, but specifically for the fabrication of microstructures that need specific surface chemistries.

We have also made a number of advancements using sol-gel chemistry and laminar flow within microfluidic channels to fabricate nanoporous membranes. Sol-gel patterned membranes are a simple and facile method of incorporating nanoscale diameter channels within a microfluidic manifold. These membranes have been used to perform preconcentration of amino acids, proteins and small particles for further analysis and separation using CE. We are also using these membranes for further study in desilanzation and protein recrystallization studies.

THE FABRICATION OF NOVEL MICROFLUIDIC DEVICES FOR CHEMICAL  
SEPARATION AND CONCENTRATION ENRICHMENT OF AMINO ACIDS, PROTEINS,  
PEPTIDES, PARTICLES, AND CELLS

by

GREGORY T. ROMAN

B.A., Bard College, 2002

A DISSERTATION

submitted in partial fulfillment of the requirements for the degree

DOCTOR OF PHILOSOPHY

Department of Chemistry  
College of Arts and Sciences

KANSAS STATE UNIVERSITY  
Manhattan, Kansas

2006

Approved by:

Major Professor  
Dr. Christopher T. Culbertson

## Abstract

My doctoral dissertation consists of three fundamental studies: 1) synthesis of biocompatible materials that can be used as microfluidic substrates, 2) characterizing these materials with respect to properties important to microfluidic fabrication, biochemical separations and concentration enrichment, and 3) employing these novel devices for real world applications in bioanalytical chemistry.

The surface properties of a substrate will dramatically affect the resolution and efficiency that can be obtained for a specific CE separation. Thus, the ability to modify the surface is very useful in tailoring a microfluidic chip to a specific separation mode. The substrates we have synthesized for microfluidic devices include metal oxide modified poly(dimethylsiloxane) (PDMS), poly(ethyleneoxide)-PDMS (PEO-PDMS) coblock polymers, and surfactant coated PDMS. The metal oxide modified PDMS materials we synthesized include silica-PDMS, titania-PDMS, vanadia-PDMS and zirconia-PDMS. The surfaces of these materials were characterized using contact angle, X-ray photoelectron spectroscopy (XPS), Raman, transmission electron microscopy (TEM), scanning electron microscopy (SEM), atomic force microscopy (AFM) and electroosmotic mobility (EOM) measurements. All of the metal oxide modified PDMS surfaces were significantly more hydrophilic than native PDMS, suggesting potential application in separations of biopolymers. In addition to being more hydrophilic the EOF and zeta potential of the channels were stable and quite durable with aging. Well characterized silane chemistry was used to derivitize the surface of the PDMS metal oxide surfaces allowing a number of different functionalities to be placed on the surface. This method has the potential for wide applicability in many different fields, but specifically for the fabrication of microstructures that need specific surface chemistries.

We have also made a number of advancements using sol-gel chemistry and laminar flow within microfluidic channels to fabricate nanoporous membranes. Sol-gel patterned membranes are a simple and facile method of incorporating nanoscale diameter channels within a microfluidic manifold. These membranes have been used to perform preconcentration of amino acids, proteins and small particles for further analysis and separation using CE. We are also using these membranes for further study in desilanzation and protein recrystallization studies.

## Table of Contents

List of Figures .....	xi
List of Tables .....	xxi
Acknowledgements .....	xxii
Dedication .....	xxiii
CHAPTER 1 - Introduction .....	1
1.1 Microfluidic Fabrication .....	2
1.1.1 Photolithography .....	3
1.1.2 SU-8 Resist Photolithography .....	4
1.1.3 Soft Lithography .....	7
1.2 Fluid Dynamics of Microfluidics .....	10
1.2.1 Reynolds Number and Laminar Flow .....	11
1.2.2 Diffusion .....	11
1.2.3 Fluidic Resistance .....	12
1.2.4 Surface area to Volume Ratio .....	14
1.2.5 Surface Tension .....	14
1.3 Laser Induced Fluorescence .....	15
1.3.1 Introduction .....	15
1.3.2 Theory .....	16
1.3.3 Fluorescent conjugation chemistry .....	18
1.3.4 LIF Apparatus .....	21
1.4 Capillary Electrophoresis .....	23
1.4.1 Theory .....	23
1.4.2 Analytical CE Parameters .....	25
1.4.3 CE Apparatus .....	27
CHAPTER 2 - The Origin of Electroosmotic Flow on PDMS Microfluidics .....	29

2.1 Introduction.....	29
2.2 EOF Theory .....	29
2.3 Methods of Measuring EOF.....	34
2.3.1 Current Monitoring Method.....	34
2.4 EOF of PDMS Microfluidics .....	37
2.4.1 Introduction .....	37
2.4.2 Fillers and Catalyst Effects .....	38
2.4.3 Adsorption of Ions on the PDMS Surface.....	41
CHAPTER 3 - Silica Sol-Gel modified PDMS Microfluidics .....	44
3.1 Introductory Sol-Gel Chemistry.....	44
3.1.1 Chemical Reaction Mechanisms .....	45
3.2 Introduction to Silica Sol-Gel Modified PDMS Microfluidics.....	46
3.3 Experimental for Silica Modified PDMS .....	51
3.3.1 Masks. ....	52
3.3.2 Molds. ....	52
3.3.3 PDMS chip fabrication.....	53
3.3.4 Contact Angle measurements.....	54
3.3.5 Rhodamine B absorption measurements.....	54
3.3.6 TEM Sample Preparation. ....	55
3.3.7 Weight measurements.....	55
3.3.8 Young's modulus measurement. ....	55
3.3.9 Hardness.....	56
3.3.10 i-E curves.....	56
3.3.1.1 EOF Measurements.....	57
3.3.1.2 Electrophoretic Separations.....	58
3.3.1.3 Single point detection setup.....	58
3.4 Results for Silica Modified PDMS.....	59
3.4.1 Physical Characterization.....	59
3.4.2 EOF Measurements.....	64
3.4.3 Separations. ....	65
3.4.4 Mold robustness.....	71

3.4.5 Conclusion.....	71
3.6 Thin Sol-Gel Films Using the “Coat and Go” Technique .....	72
3.6.1 Introduction to Coat and Go.....	73
3.6.2 Experimental Coat and Go .....	75
3.6.3 EOF measurements.....	75
3.6.4 Solid Phase Monoliths Fabricated Using Sol-Gel Tin Catalysis.....	76
3.6.5 Separations on PDMS coated channels.....	77
CHAPTER 4 - Sol-Gel Transition Metal Modified PDMS .....	79
4.1 Introduction.....	79
4.2 Experimental Section.....	84
4.2.1 Reagents.....	85
4.2.2 Microchip Fabrication and Surface Modification.....	85
4.2.3 Diffusion Measurements.....	86
4.2.4 Contact Angle Measurements.....	87
4.2.5 TEM Preparation.....	87
4.2.6 XPS and Raman Measurements.....	88
4.2.7 Measurement of EOM.....	89
4.2.8 SEM and AFM Preparation.....	89
4.3 RESULTS AND DISCUSSIONS.....	90
4.3.1 Fabrication of sol-gel modified PDMS microchips.....	90
4.3.2 Characterization of Titania, Vanadia, and Zirconia Surfaces.....	92
4.3.3 Measurement of EOM in Titania, Vanadia, and Zirconia PDMS Channels....	98
4.3.4 Characterization of oligoethyleneoxide, thiol, perfluoro and amino derivitized PDMS- TiO <sub>2</sub> .....	102
4.3.5 Thermochromic Gels .....	103
4.3.6 Waveguides .....	104
4.3.7 Separations .....	104
4.3.7.1 Amino Acids.....	105
4.3.7.2 Proteins.....	110
4.4 CONCLUSION.....	111
CHAPTER 5 - MEKC of Small Molecules on PDMS .....	113

5.1 Introduction.....	113
5.2 Experimental.....	116
5.2.1 Reagents and Solutions.....	116
5.2.2 Microchip Fabrication.....	117
5.2.3 BODIPY <sup>®</sup> Labeling Protocol.....	119
5.2.4 Amine/Protein Extraction Protocol.....	119
5.2.5 E. coli Homogenate and Polyamine Labeling.....	119
5.2.6 Calculation of Diffusion Coefficient.....	120
5.2.7 Separations and Detection.....	120
5.2.8 Electroosmotic Flow Measurements.....	121
5.2.9 Imaging of Rhodamine B Injections.....	121
5.3 Results and Discussion.....	122
5.3.1 Buffer Optimization and Use.....	122
5.3.2 Rhodamine B Injections.....	123
5.3.3 Rhodamine B Separations.....	125
5.3.4 Amino Acid Separations.....	127
5.3.5 Bacterial Homogenate separations.....	131
5.4 Concluding Remarks.....	133
CHAPTER 6 - MEKC of Proteins on PDMS.....	135
6.1 Introduction.....	135
6.2 Materials and Methods.....	138
6.2.1 Reagents and Fluorescent Derivatization.....	139
6.2.2 Microchip Design and Fabrication.....	139
6.2.3 Protein Detection.....	141
6.3 Results and Discussion.....	141
6.3.1 MEKC Buffer Optimization.....	141
6.3.2 MEKC Separations of Proteins.....	144
6.3.3 MEKC of Proteins on Serpentine Chip.....	148
6.4 Concluding remarks.....	151
CHAPTER 7 - Amyloid Beta Peptide Separations.....	153
7.1 Introduction.....	153

7.2 Materials and methods.....	157
7.2.1 Reagents.....	157
7.2.2 Peptide and CP2 Synthesis.....	157
7.2.3 Microchip Fabrication.....	157
7.2.4 A $\beta$ 40 Sample Preparation: .....	158
7.2.5 Microchip preparation:.....	158
7.2.6 Separation and detection: .....	159
7.3 Results and Discussion .....	159
7.3.1 A $\beta$ 40 CE Separation: .....	159
7.3.2 Real Time monitoring of A $\beta$ 40 Aggregation:.....	162
7.3.3 Monitoring of Aggregation Inhibitors .....	164
7.4 Conclusion .....	166
CHAPTER 8 - Sol-Gel Membranes for Preconcentration, Separation, Purification and Novel Sensors .....	167
8.1 Introduction to Sol-Gel Patterning of Membranes.....	167
8.2 Theory of Ion Depletion and Enrichment in Nanochannels .....	168
8.3 Experimental.....	171
8.4 Ion Depletion and Enrichment Using Microfluidic Membranes .....	174
8.5 Preconcentration on Titania Membranes Coupled to Separation.....	179
8.6 Titania Membrane Sensors .....	181
8.7 Conclusion .....	183
CHAPTER 9 - Coblock PEO-PDMS Polymers for $\mu$ fluidic Devices .....	183
9.1 Introduction.....	183
9.2 Experimental.....	186
9.2.1 Synthesis of PDMS-PEO Polymer .....	186
9.2.1.1 The protocol for PDMS-PEO prepolymer: .....	186
9.2.1.2 Reinforcement and Crosslinking: .....	187
9.3 Results and Discussions.....	188
9.3.1 Contact Angle and RhB Absorption Measurements.....	188
9.3.2 EOF Measurements.....	190
9.3.3 Separations on PDMS-PEO Microfluidics.....	191

CHAPTER 10 - Microfluidic Separations in Microgravity .....	193
10.1 Introduction.....	193
10.2 Sample Preparation.....	195
10.3 Chip Preparation and Operation.....	196
10.4 Results and discussion .....	196
10.5 Conclusion .....	199
CHAPTER 11 - Single Cell Analysis Using PDMS Microfluidic Devices .....	201
11.1 Introduction.....	201
11.1.2 Microfluidic Single Cell Manipulation and Analysis .....	202
11.2 Outlook .....	206
CHAPTER 12 - Summary and Closing Remarks .....	208
CHAPTER 13 - REFERENCES.....	210

## List of Figures

Figure 1.1 Demonstrates the structure of both the Novolak polymer and the Wolf Rearrangement to form a carboxylic acid. The carboxylic acid in this case helps dissolve the Novolak polymer. The exact mechanism for dissolution varies and is presently unknown. <sup>24</sup> .....	4
Figure 1.2 Mechanism of reaction for epoxy based SU-8.....	5
Figure 1.3 Photolithographic steps for the generation of micron scale features using SU-8.....	7
Figure 1.4 The micromolding of a PDMS channel using an SU-8 mold and a flat.....	8
Figure 1.5 Synthesis Scheme for the hydrosilation reaction responsible for polymerizing PDMS. The polymerization is catalyzed by a platinum catalyst which is used for polymerization of the hydride terminated PDMS and the vinyl terminated PDMS.....	9
Figure 1.6 Features molded using SU-8 lithography and PDMS soft lithography. Left: profile of a PDMS channel, Center: turn in a PDMS channel, Right: cross intersection of a PDMS channel.....	10
Figure 1.7 Electronic State diagram illustrating the singlet transition in (1), followed by an excited state relaxation (2), which yields a slightly lower electronic state, followed by an emission (3). The energy difference between S1' and S1 yield the stokes shift. <sup>37</sup> .....	16
Figure 1.8 A) Stokes Shift diagram and B) the Stokes shift of BODIPY-FL <sup>37</sup> .....	17
Figure 1.9 Fluorescent probes used for CE on microfluidic devices <sup>40</sup> .....	20
Figure 1.10 Single point setup for laser induced fluorescence detection on microfluidic devices. ....	22
Figure 1.11 Illustrates the homemade power supply used to apply 1- 5 kV/ cm electric fields....	28
Figure 2.1 Diagram of the electric double layer at the surface of a capillary. The double layer consists of the Helmholtz plane .....	30
Figure 2.2 Illustrates the location of the $\zeta$ potential within the electric double layer. <sup>46</sup> .....	33
Figure 2.3 The current monitoring method using 25 mM sodium borate, replaced with 50 mM sodium borate by EOF. The migration time in this case was 110 s. ....	35
Figure 2.4 EOF of native PDMS described as Gelest PDMS, native PDMS that was doped with methylated silica, and the commercially available Sylgard PDMS. The y axis has units of	

<p>cm<sup>2</sup>/Vs. These measurements were performed in sodium tetraborate buffer with concentration differences between 25 and 50 mM and pH ~ 9.5. Each polymer has been tested with three different pretreatments. The left (red) indicates an initial measurement with no wash, center (blue) indicates an acid-base wash, and the right (yellow) indicates a base sodium hydroxide wash. ....</p>	40
<p>Figure 2.5 FT-ATR of monomeric PDMS and polymerized PDMS. The polymerized PDMS is blue shifted which suggests larger Si-O-Si bond strain. The blue shifted areas are pointed to by the arrows.....</p>	43
<p>Figure 3.1 Schematic figure of the vast number of materials that can be generated using sol-gel chemistry.<sup>61</sup> .....</p>	45
<p>Figure 3.2 Schematic of Cross Chip used for Amino Acid Separations. The analyte, buffer, analyte waste, and separation waste reservoirs are designated as SR, BR, SW, and BW, respectively. ....</p>	52
<p>Figure 3.3 Plots of current versus field strength for both PDMS and PDMS-SiO<sub>2</sub> were consistent with Ohm's Law up to 1100 V/cm.....</p>	56
<p>Figure 3.4 TEM and Optical Images of the PDMS and PDMS-SiO<sub>2</sub> chips. TEM images of the PDMS and PDMS-SiO<sub>2</sub> are shown in A and B, respectively. Optical micrographs of the PDMS and PDMS-SiO<sub>2</sub> channel cross-sections are shown in C and D, respectively. ....</p>	60
<p>Figure 3.5 Figure 3 Young's modulus measurements on PDMS (red traces, <i>n</i> = 3, top set) and PDMS-SiO<sub>2</sub> (blue traces, <i>n</i> = 4, bottom set).....</p>	62
<p>Figure 3.6 Contact angles for PDMS and PDMS-SiO<sub>2</sub>.....</p>	63
<p>Figure 3.7 Rhodamine B Absorption Measurements. Images of PDMS (A-C) and PDMS-SiO<sub>2</sub> (D-F) devices are shown. The channels on these devices are filled with 10μM Rhodamine B in a 10 mM (pH 9.5) sodium borate solution. The images were acquired over a 4 hour period. Fluorescent profiles of the PDMS and PDMS-SiO<sub>2</sub> channels are also shown in G and H, respectively. These profiles were taken along the white dotted line in images A-F.</p>	64
<p>Figure 3.8 Separation of FITC labeled amino acids on PDMS (A) and PDMS-SiO<sub>2</sub> (B) chips. The concentration of the labeled amino acids was 2 μM. The separation distance was 3.5 cm, and the separation field strength was 650 V/cm.....</p>	68

Figure 3.9 Separation of TAMRA labeled amino acids on PDMS (A) and PDMS-SiO <sub>2</sub> (B) chips. The concentration of the labeled amino acids, the separation distance, and the separation field strength are the same as reported in Figure 3.5.....	69
Figure 3.10 Plot of migration time vs peak variance of TAMRA-serine on PDMS microchips (circles) and PDMS-SiO <sub>2</sub> microchips (squares).....	71
Figure 3.11 Left: A profile of a square PDMS channel prior to coating, Right: A profile of a square PDMS channel after it has been coated with a sol-gel film. The surface tension of the coating tends to form cylindrical profiles for the square PDMS channels, thus the thickness of the film that is formed depends on the orientation to the square side wall. ....	73
Figure 3.12 The reaction between the tin catalyst, the hydroxyl functionalized PDMS and APTES is shown. The reaction is oxygen sensitive. ....	74
Figure 3.13 Durability tests of the APTES derivitization on the PDMS surface using the coat and go coatings. The conditions used for this measurement were 25 mM sodium borate with a field strength of 300 V/cm. A higher conductivity buffer of 50 mM sodium borate was used to measure the EOF. ....	76
Figure 3.14 Thiol stationary phase generated using sol-gel chemistry on a PDMS microfluidic device. ....	77
Figure 3.15 Separations of FITC labeled amino acids on a variety of coated PDMS microfluidic channels. ....	78
Figure 4.1 A. Diffusion of titanium isopropoxide into the sidewalls of a 25 μm PDMS channel imaged over a period of 5 seconds. As the titanium isopropoxide diffuses into the PDMS a parallel interface is formed due to the differences in refractive index. B. Calculation of diffusion rate of the titanium isopropoxide into the bulk PDMS polymer yielded a linear rate of 2.6 μm/s. ....	91
Figure 4.2 Radial diffusion of titanium isopropoxide from the capillary forming a horizontally aligned waveguide. ....	91
Figure 4.3 XPS survey of PDMS, PDMS-TiO <sub>2</sub> and PDMS-ZrO <sub>2</sub> showing the O(1s) orbitals for both Si-O-Si and metal oxides. ....	94
Figure 4.4 Transmission electron microscopy images of metal oxide modified PDMS. A. PDMS, B. PDMS-SiO <sub>2</sub> , C. PDMS-TiO <sub>2</sub> , D. PDMS-vanadia, E. PDMS-ZrO <sub>2</sub> .....	95

Figure 4.5 Rhodamine B Absorption Measurements. Images of PDMS (A), PDMS-TiO<sub>2</sub> (B), PDMS-Vanadia (C), PDMS-SiO<sub>2</sub> (D), and PDMS-ZrO<sub>2</sub>(E) devices are shown. The channels on these devices are filled with 100 μM Rhodamine B in a 10 mM (pH 9.5) sodium borate solution. The images were acquired over a 4 hour period. The PDMS-Vanadia device was pulled dry and was shown to not display significant adsorption to the surface.....96

Figure 4.6 AFM images of PDMS and PDMS-TiO<sub>2</sub> taken from the interior of a microfluidic channel. (A) AFM 2D image of PDMS (10 μm × 10 μm), (B) AFM 2D image of PDMS-TiO<sub>2</sub> (10 μm × 10 μm), (C) AFM 3D image of PDMS with each division equal to 2 μm, and (D) AFM 3D image of PDMS-TiO<sub>2</sub> with each division equal to 2 μm.....98

Figure 4.7 EOM measurements using 1 mM phosphate and 10 mM KCl solutions on transition metal oxide modified PDMS, using field strength of 300 V/cm. ....99

Figure 4.8 EOM measurements using 25 mM sodium borate solutions on metal oxide modified PDMS, using field strength of 300 V/cm. .... 101

Figure 4.9 Right: Vanadia coated channel at room temp, Left: Vanadia coated channel with 2,000 V/cm applied across the channel. The heat generated from the Joule heating converted the vandia and changed its adsorbance spectrum..... 103

Figure 4.10 Left: rhodamine B doped waveguide acting as a laser rod, Center: titania doped PDMS, Right: rhodamine B and titania doped PDMS..... 104

Figure 4.11 Comparison of FITC labeled amino acids separated on PDMS and PDMS-TiO<sub>2</sub>... 106

Figure 4.12 FITC-labeled amino acids separated on PDMS-TiO<sub>2</sub> coated channels..... 106

Figure 4.13 Left: TRITC chromophore used for amine reactive labeling, Right: FITC chromophore used for amine reactive labeling..... 107

Figure 4.14 TRITC derivitized amino acids S,P,D,E,H, and R were separated on PDMS. All amino acids exhibited fairly large band broadening due to the adsorption to the sidewall of the capillary, but arginine had the largest partition coefficient with PDMS. .... 108

Figure 4.15 TRITC derivitized Amino acids S,P,D,E, and R were separated on a titania modified PDMS channel. Several amino acids most notably arginine continues to adsorb to the surface..... 108

Figure 4.16 TRITC derivitized amino acids R, S, P, E, and D separated on PEG derivitized titania..... 109

Figure 4.17 TRITC derivitized amino acids E, P, S and R separated on APTES derivitized titania. ....	110
Figure 4.18 Proteins separated on PEG-TiO <sub>2</sub> derivitized channel.....	110
Figure 4.19 Proteins and amino acids separated on APTES-TiO <sub>2</sub> derivitized channel. ....	111
Figure 5.1 Serpentine PDMS microfluidic chip with tapered turns and a 30 cm separation channel. The separation channel depth and width was 20μm and 75μm, respectively, while the tapered turns had a width of 20μm. SR: Sample Reservoir, SW: Sample Waste, BR: Buffer Reservoir, BW: Buffer waste. ....	118
Figure 5.2 Gated injections of rhodamine B on a PDMS chip with $t_{inj} = 0.2$ sec and $E = 200$ V/cm. (A) Buffer, 10 mM sodium borate; sample, 10 μM rhodamine B. (B) Buffer, 10 mM sodium tetraborate, 50 mM SDS and 20% (v/v) acetonitrile; sample 10 μM rhodamine B. ....	124
Figure 5.3 Illustrates the injection of Rhodamine B on PDMS microfluidic devices using both pinched injections (top) and gated injections (bottom). ....	125
Figure 5.4 A series of electropherograms of rhodamine B performed on PDMS microfluidic devices. Device: cross channel PDMS chip with 4.0 cm separation channel; separation distance = 3.4 cm and applied electric field = 650 V/cm; buffer: 10 mM sodium tetraborate, 50 mM SDS, 20% ACN; sample, 10 μM rhodamine B. ....	127
Figure 5.5 Electropherogram of 10 μM rhodamine B, tryptophan, phenylalanine, serine, proline, aspartic acid. Device: cross channel PDMS chip with 4.0 cm separation channel; separation distance = 3.65 cm and applied electric field = 650 V/cm; buffer, 10 mM sodium tetraborate, 50 mM SDS, 20% ACN. ....	128
Figure 5.6 Electropherogram of 17 labeled BODIPY amino acids; device: serpentine channel PDMS chip with 30 cm separation channel; separation distance of 27 cm and applied electric field of 750 V/cm; buffer: 10 mM sodium tetraborate, 50 mM SDS, 20% acetonitrile.....	130
Figure 5.7 Efficiency of glutamic acid and arginine labeled with BODIPY as a function of migration time. Electropherograms were collected using buffer of 10 mM sodium tetraborate, 50 mM SDS, and 20% acetonitrile, separation field strengths for the separation were 750 V/ cm. ....	131

Figure 5.8 Electropherogram of AlexaFluor 488 TFP labeled E-coli. homogenate; device: serpentine channel PDMS chip with 30 cm separation channel; separation distance of 20 cm and applied electric field of 750 V/cm; buffer: 10 mM sodium tetraborate, 50 mM SDS, 20% ACN..... 133

Figure 6.1 Electropherograms of standard proteins; buffers: 0 mM SDS, 5 mM SDS, 25 mM SDS, all with 10 mM sodium borate and 20% ACN; analytes: cytochrome c, lysozyme, ribonuclease A and myoglobin in order of shortest to longest migration time, analytes diluted 1:100 from labeling cocktail; device: cross channel PDMS chip with a 4.0 cm separation channel detected at 2.5 cm, and a field strength of 650 V/cm. .... 143

Figure 6.2 Electropherogram of BSA-AF; buffer: 25 mM SDS, 10 mM sodium borate, 20% acetonitrile; analytes: BSA AlexaFluor 488 with 1:100 dilution from labeling cocktail; device: PDMS cross channel chip, field strength of 850 V/cm at a detection distance 3.0 cm. The minor peak located at 16.9 s is either a protein contaminate, or a result of an isomer of AlexaFluor 488..... 145

Figure 6.3 Electropherogram of lysozyme, cytochrome c, myoglobin, ribonuclease A and  $\alpha$ -lactalbumin; buffer: 10 mM sodium borate, 25 mM SDS, and 20% acetonitrile; analytes: standard proteins diluted 1:100 from labeling cocktail; device: cross channel PDMS chip with a 4.0 cm PDMS separation channel detected at 3.0 cm with a field strength of 650 V/cm. .... 146

Figure 6.4 Electropherogram of lysozyme, cytochrome c, myoglobin, ribonuclease A, BSA,  $\alpha$ -lactalbumin; buffer: 25 mM SDS, 10 mM sodium borate and 20% ACN; analytes: standard protein diluted 1:100 from labeling cocktail; device: cross channel PDMS chip with a 4.0 cm PDMS separation channel detected at 2.0 cm with a field strength of 1,200 V/cm. .... 147

Figure 6.5 Separation efficiency of BSA-AF and resolution between myoglobin-AF and BSA-AF as a function of both separation distance and time; buffer: 25 mM SDS, 10 mM sodium borate and 20% ACN; analytes: standard proteins diluted 1:100 from labeling cocktail; device, serpentine chip with field strength of 150 V/cm. Closed circles represent efficiency versus migration time. Closed squares represent resolution versus migration distance..... 149

Figure 6.6 Electropherogram of an *E. coli* homogenate of metabolic amines doped with internal protein standards of lysozyme-AF and  $\alpha$ -lactalbumin-AF that were diluted 1:100 from the

labeling cocktail, device: serpentine chip with detection length of 25 cm; buffer: 25 mM SDS, 10 mM sodium borate and 20% ACN. ....	151
Figure 7.1 Schematic of Cross Chip used for A $\beta$ 40 peptide separations. The chip is fabricated using the glass etching and bonding protocols listed in the experimental section.....	161
Figure 7.2 An electropherogram of A $\beta$ 40 generated using glass microfluidic device. Device: cross channel glass chip with 2.0 cm separation distance and applied electric field of 200 V/cm; buffer: 20% TFE and 20 mM sodium phosphate buffer at pH 7.4; sample, 1 $\mu$ M A $\beta$ 40 peptides. ....	162
Figure 7.3 A series of electropherograms of A $\beta$ 40 filtered with MWCO filters to isolate specific oligomers. Device: cross channel glass chip with 2.0 cm separation distance and applied electric field of 200 V/cm; buffer: 20% TFE and 20 mM sodium phosphate buffer at pH 7.4; sample, 1 $\mu$ M A $\beta$ 40 peptides. ....	163
Figure 7.4 A series of electropherograms of A $\beta$ 40 separated continuously over 3 hrs to monitor the formation of larger aggregates. Device: cross channel glass chip with 2.0 cm separation distance and applied electric field of 200 V/cm; buffer: 20% TFE and 20 mM sodium phosphate buffer at pH 7.4; sample, 1 $\mu$ M A $\beta$ 40 peptides. ....	164
Figure 7.5 A series of electropherograms of A $\beta$ 40 separated continuously over 3 hrs with the presence of toluidine blue O. Device: cross channel glass chip with 2.0 cm separation distance and applied electric field of 200 V/cm; buffer: 20% TFE and 20 mM sodium phosphate buffer at pH 7.4; sample, 1 $\mu$ M A $\beta$ 40 peptides and 1 $\mu$ M toluidine blue O. ....	165
Figure 7.6 A series of electropherograms of A $\beta$ 40 separated continuously over 3 hrs with the presence of CP2, a novel synthetic inhibitor. Device: cross channel glass chip with 2.0 cm separation distance and applied electric field of 200 V/cm; buffer: 20% TFE and 20 mM sodium phosphate buffer at pH 7.4; sample, 1 $\mu$ M A $\beta$ 40 peptides, and 1 $\mu$ M CP2. ....	166
Figure 8.1 Green arrows indicate the movement of cations, whereas orange arrows indicate the movement of anions through the nanochannel circuit.....	170
Figure 8.2 Schematic of membrane fabrication within a microfluidic manifold. ....	173
Figure 8.3 A) Optical micrograph of a 4 $\mu$ m x 75 $\mu$ m x 20 $\mu$ m titania membrane fabricated within a glass microfluidic manifold. B) Multiphoton XY scans at various depths within the	

glass channel ( $z = 4 \mu\text{m}, 8 \mu\text{m}, 12 \mu\text{m}, 16 \mu\text{m}$ ). C) PDMS microfluidic device with a membrane fabricated at the intersection. ....	174
Figure 8.4 A) Preconcentration voltage scheme for amino acids, proteins and latex particles, B) Series of CCD images of the preconcentrated plug near the charge depleted region that was formed by the titania membrane. The imaged area is illustrated in the voltage scheme above. The buffer was 80 mM sodium phosphate at pH of 11.5, 110 V/cm applied across the membrane and 150 nM lysozyme concentration. Color scale shows fluorescence, red: max, black: min. ....	175
Figure 8.5 Plot of three different fluorescein concentrations that were preconcentrated against a $20 \mu\text{m} \times 20 \mu\text{m} \times 100 \mu\text{m}$ titania membrane in a glass microfluidic manifold. The run buffer was 20 mM sodium phosphate, pH = 11.5, with an electric field of 110 V/cm applied across the membrane. ....	176
Figure 8.6 Ion enrichment and depletion zones monitored by epi-illumination microscopy. Initially the channel manifolds were filled with 1 mM fluorescein in 80 mM sodium tetraborate at pH 11.5. The concentration enrichment and depletion was performed after applying a field strength of 100 V/cm across the membrane while floating the other two reservoirs. Colorscale shows fluorescence, min: blue, max: white. ....	177
Figure 8.7 Preconcentration studies performed using identical titania membranes with different buffer compositions. The membrane was demonstrated to preconcentrate on opposite side. ....	178
Figure 8.8 Ion depletion of fluorescein demonstrated in the far left channel, over time the ions are depleted in this region and the sample is deionized yielding very low currents. ....	179
Figure 8.9 Voltage scheme for preconcentration and electrophoretic separation. ....	180
Figure 8.10 Preconcentration of 150 pM lysozyme and separation using the voltage scheme shown in Figure 8.9. The peaks shown here indicate the hydrolysis of the protein under extremely basic conditions. The buffer used was 80 mM sodium phosphate at a pH of 11.5. ....	181
Figure 8.11 Titania sensors functionalized with Nile red. Left: Nile-Red-Titania membrane in H <sub>2</sub> O, Right: Nile-Red-Titania membrane in hexane. ....	182
Figure 8.12 Measurement of membrane fluorescence for a number of solvents. ....	182
Figure 9.1 Diagram of a PDMS surface generated under air. ....	185

Figure 9.2 Diagram of a PDMS-PEO surface generated under water after the PEO reorients itself at the interface.....	185
Figure 9.3 Reaction scheme for the copolymer synthesis of PDMS-PEO.....	187
Figure 9.4: Left: PDMS-PEO well formed using a stamping method, Right: PDMS-PEO channels formed using SU-8 molds.....	188
Figure 9.5 Contact angles of PDMS-PEO (40°) and PDMS (110°).....	189
Figure 9.6 Rhodamine B absorption profiles for PDMS-PEO microfluidics.....	190
Figure 9.7 Separations of TAMRA labeled amino acids on PDMS and PDMS-PEO.....	192
Figure 10.1 FTC Chip design .....	194
Figure 10.2 FTC External Pumping Schematic .....	195
Figure 10.3 On-line sample of AA's in zero gravity. ....	197
Figure 10.4 Online sampling of reGFP using the flow through chip.....	198
Figure 10.5 On-line sample of reGFP and separation using the flow through chip. ....	199
Figure 11.1 Schematic of the various types of methods reported for transporting and manipulating cells. (A) Cells can be hydrodynamically focused at an intersection so that they all flow past an interrogation region in single file. (B) Cells can be hydrodynamically transported to an intersection where they can be lysed either electrically or chemically and the lysate injected into a separation channel. (C) Cells can be incorporated into droplets and hydrodynamically transported to an interrogation region. Cells can be trapped geometrically using pillars (D), weirs (E), or hydrodynamically balanced flows (F).....	203
Figure 11.2 A) Schematic illustrating a cross section of a PDMS microfluidic device designed for microfluidic elastomeric valving. Two cross sections are illustrated including an unactuated valve and an actuated valve. The actuated valve has a high pressure of ~ 25 kPa applied to the actuation channel which causes the PDMS membrane to deform into the fluidic channel below. This can function as a check valve or when applied in series can be used as a peristaltic pump. B) A fluidic channel was filled with 10 mM fluorescein and imaged prior to valve actuation (left) and during valve actuation (right). After the valve is actuated the fluorescein is displaced yielding a low intensity in the areas of the membrane depression. White lines represent areas where the actuation channel is located relative to the fluidic channel. C) Three actuation valves labeled 1-3 were positioned around a fluidic cross intersection labeled with an arrow. The fluidic cross intersection allows for the transport of	

cells either hydrodynamically or electrokinetically. D) Trapping of a single cell is accomplished by transporting it to the intersection hydrodynamically followed by isolation by actuating check valves 1-3. A single Jurkat cell loaded with Calcein AM is shown trapped at the cross intersection. ....205

## List of Tables

Table 1 Electroosmotic flow of a series of polymers and glass using phosphate buffers measured using the current monitoring method. ....	47
Table 2 Migration times, separation efficiencies, and rate of plate generation for fluorescently labeled amino acids on PDMS and PDMS-SiO <sub>2</sub> chips. Three replicate measurements were made to obtain the average values and standard deviations reported above. The number in parentheses next to the analytes are their nominal charges. ....	67
Table 3 X-ray photoelectron spectra of oxygen (1s) and carbon (1s), silicon (2s) and silicon (2p) of PDMS and the PDMS transition metal oxides.....	93
Table 4 Number of plates, standard deviation of the number of plates, plates per second, plate height, and plates per meter for proteins labeled with AlexaFluor 488 and separated on a 4.0 cm PDMS cross channel chip with a detection point of 3.0 cm using 25 mM SDS, 10 mM sodium borate and 20% ACN. The applied field strength was 650 V/cm.....	148
Table 5 Efficiencies obtained on PDMS and PDMS-PEO for TAMRA labeled amino acids. ...	192

## Acknowledgements

To all the people who have helped me through my graduate work, teachers, coauthors, friends and family: thank you. Your wisdom and guidance has been instrumental in helping provide a path to traverse and your friendship and company has provided the proverbial light at the end of the tunnel.

Especially to Chris: Sometimes it seems like it was just yesterday that I walked into your tiny office, near the boats, with a full beard and long scrappy hair, and we discussed projects ranging from designing neutrally charged fluorophores, 2D protein separations using quake valving, and designing octyldecyl derivitized PDMS to partion SDS at the surface. All of this while jumping on a mini-trampoline. I must say I have come a long way over the past four years. I have to thank you for teaching me a tremendous amount of optics, electronics, and separation science that will hopefully serve as a healthy basis for my research pursuits over the next thirty years. Your energy and enthusiasm is contagious and your ability to merge family and a vigorous academic research group is inspiration to us all that it is all possible.

Especially to Amanda and Pernilla: Some people you meet in life are simply acquaintances, others may call themselves friends, and then there are really good friends (RGF's). RGF's are the kind of people you will always keep in touch with, and for some reason will always remember, simply because they are just good people. Thanks for being an RGF! I had never known about the aerosolized bacteria that emerge from a toilet immediately after usage until I met you! Thanks a lot...

## **Dedication**

This work is dedicated to my nearest and dearest, Laura. Thank you for your support, wisdom, and sacrifice during these years in Kansas.

## CHAPTER 1 - Introduction

Microfluidic devices were originally developed to sample microliter volumes for biological applications.<sup>1</sup> Over the last decade microfluidic technologies have burgeoned into a multi-million dollar industry aimed at analyzing low concentration biomolecules such as proteins, mRNA, or DNA. Microfluidic devices have the potential to transform the chemical lab-bench in a similar fashion to how the transistor and semiconductor industry transformed electrical engineering. Miniaturization of microfluidic components allows both high throughput analysis and low detection limits for biochemical analysis. The high throughput capability of microfluidics could potentially generate thousands to millions of chemical assays per day, which could begin to address some of the issues surrounding the biochemical complexity of cellular systems. Some other advantages that microfluidic technologies offer for chemical analysis derive from the fundamental fluid dynamics that is exhibited by channels or capillaries with diameters  $< 100 \mu\text{m}$ .<sup>2</sup> Generally, such channels have laminar flow, low convection and limit dilution. The fluid dynamics of microfluidic channels can be employed to generate a number of novel experiments that can't be generated using conventional techniques. Some include the ability to manipulate single cells<sup>3</sup>, perform single cell assays<sup>4</sup> or generate complex concentration gradients<sup>5</sup>. These devices also offer the capability of integrating multiple chemical processing steps along with separations in a single channel manifold so that a complete chemical analysis can be performed on a chip. The advantages of such a strategy over conventional chemical analysis instrumentation are manifest and include: 1) automation, 2) reduced consumption of reagents and analytes, 3) reduced waste generation, 4) high speed analysis with

equivalent/increased performance, 5) operational simplicity, and 6) compactness. Many different types of chemical manipulations and separations have been demonstrated on microfluidic devices which confirm these advantages, and several books and reviews are written annually to report such progress.<sup>6-20</sup>

The following sections of this chapter I will describe how to fabricate microfluidic devices, physical and chemical properties of microfluidics, laser induced fluorescence which can be used as a detection scheme, and capillary electrophoresis which can be used as a separation scheme on microfluidics. These topics will introduce the fundamental background for my dissertation. I also take some time in this section to introduce the basic science behind many of the topics that are at the heart of my dissertation.

## **1.1 Microfluidic Fabrication**

The inception of the semiconductor industry in the early 1980s has led to a number of well characterized techniques for fabricating micron scale features. Some common micro and nano features that can be fabricated using semiconductor lithographic techniques include, rods, trenches, needles, wires and platforms. Some common fabrication tools include, low pressure chemical vapor deposition (LPCVD), reactive ion etching (RIE), positive and negative tone photoresist, wet chemical etching, and evaporative metal vapor deposition. A common tool in photolithography includes the “stepper” which is a device that allows for nanometer alignment of mask layers, known as registration, and is currently available in state-of-the-art configurations for nearly \$10 million. More exotic non-photolithographic techniques include e-beam lithography, X-ray, ion beam milling and “dip-pin” AFM which has been demonstrated to be capable of achieving, at best, 1 nm features. Although these non-photolithographic techniques can generate high resolution and low feature size they all have serious limitations in a

commercial atmosphere; thus, photolithography is by choice the most robust technique for generating micron scale features.

### ***1.1.1 Photolithography***

Gordon Moore, the Intel founder, observed the trend of smaller IC's with time, affectionately known as Moore's Law. Specifically, Moore's Law suggests that the number of electrical components within a specified area, for instance transistors, doubles every 18 months. Photolithography is currently one of the primary challenges to the engineering community for developing smaller integrated circuits (IC's).

Photolithography is limited by the physical properties of light. The Rayleigh equation, E.1., describes the resolution that can be obtained using a given wavelength and objective, where  $\lambda$  and NA are the wavelength and numerical aperture of the light and lense.<sup>21</sup>

$$E.1 : R = \frac{k\lambda}{NA}$$

Although the Rayleigh equation suggests the theoretical resolution limit of  $\sim \lambda/2$ , the practical limit is much closer to  $\lambda$  due to chromatic aberrations and light scattering. Some methods of improvement include shorter wavelength UV optics, higher NA objectives, vibration isolation, and cleaner facilities. The current minimum feature size that can be obtained using photolithography is 180 nm.<sup>22</sup> This feature size was performed using state-of-the-art instrumentation. It is commonly accepted that 1  $\mu\text{m}$  features can be easily generated using standard photolithography instrumentation and techniques.<sup>23</sup>

### 1.1.2 SU-8 Resist Photolithography

Photoresist generally comes in two forms: positive and negative. The terminology refers to the areas of removal after exposure. Positive refers to the removal of areas that have been exposed, whereas negative refers to areas removed that have not been exposed. Positive photoresists have photoactive elements which will weaken the polymer matrix, allowing them to be dissolved when developed. For example, the Novolak polymer with some diazonaphthaquinone dissolved in it is considered a positive photoresist.<sup>24</sup> When the diazonaphthaquinone is irradiated it undergoes a Wolf Rearrangement to form a carboxylic acid. The carboxylic acid assists in the dissolution of the coating and can generate high resolution features, shown in **Figure 1.1**. It has been observed that positive photoresists yield the highest resolution and are the most common photoresists found in the IC industry.<sup>25</sup>

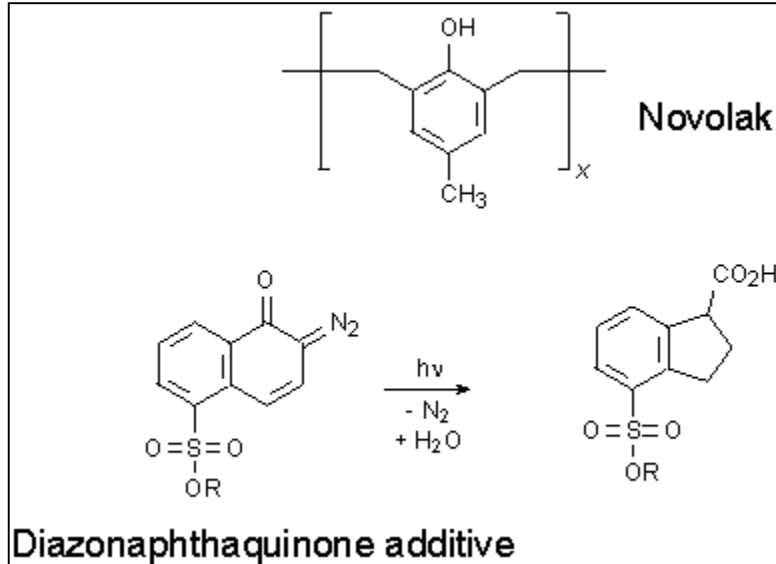


**Figure 1.1** Demonstrates the structure of both the Novolak polymer and the Wolf Rearrangement to form a carboxylic acid. The carboxylic acid in this case helps dissolve the Novolak polymer. The exact mechanism for dissolution varies and is presently unknown.<sup>24</sup>

Negative photoresists on the other hand have photoactive elements which polymerize the polymer and are not dissolved when developed. A popular negative photoresist is SU-8 and has been used extensively for the fabrication of molds for microfluidic devices. SU-8 is an epoxy based photoresist which is polymerized through a cation polymerization mechanism. The commercial resist contains three basic components: 1) an epoxy called EPON SU8, 2) a solvent called gamma-butyrolactone (GBL), and 3) a photoinitiator from the triarylium-sulfonium salt family.<sup>26</sup> The photoinitiator,  $\text{HSbF}_6$ , generates protons when exposed to light. These protons protonate the epoxy ring, and entices the nucleophilic attack from a nucleophile, in this case an alcohol. After the nucleophilic attack the epoxy ring is opened generating another alcohol. The alcohol can next react with another epoxy and further polymerize the polymer. The mechanism for this reaction is shown in **Figure 1.2**.

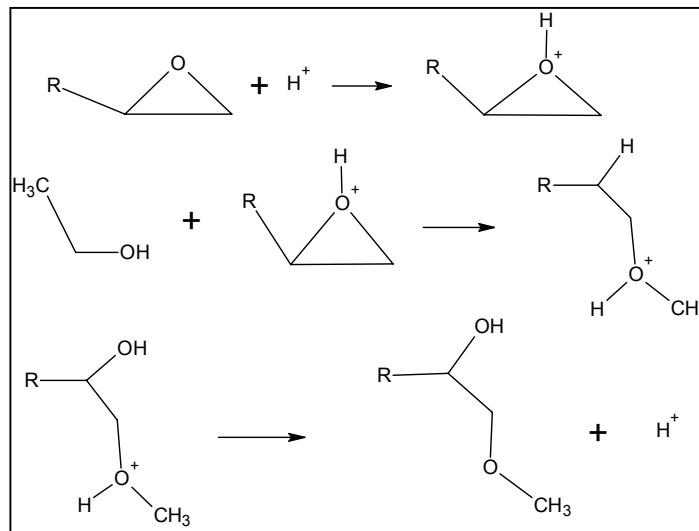


**Figure 1.2** Mechanism of reaction for epoxy based SU-8.

When using SU-8 for the development of lithographic features generally the SU-8 is spin coated onto a glass or silica substrate. First a series of thorough cleansing steps must be applied

to the substrates to remove any debris that may affect the adhesion of the SU-8. Sodium dodecyl sulfate, acid and base wash, followed by 200°C drying for 2 hrs is used to initially prepare the substrates. Additional adhesion promoters have been used to further assist in the attachment of the SU-8 to the substrate. Some of these adhesion promoters include epoxy derivitized silanes such as: 5,6- epoxyhexyltriethoxysilane which will covalently bond to the silicon under a silanization procedure, and the epoxy, upon irradiation, will attach to the bulk of the SU-8. After spin coating the resist on the cleaned and treated substrate, a mask is aligned onto the photoresist and is placed under a UV flood exposure system. The flood exposure systems use mercury arc lamps that have a number of intense lines in the UV region including: 280-290 nm, 310-320 nm, and 360-370 nm. For SU-8 processing the 360-370 nm emission line of the mercury arc lamp is used. The collimated light that exits the lens of the flood exposure is used to expose the photoresist in spatial areas defined by the mask. After the exposure the photoresist is placed through a series of development steps aimed at removing any un-polymerized polymer, resulting in a series of raised edges which will be used for soft polymer lithography. **In Figure 1.3**, the steps of the photolithographic process are illustrated.

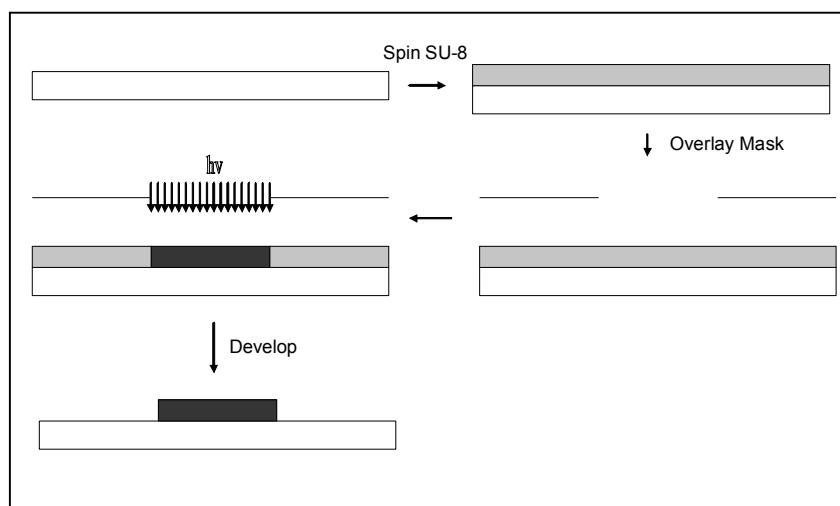


**Figure 1.3** Photolithographic steps for the generation of micron scale features using SU-8.

### ***1.1.3 Soft Lithography***

Soft lithography is a technique of fabricating micron-scale structures using a variety of polymers. It goes by many names some including: replica molding (REM), microcontact printing (uCP), micromolding in capillaries (MIMIC), micro-transfer molding (uTM), solvent-assisted micromolding (SAMIM), and near-field conformal photolithography.<sup>27</sup> Soft lithography is extremely convenient for biological applications that require features  $\geq 10 \mu\text{m}$ . The two primary features of soft lithography include: 1) use of an elastomeric material that is capable of micromolding, and 2) ability to pattern complex biochemicals using PDMS stamps.<sup>28</sup>

Soft lithography relies on a mold that was described in section 1.1.2. This mold defines the features that will be replicated in the polymer. In this case, poly(dimethylsiloxane) is used primarily due to its physical properties, some including a) low interfacial free energy ( $\sim 21.6 \text{ dyn/cm}$ ), b) inertness, c) gas permeability, d) optically transparent down to  $\sim 300 \text{ nm}$ , and e) durability.<sup>29</sup> Soft lithography has been demonstrated to be capable of obtaining features between

30-80 nm. Some fundamental advantages of this method is that it is extremely fast with concept to chip times in under 24 hrs, inexpensive, and can be implemented using a wide variety of different polymers, not just PDMS.

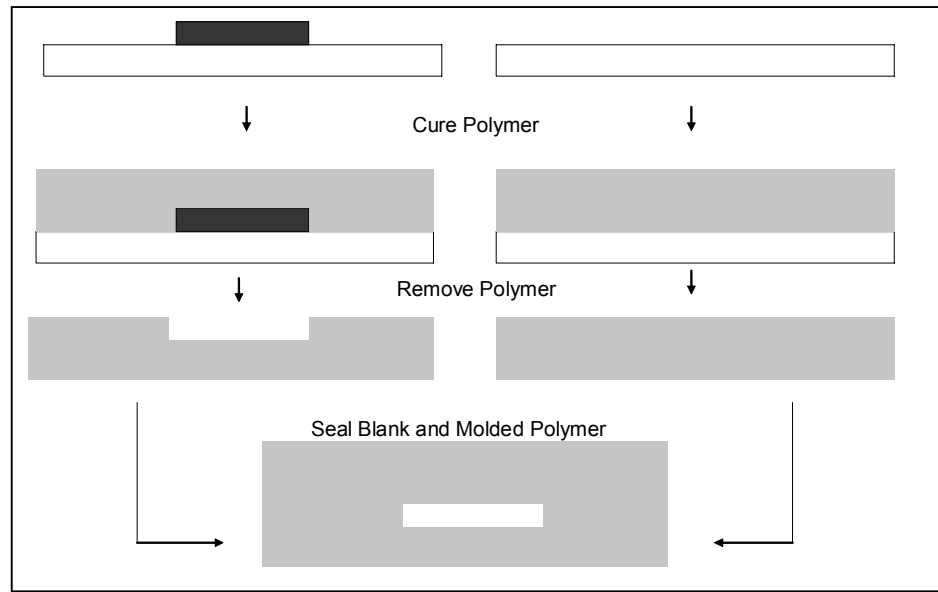


**Figure 1.4** The micromolding of a PDMS channel using an SU-8 mold and a flat.

The fabrication scheme for PDMS microchips is illustrated in **Figure 1.4**. First a mold is cleaned of any debris by either acetone or dry nitrogen. After the mold has been cleaned the polymer is constituted and applied to the mold, cured and removed from the mold. Several polymers are available for soft polymer lithography, most notably poly(vinyl alcohol) (PVA), poly(dimethylsiloxane) (PDMS) and poly(methylmethacrylate) (PMMA). Generally, the polymerization procedure involves mixing two reactive monomers with a catalyst, degassing the polymer to remove air bubbles, and consequently pouring this mixture onto a glass slide and the mold. After a set amount of “cure time” the polymer is mechanically strong enough to release from the mold and can be placed in conformal contact with a PDMS flat. The surface energy of

the PDMS generates a conformal bond that can generate water tight microfluidic manifolds. In the case of PDMS and PVA the low surface energy usually forms a water tight conformal bond, but often times an irreversible bond is desired and this involves surface plasma ionization to ionize the surface to irreversibly bond the two surfaces. An irreversibly bonded chip can be generated by first plasma oxidizing the surface of the PDMS with a corona discharge. The oxidation generates extremely reactive silanol functionalities at the surface. Once two slabs of PDMS have been oxidized they are placed in conformal contact, the reactive moieties react to form an irreversibly bonded substrate.

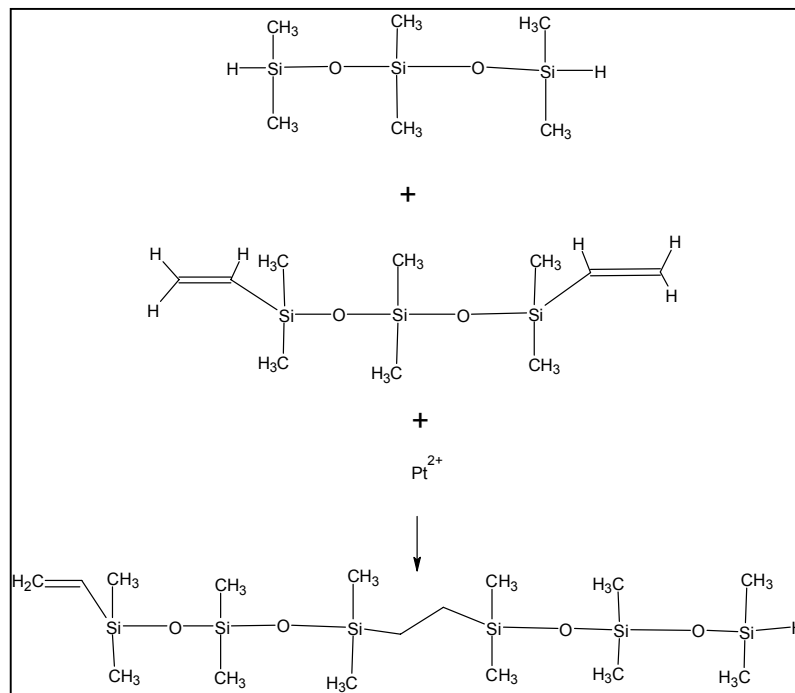


**Figure 1.5** Synthesis Scheme for the hydrosilylation reaction responsible for polymerizing PDMS. The polymerization is catalyzed by a platinum catalyst which is used for polymerization of the hydride terminated PDMS and the vinyl terminated PDMS.

Using both SU-8 photolithography and soft polymer lithography we were able to generate a number of microfluidic manifolds. The resulting PDMS channels are illustrated in **Figure 1.6**.

Several aspects are important in characterizing the features that are generated in microfluidic fabrication including the aspect ratio of the features, the resolution, and smallest feature size. Using 8,000 dpi masks we were capable of easily fabricating 20  $\mu\text{m}$  diameter channels, with variable depths between 5 and 50  $\mu\text{m}$ . The aspect ratio is generally the height of a feature divided by the width of the feature. Thus, high aspect ratio features are generally very tall and slender, whereas low aspect ratio features are short and squat. Our aspect ratios were approximately 1.

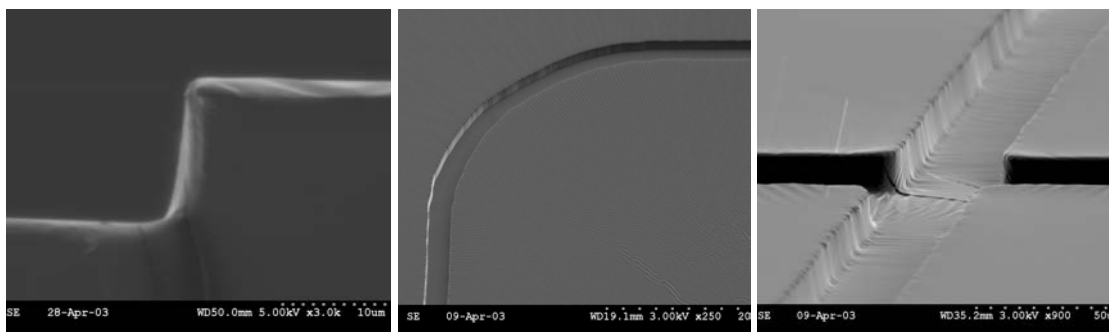


**Figure 1.6** Features molded using SU-8 lithography and PDMS soft lithography. Left: profile of a PDMS channel, Center: turn in a PDMS channel, Right: cross intersection of a PDMS channel.

## 1.2 Fluid Dynamics of Microfluidics

Microfluidic devices have the potential of fundamentally changing the way chemical analysis is performed, specifically with biochemical analysis. Many characteristics of microfluidics that lend itself useful for chemical analysis derive directly from the fluid dynamics of micron scale channels. For instance micron diameter channels or capillaries have low Peclet and Reynolds numbers that result in low convection and laminar flow, respectively. Additionally, the large surface area to volume ratio of microfluidic channels leads to a number of interesting phenomena including capillarity. These fluidic characteristics can be used to generate stable chemical gradients, virtual walls and emulsions. The use of microfluidic devices allow for

techniques and experiments which are impossible with conventional macroscale techniques, thus yielding new functionality or experimental paradigms.

### ***1.2.1 Reynolds Number and Laminar Flow***

The fluid dynamics within microfluidic devices are classified by the Reynolds number. The Reynolds number relates the fluid density ( $\rho$ ), velocity ( $v$ ), viscosity ( $\mu$ ) and hydraulic diameter ( $D$ ). The Reynolds number also relates the inertial to the viscous forces shown in equation E.2.

$$E.2 : \text{Re} = \frac{\rho v D}{\mu}$$

The Reynolds number is a unit-less quantity that describes the turbulence of fluid flow within a cylindrical capillary. A Reynolds number  $< 2,300$  indicates a non turbulent flow, although as the Reynolds number approaches 2,300 the fluid flow becomes more turbulent in nature.<sup>30</sup> The Reynolds number for capillaries with diameters of  $< 100 \mu\text{m}$  and low fluid viscosities (i.e.  $\text{H}_2\text{O}$ ) is often  $< 1$ . Two laminar flow streams that meet will simply mix by diffusion alone, which can be used for several different experiments including molecular mass sensors, chemical assays, membraneless microfluidic fuel cells, immunoassays, chemotaxis studies, and intracellular protein trafficking.<sup>30</sup> We will show a neat example of microfluidic membrane fabrication using laminar flow in Chapter 8.

### ***1.2.2 Diffusion***

Diffusion can be considered to be the Brownian motion of a molecule or particle in a volume element.<sup>30</sup> Diffusion is described in one dimension using the Einstein-Smoluchowski

equation E.3, where  $\sigma$ ,  $D$ , and  $t$  are the variance, diffusion coefficient, and  $t$  assuming a Gaussian diffusion profile.

$$E.3: \sigma^2 = 2Dt$$

Sigma can be considered the distance a particle or molecule moves in the time element  $t$ . The squared dependence of the spatial motion of a molecule is extremely important. For example, it takes approximately a billion seconds for Lysozyme to diffuse 1 cm, but only 1 second for it to diffuse 10  $\mu\text{m}$ .<sup>30</sup> The importance of this fact has been utilized thoroughly in biological systems that work at the nano- micro scale. Many physiological events heavily depend on the diffusion of biomolecules. Since the diffusion times are relatively fast for microscale systems a number of novel experiments can be developed, for example using diffusive mixing or the generation of concentration gradients using diffusion and laminar flow. We use the Einstein Smoluchowski equation to calculate the effective diffusion coefficients for several different compounds to assess the efficiency of our chemical separations.

### ***1.2.3 Fluidic Resistance***

The flow rate within a microfluidic device is proportional to the change in pressure ( $\Delta P$ ) and inversely proportional to the resistance of the fluidic flow ( $R$ ), shown in E.4.

$$E.4: Q = \frac{\Delta P}{R}$$

This approximation can be used to program a number of fluidic operations, specifically those that require hydrodynamic fluidic flows. The resistance for a capillary can be calculated from equation E.5 where  $\mu$  is the fluid viscosity,  $L$  is the channel length, and  $r$  is the radius of the capillary.

$$E.5 : R = \frac{8\mu L}{\pi r^2}$$

The flow rate with the resistance substituted in E.4. yields equation E.6. This again describes the flow rate for a capillary.

$$E.6 : Q = \frac{\Delta P \pi r^2}{8\mu L}$$

In most microfluidic devices the channels are rectangular rather than cylindrical. Thus the average flow rate for a rectangular capillary is described in E.7.<sup>31</sup> Where w, d, and L are the half width, half depth and length of the channel, respectively and  $\mu$  is the viscosity,  $\Delta P$  is the pressure difference and F is a form factor.

$$E.7 : Q = \frac{wd}{\mu} \frac{\Delta P}{L} F$$

$$E.7.1 : \Delta P = \frac{\mu L Q}{wdF} = Q \frac{4}{A} \frac{\mu L}{F}$$

Equation E.7 can be rewritten in the form E.8, where the cross sectional area is A.

$$E.8 : \Delta P = \frac{Q}{A} \left( \frac{\mu L}{wdf} \right) = Q \left( \frac{4\mu L}{(wd)^2 F} \right)$$

Interestingly there is an analogy that can be established between volumetric flow and electronic current. For example,  $\Delta P$  can be viewed as a voltage difference, while Q can be viewed as an electronic current flow. In electronic circuits Kirchoff's laws is used to describe the additive nature of voltages and currents. The same is also true for bulk fluid flow where  $\Delta P$  and Q are also additive in nature. Ohm's law,  $V = IR$ , can be rewritten as  $\Delta P = Qr$ , where the fluidic resistance of a square channel is approximated in E.9.

$$E.9 : r = \frac{4\mu L}{AF}$$

This analogy has several consequences, some of them being relationships between how electrical resistances are calculated when they are placed in a parallel format or a series format. For instance, flow resistances will add when they are located in series, but alternatively they will add inversely when placed in parallel. These points are critical when determining fluid flow in a complex microfluidic circuit.<sup>31</sup>

### ***1.2.4 Surface area to Volume Ratio***

As lateral dimensions of fluidic systems decrease the surface area to volume ratios often increase dramatically. For instance, a Petri dish with a 35 mm diameter that contains 2.5 mL will have a surface area to volume ratio of  $4.2 \text{ cm}^{-1}$ . On the other hand a  $50 \mu\text{m}$  wide,  $30 \mu\text{m}$  long, 75 nL volume microfluidic channel will have a surface area to volume ratio of nearly  $800 \text{ cm}^{-1}$ .<sup>30</sup> The huge difference in surface area to volume ratios can have dramatic effects on microfluidic performance.<sup>30</sup> Thus being able to modify the surface characteristics of a microfluidic channel can be critical to developing an analytical technique for microfluidic devices.

### ***1.2.5 Surface Tension***

Intermolecular interactions between molecules at the surface of a solution give rise to what is defined as surface tension.<sup>30</sup> The surface free energy quantitatively analyzes the strength of these intermolecular interactions at the surface and translates into a tension or cohesion of a surface ( $\gamma$ ). The surface tension is the phenomena that allows spiders to walk on a water surface. The spiders legs distributes its weight over an area that is large enough to support its weight. We employ surface tension to apply some thick coatings on the sidewall of capillaries in section 3.6.

Surface tension or energy has been used in microfluidic devices to further explore the development of virtual walls. The Young-Laplace equation, E.10 is often a good starting point

for a discussion of surface tension in microfluidic channels. In the Young Laplace equation,  $R_1$  and  $R_2$  represent the radii of curvature for a liquid interface. Gamma ( $\gamma$ ) represents the surface tension of the specific solution.

$$E.10 : \Delta P = \gamma \left( \frac{1}{R_1} + \frac{1}{R_2} \right)$$

The  $R$  that defines the wall will go to infinity hence dropping it out of the equation, simplifying to E.11.

$$E.11 : \Delta P = \frac{\gamma}{R}$$

This is the pressure apparent between two parallel plates separated by distance  $2R$ . If the surface is spherical the equation reduces to E.12.

$$E.12 : \Delta P = \frac{2\gamma}{R}$$

## **1.3 Laser Induced Fluorescence**

### ***1.3.1 Introduction***

The detection of single molecules represents the ultimate sensitivity for a chemical assay. The sensitivity of fluorescence has allowed a number of different applications including flow cytometry<sup>3</sup>, chromatography<sup>32</sup>, electrophoresis<sup>33,34</sup>, and DNA sequencing<sup>35</sup>. Over the last decade fluorescence has been used to detect single molecules with detection limits down to the low picomolar limit<sup>36</sup>. In addition, a number of new fluorescent probes have been synthesized which allow research on specific biomolecular assemblies, some including: reactivities of individual lactate dehydrogenase, individual adenosine triphosphate (ATP) molecules have been visualized

on single myosin molecules, intramolecular transitions, and a number of photochemical reactions.

### 1.3.2 Theory

Fluorophores are often polyaromatic compounds which react through a variety of reactive functional groups that localize it to a specific biomolecule. The absorption and emission properties of a fluorophore allow researchers to locate this compound within a biological specimen. The physical process that is responsible for the absorption and emission properties of a fluorophore is illustrated in the electronic state diagram (i.e. Jablonski Diagram) in **Figure 1.7**.

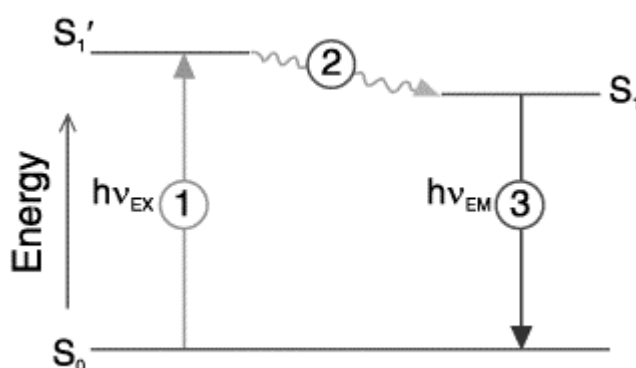


**Figure 1.7** Electronic State diagram illustrating the singlet transition in (1), followed by an excited state relaxation (2), which yields a slightly lower electronic state, followed by an emission (3). The energy difference between  $S_1'$  and  $S_1$  yield the Stokes shift.<sup>37</sup>

A photon produced by an external excitation source such as a laser drives the fluorophore into an excited singlet state. It should be noted that chemiluminescence is different from fluorescence in that a chemical reaction populates the singlet state rather than a photon from a light source. The excited state electron exists for 1-10 ns before relaxing back to the ground state. During this finite time period a number of phenomena can depopulate the singlet state including rotational and vibrational relaxation. The energy dissipation during the excited state is responsible for a

Stokes shift. A Stokes shift is the difference between the absorption spectra and the emission spectra. Experimentally, the Stokes shift is extremely important. The shift in wavelength allows for the isolation of excitation light from emission light using a number of bandpass or holographic notch filters. This results in low backgrounds and high signal to noise ratios. The Stokes shift is shown in **Figure 1.8**.

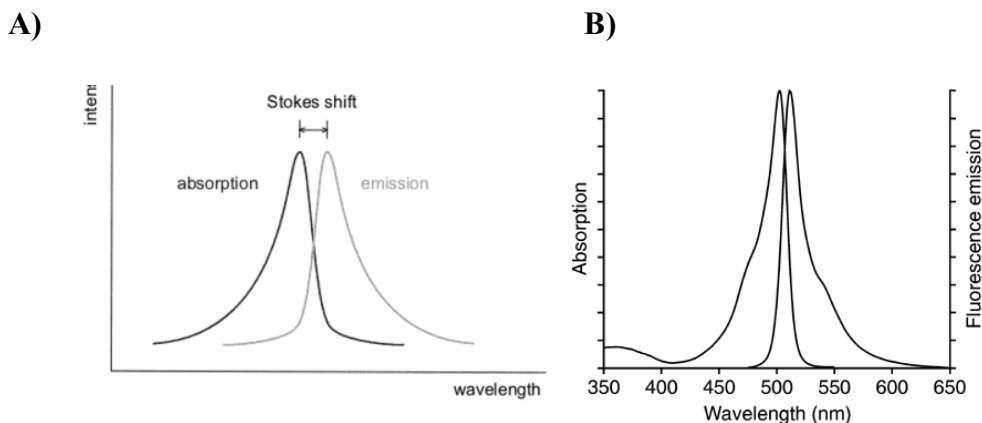


Figure 1.8 A) Stokes Shift diagram and B) the Stokes shift of BODIPY-FL<sup>37</sup>

Some other experimental factors that are important in LIF detection studies include autofluorescence, photobleaching, signal amplification and multicolor labeling. Autofluorescence is generally considered to be a background contribution from endogenous sample constituents in the pathlength of the light source which excite at a similar wavelength and emit at a similar wavelength as the fluorescent probe. Autofluorescence will limit the detection limit by contributing a background fluorescence. Some experimental features that may be useful in avoiding autofluorescence include modifying the excitation wavelength, probe absorption/ emission features, or using specific optical filters that are capable of removing the autofluorescence. For example, autofluorescence of cells or tissues can be minimized by using probes with absorbance maxima  $> 500$  nm.<sup>21, 37</sup> The light scattering at longer wavelengths is also greatly reduced at such wavelengths, although minimum waist diameters for lasers will increase

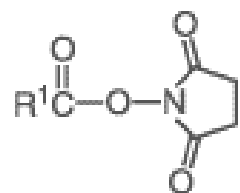
proportional to  $\lambda/2$ . The development of a number of different fluorescent probes has extended the number of fluorescent assays that can be performed using laser induced fluorescence.

### ***1.3.3 Fluorescent conjugation chemistry***

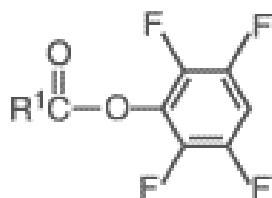
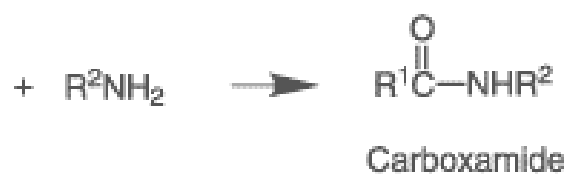
Joseph Bruckhalter and Robert Seiwald synthesized the first antibody labeling reagent known as fluorescein isothiocyanate (FITC) on May 17, 1960.<sup>38</sup> The official patent number is 2,937,186 with the title "Isothiocyanate Compounds and Means of Producing the Same Isothiocyanate Compounds". Since its development in the early 1960's FITC has become a common and extremely useful reagent for several assays in molecular biology. It has even reached the market of "e-bay" where a few grams has a street price of about \$10. A number of other fluorophores have been discovered since this time, most notably TAMRA and reGFP.<sup>39</sup> The fluorescent probes that we have utilized are listed on **Figure 1.9**.

Commercially there are several ways to attach a fluorophore to a molecule of interest. The most common involve chemistries that link with amines, thiols or alcohols. Generally amine derivitization is useful for: modifying proteins, ligands and peptides, which are used for immunochemistry, cell tracing, fluorescence in situ labeling, and receptor labeling. On the other hand, activation for thiol derivitization can be used to study protein function and structure. The reactions that are often used to link a fluorophore to an antibody, or a biochemical, involves well characterized organic reactions with primary amines. There are three classes of commonly used reagents used to activate a fluorophore. These include succinimidyl esters (SE), isothiocyanates (ITC), and sulfonyl chlorides. The reaction is illustrated below between a SE and an amide in **scheme 1**:

**Scheme 1** Reaction between an SE or TFP ester with an amine. <sup>40</sup>

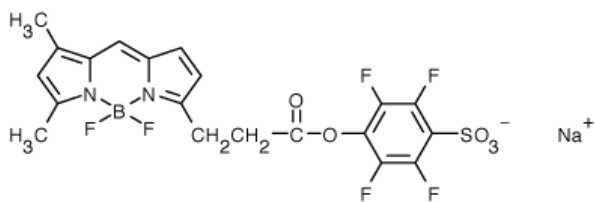


Succinimidyl Ester

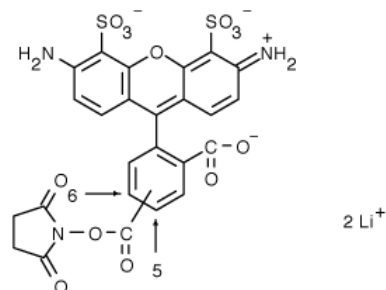


TFP Ester

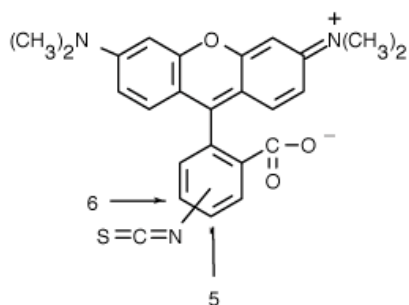
**Figure 1.9** Fluorescent probes used for CE on microfluidic devices<sup>40</sup>



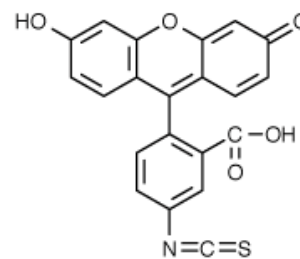
BODIPY® FL, STP ester, sodium salt



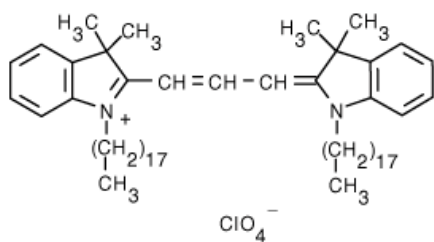
Alexa Fluor® 488, succinimidyl ester



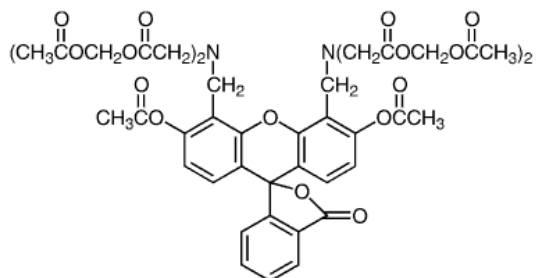
TRITC: tetramethylrhodamine-5-or 6-isothiocyanate



FITC: fluorescein-5-isothiocyanate



DiI: 2-[3-(1,3-dihydro-3,3-dimethyl-1-octadecyl-2H-indol-2-ylidene) -1-propenyl] -3,3-dimethyl-1-octadecyl-, perchlorate



Calcein AM

### ***1.3.4 LIF Apparatus***

Cheng and Dovichi were the first to demonstrate the use of fluorescence as a detection mode for capillary electrophoresis.<sup>41</sup> They initially demonstrate detection limits in the high fM range, although several experiments using much more sensitive equipment over the last decade have reported detection limits in the low fM range. An important experimental point for the determination of detection limits in capillary electrophoresis involves both the injection volume or injection time and the detection window. This concept will be developed in the following CE discussion.

The apparatus that we have constructed employs an argon ion laser capable of producing 70 mW laser lines at 488 nm and 514 nm. The laser is reflected through a dichroic mirror and is focused by an objective (10-20X). The excitation light from the fluorophore is next collected by the objective, transmitted through the dichroic mirror, spatial filter, bandpass filter and is finally focused onto a photomultiplier tube (PMT). The signal from the PMT is amplified and acquired using PCI data acquisition cards. Finally, LabView is used to analyze the signal.

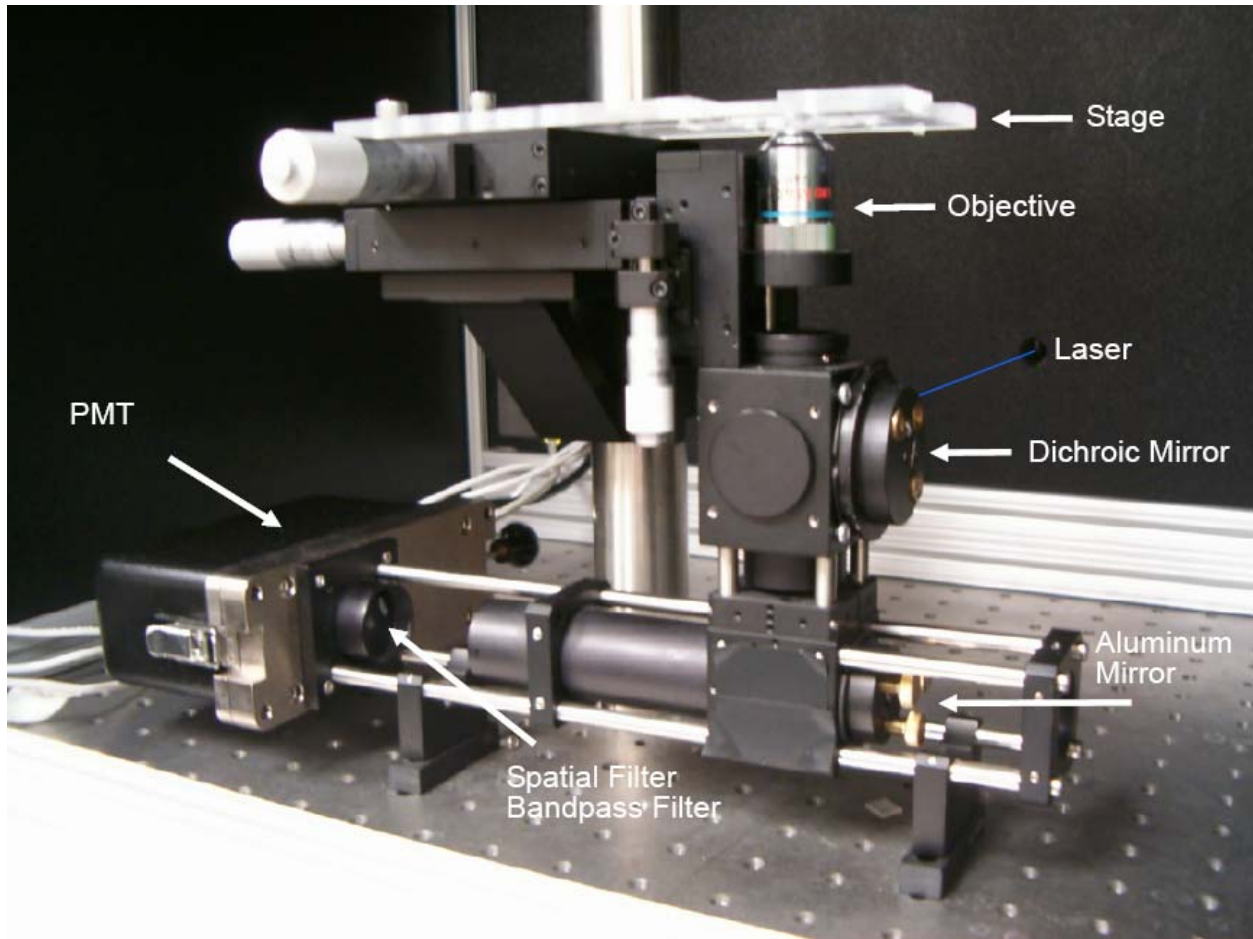


**Figure 1.10** Single point setup for laser induced fluorescence detection on microfluidic devices.

Several optical components including bandpass filters and dichroic mirrors are critical for this setup. Briefly, dichroic mirrors are optical components that allow a specific range of wavelengths to transmit through the filter, yet reflect another range of wavelengths. In more detailed terms a dichroic mirror is a color selective beamsplitter which has the capability of reflecting or transmitting light based on a wide variety of coating technologies. Coatings on a wide variety of substrates can be used from the IR to UV range of the spectrum and use the principle of interference to reflect or transmit certain spectral regions. A popular use for such

devices include heat reflectors which serve to reflect the IR region of the spectrum due to a specific coating, but allow most of the rest of the spectrum to pass. These are used in everything from movie projectors and solar cells to astronaut visors.

## **1.4 Capillary Electrophoresis**

Microfluidic devices are useful for a number of operations including capillary electrophoresis (CE). CE has been developed for the separation of molecules using a number of different chemical forces, all of which involve the use of an electric field in a low convection, low Peclet number, low Reynolds number fluidic manifold or capillary. CE at its most basic form can be envisioned as a method of separating compounds based on charge and hydrodynamic radius. The history of CE dates back to 1937 when Tiselius separated a number of proteins in a tube by applying an electrical field.<sup>42</sup> Tiselius was awarded the Nobel Prize in chemistry for his work in separation science. Hjerten furthered work in CE by using millimeter-bore capillaries.<sup>43</sup> Interestingly he found that the spinning of these capillaries along the longitudinal axis greatly reduced the effects of convection and further advanced the separation science of CE. In the mid 80's Jorgenson advanced CE by using 75  $\mu\text{m}$  id fused silica capillaries, in addition to clarifying much of the theory involved.<sup>44</sup>

### ***1.4.1 Theory***

Capillary electrophoresis (CE) operates on the fundamental physical principle that a charged particle accelerates in an electric field according to E.13 where  $F_E$  is the force applied,  $q$  is the charge, and  $E$  is the electric field. In CE the hydrodynamic radius of the charged molecule,  $r$ , and the solution viscosity,  $\eta$ , are variables that generate a frictional drag, shown in E.14.<sup>45</sup>

Alternatively, the electric field and the charge of a molecule or ion are considered to be accelerative forces. Acceleration only takes  $\sim 10^{-12}$  seconds to occur.

$$E.13: F_E = qE$$

$$E.14: F_F = -6\pi\eta r v$$

A steady state is reached during electrophoresis where the frictional drag and the electrostatic forces equal each other, illustrated in E.15 and E.16. The velocity can be rewritten as E.17.

$$E.15: F_E = -F_F$$

$$E.16: qE = 6\pi\eta r v$$

$$E.17: v = \frac{qE}{6\pi\eta r}$$

The velocity of an ion or charged molecule is thus proportion to the charge (q) and the electric field (E), yet inversely proportional to the hydrodynamic radius (r) and the viscosity ( $\eta$ ). The equation can be further simplified by generating a constant value called the electrophoretic mobility ( $\mu_e$ ) described in E.18.

$$E.18: \mu_E = \frac{q}{6\pi\eta r}$$

The electrophoretic mobility is a term that relates the charge of a molecule or ion to the hydrodynamic radius and solution viscosity to again compare accelerative forces and frictional forces. Qualitatively the higher the charge and the lower the radius and viscosity of a solution the faster the velocity, and vice versa. The velocity can thus be rewritten in E.19.

$$E.19: v = \mu_E E$$

### 1.4.2 Analytical CE Parameters

A number of analytical parameters exist, many of them derived from separation science, to further classify electrophoresis of analytes. Many of these analytical parameters will embody the physical parameters such as electric field written as  $E = V/L$ , where  $L$  is the length of the capillary and  $V$  is the potential applied across that capillary. Other important analytical parameters include the peak width ( $w$ ), efficiency ( $N$ ), and resolution ( $R$ ). The peak width is given in E.20, where  $\sigma$  is the standard deviation of the peak. The relation of  $\sigma$  to diffusion can also be observed in the Einstein-Smoluchowski equation (E.3), which assumes a Gaussian shaped analyte band. The units of sigma may be either in temporal or spatial units depending on the axis of the electropherogram.

$$E.20 : w_b = 4\sigma$$

The width of a solute zone is determined by many things, some including dispersion, injection volume, temperature, adsorbance-adhesion, detection distance/ focal volume, or electrodispersion. These factors contribute to “band broadening” and can be rewritten as a summation, shown in E.21. In an ideal situation where diffusion, injection and detection length, E.22, are the primary contribution to the band width, all of the other factors would approach zero, or the limit of zero.

$$E.21 : \sigma_T^2 = \sigma_{Diffusion}^2 + \sigma_{Injection}^2 + \sigma_{Temperature}^2 + \sigma_{Adsorbance}^2 + \sigma_{Detection}^2 + \sigma_{Electrodispersion}^2$$

$$E.22 : \sigma_{Injection}^2 = \frac{w_i^2}{12}$$

Another important factor that relates the width of a solute zone to the distance in which it has traveled is the number of theoretic plates ( $N$ ), where  $l$  is the migration distance, and  $\sigma$  can be rewritten as the band width (E.23)

$$E.23 : N = \frac{l^2}{\sigma^2} = \frac{t^2}{\sigma_t^2}$$

The equation E.23 allows quantitative benchmark standards for determining the usefulness of a separation. For instance, the number of theoretical plates will give a quantitative measurement of the broadness of a solute zone over a given length. High theoretical plate numbers indicate that over a long distance the solute plug length will be relatively short. A poor separation will have low theoretical plate numbers which will indicate excessive band broadening due to many of the terms indicated in E.21.

Using these analytical parameters there are a number of important experimental relations that can be generated. First, relations between the band width of a solute plug to the mobility, electric field (V/L), and detection length ( $l_{\text{det}}$ ) using the original Einstein-Smoluchowski equation E.3, shown in E.24. This equation shows that as the field strength and mobility increase the lateral length of the solute plug will decrease. Qualitatively this is because the solute plug will migrate faster through the capillary, allowing less time for the analytes to diffuse laterally.

$$E.24 : \sigma^2 = 2Dt = \frac{2Dl_{\text{det}}L}{\mu_e V}$$

$$E.24.1 : t = \frac{l_{\text{det}}L}{\mu_e E} = \frac{l_{\text{det}}}{v_e}$$

Equation E.23 can be substituted for  $\sigma$  in equation E.24 and rewritten in terms of the number of theoretical plates, E.25.

$$E.25 : N = \frac{\mu_e V l_{\text{det}}}{2DL} = \frac{\mu_e E l_{\text{det}}}{2D}$$

In addition to efficiency (N) another important analytical parameter is resolution. Resolution can be formulated by comparing two Gaussian analyte peaks each with a baseline width (w) and each with a migration time (t). The resolution for such a situation is illustrated in E.26.

$$E.26: R = \frac{t_2 - t_1}{4\sigma} = \frac{2(t_2 - t_1)}{(w_1 + w_2)}$$

This resolution equation can also be rewritten in terms of both efficiency (N) and mobility differences between each analyte, described in both E.27 and E.28.

$$E.27: R = \frac{1}{4} N^2 \left( \frac{\Delta\mu}{\mu} \right)$$

$$E.28: R = \left( \frac{1}{4\sqrt{2}} \right) (\Delta\mu) \left( \frac{V}{D(\mu + \mu_{EOF})} \right)^{1/2}$$

### 1.4.3 CE Apparatus

To perform capillary electrophoresis generally two things are needed, a capillary and an electric field. The capillaries can be fabricated using standard glass melting and capillary pull technologies, and also using common semiconductor micromachining techniques, as those described previously. The electric potential that are needed range between 1-30 kV with currents that range from 1-500  $\mu$ A, respectively. Our lab has developed a number of homemade high voltage supplies that are capable of providing the correct current and voltages for CE systems. For instance **Figure 1.11** illustrates our homemade power supplies. The components for our power supplies consist of a 12 V power supply which powers 5 OEM high voltage power supplies from UltraVolt or EMCO and several high resistance “bleed” resistors for safe operation of the high voltage power supplies. The digital control lines for the OEM high voltage power

supplies are fed to a PCI data acquisition card, which was run and operated using in house code written in LabVIEW.

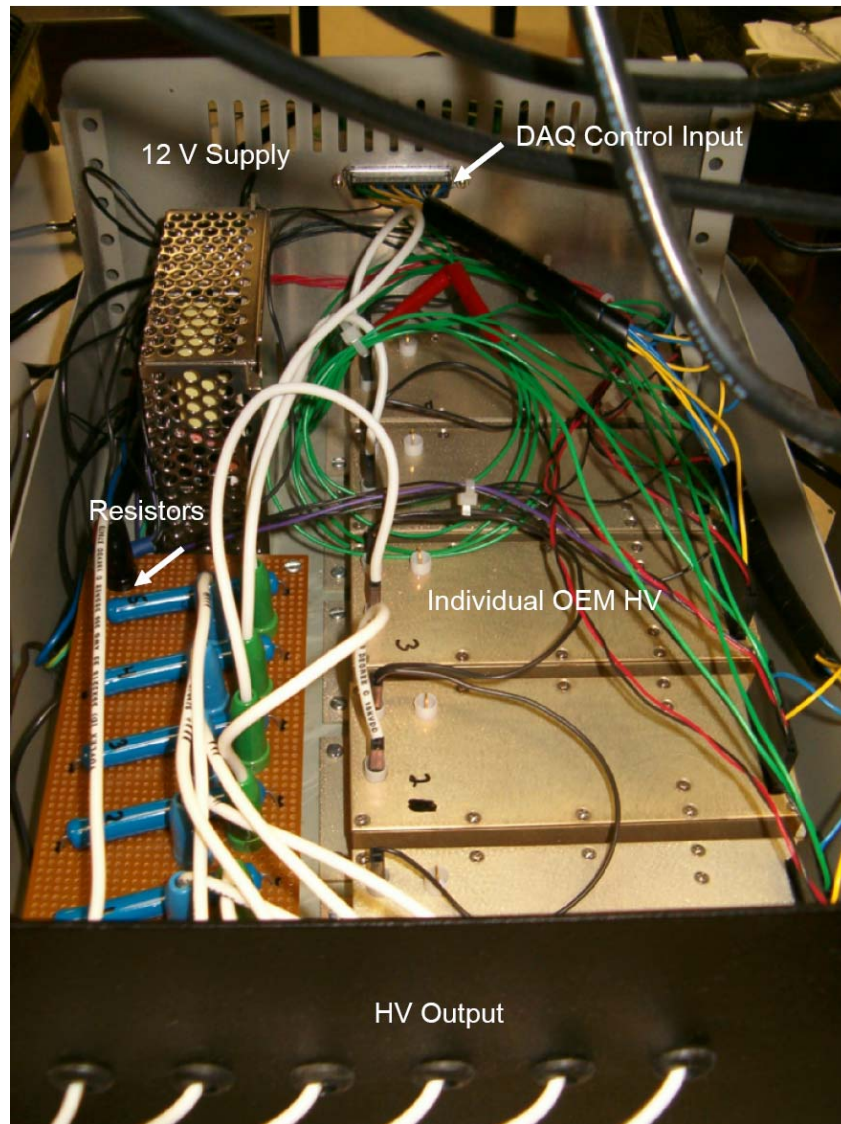


**Figure 1.11** Illustrates the homemade power supply used to apply 1- 5 kV/ cm electric fields.

## CHAPTER 2 - The Origin of Electroosmotic Flow on PDMS

### Microfluidics

#### 2.1 Introduction

Electroosmotic flow (EOF) is a very useful phenomena in microfluidic devices for several reasons including its flat flow profile. In many separation schemes EOF is used to either increase separation efficiency or resolution. Since EOF is a surface derived phenomena it can be tailored using chemical surface modifications. As mentioned previously, the resolution of a separation depends primarily on the difference in electrophoretic mobility between two analytes. If this difference is large then a high EOF would be desired to produce a rapid separation of the two analytes. On the other hand, if the two analytes have a low electrophoretic mobility difference a low EOF would be desired to allow more time to separate the compounds to full resolution. I will discuss EOF theory, measurement methods and the EOF of PDMS.

#### 2.2 EOF Theory

Electroosmotic flow (EOF) occurs when a charged double layer forms at the surface of a capillary wall and an electrical field is applied axially along the capillary to generate a bulk fluid flow. The two components of this charged double layer are called the 1) Helmholtz plane or rigid layer, and 2) the diffuse layer, both of which are illustrated in **Figure 2.1**. Near the surface of the channel the law of electroneutrality is violated for a finite volume within the diffuse layer. As illustrated in **Figure 2.1** there is more positive charge within the region of the diffuse layer than

negative charge. The net positive charge within this area is the driving force for EOF and is implicated in the directionality or polarity of the EOF. As the distance from the capillary wall increases to  $> 200$  nm the law of electroneutrality is restored for a finite volume of solvent. Once an electric field is applied parallel to the capillary, the diffuse layer is accelerated to a steady velocity that results from the balance between the friction due to the hydrodynamic radius, viscosity and the applied Coulombic force on the ions. Since the ions are hydrated, they impart momentum to the solution as they are accelerated to a steady velocity. This momentum generates a net bulk flow whose magnitude is dependant primarily upon the  $\zeta$  potential of the surface, and the electric field applied across the capillary. The direction of the EOF depends not only on the polarity of the electric field, but also on the surface charge of the capillary. The surface charge of the capillary will generate either a net positive or negative diffuse layer which will determine the direction in which the hydrated ions are accelerated.<sup>45</sup>

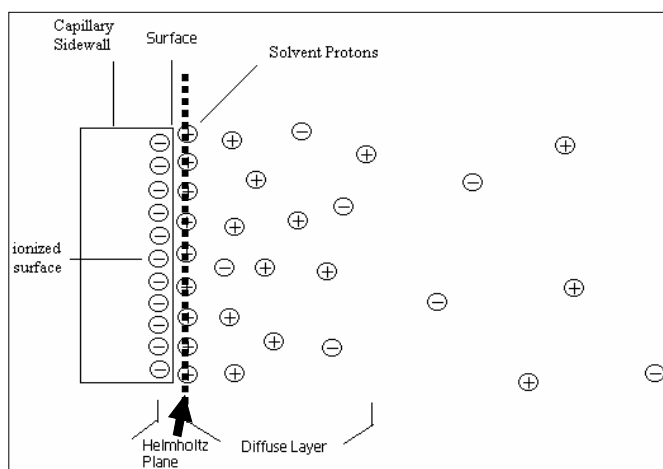


**Figure 2.1** Diagram of the electric double layer at the surface of a capillary. The double layer consists of the Helmholtz plane

EOF is used in chemical separations because it provides less band broadening than hydrodynamic driven fluid. The differences in band broadening between fluidic flow that is

electroosmotically driven versus hydrodynamically driven is largely due to differences in transverse velocities near the surface of the capillary that result from sidewall friction. The movement of solvent due to the application of a Coulombic force on the electrical double layer has much less fluidic friction on the capillary sidewalls than hydrodynamic fluid flow. Generally EOF velocities can range from 0.2 cm/s to 1 cm/s and is dependent upon the applied electric field, zeta potential and viscosity, whereas hydrodynamic flow generally is performed with flow rates of  $> 1$  cm/s.

Mathematically EOF can be modeled using a number of equations. These include the Poisson-Boltzmann, net charge density, and basic electrostatic equations.<sup>46</sup> These equations cover the primary variables that determine the EOF. From an experimental standpoint a rough understanding of these equations will yield insights into how certain physical phenomena will affect the fluidic dynamics of EOF. The Poisson-Boltzmann equation (E. 29) models the electric potential,  $\phi(y)$ , of the outer Helmholtz layer as a function of distance from the surface of the Helmholtz plane. It is named Poisson-Boltzmann because it uses the Poisson equation that relates the charge density,  $\rho(y)$ , and the dielectric constant, ( $\epsilon$ ) to the potential, but also uses an exact equation to describe charge density  $\rho(y)$  and where it is found, an idea developed by Boltzmann. The Poisson-Boltzmann equation often is written with a dielectric constant that depends on position, by neglecting this position dependence we significantly simplify the equation.

$$E.29: \frac{\partial^2 \phi(y)}{\partial y^2} = -\frac{\rho(y)}{\epsilon}$$

The equation, E.29, is very similar to Maxwell's equations of electromagnetic theory, specifically: Gauss's law of electricity. Gauss's law of electricity depends on charge density enclosed in a sphere. The amount of charge enclosed within a spherical volume element will determine the electrical potentials that exit the sphere. The same is true for the Poisson-

Boltzmann equation, in one dimension, which relates the charge at a distance  $y$  with the gradient of the potential. The gradient of the potential is inversely proportional to the dielectric constant of the solution. This suggests that in a comparison between two solvents, one with a high dielectric constant and one with a low dielectric constant, the solvent with a high dielectric constant will have a lower gradient of potential and vice-versa.

Boltzmann's contribution, the net charge density  $\rho(y)$ , varies as a function of distance  $y$  from the Helmholtz layer. The net charge density equation describes how the spatial orientation of the charge changes as a function of  $y$ , shown in E.30.<sup>46</sup> The net charge density depends on  $F$ : the Faraday constant,  $C$ : the ion concentration,  $Z$ : the ionic charge, and the electric potential  $\phi(y)$ .

$$E.30: \rho(y) = F \sum C_i^0 Z_i e^{-\frac{ZF\phi(y)}{RT}}$$

The charge density decreases exponentially as the distance ( $y$ ) from the outer Helmholtz layer increases. The electric potential at  $y = 0$  will be referred to as the  $\zeta$  potential, or the point at which the Helmholtz layer meets the diffuse layer. The  $\zeta$  potential and its location relative to the Helmholtz layer and the diffuse region is labeled in **Figure 2.3**. The electric potential varies linearly from the wall of the capillary to the edge of the Helmholtz plane. After the Helmholtz plane, as described by E.30, the potential varies exponentially due primarily to the spatial change in charge density over distance.<sup>46</sup>

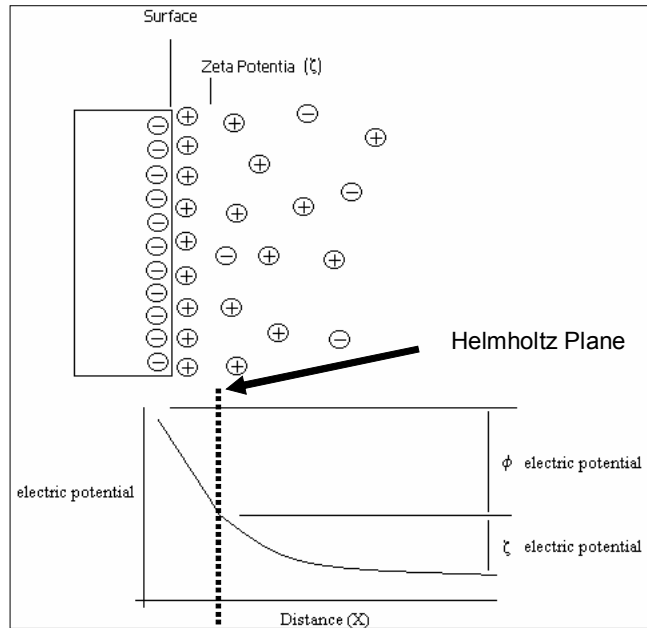


**Figure 2.2** Illustrates the location of the  $\zeta$  potential within the electric double layer.<sup>46</sup>

The concentration of ions in the bulk solution has a huge impact on the  $\zeta$  potential. As the concentration of ions within the bulk solution increase the  $\zeta$  potential decreases. It is approximated that the EOF is proportional to  $1/\sqrt{C}$ , where  $C$  is the concentration of the ions. This approximation is derived from the Guoy-Chapman model which describes the thickness of the ion double layer.

The velocity of the electroosmotic flow is dependent on the  $\zeta$  potential, solution viscosity ( $\eta$ ) and the electric field ( $E$ ). Using the equation  $v = E\mu$  it is possible to generate a relation for the electroosmotic flow, which relates the aforementioned variables in E.31.

$$E.31: V_{EOF} = E \left( \frac{\epsilon \zeta}{\eta} \right)$$

The surface charge within a microfluidic channel is greatly affected by the pH of the solution, as the ionizable groups which impart charge to the surface can change dramatically. For instance,

glass has a  $pK_a$  of  $< 2.0$ , so as the pH of the solution decreases from 10 to 2 so does the EOF. This is primarily due to the surface silanol groups becoming protonated making the surface less neutrally charged, lowering the  $\zeta$  potential, and hence the EOF.

## 2.3 Methods of Measuring EOF

Several different methods have been devised for the measurement of the EOF on microfluidic devices and commercial capillary electrophoresis systems. These include the current monitoring method, neutral marker injection, and the streaming potential measurement, which can yield information on the  $\zeta$  potential and thus yield information on the EOF of the channel. I will discuss each method in the following sections.

### 2.3.1 Current Monitoring Method

EOF measurements can be performed using the current monitoring method originally reported by Dick Zare's<sup>47</sup> group which was consequently used by Cheng Lee<sup>48</sup> and Jed Harrison<sup>49</sup> et al. Experimentally the current monitoring method involves applying a voltage across a straight capillary filled with a buffer and monitoring the current as a second more dilute or concentrated buffer is pumped into the capillary via EOF. Knowing both the time it takes for this buffer to fill the channel ( $t$ ), the length of the channel ( $L$ ) and the applied voltage it is possible to calculate the mobility of the EOF shown in E.32.

$$E.32 : \mu_{eof} = \frac{L^2}{Vt}$$

**Figure 2.3** demonstrates the measurement of the EOF in a PDMS microfluidic channel using the current monitoring method. In equation E.32 the important experimental variables include the field strength, length of capillary and the migration time of the solution. The length of the

capillary and the electric field strength are simple variables to quantify. This experiment distills down to determining the time it takes for a solution of higher or lower conductivity to traverse the length of the capillary. Initially the PDMS channel was filled with 25 mM sodium borate solution and was allowed to come to equilibrium for ~30 seconds. Once the current reached an equilibrium, or steady current, a 50 mM sodium borate solution replaced the 25 mM sodium borate solution. As the EOF pumped this higher concentration buffer into the channel the current increased, until at some point the higher concentration buffer reached the end of the capillary. At this point the current would plateau. The time that it would take to accomplish this would be considered the migration time.

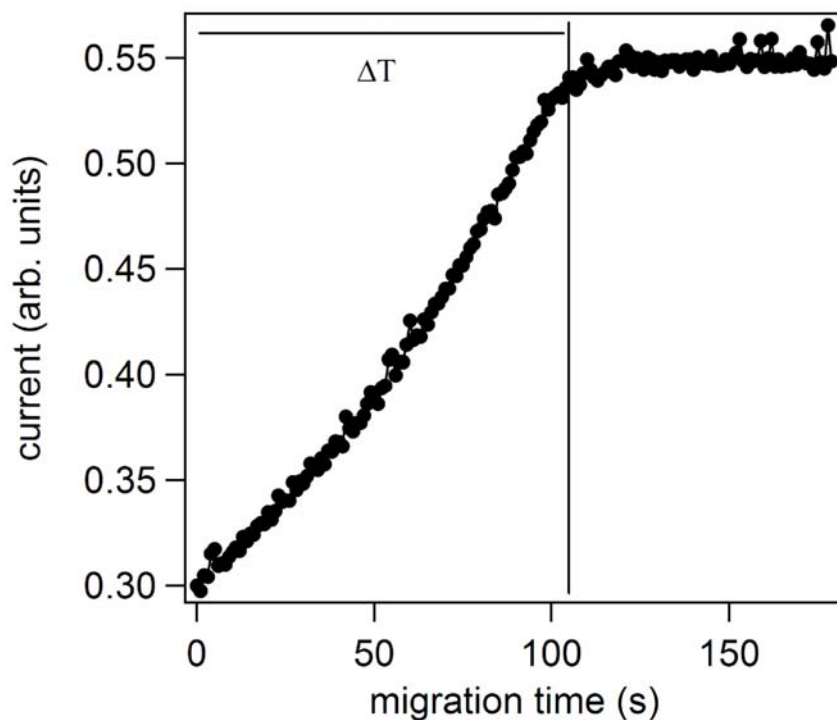


**Figure 2.3** The current monitoring method using 25 mM sodium borate, replaced with 50 mM sodium borate by EOF. The migration time in this case was 110 s.

There are several important physical parameters to keep in mind when performing this experiment. The foremost of these involve the use of different concentration buffers and Joule heating. The double layer thickness is inversely proportional to the square root of the concentration of the buffer. So as the concentrations increase the double layer will necessarily decrease, thus yielding slower EOF's, and vica versa. Joule heating can also have huge impacts on the EOF as heat changes the viscosity of the solution and consequently the EOF. Insuring that the EOF measurements are taken in conditions with minimal Joule heating is a critical point. We insured this by performing an Ohm's law,  $V=IR$ , test for our microfluidic channels. A plot of  $V$  versus  $I$  should yield a linear line, but when Joule heating begins to take affect non-linearities are present. We insured that the EOF measurements were conducted in the linear range for the  $V=IR$  plots. Since the EOF is surface chemistry dependent changes in surface chemistry will dramatically change the EOF for a particular channel.

For our EOF experiments we used the following protocol: The exact channel length was measured for each chip using calipers. The channel was initially filled with a solution of 1 mM (pH 8.3) sodium phosphate/10 mM KCl buffer. This buffer was replaced by a solution of 1 mM (pH 8.3) sodium phosphate/9 mM KCl in the anodic reservoir. Voltage potentials of 300 V/cm were applied using a Spellman CZE1000 (Hauppauge, NY) resulting in the migration of the lower conductivity buffer into the channel due to electroosmotic flow. This resulted in a linear decrease in conductivity as the higher conductivity buffer was replaced by the lower conductivity buffer. Once the lower conductivity buffer made it all the way to the cathodic reservoir the conductivity reached a constant value. Straight lines were drawn on the two conductivity sections. Their intersection was used as the time for the EOF measurements.<sup>2</sup>

Other than using the current method it is also possible to use neutral markers to mark the migration of the electroosmotic flow. For instance, a fluorescent neutral marker, Rhodamine B or phenol can be used for neutral markers in fluorescence or UV detection schemes. In our case neutral markers that were fluorescent and also didn't adsorb or absorb into the substrate were not available, so we were limited to the use of the current monitoring method.

## **2.4 EOF of PDMS Microfluidics**

### ***2.4.1 Introduction***

Poly(dimethylsiloxane) (PDMS) has become a very popular polymer for several microfluidic applications. The properties of PDMS that make it attractive include its elastomeric nature yielding a Young's modulus of 2.2 MPa, low surface energy of 20 erg/cm, outstanding gas permeability, and the non-toxicity of silicones. These advantages are useful in the fabrication of microfluidic devices using soft lithography, incorporating valves and actuated systems into the microfluidic devices, and applying these devices to biomedical applications. Although PDMS has numerous advantages in the field of microfluidics there exists some serious drawbacks. Some of these drawbacks include its nonspecific protein adsorption, and low electroosmotic flow. Developing PDMS derivatives that combat these issues will serve to extend the scope of PDMS in microfluidic technology. PDMS has become very popular due to the wide varieties of applications that it can be designed towards. Besides microfluidic prototyping and separations initially developed by Effenhauser<sup>50</sup> and Duffy<sup>51</sup>, PDMS can also be used for paper release agents, fiber lubricants, textile hand modifiers, corrosion inhibitors, mold release agents, antifouling materials and water repellents. To a large extent these applications take advantage of the unique surface properties of silicones.

Although the bulk surface properties of PDMS has been well characterized and include a hydrophobic surface with low surface tension, significantly less is known about the molecular properties of a PDMS surface, and more importantly how this surface generates electroosmotic flow (EOF) during capillary electrophoresis (CE). EOF depends primarily on the surface charge of a capillary, the applied electric field and the characteristics of the buffer including concentration and pH. In theory, the surface of a PDMS  $(-\text{O}-\text{Si}(\text{CH}_3)_2)_n$  channel contains no charge and should result in an EOF of  $< 1.0 \times 10^{-5} \text{ cm}^2/\text{Vs}$ . Experimentally the EOF of PDMS channels has been reported to vary sigmoidly from  $5 \times 10^{-5} \text{ cm}^2/\text{V}\cdot\text{s}$  to  $6 \times 10^{-4} \text{ cm}^2/\text{V}\cdot\text{s}$  for pH's between 3 and 10.5 respectively. The EOF dependence on pH suggests the presence of ionizable functionalities on the PDMS surface.

Spectroscopic studies contradict the idea that the observed EOF is due to ionization of silanol functionalities. Studies of commercial PDMS have shown that the two part mixture contains no silanol functionalities prior to curing using FT-IR and NMR, or after curing using ATR-FT-IR.

#### ***2.4.2 Fillers and Catalyst Effects***

Although PDMS has no ionizable functionalities the polymer has many other constituents that may contribute to the EOF. Some of the other constituents of the final polymer include silica fillers which reinforce the polymer, and platinum catalyst (tetramethyl-divinyl coordinated complex whos structure is shown in Chapter 10) which is used to catalyze the hydrosilation reaction between the vinyl terminated PDMS monomer and the hydride terminated monomer. To further investigate the effect of platinum catalysist and silica filler we synthesized pure PDMS with negligible silica filler and compared this polymer with the commercially available PDMS

that has >60% silica fillers, and our own in house native PDMS polymer which was filled with 30% hexamethylated silica filler.

We found that the in house native PDMS has an EOF of  $1.5 \pm 0.2 \times 10^{-4} \text{ cm}^2/\text{V}\cdot\text{s}$  while the EOF of the Sylgard 184 PDMS was  $2.2 \pm 0.2 \times 10^{-4} \text{ cm}^2/\text{V}\cdot\text{s}$ , using a 25 mM sodium borate solution at a pH of 9.5. The other primary additive to PDMS hydrosilation reactions, platinum-divinyl tetramethyl- disiloxane, was also investigated for effects of surface charge generation. We found no correlation between the amount of platinum catalyst and EOF for the native PDMS. Although native PDMS has a 33% lower EOF it is still much higher than what is expected for a neutral polymer chain suggesting another mechanism of surface charge generation.

**Figure 2.4** shows EOF measurements for three different polymers. Gelest PDMS is a synthetic blend that we formulated in the lab and took special precautions to keep the polymer as pure as possible. The Gelest PDMS was constituted with a hydride terminated PDMS monomer, a vinyl terminated PDMS monomer and the platinum catalyst. The second polymer was the Gelest PDMS with the doped tetramethyl silicate. This polymer has 30% tetramethylsilicate doped to the Gelest PDMS. Finally, Sylgard PDMS is the commercially available blend from Dow Corning.

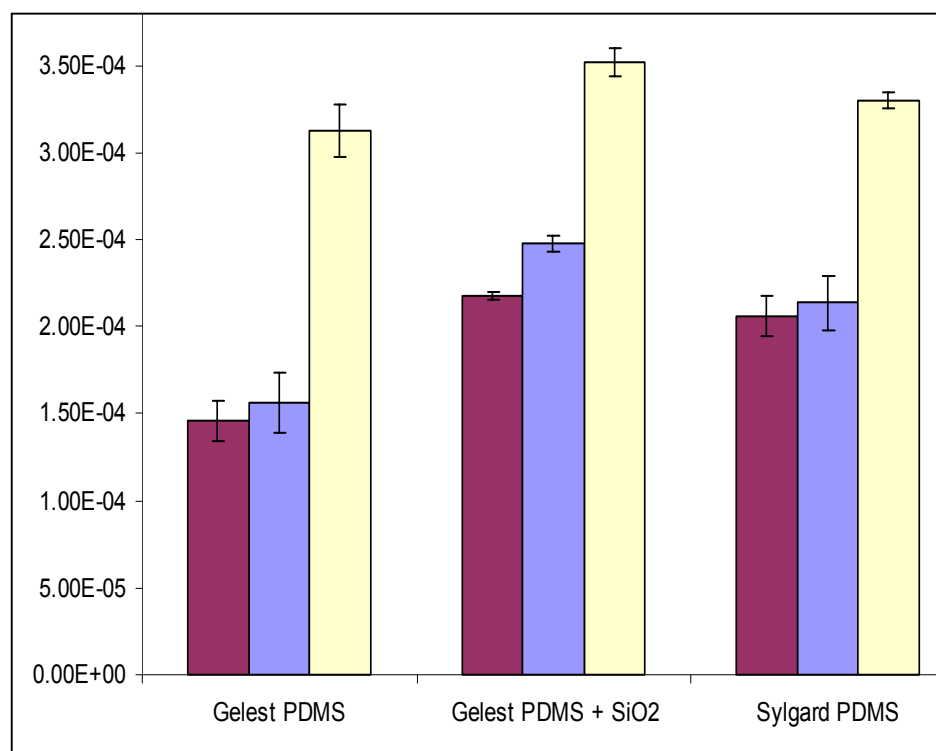


**Figure 2.4** EOF of native PDMS described as Gelest PDMS, native PDMS that was doped with methylated silica, and the commercially available Sylgard PDMS. The y axis has units of cm<sup>2</sup>/Vs. These measurements were performed in sodium tetraborate buffer with concentration differences between 25 and 50 mM and pH ~ 9.5. Each polymer has been tested with three different pretreatments. The left (red) indicates an initial measurement with no wash, center (blue) indicates an acid-base wash, and the right (yellow) indicates a base sodium hydroxide wash.

We ran a series of EOF measurements on these polymers. The first was to measure the PDMS without any buffer rinses (blue/middle). The second was to rinse with 1 M NaOH and measure the EOF (yellow/right). The final was to rinse with both 1 M NaOH, 1 M HCl, and H<sub>2</sub>O. The Gelest PDMS with the silica filler and the Sylgard-PDMS gave similar EOF's suggesting similar compositions, but the in house Gelest PDMS yielded a 33% lower EOF. After a mild rinse of 1M NaOH we found a dramatic increase in EOF, suggesting that the OH<sup>-</sup> ions may be adsorbing to the PDMS. Another potential scenario includes the hydrolysis of the PDMS at the

surface by the sodium hydroxide, and the consequential recovery by HCl. Although this is possible it is unlikely due to the amount of time that a mild solution of sodium hydroxide was allowed to reside within the channel. Recent studies by Allbritton have demonstrated that it takes about 6 hours to hydrolyze the surface of PDMS using a 6M sodium hydroxide solution.

### ***2.4.3 Adsorption of Ions on the PDMS Surface***

The initial results reported here further suggest that the bulk EOF of the PDMS is not a result of silica fillers or platinum catalysts. Another physical phenomena to consider is the adsorption of ions to the surface. It has been reported by Wagenen on November 1981 in the Journal of Colloid and Interface Science that non-ionizable polymers that exhibit surface charge are a result of specific adsorption of ions including potential-determining ions such as OH<sup>-</sup> and Cl<sup>-</sup>. Generally the more polarizable, smaller, and less hydrated ions will partition at an interface especially if the interface is hydrophobic. Other studies using AFM chemical force titrations with a 16-thiohexadecanoic acid terminated tip have shown that a large hydrophobic adhesive force exists that does not change with pH<sup>52, 53</sup>. This large hydrophobic adhesive force may be one of the driving forces for ion adsorption.

In addition to a difference in hydrophobicity, dipoles generated at the surface may also greatly contribute to the adsorption of ions. Silsesquioxanes have the potential to either form polycyclic oligomers or ladder polymers. The mechanical properties, such as the Young's modulus and Shore hardness, of commercial PDMS depend on the relative amount of either the polycyclic oligomer (cage type) or the ladder polymer (network type). Differences between the cage and network type silsesquioxanes can be distinguished using FTIR. Specifically the bond angle of the Si-O-Si becomes larger for the cage type oligomers as compared to the network type oligomers. The Si-O-Si cage and network structures show IR peaks in the 1200 to 1000 cm<sup>-1</sup>

region. Tetrahedral SiO<sub>2</sub> has Si-O-Si bond angles of 144° with a Si-O-Si asymmetric stretch at 1080 cm<sup>-1</sup>. For molecules with more cage like structure the Si-O-Si bond angle is generally 150° or higher with an asymmetric stretch shifting to higher energy and wavenumbers as high as 1180 cm<sup>-1</sup>. For molecules with network like structures the Si-O-Si bond angle reduces to < 144° and the Si-O-Si asymmetric peak shifts down to ~1030 cm<sup>-1</sup>.<sup>54-57</sup>

In **Figure 2.5** we measured the IR shifts for the prepolymer and the polymerized polymer using ATR-IR. We found that the IR regions in the polymer were blue shifted to higher wavenumbers, which further suggests that at the surface of the PDMS polymer there exists a dramatically different surface than the bulk PDMS, much of this due to strained bond angles. The strained bond angles of the Si-O-Si will likely contribute to ion bonding on the surface and dipole-dipole interactions.

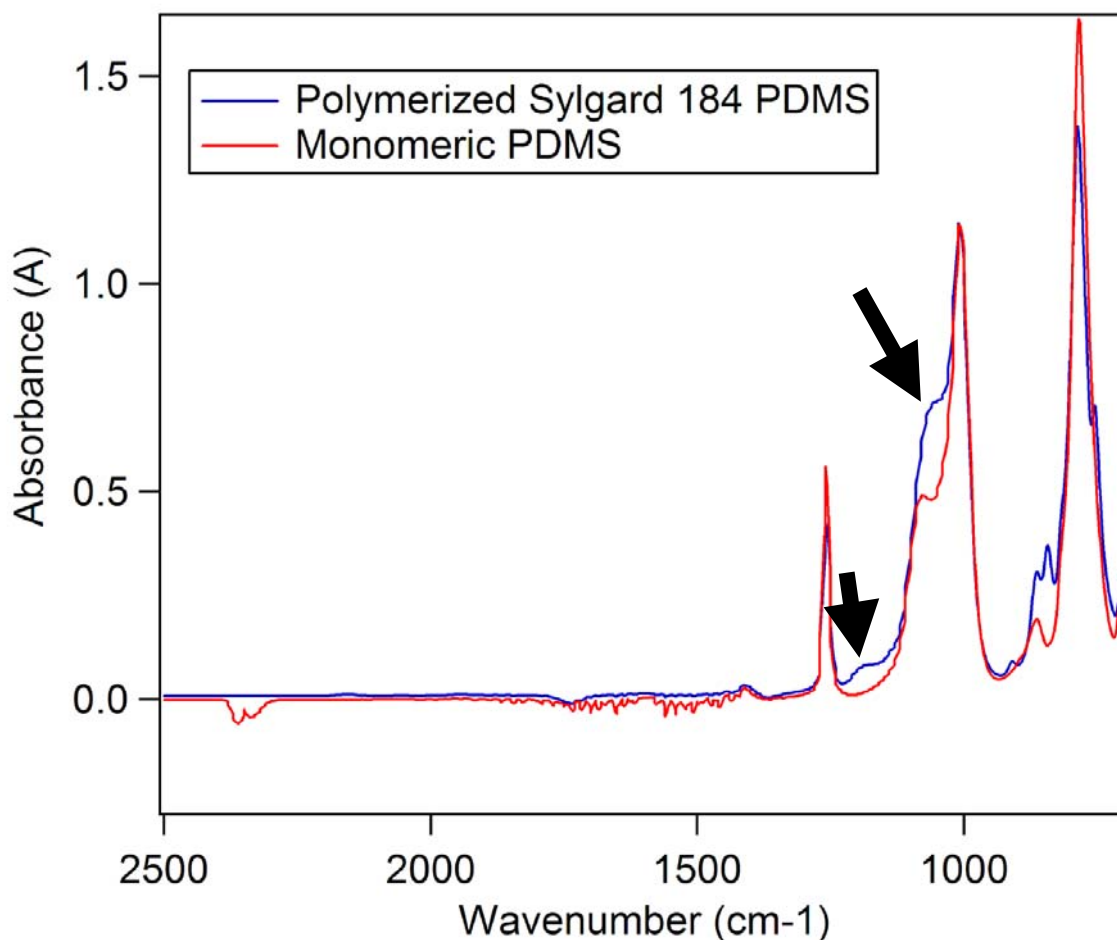


**Figure 2.5** FT-ATR of monomeric PDMS and polymerized PDMS. The polymerized PDMS is blue shifted which suggests larger Si-O-Si bond strain. The blue shifted areas are pointed to by the arrows

To further investigate the effect of hydrophobicity/ hydrophilicity on the EOF we synthesized a PDMS-polyethylene oxide (PDMS-PEO) coblock polymer with a contact angle of 40°. This polymer generated an EOM of  $0.2 \times 10^{-4} \text{ cm}^2/\text{Vs}$ . The reduced EOM for this polymer suggests that the EOM of native PDMS can be suppressed by two factors, ion adsorption or “polymer surface entanglement”. We further discuss the synthesis and characterization of PDMS-PEO in chapter 10.

## CHAPTER 3 - Silica Sol-Gel modified PDMS Microfluidics

### 3.1 Introductory Sol-Gel Chemistry

Sol-gel chemistry has been around for more than 150 years. The first metal alkoxide was synthesized by Ebelman in 1846.<sup>58</sup> Ebelman noticed that the compound gelled when exposed to the ambient humidity. It wasn't until the mid 1930's however that it was realized that metal alkoxides could be used to generate metal oxide films, initially realized by Geffcken.<sup>59</sup> Since that time sol-gel processing has become an extremely versatile technique. The versatility of sol-gel science derives from the vast number of metal alkoxide precursors that can be used in addition to the number of different physical properties that can be imparted to the final materials.

Metal alkoxides readily form hydrolysis products with weak nucleophiles such as H<sub>2</sub>O. The hydrolysis products that are produced will react through condensation reactions to form metal oxide colloids. A mixture of metal oxide colloids is called a sol. A colloid is considered to be a particle with a diameter < 1 μm. Such particles are not affected by gravity, rather their motion is dominated by short range forces, or van der Waals and dispersion forces. A sol can form a gel if the colloids react to form a metal oxide scaffold. Depending on the evaporation and aging of the gel a number of different materials can be generated.

**Figure 3.1** shows several methods of generating a number of different materials. For example, it is possible to generate films, fibers, particles or even monoliths starting from the same precursors. Furthermore, there is great chemical flexibility in the metal alkoxides available, and the different dopants that can be added.<sup>60</sup> For instance a sol can be generated and

consequently doped with a number of reagents including proteins, enzymes, antibodies, organics, chelating agents, indicator dyes, zeolites, cyclodextrins, or crown ethers.<sup>61</sup> The broad number of chemical functionalities that can be generated on the surface of sols make these materials extremely applicable for a number of applications including sensors and separations.

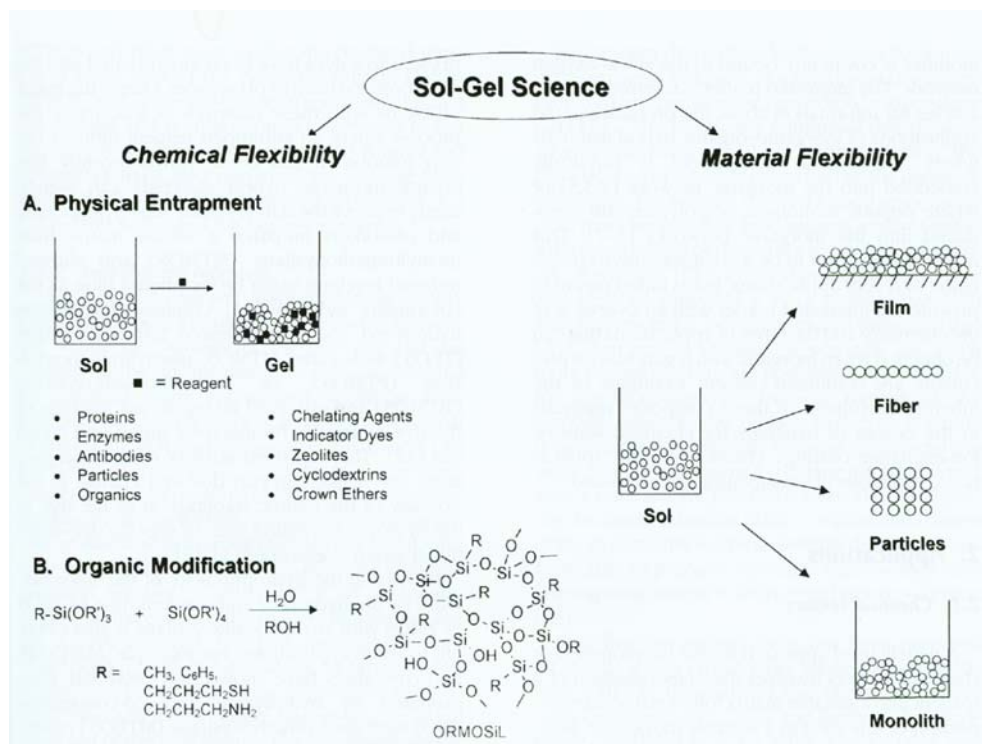
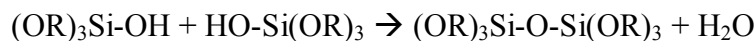


**Figure 3.1** Schematic figure of the vast number of materials that can be generated using sol-gel chemistry.<sup>61</sup>

### 3.1.1 Chemical Reaction Mechanisms

The most commonly used metal alkoxide in sol-gel chemistry is tetraethylorthosilicate,  $Si(OCH_2CH_3)_4$  often abbreviated TEOS. TEOS can form hydrolysis products with water, and cocondensation reactions with similarly hydrolyzed TEOS products as shown in the following reactions.





The hydrolysis and condensation of this produces colloids between 1-1000 nm in diameter.<sup>60</sup>

The processing parameters determine the size of the colloids that are formed. For instance, acidic properties tend to form smaller colloids, whereas basic properties will consequently form larger particles generally on the range from 10-100 nm in diameter. The basic conditions make the generate larger particles due to the surface charge of the silica colloids at higher pH's. Reactivity of the metal alkoxide depends on two factors, the periodic characteristics of the metal and the ligand properties. These factors arise from the mechanism of the sol-gel reaction. Since the reactions proceed through an S<sub>N</sub>2 mechanism the leaving group and the electronegativity of the molecule are critical. The better the leaving group the faster the reactions occur. Also transition metal centers are generally much more reactive than metalloid centers such as Sn or Si.

The sol stability or gel time, which is the time it takes for the sol to aggregate to form a matrix, is also dependent on pH. Generally the fastest gel times are recorded in the pH range from 4-8, whereas slower gel times are recorded between 0-2 and 8-12. Interesting at pH > 8 or pH < 2 the colloids are appreciably ionized so that they can not gel to form a colloidal mixture. Once the pH enters the 2-8 pH range the colloids begin to branch and form networks. Depending on the mixture colloidal mixtures can be prepared at a pH extreme and consequently modified to a gelling pH to rapidly form a gel.

### **3.2 Introduction to Silica Sol-Gel Modified PDMS Microfluidics**

Pure PDMS does not have any ionizable functional groups on the surface, but by using sol-gel chemistry it is possible to precipitate SiO<sub>2</sub> particles onto the surface and into the bulk of the polymer. The silica particles on the surface impart a large zeta potential and thus dramatically increases the EOF at higher pH. The ability to tailor the surface characteristics for a particular

electrophoretic separation is an important variable. The incorporation of silanol functionality on the surface also makes it possible to dramatically increase the EOF in a PDMS microchannel and also changes the hydrophobicity of the channel. Listed in **Table 1** are popular substrates for microfluidics and the measured EOF using a phosphate buffer.<sup>62</sup>

SUBSTRATE	EOF (cm <sup>2</sup> /Vs)	pH (PO <sup>4-</sup> )
PDMS	4.30 x 10 <sup>-4</sup>	8
PDMS-SiO <sub>2</sub>	8.10 x 10 <sup>-4</sup>	8
Glass	5.35 x 10 <sup>-4</sup>	8
PMMA (acrylic)	3.25 x 10 <sup>-4</sup>	7
Polystyrene	1.70 x 10 <sup>-4</sup>	7
Copolyester	3.60 x 10 <sup>-4</sup>	7
PEO-PDMS	0.90 x 10 <sup>-4</sup>	8

**Table 1** Electroosmotic flow of a series of polymers and glass using phosphate buffers measured using the current monitoring method.

The microfluidic devices reported thus far have been fabricated from a variety of materials including silicon, glass, and plastics. In the chemical analysis community, glass and plastics have been the most popular because their electrically insulating properties allow the application of electrical fields for the manipulation of fluids and the separation of analytes. Glass, in addition to its electrical insulating properties, has several advantages as a substrate material: (1) it is optically transparent over a wide range of wavelengths; (2) it supports a high electroosmotic flow (EOF); (3) its surface is hydrophilic and wetting; (4) its surface chemistry is well understood; and (5) there are numerous methods available to modify the surface if needed.

Glass, however, is also expensive and fragile. In addition, the fabrication process is time consuming, tedious, and requires the use of caustic chemicals, e.g., hydrofluoric acid, and cleanroom facilities. For these reasons the use of several different plastics as substrates for microfluidic devices has been explored. Plastics are generally less expensive and are amenable to rapid and facile fabrication methods such as casting, molding and embossing.<sup>16, 63</sup> In addition, the fabrication chemistry is generally less hazardous and does not require cleanroom facilities.

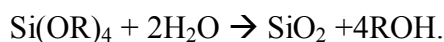
While the fabrication of microfluidic devices from several different types of plastics<sup>8, 9, 16, 17, 19, 20, 63</sup> including poly(carbonate), poly(ester),<sup>64</sup> poly(styrene),<sup>65, 66</sup> poly(ethylene terephthalate glycol),<sup>65, 66</sup> poly(methylmethacrylate), and poly(olefins) have been demonstrated, the most popular material has become poly(dimethylsiloxane) (PDMS). PDMS is a relatively inexpensive substrate material, and devices can be rapidly and easily molded from the prepolymer. Similar to glass, PDMS offers good optical transmission characteristics, good electrical resistivity, and good thermal conductivity.<sup>17</sup> PDMS, however, suffers from some significant limitations. For example, the EOF of native PDMS is only about 1/4 to 3/4 that of glass depending upon the ionic strength and pH of the buffer.<sup>67-69</sup> PDMS is also very hydrophobic, and so the channels in a PDMS device can be difficult to wet. More importantly, however, hydrophobic analytes will actually absorb into the bulk PDMS or adsorb onto its surface. This significantly limits the analytes that can be separated on devices made from PDMS and generally results in separation efficiencies which are significantly lower than reported for glass devices.<sup>69</sup> Finally, the inert surface provides no simple direct, route for modification. Even with these limitations many elegant devices have been demonstrated using PDMS.<sup>8, 70-84</sup>

To improve electroosmotic flow and to make the surface more hydrophilic and resistant to analyte adsorption/absorption, channel wall surfaces on PDMS devices have been modified in several ways. For example, treatment with an oxygen plasma can be used to generate silanol groups on the channel wall surfaces. This has been shown by many groups to create a wettable surface with higher EOF's.<sup>9, 17, 85</sup> It also serves to irreversibly bond the PDMS with another surface to create an enclosed channel network. The surface with this treatment, however, is unstable in air and EOF's will quickly decrease back to that of native PDMS.<sup>85-88</sup> The EOF is significantly more stable if the surface is kept wetted; again, however, there is a significant decrease in the magnitude of the flow over the course of several days.<sup>87, 89</sup>

The oxidation of the PDMS channel walls is also the most popular route for covalently modifying the surface.<sup>9</sup> Surface oxidation using an oxygen plasma has been followed by the use of free radical chemistry for the attachment of acrylic acid, acrylamide, dimethylacrylamide, 2-hydroxyethylacrylate, and poly(ethyleneglycol) monomethoxyacrylate;<sup>90-92</sup> and surface oxidation using UV light followed by atom transfer radical polymerization has been reported for the attachment of acrylamide and poly(ethyleneglycol).<sup>93-96</sup> In addition, surface oxidation through the use of Cerium(IV) and nitric acid has been described for the attachment of acrylamide.<sup>97, 98</sup> Finally, chemical vapor deposition has been demonstrated for the attachment of poly-(para-xylylene carboxylic acid pentafluorophenylester-co-para-xylylene).<sup>99, 100</sup>

Non-covalent modifications to the surface have also been described. Simple non-covalent anionic coatings such as sodium dodecylsulfate<sup>68, 101</sup> can be used to significantly increase the EOF while cationic surfactants such as poly(brene) can be used to reverse the EOF.<sup>85</sup> Polyelectrolyte layers (PEL) can be used to increase, decrease, or even reverse the EOF depending upon the charge on the PEL and how many layers have been laid down.<sup>102</sup>

A potential alternative method for modifying the surface (and bulk) properties of PDMS is to use a sol-gel process to form nanometer-sized silica particles throughout a polymerized PDMS matrix.<sup>60, 61, 103, 104</sup> To form the particles, an alkoxy silane precursor such as tetraethylorthosilicate (TEOS), which is soluble in the polymerized PDMS, is first hydrolyzed. Particles are then formed through the condensation of the hydrolyzed silanes. The condensation reaction is generally catalyzed using either an acid or a base, shown below.<sup>105-113</sup>



This process should result in the generation of permanent free silanol groups at the surface of the PDMS, thereby, increasing the EOF and the wettability and decreasing the absorption of hydrophobic materials into the PDMS. Particle formation in the bulk PDMS should also allow for irreversible sealing of PDMS with another piece of PDMS to form enclosed channel structures. Finally, the silanol groups on these particles should allow the wide range of surface modifications developed for glass to be used on these modified PDMS devices.

The use of sol-gel processes to generate SiO<sub>2</sub> particles in PDMS polymers has been studied extensively by Mark's group over the past 20 years with the aim of creating better PDMS-based materials.<sup>105-113</sup> Incorporating silica into "pure" PDMS substantially increases the tear strength of the resulting material making it commercially viable for a variety of applications. In fact, modern commercial varieties of PDMS, such as Sylgard 184, contain about 40% silica by weight.<sup>114</sup> To homogeneously distribute the silica in commercial prepolymer formulations, however, it must first be neutralized by trimethylsilylating the surface.<sup>113, 115</sup> These commercial polymer formulations, therefore, should contain no active silanol groups; and this has been

confirmed using IR spectroscopy.<sup>68</sup> While present day commercial formulations of PDMS contain neutralized silica particles preformed in the prepolymer, some of the initial reports examining the effects of silica fillers on the mechanical strength of PDMS generated silica particles in situ in polymerized PDMS using sol-gel processes.<sup>105, 108, 109, 111</sup> We report on the use of such a process to synthesize silica particles throughout a PDMS microchip. We also report on the physical characterization of the SiO<sub>2</sub> modified PDMS polymer and on the electrophoretic separation characteristics of devices made from this modified polymer.

### **3.3 Experimental for Silica Modified PDMS**

**Chemicals.** Sodium dihydrogen phosphate, disodium hydrogen phosphate, potassium chloride, sodium tetraborate, and all amino acids were obtained from Acros Organics.

Ethylamine was purchased from Sigma Chemical Co. (St. Louis, MO). Commercial PDMS (Sylgard 184) was obtained from Dow Corning (Midland, MI). Tetraethylorthosilicate (TEOS) was obtained from Gelest (Morrisville, PA). All of the chemicals were used as received.

Tetramethylrhodamine succidimidyl ester (TAMRA) and fluorescein-5-isothiocyanate (FITC) were obtained from Molecular Probes (Eugene, OR).

All of the amino acids were individually derivatized with TAMRA or FITC by dissolving 0.5 mg of the TAMRA or FITC in 100  $\mu$ L dimethylsulfoxide (DMSO) and adding this solution in a 1 to 9 ratio to a solution of an amino acid in 150 mM sodium bicarbonate (pH 9.0).<sup>116</sup> The amino acids in the final labeling cocktail were at a concentration of 10 mM and in  $\sim$  10-fold molar excess to the dye. All solutions were made using distilled, deionized water from a Barnstead Nanopure System (Dubuque, IA) and then filtered through 0.45  $\mu$ m Acrodiscs (Gelman Sciences; Ann Arbor, MI).

### 3.3.1 Masks.

Photomasks were generated using a photoplotting process at 8,000 dpi by The Photoplot Store (Colorado Springs, CO). The mask designs were created in AutoCAD2000LT (Thomson Learning; Albany, NY) and sent to The Photoplot Store for translation and fabrication.

Two different masks were used to fabricate the chips that were used to obtain the results reported below. For the EOF measurements, a simple straight line was used. The line was 25  $\mu\text{m}$  wide and 3 cm long. For the separations a cross-shaped mask was used. The dimensions for the cross are shown in **Figure 3.2**. The line widths were again 25  $\mu\text{m}$ .

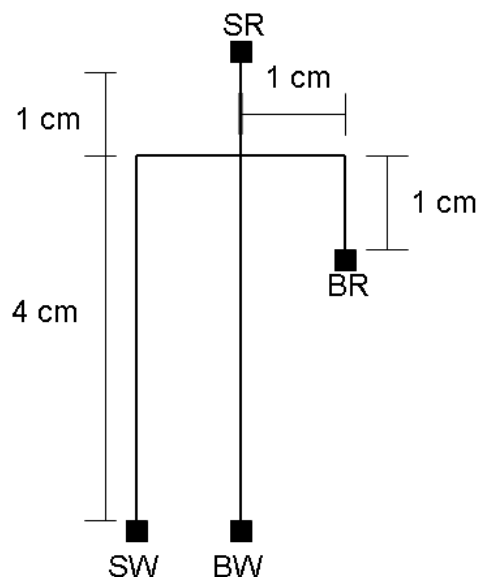


Figure 3.2 Schematic of Cross Chip used for Amino Acid Separations. The analyte, buffer, analyte waste, and separation waste reservoirs are designated as SR, BR, SW, and BW, respectively.

### 3.3.2 Molds.

The negative molds used for casting the microchips were fabricated in SU-8 2015 negative photoresist (Microchem Corp.; Boston, MA). To create the SU-8 molds, glass slides (12553; Fisher Scientific, Pittsburg, PA) were thoroughly cleaned by sonicating in deionized

water and then rinsed with a mixture of ethanol and glacial acetic acid. SU-8 was spin-coated onto the glass slides as specified by the manufacturer to give a 20  $\mu\text{m}$  thick layer. The spin-coated SU-8 slide was pre-exposure baked for 2 min at 60°C followed by a 95°C baking for 3 min. The pre-baked SU-8 slide was covered with the photomask and placed under a flood exposure system (ThermoOriel; Stratford, CT) for 5 s at a power of 45  $\text{mJ}/\text{cm}^2$ . The exposed SU-8 slide was post-exposure baked at 60°C for 2 min and then at 95°C for 3 min. The pre exposure bake is aimed at slowly evaporating the solvent in the photoresist, while the post exposure bake is aimed at helping reduce cracking in the features. The SU-8 was next developed by agitating for 3 min in SU-8 developer (Microchem Corp.). Finally the developed mold was rinsed with ethanol and blown dry with compressed argon gas.

### ***3.3.3 PDMS chip fabrication.***

The Sylgard 184 elastomer was constituted and activated as specified by the manufacturer and degassed for 1 hr. Part of this mixture was poured on an SU-8 mold and another part on a clean microscope slide (the blank). After curing for 10 min at 80°C, both parts were carefully and slowly peeled off the mold and blank. The two pieces of PDMS were then conformally contacted and placed in the oven at 95°C. After approximately 5 hrs, the chips were removed from the oven and soaked in TEOS. During the first 5 min of the soaking process the chips were shaken and swirled. If this was not done, the chips would adhere to the surface of the glass container and uneven absorption of TEOS would occur, resulting in the warping of the chips. After 30 min, the chips were removed from the TEOS solution and added to a 2.8% (v/v) solution of ethyl amine in ultrapure  $\text{H}_2\text{O}$ . After 15 hrs, the chips were removed, rinsed for 1 min, with ultra pure  $\text{H}_2\text{O}$ , and placed in an oven at 95°C for 1 hr. After the chips were removed from the oven, holes were bored at the termini of the channels using a cork borer. Finally, the finished

chips were contact sealed against a hydrolyzed glass slide to form the bottom of the reservoir. The channel dimensions of the finished chips were 18  $\mu\text{m}$  deep and 30  $\mu\text{m}$  wide. The channel lengths were nominally the same as that for the original masks.

The chips were prepared for use by pulling either sodium borate buffer or sodium phosphate buffer (pH between 7.5-9.5) through the channels for 5 min and leaving that buffer in the channels for 2 hrs.

### ***3.3.4 Contact Angle measurements.***

A homemade device was used to image water drops and measure the contact angle. It consisted of a Nikon stereoscopic zoom microscope (SMZ1500), a sony CCD color video camera (SSC-DC50A) and an in house machined platform equipped with a mirror at a 45° angle. The 45° angle of the mirror allowed the water droplet to be imaged from the side. The material upon which the contact angle measurements were to be made was placed on the platform. A 5 $\mu\text{L}$  drop of water was then placed on the material and allowed to rest on the surface for 1 min. After 1 min an image was taken. The contact angle was measured by drawing a line tangent to where the drop's edge met the surface. The angle that the line made with the surface was then measured with a protractor.

### ***3.3.5 Rhodamine B absorption measurements.***

Rhodamine B at a concentration of 10  $\mu\text{M}$  in a 25 mM (pH 9.5) sodium tetraborate solution was pulled through the channels of both Sylgard 184 and PDMS-SiO<sub>2</sub> chips. The chips were then imaged at 0, 1 and 4 hrs using a Nikon Eclipse TE2000E microscope with an epi-illumination attachment, a scientific grade CCD camera (Princeton Instrument's MicroMax; Roper Scientific; Trenton, NJ), and a Sony CCD color video camera (SSC-DC50A). IgorPro

(Version 4.0.7.0; Wavemetrics; Lake Oswego, OR) was used to create the fluorescence profiles. Between measurements, the chip was kept in the dark to minimize photobleaching.

### ***3.3.6 TEM Sample Preparation.***

One millimeter cubes of sample were infiltrated for 24 hrs at room temperature with an LR White Embedding Resin (Electron Microscopy Sciences(EMS)). Samples were placed in #3 beam capsules (EMS) and filled with resin. The samples were then cured for 24 hours at 70°C. After curing, the samples were trimmed and sliced into ultrathin sections on a Reichert Ultracut S microtome (Leica Microsystems; Bannockburn, IL) using a diamond knife. The ultrathin sections were placed on 200 mesh copper grids (EMS) and imaged on an FEI CM 100 TEM at 100 kV(FEI Company; Hillsboro, OR). Digital images were captured using a Kodak 16I camera (Advanced Microscopy Techniques, Corp.; Danvers, MA) with AMT Advantage software (Advanced Microscopy Techniques).

### ***3.3.7 Weight measurements.***

Prior to the sol-gel treatment the PDMS chips were dried at 95°C for 30 min and then weighed. After the SiO<sub>2</sub> had been precipitated within the PDMS, the chips were re-dried at 95°C for 35 min and reweighed.

### ***3.3.8 Young's modulus measurement.***

Stress-strain measurements were made on dumbbell shaped molded samples which measured 9.5 cm x 1 cm x 0.25 cm. One end of the sample was attached to the ceiling by a wire and on the other end a weight was attached. The weight was increased until the sample fractured. The elastic modulus was calculated on the linear portions of the stress-strain plots.

### 3.3.9 Hardness.

A Durometer (Instron; Canton, MA) was used to measure the Shore hardness of both the Sylgard 184 and the PDMS-SiO<sub>2</sub> polymers.

### 3.3.10 *i-E* curves.

To assess any changes in the heat dissipation capabilities of the PDMS-SiO<sub>2</sub> devices compared to PDMS devices, current-voltage plots were made. A 10 mM (pH 9.5) sodium borate buffer was used for these experiments, and the plots for both types of devices were the same and linear up to about 1100 V/cm. To ensure that no Joule heating occurred for the EOF measurements reported below, all of the EOF measurements were made at an electric field strength of 300 V/cm. This is illustrated in **Figure 3.3**.

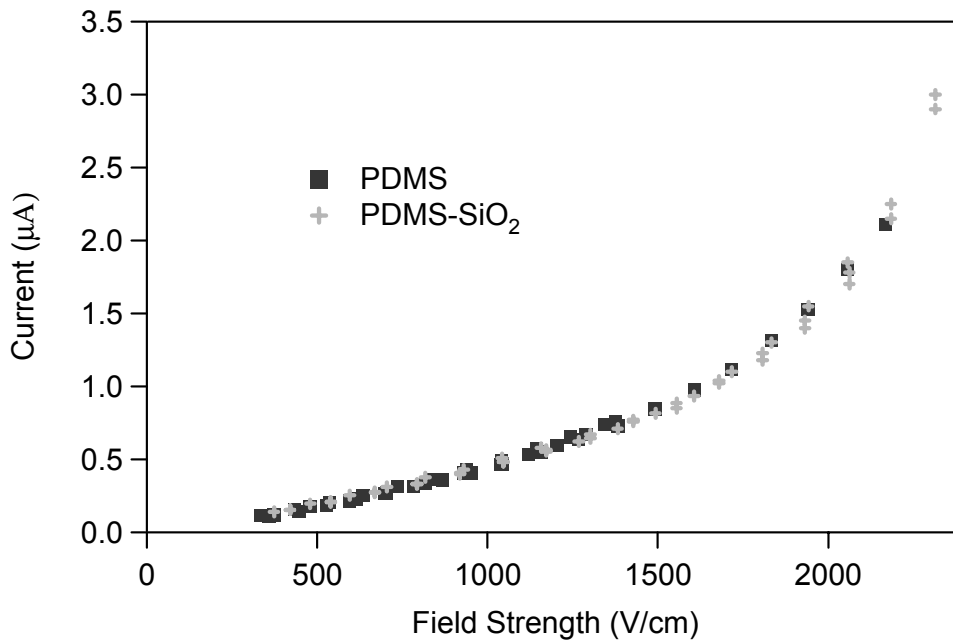


**Figure 3.3** Plots of current versus field strength for both PDMS and PDMS-SiO<sub>2</sub> were consistent with Ohm's Law up to 1100 V/cm.

### 3.3.1.1 EOF Measurements

Initial EOF measurements were made using the conductivity method described in the Experimental Section where a 1 mM (pH 8.3) sodium phosphate/10 mM KCl buffer was replaced by a 1 mM (pH 8.3) sodium phosphate/9 mM KCl buffer in the channel through electromigration. The initial electroosmotic mobilities (EOM) measured on the PDMS-SiO<sub>2</sub>, PDMS, and glass microchips were  $(8.3 \pm 0.2) \times 10^{-4} \text{ cm}^2/(\text{V}\cdot\text{s})$  (RSD = 2.6%;  $n = 10$ ),  $(4.21 \pm 0.09) \times 10^{-4} \text{ cm}^2/(\text{V}\cdot\text{s})$  (RSD = 2.2%;  $n = 10$ ), and  $(5.3 \pm 0.4) \times 10^{-4} \text{ cm}^2/(\text{V}\cdot\text{s})$  (RSD = 7.7%;  $n = 5$ ), respectively. For all of the values reported five replicate measurements were made on each of " $n$ " different chips. The results reported for PDMS-SiO<sub>2</sub> and PDMS, therefore, are the average of 50 measurements each. The average measured EOF on the PDMS-SiO<sub>2</sub> chips was 96% greater than that on the native PDMS chips and 55% greater than that on glass chips. The values measured for the glass and Sylgard 184 PDMS chips were within experimental error of those reported in a previous investigation of PDMS.<sup>21</sup> After 60 days of *dry* storage, the EOM was measured at  $(7.6 \pm 0.3) \times 10^{-4} \text{ cm}^2/(\text{V}\cdot\text{s})$  (RSD = 3.9%;  $n = 3$ ), a decrease of only 8% below that of the initially measured value. Previous methods of increasing the EOM on PDMS chips using plasma oxidation sources required that the "activated" channel walls remain in contact with an aqueous solution to maintain the higher EOM's over time.<sup>38</sup> The %RSD's obtained on the PDMS-SiO<sub>2</sub> chips were significantly better than those obtained on glass chips and similar to those obtained on PDMS chips. The repeatability of these measurements indicates that this method of surface modification is both robust and very reproducible.

### ***3.3.1.2 Electrophoretic Separations***

The electrophoretic separations were performed in a 1 mM (pH 9.5) sodium tetraborate solution. The samples were diluted 500 fold into the run buffer. The separations and gated injections<sup>117</sup> were performed using three independent and remotely programmable high voltage (0-10 kV) power sources from EMCO (Sutter Creek, CA). The proper potentials to apply at each reservoir were determined using Kirchhoff's rules and Ohm's Law.<sup>118</sup> The injection times were 0.05 s.

### ***3.3.1.3 Single point detection setup.***

All experiments were performed using a single point detection system similar to that previously described.<sup>119</sup> In brief, laser induced fluorescence (LIF) detection of the analytes was performed using either the 488 nm (FITC labeled amino acids) or 514 nm (TAMRA labeled amino acids) line of a Melles Griot Argon ion laser (35-MAP-431-208; Carlsbad, California) as the excitation source at a power of 8 mW. The 488 (or 514) nm laser beam was reflected off a 500 (or 560) nm long-pass dichroic mirror (500DRLP (or 560DRLP) Omega Optical; Brattleboro, VT) and focused using a 40x objective (CD-240-M40X, Creative Devices; Mechanic Station, NJ) into a small spot in the separation channel 3.5 cm below the cross intersection. The fluorescence emission was collected with the same objective, passed through the dichroic mirror, spatially filtered with a 1 mm pinhole (Oriel, Stratford, CT), and spectrally filtered using a 545 (or 595) nm bandpass filter (545AF75 (or 595AF60); Omega Optical). The signal was then detected with a photomultiplier tube (PMT, R1477; Hamamatsu Instruments, Inc.; Bridgewater, NJ) and amplified using an SR570 low noise current preamplifier (Stanford Research Systems, Inc.; Sunnyvale, CA) with a 100 Hz lowpass filter. The signal from the

amplifier was sampled at 200 Hz using a PCI-6036E multifunction I/O card (National Instruments, Inc.; Austin, TX) in a Dell computer (Round Rock, Texas).

The data acquisition and high voltage control software was written in-house using LabVIEW (National Instruments). All data analysis was performed using Igor Pro.

### **3.4 Results for Silica Modified PDMS**

#### ***3.4.1 Physical Characterization.***

To create the PDMS-SiO<sub>2</sub> chips, conformally bonded PDMS chips were first soaked in TEOS followed by submersion in a basic aqueous solution. TEOS is soluble in cured PDMS and so when the Sylgard 184 PDMS chip was placed in neat TEOS, the chip swelled to about 125% of its initial size. After removal from the TEOS, the chip was placed into a 2.8%(v/v) aqueous solution of ethylamine to catalyze the formation of the SiO<sub>2</sub> particles. During this process the chip quickly returned to its original size within  $\pm 1 \mu\text{m}$  and also became irreversibly sealed. After removal from the ethylamine solution, the chip was dried and weighed. The weight of the new PDMS-SiO<sub>2</sub> chip increased by  $3 \pm 0.2\%$  (RSD = 7%; n = 5). To determine if this weight increase was due to the formation of fused silica particles throughout the PDMS matrix, thin slices of the PDMS-SiO<sub>2</sub> material was imaged using TEM (**Figure 3.4A and 3.4B**). In these images, the silica particles show up as darker spots because the particles have a higher electron density than the bulk PDMS. Analysis of the images showed the particles to be about  $\sim 10$  nm in diameter, homogeneously distributed throughout the PDMS matrix,<sup>109, 111</sup> and uniform in size. While no gross deformation of the chips or channels were found, a slight change to the channel shape was observed in photomicrographs of the channel cross-sections.(**Figure 3.4C and 3.4D**). This

change in cross-section did not adversely affect the separation properties of the chip as discussed below in the Separation section.

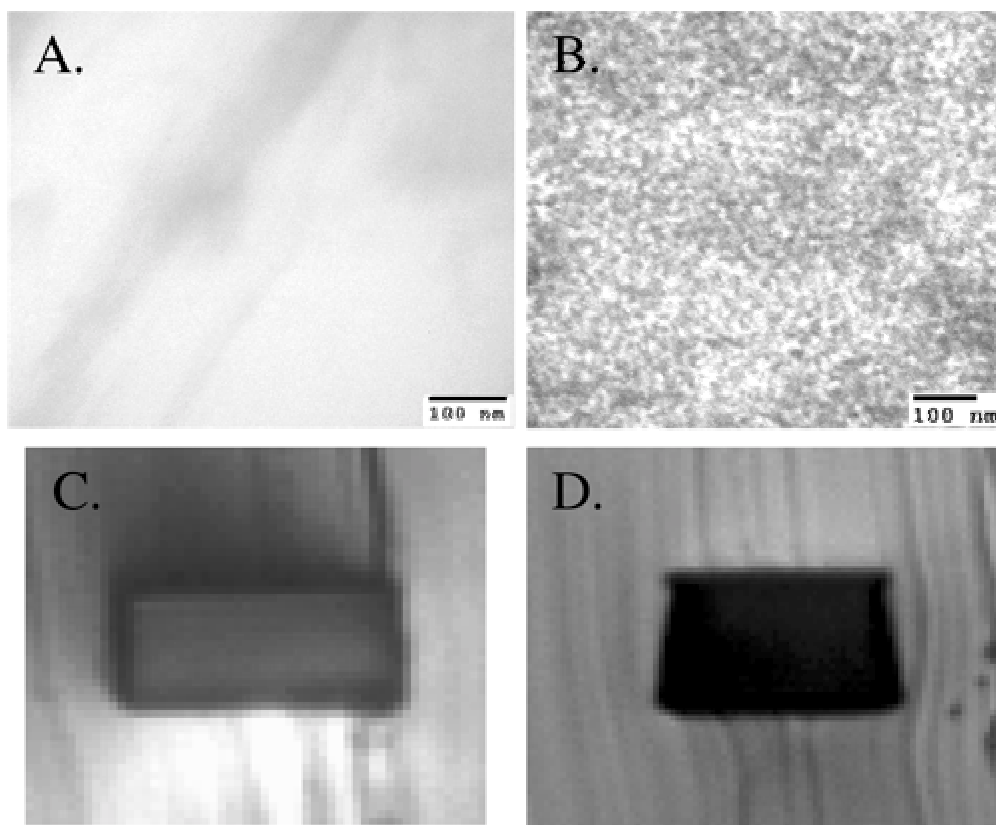


**Figure 3.4** TEM and Optical Images of the PDMS and PDMS-SiO<sub>2</sub> chips. TEM images of the PDMS and PDMS-SiO<sub>2</sub> are shown in A and B, respectively. Optical micrographs of the PDMS and PDMS-SiO<sub>2</sub> channel cross-sections are shown in C and D, respectively.

The Young's modulus of the PDMS-SiO<sub>2</sub> chips was measured and compared to that of the native Sylgard 184 PDMS chips. An increase in the modulus of 49%, from 2.31 MPa for the native PDMS chip to 3.43 MPa for the PDMS-SiO<sub>2</sub> chip was seen. **Figure 3.5** Although the Young's modulus for the PDMS-SiO<sub>2</sub> was higher than that for PDMS, the shape and slope of the stress-strain curve was still indicative of an elastomeric material.<sup>120</sup> And while the PDMS-SiO<sub>2</sub>

chips were stiffer than the native PDMS chips, they were still easily bendable and compressible. The Durometer hardness for the PDMS-SiO<sub>2</sub> was 70 versus 62 for the Sylgard 184 PDMS chips.

This change in hardness is particularly important in regard to the implementation of air actuated valves on these devices. An increase in the modulus of 50% will require an increase in actuation pressure of 50% for otherwise identical valves. Quake's group has demonstrated air actuated valves requiring a total force of 1 mN, or the application of 100 kPa over an area of 100 μm by 100 μm.<sup>71,75</sup> To actuate a valve of the same dimensions in PDMS-SiO<sub>2</sub> would require 1.5mN or 150 kPa. This value is still quite reasonable and can be generated using the same type of actuators and pressure sources used in previous PDMS valve work.

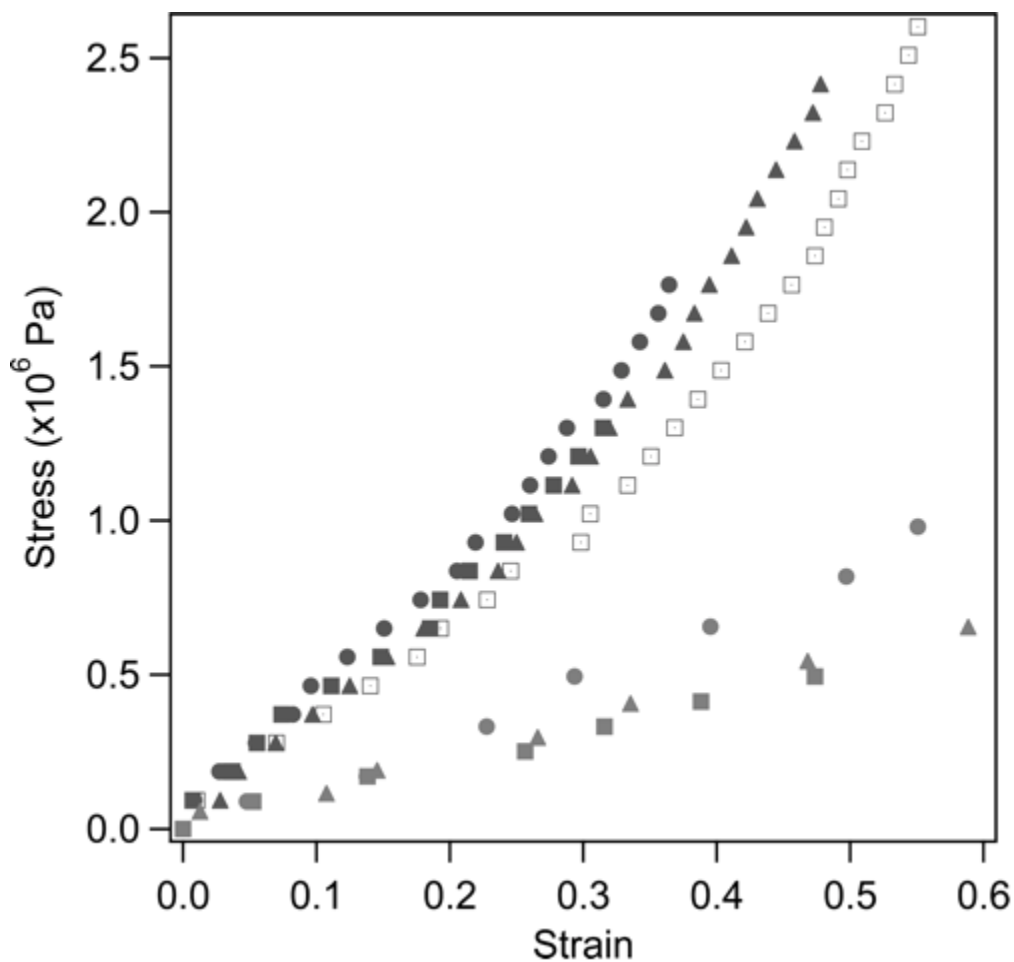
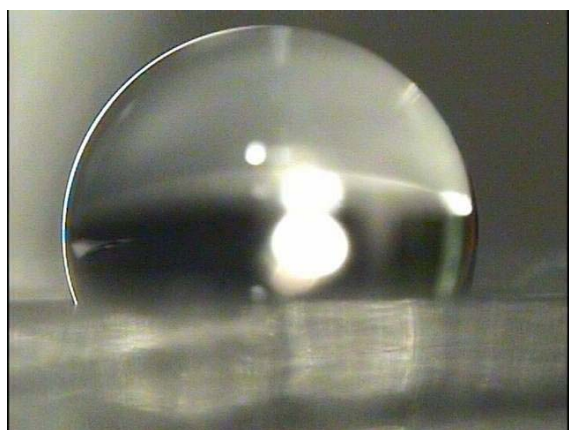


**Figure 3.5** Figure 3 Young's modulus measurements on PDMS (red traces,  $n = 3$ , top set) and PDMS-SiO<sub>2</sub> (blue traces,  $n = 4$ , bottom set).

Light transmission measurements of both the PDMS and the PDMS-SiO<sub>2</sub> chips revealed no significant difference in light transmission between 400 and 700 nm. At wavelengths < 400 nm, however, the scattering of light off the large number of closely spaced fused silica particles in the PDMS-SiO<sub>2</sub> chips significantly lowered the light transmission. This effectively limits optical detection to the visible range of the electromagnetic (EM) spectrum; however, all reports of optical detection on PDMS thus far have been between 400 and 700 nm.

One of the primary goals of this new fabrication method was to generate hydrophilic channel wall surfaces. The “hydrophilicity” of the walls was assessed using both water contact angle measurements and rhodamine B absorption measurements. Water contact angle measurements revealed a difference of 18.3° between the native Sylgard 184 PDMS (108.5°) and the PDMS-SiO<sub>2</sub> (90.2°) chips. **Figure 3.6** The water contact angle measured for the Sylgard 184 was the same as that reported previously.<sup>85</sup> This change in water contact angle indicated that the PDMS-SiO<sub>2</sub> surface was substantially more hydrophilic than that of PDMS.



PDMS  $\theta = 108^\circ$



PDMS-SiO<sub>2</sub>  $\theta = 90^\circ$

**Figure 3.6** Contact angles for PDMS and PDMS-SiO<sub>2</sub>.

Of more interest, however, were the rhodamine B absorption results. **Figure 3.7 A-F** shows a series of images taken over a 4 hour period of both PDMS-SiO<sub>2</sub> and PDMS microchips in which a 100  $\mu$ M concentration of RhB had been siphoned through the channels. As can be seen from the images, there is significant absorption of RhB into the bulk of the PDMS microchip while the absorption of RhB is completely inhibited in the PDMS-SiO<sub>2</sub> chips. A more quantitative comparison can be seen in **Figures 3.7 G and H** where the fluorescence intensity of a slice taken through the channels can be seen. While the absorption of RhB was successfully stopped using the PDMS-SiO<sub>2</sub> chips, a small amount of surface adsorption still remained. This can be seen in the “bat ears” in the intensity profiles where the fluorescent signal from the RhB adsorbed to the channel surface is integrated along the vertical channel walls. RhB does adsorb to negatively charged silica surfaces, and this is probably what is being seen in these images.<sup>121</sup>

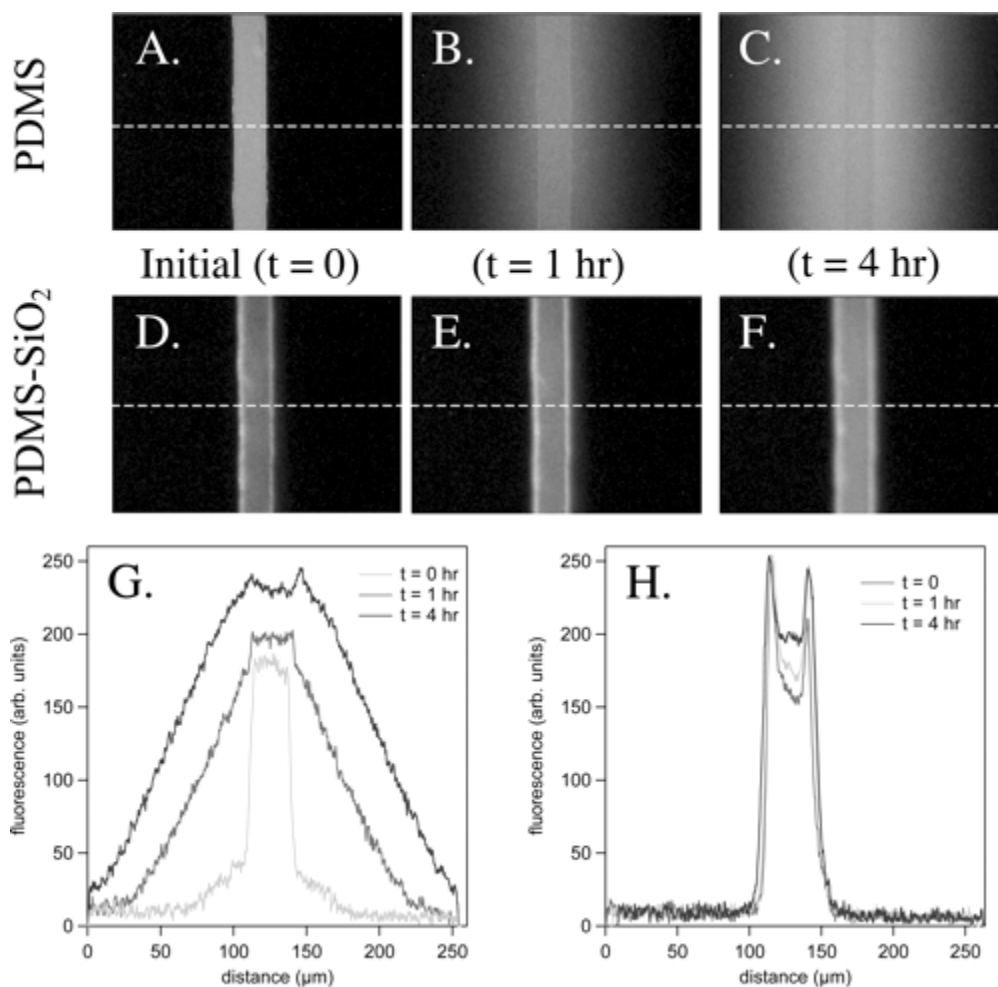


**Figure 3.7** Rhodamine B Absorption Measurements. Images of PDMS (A-C) and PDMS-SiO<sub>2</sub> (D-F) devices are shown. The channels on these devices are filled with 10 μM Rhodamine B in a 10 mM (pH 9.5) sodium borate solution. The images were acquired over a 4 hour period. Fluorescent profiles of the PDMS and PDMS-SiO<sub>2</sub> channels are also shown in G and H, respectively. These profiles were taken along the white dotted line in images A-F.

### 3.4.2 EOF Measurements.

Initial EOF measurements were made using the conductivity method described in the experimental section where a 1 mM (pH 8.3) sodium phosphate/10 mM KCl buffer was replaced by a 1 mM (pH 8.3) sodium phosphate/9 mM KCl buffer in the channel through electromigration. The initial electroosmotic mobilities (EOM) measured on the PDMS-SiO<sub>2</sub>, PDMS, and glass microchips were  $8.3 \pm 0.2 \times 10^{-4} \text{ cm}^2/\text{V}\cdot\text{s}$  (RSD = 2.6%, n = 10),  $4.21 \pm 0.09 \times 10^{-4} \text{ cm}^2/\text{V}\cdot\text{s}$

(RSD = 2.2%, n = 10) and  $5.3 \pm 0.4 \times 10^{-4} \text{ cm}^2/\text{V}\cdot\text{s}$  (RSD = 7.7%, n = 5), respectively. For all of the values reported five replicate measurements were made on each of “n” different chips. The results reported for PDMS-SiO<sub>2</sub> and PDMS, therefore, are the average of 50 measurements each. The average measured EOF on the PDMS-SiO<sub>2</sub> chips was 96% greater than that on the Sylgard 184 PDMS chips and 55% greater than that on glass chips. The values measured for the glass and Sylgard 184 PDMS chips were within experimental error of those reported in a previous investigation of PDMS.<sup>68</sup> After 60 days of **dry** storage the EOM was measured at  $7.6 \pm 0.3 \times 10^{-4} \text{ cm}^2/\text{V}\cdot\text{s}$  (RSD = 3.9%, n = 3), a decrease of only 8% below that of the initially measured value. Previous methods of increasing the EOM on PDMS chips using plasma oxidation sources required that the “activated” channel walls remain in contact with an aqueous solution to maintain the higher EOM’s over time.<sup>85</sup> The %RSD’s obtained on the PDMS-SiO<sub>2</sub> chips were significantly better than those obtained on glass chips and similar to those obtained on PDMS chips. The repeatability of these measurements indicates that this method of surface modification is both robust and very reproducible.

As we more commonly use borate buffers for separations, EOF measurements were also made by displacing 25 mM Borate solutions with a 50 mM solution. Using the borate buffer system, the EOM’s measured on the PDMS-SiO<sub>2</sub>, PDMS, and glass chips were  $3.50 \pm 0.07 \times 10^{-4} \text{ cm}^2/\text{V}\cdot\text{s}$  (RSD = 2%, n = 5),  $2.1 \pm 0.2 \times 10^{-4} \text{ cm}^2/\text{V}\cdot\text{s}$  (RSD = 7%, n = 10), and  $3.3 \pm 0.1 \times 10^{-4} \text{ cm}^2/\text{V}\cdot\text{s}$  (RSD = 4%, n = 5), respectively. The EOM’s measured for the PDMS-SiO<sub>2</sub> chips were 64% greater than on the PDMS chips and 6% greater than on glass chips.

### ***3.4.3 Separations.***

To determine the separation characteristics of the new PDMS-SiO<sub>2</sub> polymer, a series of amino acid separations were performed. Two separate derivatizations were performed. In one

set of derivatizations a hydrophilic dye – fluorescein isothiocyanate (FITC) – was conjugated to the amino acids, in the other derivatization a hydrophobic dye – carboxytetramethylrhodamine succinimidyl ester (TAMRA) - was conjugated to the amino acids. All other labeling conditions were the same. These dyes represent two of the most common families of fluorescent dyes used for amino acid and protein analysis. **Figure 3.8** shows the separation of 3 FITC labeled amino acids – Arg, Ser, and Glu - on both the Sylgard 184 PDMS and the PDMS-SiO<sub>2</sub> chips. The separation distance was 3.5 cm and the field strength applied was 650 V/cm. The migration times ( $t_m$ ), separation efficiencies (N), and rate of plate generation (N/s) are shown in **Table 2**. Due to the higher EOF, the separations on the PDMS-SiO<sub>2</sub> chips were ~32% faster. The relative standard deviation (RSD) of the migration times ranged from 1 to 1.6% for runs made on the PDMS chips and 2.4 to 2.6% on the PDMS-SiO<sub>2</sub> chips. The variation in migration time was caused by the evaporation of the buffer in the solvent reservoirs. The solvent reservoirs punched in these chips can only hold ~10  $\mu$ L. With larger buffer reservoirs in future designs of these chips such migration time variations should decrease. While the actual separation efficiencies for both chips are excellent, the rate of plate generation is 22 to 80% higher on the PDMS-SiO<sub>2</sub> chips. This increase is due primarily to the increase in EOF.

Analyte	PDMS			PDMS-SiO <sub>2</sub>		
	t <sub>mig</sub> (s)	N	N/s	t <sub>mig</sub> (s)	N	N/s
FITC Arg(-2)	9.63 ±0.15	77,000 ±1,600	8,000	6.62 ±0.17	65,000 ±2,100	9,800
FITC- Ser (-3)	14.04 ±0.14	80,700 ±1,200	5,700	9.54 ±0.25	97,900 ±2,700	10,250
FITC Glu (-4)	19.73 ±0.20	61,800 ±1,000	3,100	13.25 ±0.35	62,800 ±2,000	4,700
TAMRA -Ser(-1)	13.96 ±0.15	39,500 ±600	2,800	7.4 ±0.16	94,400 ±3,300	12,400
TAMRA-Pro(-1)	11.2 ±0.20	27,000 ±500	2,500	6.52 ±0.19	82,800 ±3,4000	13,000

**Table 2** Migration times, separation efficiencies, and rate of plate generation for fluorescently labeled amino acids on PDMS and PDMS-SiO<sub>2</sub> chips. Three replicate measurements were made to obtain the average values and standard deviations reported above. The number in parentheses next to the analytes are their nominal charges.

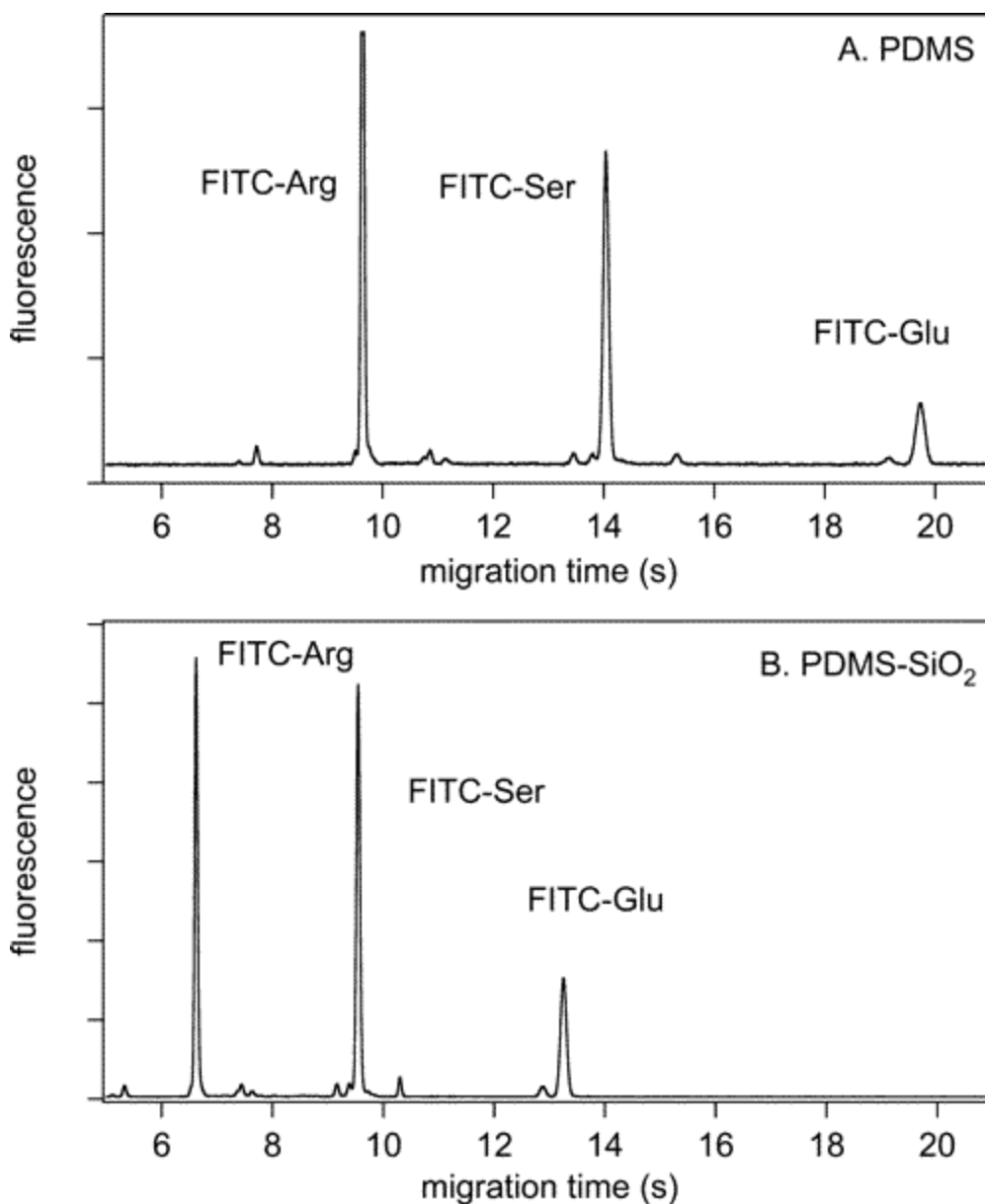


**Figure 3.8** Separation of FITC labeled amino acids on PDMS (A) and PDMS-SiO<sub>2</sub> (B) chips. The concentration of the labeled amino acids was 2  $\mu$ M. The separation distance was 3.5 cm, and the separation field strength was 650 V/cm.

**Figure 3.9** shows the separation of 2 TAMRA derivatized amino acids. The separation distance and field strength were the same as in the FITC separations. The migration times ( $t_m$ ), separation efficiencies (N), and rate of plate generation (N/s) are shown in **Table 2**. Again, due to the higher EOF exhibited on the PDMS-SiO<sub>2</sub> chips, the separations are about 50% faster than

on the Sylgard 184 PDMS chips. The migration velocities of the rhodamine labeled dyes are faster than the fluorescein as they have 2 less negative charges than the fluorescein labeled dyes.

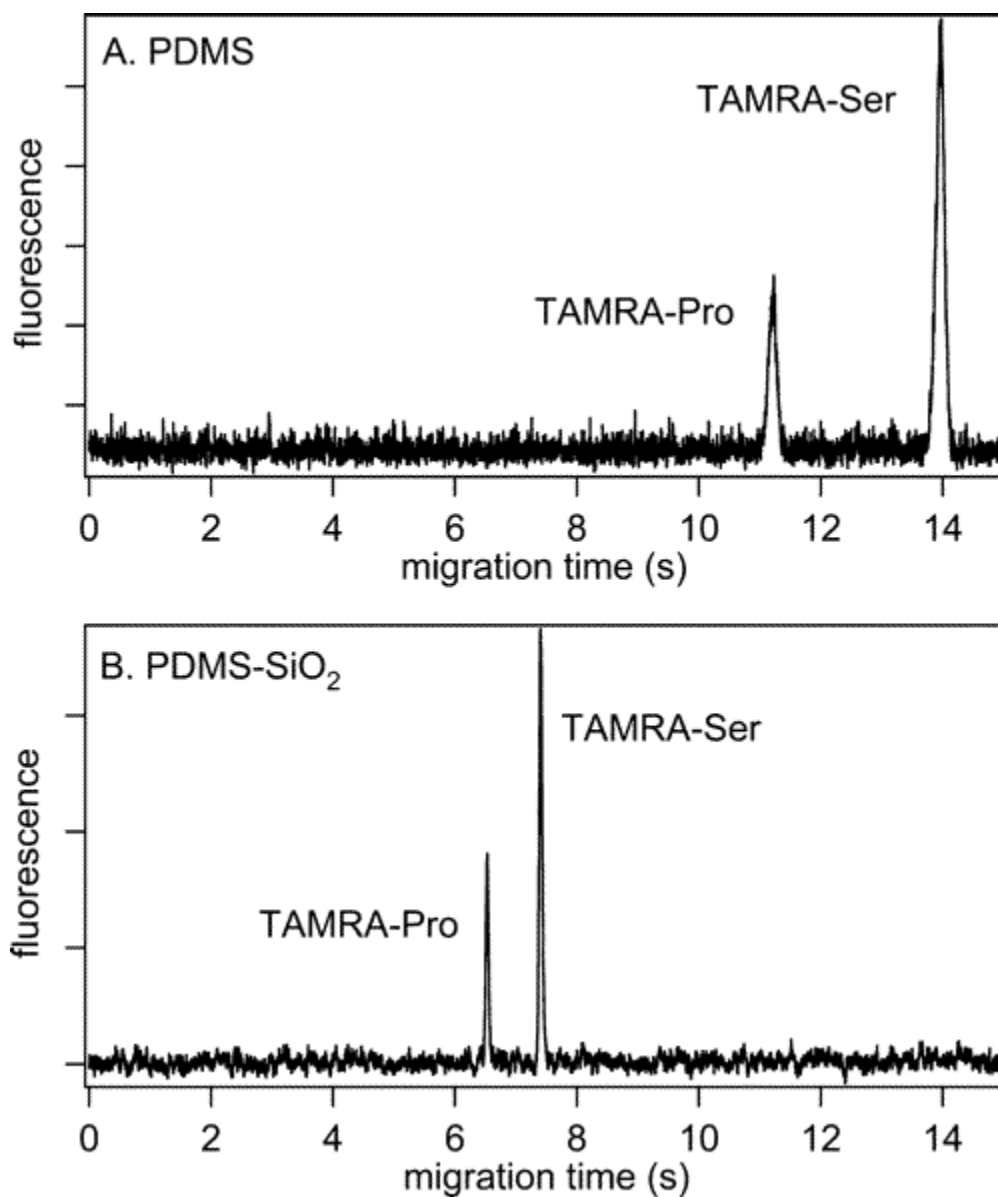


**Figure 3.9** Separation of TAMRA labeled amino acids on PDMS (A) and PDMS-SiO<sub>2</sub> (B) chips. The concentration of the labeled amino acids, the separation distance, and the separation field strength are the same as reported in Figure 3.5.

The relative standard deviation of the migration times ranged from 1.1 to 1.8% for runs made on the PDMS chips and 2.1 to 2.9% on the PDMS-SiO<sub>2</sub> chips. Again the small buffer

reservoirs were responsible for the variations seen in migration times. The advantage of having the hydrophilic surface on the PDMS-SiO<sub>2</sub> microchips can especially be seen with these analytes which have been derivatized with a hydrophobic dye. The absolute separation efficiencies are 2 to 3 times greater on the PDMS-SiO<sub>2</sub> than on the PDMS (Sylgard 184) chips. In addition, the rate of plate generation is > 4 times better on the PDMS-SiO<sub>2</sub> chips. In the case of the TAMRA dyes, the improvement in the rate of plate generation is not solely due to the increase in EOF; rather the walls of the PDMS-SiO<sub>2</sub> chips generate significantly less analyte adsorption.

To quantify the decrease in analyte absorption, the apparent diffusion coefficient of TAMRA-serine was measured on both chips through a series of runs made at different detection distances – 2.1, 2.5, 2.9, 3.3 and 3.7 cm. Assuming only random processes are leading to the band broadening, a plot of spatial peak variance versus migration time will result in a slope which is twice that of the apparent diffusion coefficient ( $\sigma^2 = 2Dt$ ).<sup>122</sup> The apparent diffusion coefficients measured for TAMRA-Serine on the PDMS (Sylgard 184) and PDMS-SiO<sub>2</sub> chips were  $6.0 \pm 0.5 \times 10^{-6} \text{ cm}^2/\text{s}$  and  $4.1 \pm 0.2 \times 10^{-6} \text{ cm}^2/\text{s}$ , respectively. The apparent diffusion coefficients are “apparent” because they are being measured in a flowing stream driven either by pressure driven or electroosmotic flow. The diffusion coefficient measured for the PDMS chip was much higher than the diffusion coefficient measured for the PDMS-SiO<sub>2</sub> indicating a reduction in the band broadening caused by adsorption to the surface. These calculations are illustrated in **Figure 3.10** The apparent diffusion coefficient measured for the TAMRA-Serine on the PDMS-SiO<sub>2</sub> chip is within ~15% of previously reported diffusion coefficient values for similar rhodamine labeled amino acids indicating that the separation on PDMS-SiO<sub>2</sub> chips is effectively diffusion limited.<sup>122</sup> It is the decrease in analyte adsorption/absorption coupled with

the higher EOF which leads to the significantly improved separation efficiencies on the PDMS-SiO<sub>2</sub> chips.

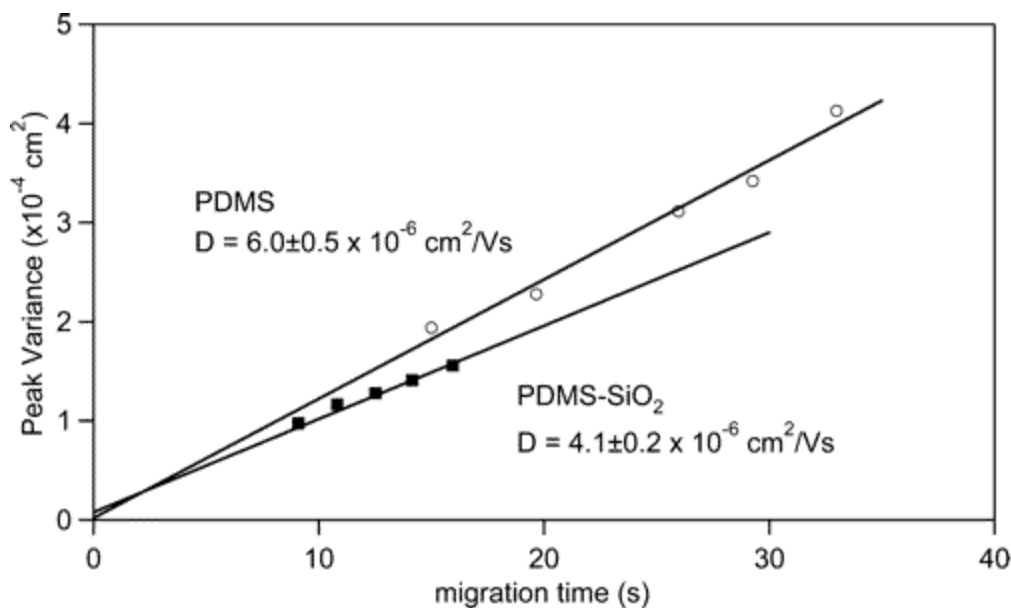


**Figure 3.10** Plot of migration time vs peak variance of TAMRA-serine on PDMS microchips (circles) and PDMS-SiO<sub>2</sub> microchips (squares).

#### ***3.4.4 Mold robustness.***

The SU-8 molds used to cast the PDMS chips against proved to be extremely robust lasting for at least a hundred replications before the fidelity of channel walls began to diminish. We generally observed losses in separation efficiency from chips cast against the same SU-8 mold after about two months of continuous use. These losses in separation efficiency were due to increased surface roughness of the mold.

#### ***3.4.5 Conclusion***

Using a sol-gel method we have fabricated poly(dimethylsiloxane) (PDMS) microchips with SiO<sub>2</sub> particles homogeneously distributed within the PDMS polymer matrix. These particles are ~ 10 nm in diameter. To fabricate such devices, PDMS (Sylgard 184) was cast against SU-8 molds. After curing, the chips were carefully removed from the mold and sealed

against flat, cured pieces of PDMS to form enclosed channel manifolds. These chips were then solvated in tetraethylorthosilicate (TEOS) causing them to expand. Subsequently, the chips were placed in an aqueous solution containing 2.8% ethylamine and heated to form nanometer-sized SiO<sub>2</sub> particles within the crosslinked PDMS polymer. The water contact angle for the PDMS-SiO<sub>2</sub> chips was ~ 90.2° compared to a water contact angle for Sylgard 184 of ~108.5°. More importantly, the SiO<sub>2</sub> modified PDMS chips showed no rhodamine B absorption after 4 hours indicating a substantially more hydrophilic and non-absorptive surface than native PDMS. Initial electroosmotic mobilities (EOM) of  $8.3 \pm 0.2 \times 10^{-4} \text{ cm}^2/\text{V}\cdot\text{s}$  (RSD = 2.6%, n = 10) were measured. This value was approximately twice that of native Sylgard 184 PDMS chips  $4.21 \pm 0.09 \times 10^{-4} \text{ cm}^2/\text{V}\cdot\text{s}$  (RSD = 2.2%, n = 10) and 55% greater than glass chips  $5.3 \pm 0.4 \times 10^{-4} \text{ cm}^2/\text{V}\cdot\text{s}$  (RSD = 7.7%, n = 5). After 60 days of **dry** storage, the EOM was  $7.6 \pm 0.3 \times 10^{-4} \text{ cm}^2/\text{V}\cdot\text{s}$  (RSD = 3.9%, n = 3), a decrease of only 8% below that of the initially measured value. Separations performed on these devices generated 80,000 to 100,000 theoretical plates in 6 to 14 s for both TAMRA and FITC derivatized amino acids. The separation distance was 3.5 cm. Plots of peak variance vs. analyte migration times gave diffusion coefficients which indicate that the separation efficiencies are within 15% of the diffusion limit.

In conclusion, we have reported a facile, robust, and reproducible method of modifying the channel wall surfaces of PDMS. This method leads to increased and stable EOF's. It also improves wettability and minimizes the absorption of hydrophilic analytes into the bulk material. In the future we will describe a variety of surface modifications that can be made on these devices using silanol-based chemistry.

### **3.6 Thin Sol-Gel Films Using the “Coat and Go” Technique**

### 3.6.1 Introduction to Coat and Go

In addition to the sol-gel method described above we also investigated a technique that is capable of placing a sol-gel thin film with a depth of  $\sim 1 \mu\text{m}$  on the PDMS capillary sidewalls. This technique is analogous to the spin or dip coating techniques used in photolithography, only it is performed in this case on capillaries. The unique surface area to volume ratios, and surface tension of the coating assist in producing more cylindrical channels, shown schematically on **Figure 3.11**. The depth of the film will greatly depend on the orientation of the film to the square channels.

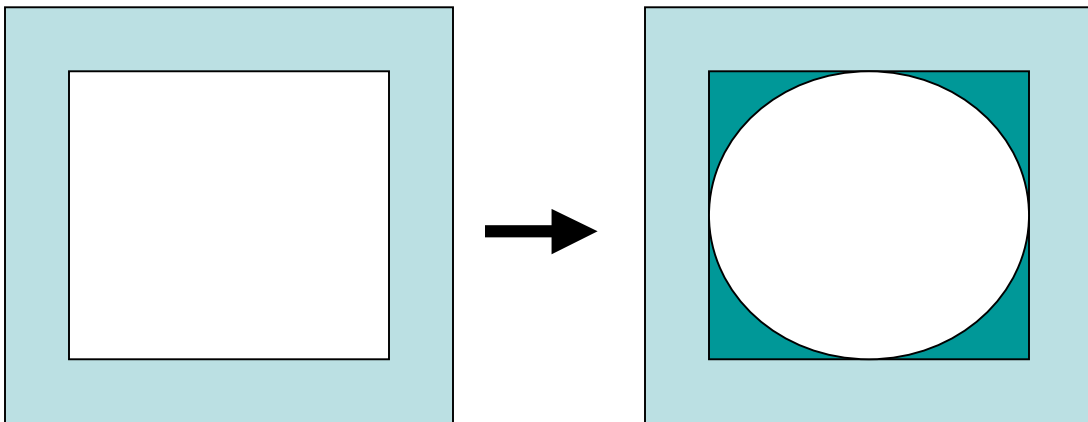


**Figure 3.11** Left: A profile of a square PDMS channel prior to coating, Right: A profile of a square PDMS channel after it has been coated with a sol-gel film. The surface tension of the coating tends to form cylindrical profiles for the square PDMS channels, thus the thickness of the film that is formed depends on the orientation to the square side wall.

A number of different films can be generated using this method. The atomic composition can be modified by using different precursors, or the physical properties can be modified by changing the processing characteristics (e.g. gelation time, or drying conditions). The reaction scheme is diagrammed in **Figure 3.12**. The sol-gel that is synthesized in this reaction is also catalyzed by oxygen. Capped under nitrogen or inert gas it does not react to form a sol and then a

gel. It can also be spin coated on glass or other substances and polymerized at room temp. It is hypothesized that the PDMS monomer assists in non-covalent adsorption of the sol-gel to the surface of the PDMS channel.

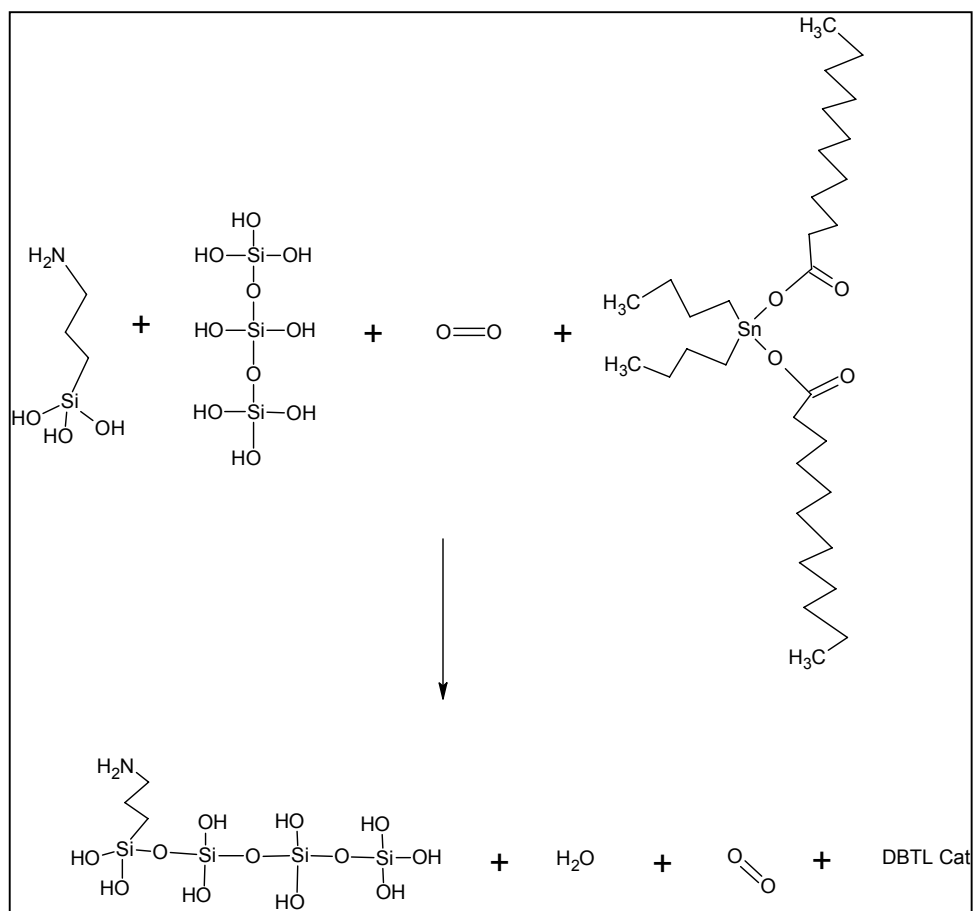


**Figure 3.12** The reaction between the tin catalyst, the hydroxyl functionalized PDMS and APTES is shown. The reaction is oxygen sensitive.

### ***3.6.2 Experimental Coat and Go***

To perform a coating using this method the following mixture was constituted: 1.5g Tin Catalyst: dibutylaurin (DBTL), 1.5g Crosslinking agent (ethylsilicate), 1.4g APTES. This yields about 1 crosslinker for every 4 APTES molecules. This solution was placed in the reservoirs of the PDMS chip and a vacuum at  $\sim 100$  kPa was applied to pull the solution through the channels. After the channel was coated the channel was dried at room temperature for 1 hr, and used in EOF measurements and electrophoretic separations. To perform a coating using another derivative substitute either one of the following reagents for APTES in the reaction scheme shown above, mixed in similar molar ratios of 1:4: 2-[Methoxy(polyethyleneoxy)propyl]heptamethyltrisiloxane, (Heptadecafluoro- 1,1,2,2- Tetra-hydrodecyl)triethoxysilane or 3-mercaptopropyltriethoxysilane.

### ***3.6.3 EOF measurements***

EOF measurements were performed using the methods previously mentioned. Initially we studied the APTES derivitization as it was simple to validate the presence of the amine at low pH as it would reverse the EOF. This study involved 3 channels coated with APTES and monitored over the period of a week, shown in **Figure 3.13**. The coatings changed in EOM between 5-35% over the period of 6 days, although the first 48 hrs were very reproducible with %RSD's less than 5%.

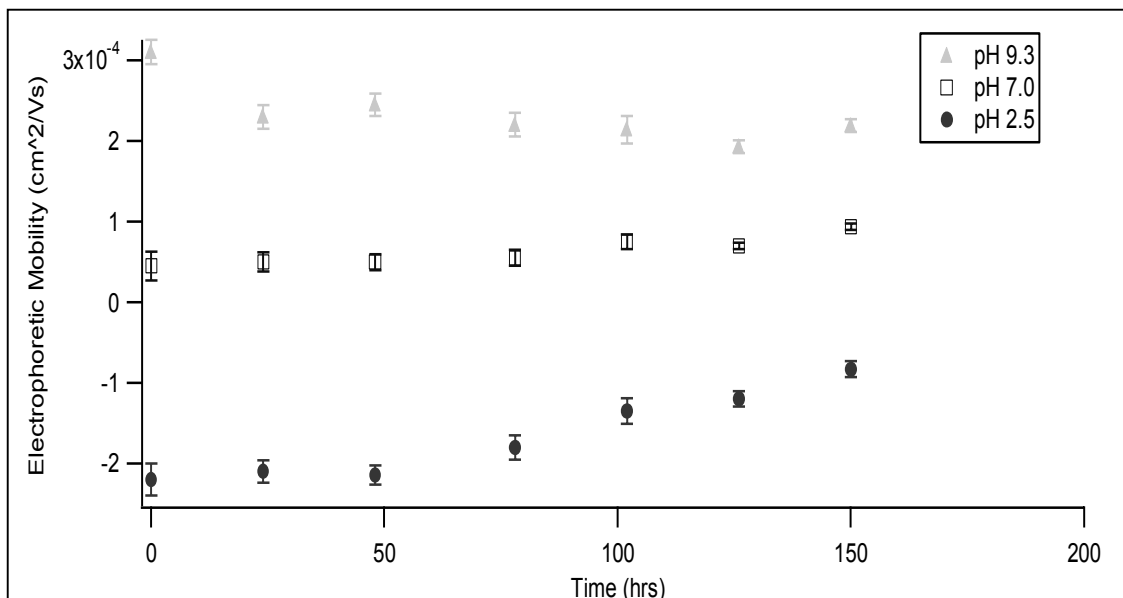


**Figure 3.13** Durability tests of the APTES derivitization on the PDMS surface using the coat and go coatings. The conditions used for this measurement were 25 mM sodium borate with a field strength of 300 V/cm. A higher conductivity buffer of 50 mM sodium borate was used to measure the EOF.

### 3.6.4 Solid Phase Monoliths Fabricated Using Sol-Gel Tin Catalysis

In addition to coating PDMS channels using this reaction it was also possible to generate a number of stationary phase monoliths. For instance, in **Figure 3.14**, demonstrates a thiol stationary phase using a similar reaction in **Figure 3.12**, with the only difference being the substitution of thiol-trimethoxysilane for aminopropyltriethoxysilane. These monoliths have the potential of being used for a number of novel separation schemes.

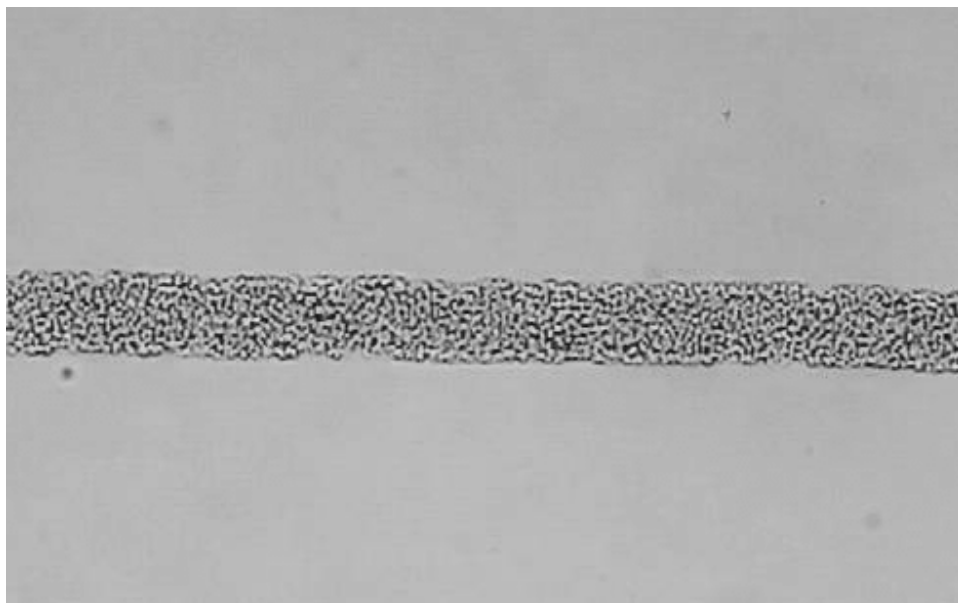


**Figure 3.14** Thiol stationary phase generated using sol-gel chemistry on a PDMS microfluidic device.

### ***3.6.5 Separations on PDMS coated channels***

A number of separations were also performed on PDMS microchips coated using this technology. A series of fluorescein labeled amino acids were separated on the native PDMS, PEG coated PDMS and perfluoro coated PDMS, and is shown in **Figure 3.15**. The fluorine derivitized surface appears to chromatographically react with proline, which tends to broaden this peak with relation to proline separated on both PDMS and PDMS-PEG. Since the PEG coated channels have a much slower EOF the migration times of each of the amino acids is much slower using this coating. The longer migration times allow for better resolution between both serine and proline on the PDMS-PEG coated chip, in comparison to the resolution between serine and proline for the native PDMS chip. The migration order for each of the amino acids was identical for all the coatings. Differences in electroosmotic flow and efficiencies were the variables of interest for these electrophoretic separations.

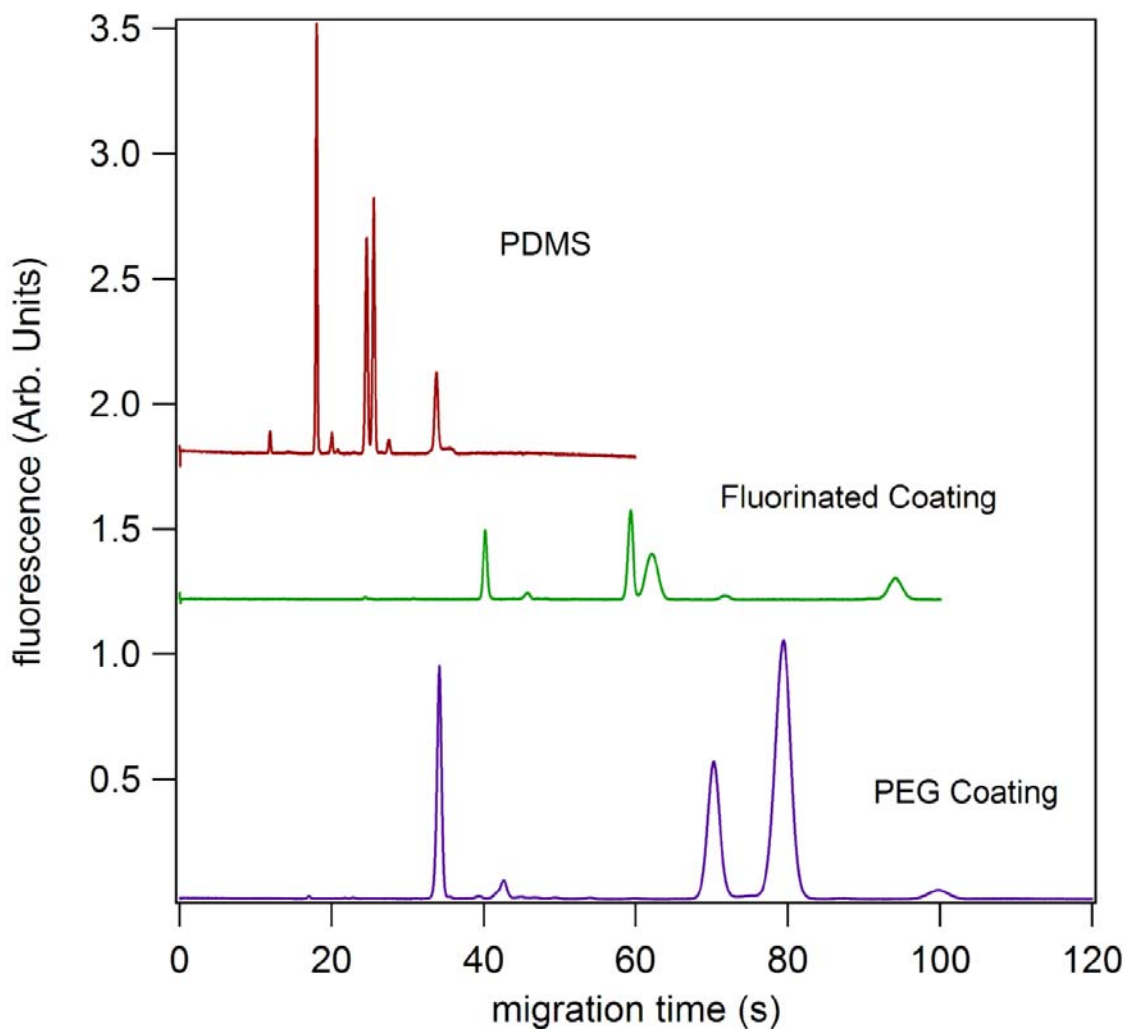


**Figure 3.15** Separations of FITC labeled amino acids on a variety of coated PDMS microfluidic channels.

## CHAPTER 4 - Sol-Gel Transition Metal Modified PDMS

### 4.1 Introduction

We report the coating of poly(dimethylsiloxane) (PDMS) microchannels using transition metal sol-gel chemistry and the subsequent characterization of the coatings. The channels were created using soft polymer lithography and three metal alkoxide sol-gel precursors were investigated - titanium isopropoxide, zirconium isopropoxide and vanadium triisobutoxide oxide. The metal alkoxides were diffused into the sidewalls of a PDMS channel and subsequently hydrolyzed using water vapor. This procedure resulted in the formation of durable metal oxide surfaces of titania, zirconia or vanadia. The resulting surfaces were characterized using contact angle, X-ray photoelectron spectroscopy (XPS), Raman, transmission electron microscopy (TEM), scanning electron microscopy (SEM), atomic force microscopy (AFM) and electroosmotic mobility (EOM) measurements. All of the metal oxide modified PDMS surfaces were significantly more hydrophilic than native PDMS. Contact angles for the coatings were 90° for PDMS-ZrO<sub>2</sub>, 61° for PDMS-TiO<sub>2</sub> and 19° for vanadia-PDMS. XPS showed the presence of titania, zirconia and vanadia on the PDMS surface. XPS spectra also showed no chemical modification of the PDMS after the *in situ* deposition of the particles either in the Si-O, Si-C or C-H bonds of the PDMS. The particles deposited *in situ* were imaged with TEM and were found to be homogeneously distributed throughout the bulk of the PDMS. EOM measurements of the inorganic coatings were stable over the period of at least 95 days. Both cathodic and anodic EOM's could be generated depending upon buffer pH used. The point of net zero charge for

PDMS-TiO<sub>2</sub>, PDMS-ZrO<sub>2</sub> and PDMS-vanadia channels were calculated using EOM vs. pH measurements and were found to be  $4.1 \pm 0.25$ ,  $6.1 \pm 0.2$  and  $7.0 \pm 0.43$ , respectively. In addition to modifying PDMS channels with inorganic coatings these inorganic coatings were derivatized with various organic functionalities including oligoethylene oxide (OEO), amino, perfluoro or mercapto groups using silane chemistry. Contact angle measurements for perfluoro, mercapto, amino and OEO coated surfaces yielded contact angles of 120°, 76°, 45° and 23°, respectively. These contact angles did not change over the period of 95 days. OEO coated channels reduced the EOM by 50% from native PDMS-TiO<sub>2</sub> to  $0.9 \times 10^{-4} \pm 0.05$  (n=5, 5.5 %RSD).

The advent of mesostructured materials in the early 1990's and the simultaneous development of *in situ* reinforced polymeric composites by sol gel processes have been the subject of intense scientific and technological interest.<sup>123-128</sup> High performance and multi-functional materials have been reported to have many advantages.<sup>129</sup> Numerous applications including catalysis,<sup>130-134</sup> electronics,<sup>135</sup> sensors and photovoltaic devices<sup>136, 137</sup> have contributed to the technological interest in these materials. New organic-inorganic hybrid materials have been created using a wide array of synthetic approaches. The routes for synthesis of these materials often use common and well known methods of sol-gel chemistry consisting of the hydrolysis and condensation of appropriate alkoxy compounds within an organic polymer or template matrix.<sup>125, 127, 138</sup> Typically tetraethylorthosilicate (TEOS) is used to generate silica, but many transition metal alkoxides can also be used to form their corresponding oxides.

Poly(dimethylsiloxane) (PDMS) is extensively used in replica micromolding applications including the fabrication of low cost, disposable microfluidic devices. The ability of PDMS to serve as a useful substrate for microfluidic fabrication extends from advantages such as 1) high gas permeability, 2) good optical transparency, 3) moldability, 4) non-toxicity or

biocompatibility, 5) low curing temperature, and 6) ease of sealing with other materials.<sup>14, 51, 139-</sup>

<sup>142</sup> Although PDMS has many advantages there are some physical properties that limit its broad application. PDMS is hydrophobic and small hydrophobic molecules, biopolymers and cells all irreversibly adsorb to the surface.<sup>49</sup> In addition the small hydrophobic molecules will also actually absorb into the bulk PDMS. Another limiting factor is the lack of reactive functional groups at the surface of PDMS that can be used to modify the surface chemistry in a manner similar to the silanol chemistry that can be performed at the surface of silica capillaries and channels to form stable coatings for open capillary electrophoretic chromatography (OCEC) and other separation modes.<sup>32, 143</sup>

Several methods have recently been reported to modify the surface of PDMS microchannels to make them more amenable for separations. Oxidation by a plasma discharge has been widely reported as a means of creating silanol functional groups at the surface of PDMS.<sup>51, 141</sup> These groups can then be used to attach 3-aminopropyl and 2-(4-chlorosulfonylphenyl) groups<sup>9, 52, 144</sup> using simple silanol condensation chemistry. These modified surfaces were shown to improve both the electroosmotic flow properties of the microchip alongside with the operational lifetime.<sup>52</sup> Surface oxidation has also been followed by the use of free radical chemistry for the attachment of acrylic acid, acrylamide, dimethylacrylamide, 2-hydroxyethylacrylate and poly(ethylene glycol) monomethoxyacrylate.<sup>90, 145, 146</sup> Additionally, surface oxidation has been followed by atom transfer radical polymerization for the attachment of acrylamide and poly(ethylene glycol).<sup>95, 147-149</sup> Covalent modifications that do not use coronal discharge or plasma have also been developed. Examples of such modifications include surface oxidation through the use of cerium(IV) and nitric acid for the attachment of acrylamide<sup>150, 151</sup> and chemical vapor deposition for the attachment of poly-(para-

xylylene carboxylic acid pentafluorophenylester-co-para-xylylene).<sup>99, 152</sup> In addition to the covalent modifications several noncovalent modifications have also been described for PDMS surfaces. Some of these noncovalent modifications include the addition of ionic surfactants,<sup>49, 153</sup> proteins<sup>128</sup> and polyelectrolyte layers (PEL).<sup>51, 154</sup> Unfortunately, most of these modified PDMS surfaces recover their original hydrophobicity with aging and do not serve as devices that can be used over extended periods of time.<sup>155</sup>

The physical properties of PDMS can be extensively modified using sol-gel chemistry. The use of sol-gel processes to generate SiO<sub>2</sub> and TiO<sub>2</sub> particles in PDMS polymers has been studied extensively by Mark's group over the past 20 years with the aim of creating better PDMS-based materials.<sup>109, 111, 113, 123, 125-127, 156, 157</sup> Most recently PDMS has been used as a template for the synthesis of metal oxide spheres, bowls, and network structures.<sup>158</sup> We have been using such sol gel processes to modify cured PDMS surfaces as opposed to the bulk prepolymerization modifications studied by Mark's group, and to use these processes as an alternative to the PDMS surface modifications currently available. The chemical modification of PDMS using these sol gel methods is advantageous for several reasons, including: 1) the high density of precipitated particles, 2) the homogenous distribution of particles near the surface and 3) the stable surface chemistry.<sup>138</sup> Fabrication of microfluidic devices using in situ precipitation is favorable because it retains the positive attributes of PDMS as an excellent substrate for replica micromolding but also allows for post fabrication modification of the surface properties of PDMS. In situ precipitation also avoids other problems associated with the addition of additives such as "structuring" or "crepe hardening" where premature gelation can cause problems in the curing process.<sup>125</sup> We have previously shown that silica modified PDMS microfluidic devices can be fabricated using common silica sol gel chemistry.<sup>159</sup> That work

illustrated the advantages of using sol-gel modified PDMS surfaces in microfluidics. The silica surface substantially increased electroosmotic flow, reduced the surface hydrophobicity, eliminated Rhodamine B absorption, and consequently increased the separation efficiencies of the devices.

Other than silica, there are several different inorganic compounds that can be imbedded within PDMS using sol gel methods. Some of these include the oxides of aluminum, germanium, hafnium, titanium, vanadium or zirconium. The acid-base characteristics of the metal oxides depend on the periodic properties of the metal. Zirconia and titania have been reported to be relatively basic compounds as compared to silica. The pI's of the rutile phases of  $\text{TiO}_2$ ,  $\text{ZrO}_2$  and silica have been calculated at 4.7, 6.7 and 1.8, respectively.<sup>160</sup> The differences in acid base properties of metal oxide coated capillaries will have effects on the  $\zeta$  potential of the surfaces and, consequently, the zero net charge. Materials that have a wider range of  $\zeta$  potentials have the potential to provide alternatives that broaden the application range for microfluidic devices. The  $\zeta$  potential for both PDMS and silica capillaries have been thoroughly studied. PDMS and silica exhibit low positive EOMs for solutions with pHs of  $\sim 2$ .<sup>49, 161-163</sup> Modifying the  $\zeta$  potential of silica capillaries using active agents, buffer pH, buffer composition, temperature or chemical derivatization has been reported<sup>164-166</sup>. In addition to these modifications, silica capillaries have been coated with titanium oxide,<sup>167-169</sup> aluminum oxide,<sup>168</sup> zirconia oxide,<sup>170, 171</sup> and magnesia zirconia oxide<sup>172</sup> in attempts to modify the  $\zeta$  potential. These modifications show that it is possible to achieve a zero net charge on modified silica capillaries in the pH range from 5-7. Lysozyme CE separations on these modified capillaries in a buffer near the zero net charge of the capillaries were achieved with an efficiency of 20,000 N/m.<sup>168</sup>

Although sol gel modified PDMS increases the range of hydrophobicities and  $\zeta$  potentials available in PDMS microchannels, it would be advantageous to be able to further modify the surface with any chemical functionality. Fortunately the surfaces generated by these inorganic coatings have the potential to be further functionalized using silanol condensation chemistry. Many of these techniques and reactions have been optimized in silica substrates. For instance, tri-functional organosilane reagents have been deposited on metal oxides and glass to create dense films.<sup>173, 174</sup> These films deposited on glass have been used for reversed phase chemical separations.<sup>175</sup> Examples of silanol condensation coatings on silica microchips include the use of (octadecyl)trimethoxysilane for OCEC,<sup>32</sup> (3-aminopropyl)triethoxysilane<sup>143</sup> for use in liquid chromatography of basic proteins<sup>176, 177</sup> and 3-glycidoxypropyltrimethoxysilane<sup>178</sup> for use in CZE protein separations. Alternative functionalities such as OEO or fluorinated triethoxysilanes may also be useful as capillary/channel wall coatings, especially on PDMS microchips. OEO has been documented as being extremely resistant to protein adsorption and when used as a self assembled monolayer or polymer it is biocompatible and useful for protein separations yielding efficiencies up to 290,000 N/m.<sup>35, 179, 180</sup>

This paper reports a sol-gel method for introducing metal alkoxy precursors into PDMS channels that allows for the creation of fast and efficient inorganic coatings on PDMS channel surfaces. These coatings were effective at modifying the hydrophobicity of the PDMS along with the  $\zeta$  potential by incorporating different types of solid oxides onto the surface of the PDMS channels. The properties of the modified PDMS microchannels were examined using XPS, Raman, EOM, TEM, SEM and contact angle. Additionally, we further functionalized these metal oxide surfaces with OEO, 3-aminopropyl-, thiol and perfluoro- groups.

## 4.2 Experimental Section

#### ***4.2.1 Reagents.***

Titanium isopropoxide, zirconium isopropoxide, vanadium triisobutoxide oxide, heptadecafluoro- 1,1,2,2- Tetra-hydrodecyl-triethoxysilane, 3-mercaptopropyltriethoxysilane and 2-[methoxy(polyethyleneoxy)propyl]-trimethoxysilane (OEO) were purchased from Gelest (Morrisville, PA) and stored in a dessicator at 25°C. The 3-aminopropyltriethoxysilane (APTES) was purchased from Aldrich (St. Louis, MO). Commercial PDMS (Sylgard 184) was purchased from Dow Corning (Midland, MI). Sodium tetraborate, sodium phosphate and 2-propanol were purchased from Acros Organics (Geel, Belgium). All solutions were made using distilled, deionized water from a Barnstead Nanopure System (Dubuque, IA) and subsequently filtered through 0.45 µm Acrodiscs (Gelman Sciences, Ann Arbor, MI). All chemicals were used as received.

#### ***4.2.2 Microchip Fabrication and Surface Modification.***

The Sylgard 184 elastomer was constituted and activated as specified by the manufacturer and degassed for 1 h. Part of this mixture was poured on an SU-8 mold and another part on a clean microscope slide (the blank). After curing for 10 min at 80 °C, both parts were carefully and slowly peeled off the mold and blank. The two pieces of PDMS were then conformally contacted and placed in the oven at 95 °C. After 90 min at 95 °C the PDMS chips were removed and cooled to 25 °C. Reservoirs were made at the termini of the channels using a disposable biopsy punch obtained from Premier Medical Products (Plymouth Meeting, PA). The PDMS channel was initially filled with reagent grade 2-propanol by applying a negative pressure ~ 50 kPa at one of the reservoirs while the remaining reservoirs were filled with 2-propanol. A 50% (v/v) solution of the metal alkoxide precursor and 2-propanol was prepared. The 2-propanol

within the reservoirs was replaced with the 50% metal alkoxide solution and pumped through the PDMS channels for 1 min. The reservoirs were then evacuated and the channels dried.

The functionalization of the inorganic coated channels with organic ligands was optimized for each ligand. For APTES, the channel was rinsed with a 30% (v/v) ethylamine solution in water for 30 min, after which a 30% (v/v) APTES in water was flowed through the channel for 10 min. For OEO, perfluoro or thiol coatings, the channels were rinsed with a 30% (v/v) ethylamine for 30 min, and followed by 50% (v/v) solutions of the functionalization groups in deionized water.

#### ***4.2.3 Diffusion Measurements.***

The diffusion of titanium isopropoxide into the sidewalls of a PDMS channel was measured on a Nikon Eclipse TE2000E microscope with an attached scientific grade CCD camera (Princeton Instrument's MicroMax; Roper Scientific, Trenton, NJ). A 20  $\mu\text{m}$  x 20  $\mu\text{m}$  x 1 cm PDMS channel was prepared and initially imaged using white light. One end of the channel was connected to a vacuum pump at a negative pressure of  $\sim 50$  kPa. After introducing a 50% (v/v) solution of titanium isopropoxide and 2-propanol, an image of the channel was taken every second. IgorPro (Version 4.0.7.0; Wavemetrics, Lake Oswego, OR) was used to calculate diffusion distances. Cross sections were obtained by slicing the PDMS channel vertically with a steel razor blade, and then coating the transverse section with H-terminated PDMS monomers obtained from Gelest (Morrisville, PA) to match the index of refraction and eliminate any light scattering off striations located within the focal plane.

#### ***4.2.4 Contact Angle Measurements.***

A homemade device was used to image water drops and measure the contact angle. It consisted of a Nikon stereoscopic zoom microscope (SMZ1500), a Sony CCD color video camera (SSC-DC50A) and an in house machined platform equipped with a mirror at a 45° angle. The 45° angle of the mirror allowed the water droplet to be imaged from the side. The material upon which the contact angle measurements were to be made was placed on the platform. A 5 $\mu$ L drop of water was then placed on the material and allowed to rest on the surface for 1 min. After 1 min an image was taken. The contact angle was measured by drawing a line tangent to where the drop's edge met the surface. The angle that the line made with the surface was then measured with a protractor.

#### ***4.2.5 TEM Preparation.***

PDMS was prepared in a 1:10 ratio and molded in 1 cm x 0.5 cm x 0.5 cm cubes. These cubes were then soaked in either 50% (v/v) titanium isopropoxide in 2-propanol, 50% (v/v) zirconium isopropoxide in 2-propanol or 50% (v/v) vanadium triisobutoxide oxide in 2-propanol for 30 min to penetrate the entire depth of the PDMS block. One-millimeter cubes of sample were infiltrated for 24 hrs at room temperature with an LR White Embedding Resin (Electron Microscopy Sciences (EMS)). Samples were placed in #3 beam capsules (EMS) and filled with resin. The samples were then cured for 24 hours at 70°C. After curing, the samples were trimmed and sliced into ultrathin sections on a Reichert Ultracut S microtome (Leica Microsystems; Bannockburn, IL) using a diamond knife. The ultrathin sections were placed on 200 mesh copper grids (EMS) and imaged on an FEI CM 100 TEM at 100 kV (FEI Company; Hillsboro, OR). Digital images were captured using a Kodak 16I camera (Advanced Microscopy

Techniques, Corp.; Danvers, MA) with AMT Advantage software (Advanced Microscopy Techniques).

#### ***4.2.6 XPS and Raman Measurements.***

PDMS cubes were molded and treated in a manner similar to that reported for the TEM preparation above. All spectra reported were recorded on a SPECS Sage100 spectrometer operating in the fixed analyzer transmission (FAT) mode using achromatic Mg K $\alpha$  (1253.6 eV) radiation at 240 W (12kV and 20 mA) using a water-cooled X-ray gun cap. The water-cooled cap reduced sample decomposition due to heat from the X-ray gun, as well as hydrocarbon contamination.<sup>181</sup> The base pressure of the chamber was  $\sim 2 \times 10^{-8}$  Torr and the energy scales were calibrated using copper<sup>182, 183</sup> and the separation between photoelectron peaks generated by Mg and Al K $\alpha$  X-rays. Survey spectra were collected with a pass energy of 30 eV; a pass energy of 15 eV was used for both core and valence band spectra. Spectra were calibrated by taking the C(1s) peak due to residual hydrocarbon at 284.6 eV. Valence band spectra are reported after removal of the K $\alpha_{3,4}$  X-ray satellite features from the O(2s) region<sup>184</sup> and a non-linear background.<sup>185</sup>

FT-Raman spectra were collected on a Nicolet Nexus 670 with a Raman module (Termo-Oriel, MA). The system used a continuous wave Nd:YAG laser (1064 nm) and either a cooled liquid nitrogen or InGaAs detector within the 4000-100 cm<sup>-1</sup> range. The instrument was purged with dry air and the laser power was kept in the range of 0.2-0.6 W with a data point spacing of 3.5 cm<sup>-1</sup>.

#### ***4.2.7 Measurement of EOM.***

EOM measurements were made on both the sol-gel modified PDMS chips and unmodified chips using the previously reported conductivity method.<sup>49, 186, 187</sup> The chip pattern consisted of a simple straight channel. The length of the channels varied slightly from chip to chip due to the error in boring the holes. The exact channel length was measured for each chip using calipers. The channel was initially filled with a solution of 1 mM sodium phosphate/10 mM KCl buffer. This buffer was replaced by a solution of 1 mM sodium phosphate/9 mM KCl in the anodic reservoir. The measurements were made over a series of pH's. In addition to the phosphate buffers we also used 25 mM and 50 mM sodium borate solutions, at a series of different pHs. Voltage potentials of 300 V/cm were applied using a Spellman CZE1000 (Hauppauge, NY) resulting in the migration of the lower conductivity buffer into the channel due to electroosmotic flow. This resulted in a linear decrease in conductivity as the higher conductivity buffer was replaced by the lower conductivity buffer. Once the lower conductivity buffer migrated to the cathodic reservoir the conductivity reached a constant value. Straight lines were drawn on the two conductivity sections. Their intersection was used as the time for the EOM measurements.

#### ***4.2.8 SEM and AFM Preparation.***

The PDMS chips were dismantled by peeling the two layers of PDMS apart revealing the interior of the inorganic coated PDMS channels. Samples were coated with 50 nm of aluminum using the desk II sputter/etch unit (Denton Vacuum, LLC, Moorestown, NJ), and imaged on a Hitachi Science S-3500N SEM (Hitachi Science Systems, Hitachinaka, Ibaraki, Japan). AFM images were obtained using a Digital Instruments Multimode AFM with Nanoscope IIIa Controller. The experiments were performed in the deflection mode in dry air (RH ~ 20%) using

etched silicon (TESP, Veeco) tips. Integral and proportion gains were set to 0.75 and 1.0, respectively, with a scan rate of 1.00 Hz. Root-mean-square surface roughness values were acquired from 10 x 10  $\mu\text{m}$  images using the software provided with the instrument.<sup>188</sup>

## 4.3 RESULTS AND DISCUSSIONS

### *4.3.1 Fabrication of sol-gel modified PDMS microchips.*

The channel coatings were fabricated using an “inside out” approach where the metal alkoxide precursor was flowed through the channel and diffused into the sidewalls illustrated in **Figure 4.1A**. Our previous work has demonstrated that tetraethoxysiloxane (TEOS) can be diffused from the “outside in” and subsequently hydrolyzed and condensed within the bulk chip to generate both channel surface and bulk modification of PDMS.<sup>159</sup> Given the large index of refraction of some of the metal alkoxy precursors it is possible to monitor their diffusion into the sidewall of the channel using a light microscope. For example, as the titanium isopropoxide diffuses into the walls of the channel an interface is formed and can be visualized with a microscope. The rate at which the titanium isopropoxide diffused into the polymer was 2.6  $\mu\text{m/s}$  and appeared to be non-Fickian in behavior as shown in **Figure 4.1B**. A cross section of a PDMS channel treated with the titanium isopropoxide reveals radial diffusion from the channel developing a cylindrical zone with a higher index of refraction ( $n \sim 1.5$ ) than the outer PDMS ( $n = 1.465$ ).<sup>189</sup> Once the titanium isopropoxide was removed from the channel the zone of migration would halt. **Figure 4.2** shows a cross section of a 35 day old PDMS-TiO<sub>2</sub> channel. The radius of the sol-gel doped zone did not change over this time period. Depending upon the time for which

the titanium isopropoxide precursor is left within the channel, sol-gel modified zones can be constructed with radii of 25  $\mu\text{m}$  and up.

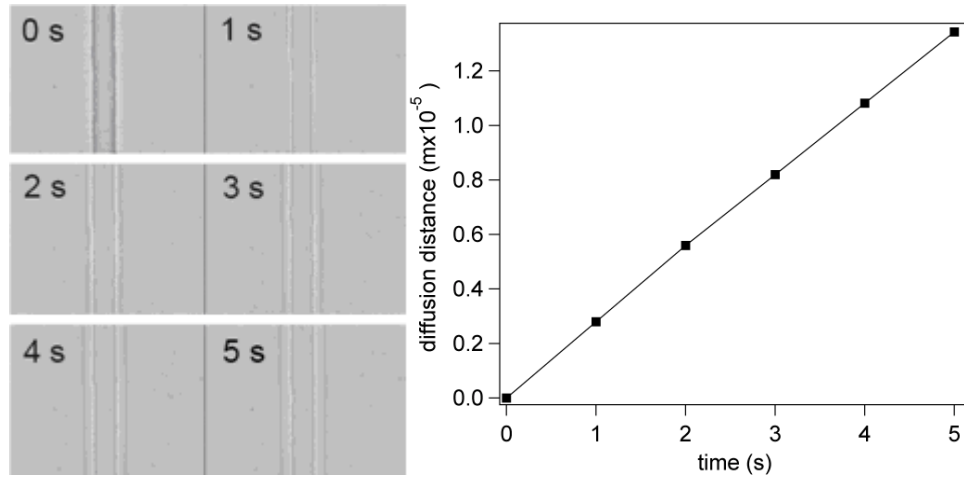


**Figure 4.1** A. Diffusion of titanium isopropoxide into the sidewalls of a 25  $\mu\text{m}$  PDMS channel imaged over a period of 5 seconds. As the titanium isopropoxide diffuses into the PDMS a parallel interface is formed due to the differences in refractive index. B. Calculation of diffusion rate of the titanium isopropoxide into the bulk PDMS polymer yielded a linear rate of 2.6  $\mu\text{m}/\text{s}$ .

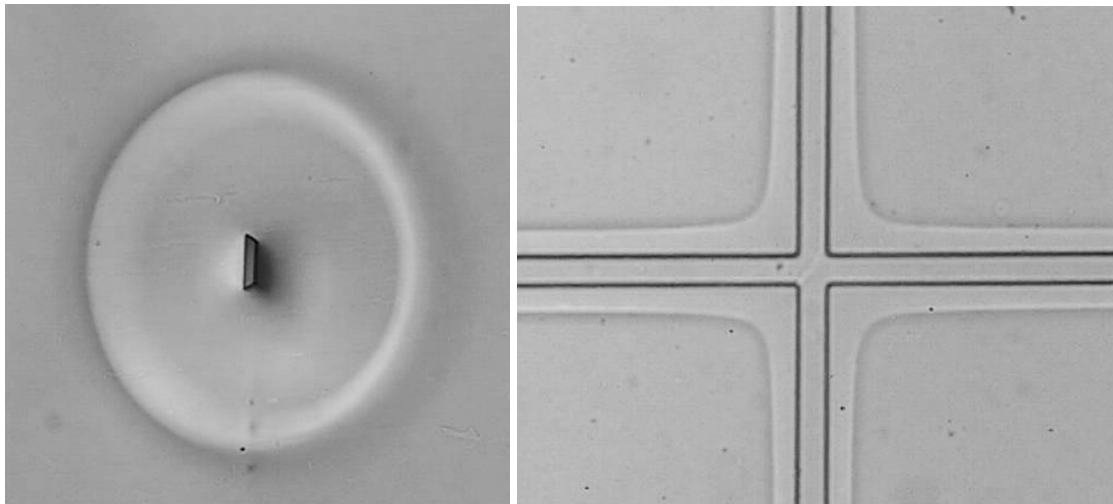


**Figure 4.2** Radial diffusion of titanium isopropoxide from the capillary forming a horizontally aligned waveguide.

In addition to titania and zirconia, which produced transparent sol-gel zones, we also investigated vanadia waveguides that were colored. The color is dependent upon the oxidation state of the vanadia oxide. The vanadia waveguides would initially exhibit a sharp yellow shortly after coating the PDMS channel with the vanadium alkoxy precursor. The yellow was followed by a transition to blue and then to a dark green-blue over a period of 24 hrs. This color scheme has been well documented in the literature as corresponding to the oxidation states of  $V_2O_5$  ( $V^{+5}$ , yellow),  $VO_2$  ( $V^{+4}$ , blue),  $V_2O_3$  ( $V^{+3}$ , blue-green) and  $VO$  ( $V^{+2}$ , violet). From optical observations, the final coating appeared to consist of both blue-green and violet colors which would suggest primarily  $V_2O_3$  and  $VO$  species.<sup>190</sup>

#### ***4.3.2 Characterization of Titania, Vanadia, and Zirconia Surfaces.***

To determine the surface characteristics and effectiveness of these inorganic coatings, we performed several different characterizations of both the bulk properties of the polymer along with characterizations of the surface chemistry. Contact angle is a common way to calculate the macroscale hydrophobicity of a surface. A reference contact angle of  $110^\circ$  was measured for native Sylgard 184 PDMS. Contact angle measurements were also measured for PDMS- $TiO_2$ , PDMS- $ZrO_2$  and PDMS-vanadia yielding  $61^\circ$ ,  $90^\circ$  and  $19^\circ$ , respectively. These contact angle measurements reveal a significantly more hydrophilic surface than the native Sylgard 184 PDMS. Further, UV sensitized PDMS- $TiO_2$  generated a contact angle of  $20^\circ$ . Over a period of 5 hrs, however, the contact angle of this UV sensitized PDMS- $TiO_2$  would return to its original value.

X-ray photoelectron surveys of both PDMS and modified PDMS were collected. Native PDMS gave peaks at 532, 284 and 102 eV due to oxygen (1s), carbon (1s) and silicon (2p) respectively. These results are very similar to previously reported spectra for native PDMS.<sup>191</sup>

The XPS spectra for each modified PDMS exhibited two oxygen (1s) peaks at 532 and 531 eV characteristic of the siloxane bonds of the PDMS and the metal oxide, respectively (**Table 3**). The oxygen (1s) peak at 531 eV is indicative of the titania (Ti-O), zirconia (Zr-O) and vanadia oxides (V-O) present at the surface of the PDMS modified material (**Figure 4.3**). Interestingly the Si-O, Si-C and C-H bonds of PDMS did not change during the in situ precipitation of the particles as evidenced by the constant peak location for the PDMS oxygen (1s), silicon (2p) and carbon (1s) peak for all PDMS modified materials (**Table 3**). The valence band was observed in each material and was found to consist of the Ti(3p) at 38 eV for PDMS-TiO<sub>2</sub>, Zr(4p) at 31 eV for PDMS-ZrO<sub>2</sub> and the V(3p) at 42 eV for PDMS-vanadia. Further spectral characterization of the PDMS-TiO<sub>2</sub> using Raman yielded broad peaks with maxima at 611 cm<sup>-1</sup> and 426 cm<sup>-1</sup> which suggest that the phase of the imbedded TiO<sub>2</sub> is amorphous in nature.

	PDMS	PDMS-TiO <sub>2</sub>	PDMS-ZrO <sub>2</sub>	PDMS-VO <sub>2</sub>
<b>O(1s) (eV)</b>	<b>532.2</b>	<b>532.2</b>	<b>532.5</b>	<b>532.2</b>
		<b>531.0</b>	<b>530.9</b>	<b>530.9</b>
<b>Si(2p) (eV)</b>	<b>102.2</b>	<b>102.2</b>	<b>102.2</b>	<b>102.2</b>
<b>Si(2s) (eV)</b>	<b>153.5</b>	<b>153.5</b>	<b>153.5</b>	<b>153.5</b>
<b>C(1s) (eV)</b>	<b>284.8</b>	<b>284.8</b>	<b>284.8</b>	<b>284.8</b>
<b>V.B. (eV)</b>	<b>25.5 O(2s)</b>	<b>38 Ti(3p)</b>	<b>31 Zr(4p)</b>	<b>42 V(3p)</b>

**Table 3** X-ray photoelectron spectra of oxygen (1s) and carbon (1s), silicon (2s) and silicon (2p) of PDMS and the PDMS transition metal oxides.

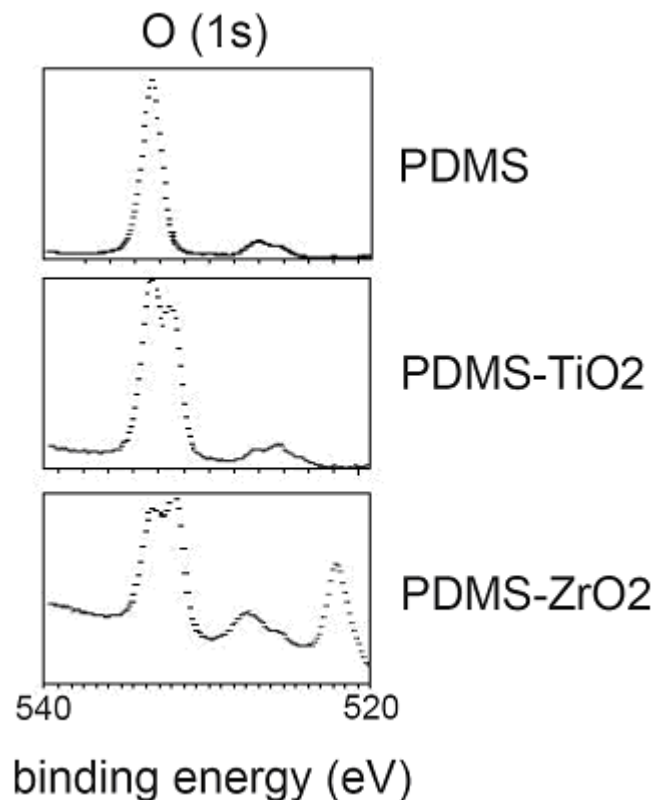


**Figure 4.3** XPS survey of PDMS, PDMS-TiO<sub>2</sub> and PDMS-ZrO<sub>2</sub> showing the O(1s) orbitals for both Si-O-Si and metal oxides.

TEM images were taken of each modified PDMS material in an attempt to examine the homogeneity of the particles precipitated within the PDMS (**Figure 4.4**). In these images, the silica, titania, zirconia, and vanadia particles show up as darker spots because the particles have a higher electron density than the bulk PDMS. Analysis of the images showed the silica particles within the PDMS to be  $< \sim 10$  nm in diameter, homogeneously distributed throughout the PDMS matrix and uniform in size. The titania and zirconia particles were much smaller and appeared to be more tightly packed together than the silica. The vanadia appeared to show the formation of tightly packed wires or lines through the PDMS. This morphology was consistent with previously reported electron microscopy studies.<sup>192</sup>

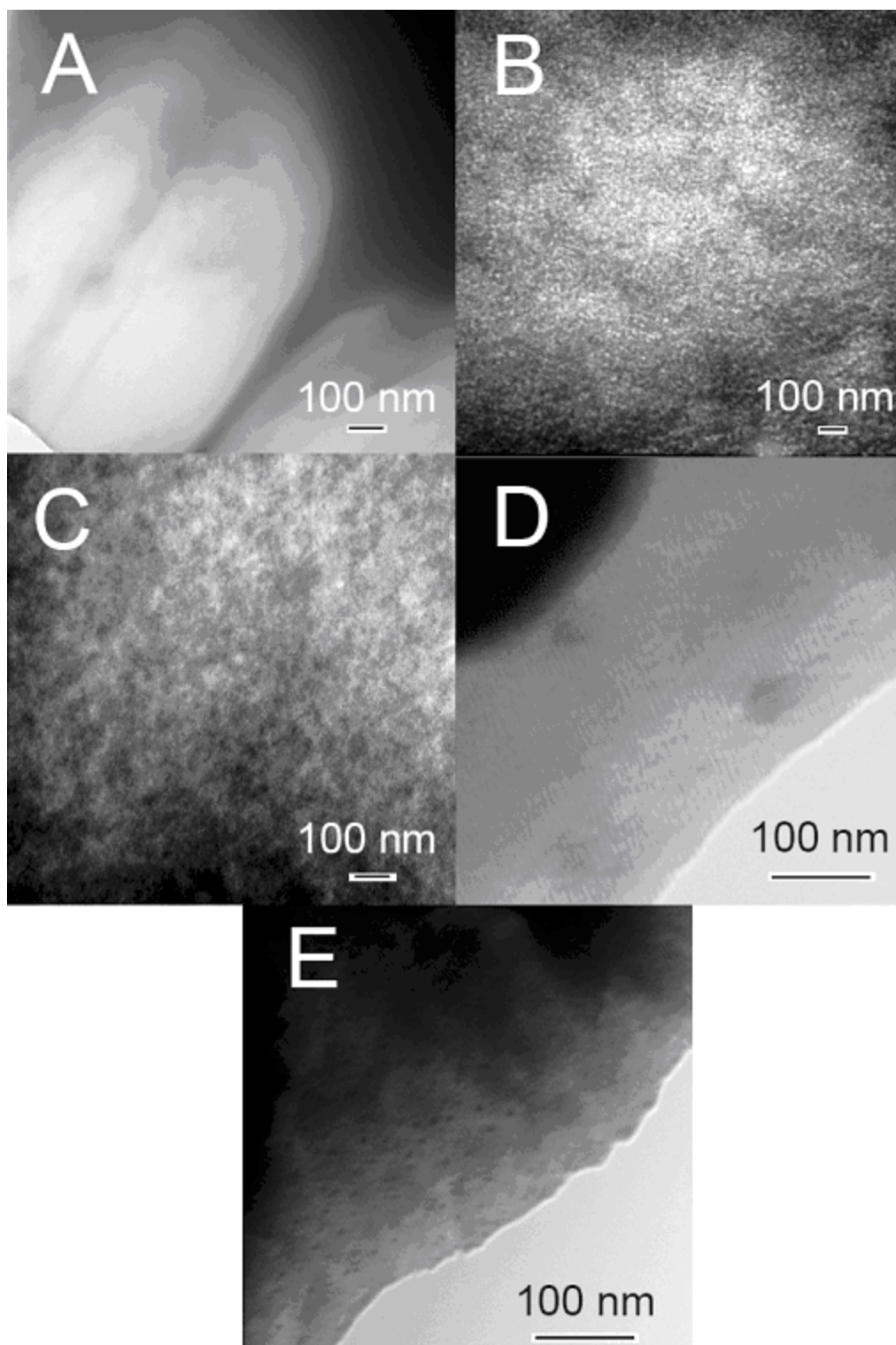


**Figure 4.4** Transmission electron microscopy images of metal oxide modified PDMS. A. PDMS, B. PDMS-SiO<sub>2</sub>, C. PDMS-TiO<sub>2</sub>, D. PDMS-vanadia, E. PDMS-ZrO<sub>2</sub>.

The metal oxide modified PDMS was also examined for absorption and adsorption of hydrophobic analytes such as Rhodamine B (RhB). **Figure 4.5A-4.5E** shows a series of images of PDMS modified channels filled with a 100  $\mu\text{M}$  concentration of RhB that had been siphoned through the channels. As can be seen from the images there is significant absorption of RhB into the bulk of the PDMS microchip while the absorption of RhB is completely inhibited in the PDMS modified channels. Additionally, more hydrophilic coatings such as the vanadia-PDMS were resistant to RhB adsorption and did not fluoresce when the solvent was removed from the channel (**Figure 4.5F**).

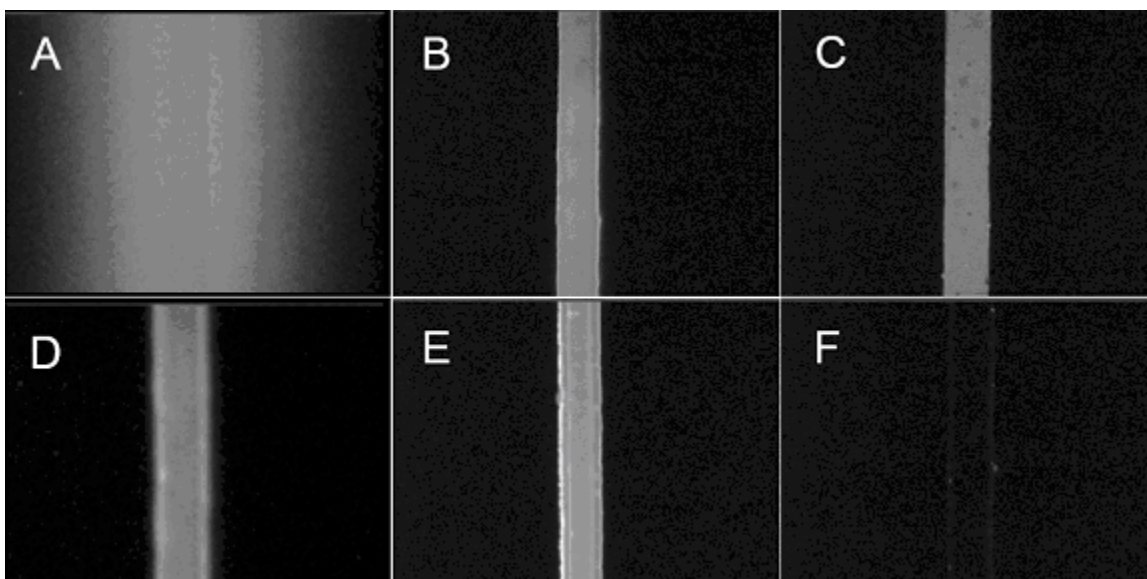


**Figure 4.5** Rhodamine B Absorption Measurements. Images of PDMS (A), PDMS-TiO<sub>2</sub> (B), PDMS-Vanadia (C), PDMS-SiO<sub>2</sub> (D), and PDMS-ZrO<sub>2</sub>(E) devices are shown. The channels on these devices are filled with 100  $\mu\text{M}$  Rhodamine B in a 10 mM (pH 9.5) sodium borate solution. The images were acquired over a 4 hour period. The PDMS-Vanadia device was pulled dry and was shown to not display significant adsorption to the surface.

Finally, surface roughness of the channels was assessed by SEM and AFM (**Figure 4.6**). Both coated and native PDMS channels have similar maximum vertical displacements of less than 1  $\mu\text{m}$  with an RMS roughness of 0.8  $\mu\text{m}$  that indicate that the addition of the metal oxide coating does not increase the intrinsic roughness of the surface. The actual thickness of the

surface films on the walls of the PDMS was measured at  $300 \pm 200$  nm ( $n = 3$ ). This was done by pulling a coated chip apart and measuring the thickness of the coating on the flat surface that was originally used to seal the molded channel. The actual measurements were performed using AFM.

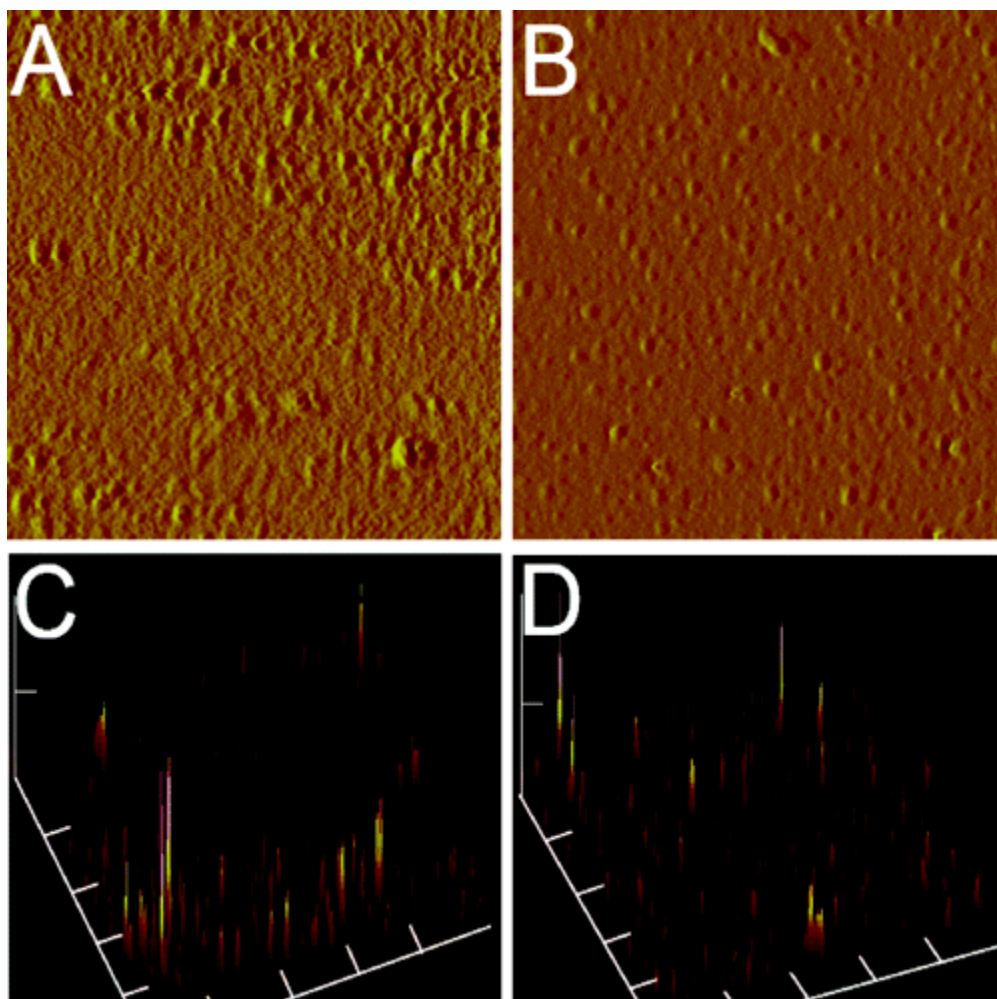


**Figure 4.6** AFM images of PDMS and PDMS-TiO<sub>2</sub> taken from the interior of a microfluidic channel. (A) AFM 2D image of PDMS (10 μm × 10 μm), (B) AFM 2D image of PDMS-TiO<sub>2</sub> (10 μm × 10 μm), (C) AFM 3D image of PDMS with each division equal to 2 μm, and (D) AFM 3D image of PDMS-TiO<sub>2</sub> with each division equal to 2 μm.

#### ***4.3.3 Measurement of EOM in Titania, Vanadia, and Zirconia PDMS Channels.***

We measured the EOM of TiO<sub>2</sub>-PDMS, ZrO<sub>2</sub>-PDMS, vanadia-PDMS, SiO<sub>2</sub>-PDMS, native PDMS and borosilicate glass using 1 mM sodium phosphate and 10 mM KCl solutions at a series of pH values ranging from 3 to 11 (**Figure 4.7**). The titania and zirconia modified PDMS channels exhibit positive EOM's that were not dependent on the pH of the buffer. The titania coated PDMS gave an EOM of  $2.14 \pm 0.2 \times 10^{-4} \text{ cm}^2/\text{Vs}$  (n=10, 9.3% RSD) for pH 3 while the EOM of zirconia coated PDMS was  $3.0 \pm 0.14 \times 10^{-4} \text{ cm}^2/\text{Vs}$  (n = 5, 4.6 %RSD) for a pH of 3.

As the pH was incrementally increased no sigmoidal dependence on the EOM was observed. The constant EOM versus pH suggests that the phosphate ion is adsorbing strongly to the titania and zirconia modified PDMS surfaces. Previous reports indicated that titania and zirconia will adsorb and react with buffer ions including phosphate.<sup>193</sup> Titania, a common material used in implants, has been extensively investigated for its calcium phosphate ion adsorption in physiological solutions.<sup>194-198</sup> In addition, electrophoretic studies in titania modified silica capillaries have demonstrated that the adsorption of phosphate to the titania surfaces generates a positive EOM at low pH's primarily due to the negative charge that the phosphate ion imparts at the surface.<sup>167, 170</sup>

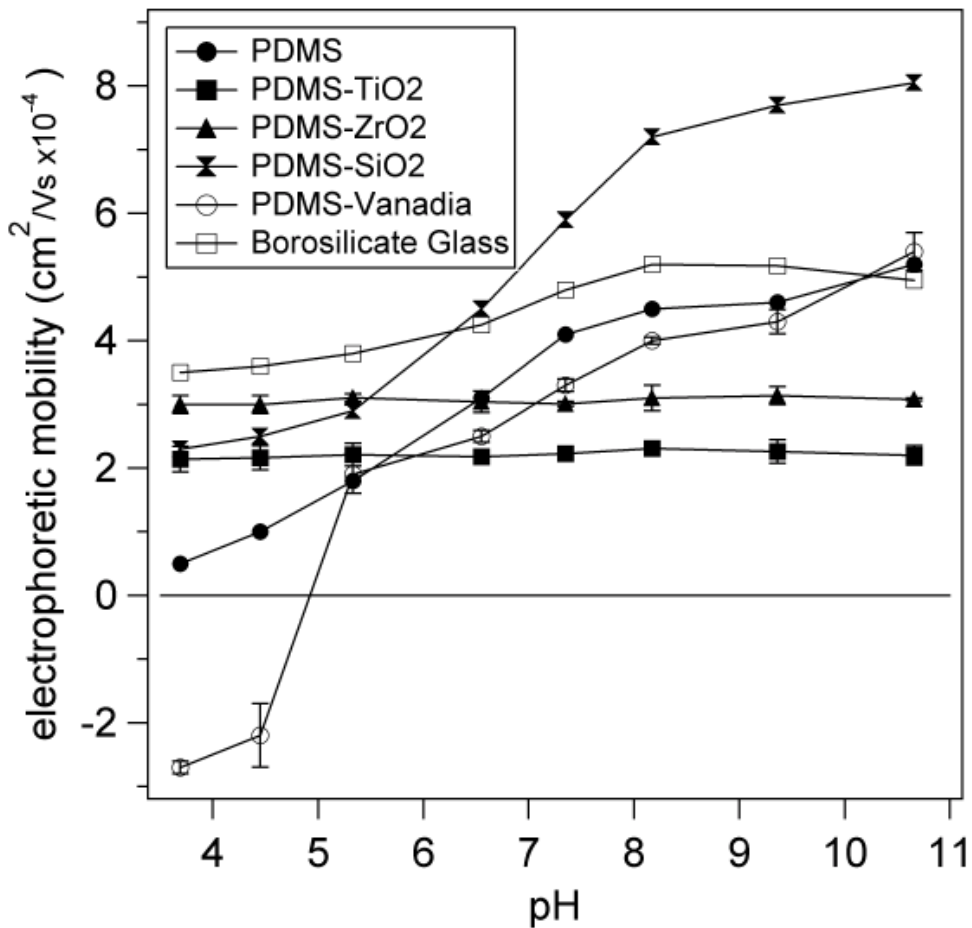


**Figure 4.7** EOM measurements using 1 mM phosphate and 10 mM KCl solutions on transition metal oxide modified PDMS, using field strength of 300 V/cm.

The EOM of native PDMS, in contrast, exhibits the expected sigmoidal dependence on the pH of the buffer as initially shown by Ocvirk *et al.*<sup>49</sup> A similar sigmoidal dependence of EOM on pH was observed for both borosilicate channels and silica modified PDMS channels. Unlike titania and zirconia, vanadia coated channels displayed a pH dependent EOM. A point of zero net charge of 4.8 was recorded in this buffer system suggesting that the phosphate is not binding to the surface. Due to the relative acidic pI of silica no regions of net zero charge were observed for silica modified PDMS and borosilicate glass.

EOM measurements were also made using borate buffers which do not complex with the metal oxide surface like that of phosphate. Using a 25 mM sodium borate buffer at a series of pH's we were able to calculate approximate regions of zero net charge of the PDMS modified channels. Titania and zirconia have greater basicities than silica, and this is manifested in both the position of the zero net charge for the PDMS channels and the magnitude of the EOM's at pH 3 (**Figure 4.8**). The EOM of native Sylgard 184 PDMS at pH of 3.0 for the borate buffer system is  $3.6 \pm 0.3 \times 10^{-5} \text{ cm}^2/\text{Vs}$ . The titania, vanadia and zirconia metal oxide coated channels all had reversed EOM's at pH 3 in borate solutions. The EOM for the PDMS-TiO<sub>2</sub>, PDMS-ZrO<sub>2</sub> and PDMS-Vanadia in pH 3 borate solutions were  $-5.4 \pm 0.3 \times 10^{-5} \text{ cm}^2/\text{Vs}$ ,  $-1.4 \times 10^{-4} \pm 0.33 \times 10^{-4} \text{ cm}^2/\text{Vs}$  and  $-2.41 \pm 0.4 \times 10^{-4} \text{ cm}^2/\text{Vs}$  respectively. The corresponding net zero charge for the PDMS-TiO<sub>2</sub>, PDMS-ZrO<sub>2</sub> and PDMS-Vanadia systems were  $4.1 \pm 0.25$ ,  $6.1 \pm 0.2$  and  $7.0 \pm 0.43$ , respectively. The titania and zirconia oxide coatings are very durable with the EOMs changing less than 8% over the period of 95 days.

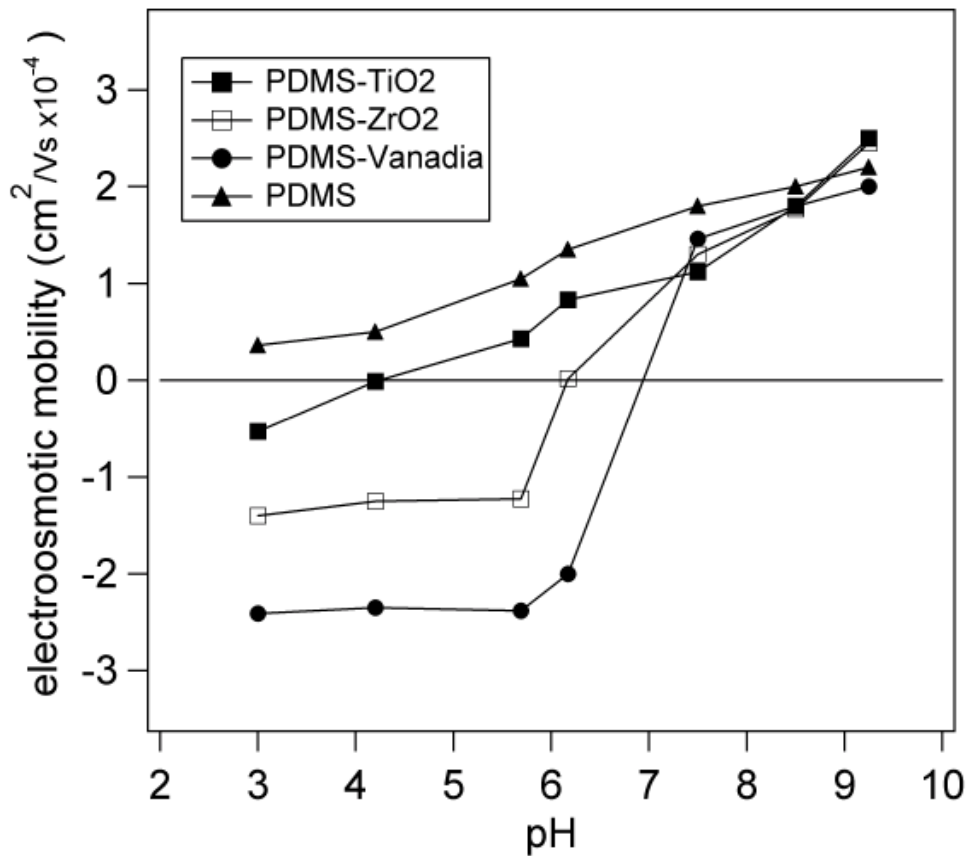


**Figure 4.8** EOM measurements using 25 mM sodium borate solutions on metal oxide modified PDMS, using field strength of 300 V/cm.

The characterization of these coatings suggests that the base-catalyzed sol-gel growth of the transition metal alkoxides resulted in the formation of nanoparticles that were subsequently crosslinked into a 3-D gel matrix. While there is a thin “glass-like” film of the metal oxide coating on the surface of the PDMS in the channels, the bulk of the metal oxide matrix is intercalated within the bulk crosslinked PDMS. It is this intercalation that effectively anchors the metal oxide film to the surface thus eliminating the need for direct covalent bonds between the PDMS and the metal oxide surface coating. This is supported not only by the XPS data that show no shift in the energy of the oxygen valence band energy but by other studies which have shown that there are no reactive groups in cured Sylgard 184. This should not be surprising as

Sylgard 184 polymerizes through hydrosilation reactions and the silica present in the formulation is trimethylsilylated and so is not reactive. Finally another recent report demonstrating the growth of networked silica structures in PDMS using sol-gel chemistry also strongly supports this conclusion.

#### ***4.3.4 Characterization of oligoethyleneoxide, thiol, perfluoro and amino derivitized***

##### ***PDMS-TiO<sub>2</sub>***

Further derivitization of the inorganic coatings was performed using common and well known silanol condensation chemistry. We used triethoxy silanes primarily due to their wide commercial availability (i.e. Gelest) and broad application as silanizing agents for glass and other metal oxides. These triethoxy and trimethoxy silanes were hydrolyzed and condensed on the surface of the metal oxides to form stable surface coatings on PDMS. To analyze the robustness of these coatings we measured contact angle and EOM changes as a function of time. Contact angle measurements of the PDMS-TiO<sub>2</sub> derivitized surfaces yielded a value of 61° prior to functionalization. Contact angle measurements after the functionalization of perfluoro, thiol, APTES and OEO on PDMS-TiO<sub>2</sub> yielded initial contact angles of 120°, 76°, 45°, 23°, respectively. These contact angles did not change significantly over a 30 day period. Initial EOM measurement of PDMS-TiO<sub>2</sub> using sodium tetraborate at pH 9.0 was  $2.1 \times 10^{-4} \pm 0.1 \text{ cm}^2/\text{Vs}$ . After functionalizing this surface with OEO the EOM dropped to  $0.9 \times 10^{-4} \pm 0.05 \text{ cm}^2/\text{Vs}$ . The stability of this EOM was measured over 21 days and was found to change less than 13%. Amine functionalized PDMS-TiO<sub>2</sub> was also investigated using EOM measurement. APTES functionalized PDMS-TiO<sub>2</sub> had an initial EOM of  $2.4 \times 10^{-4} \text{ cm}^2/\text{Vs}$  at a pH of 9.0,  $-5.0 \times 10^{-5} \text{ cm}^2/\text{Vs}$  at a pH of 7.0 and  $-2.14 \times 10^{-4} \text{ cm}^2/\text{Vs}$  at a pH of 3.0. The reversal of the EOM occurs at a much higher pH than that of the PDMS-TiO<sub>2</sub> further suggesting the functionalization of the

surface with primary amines with a pKa of  $\sim 10.6$ . The continued cathodic EOM at a pH of 9.0 is likely due to the coexistence of unreacted oxides and primary amines at the surface of the channel. We are presently in the process of exploring ways to further improve surface coverage to help reduce the EOM at pH of 9.0 for amine functionalized TiO<sub>2</sub>-PDMS channels.

#### ***4.3.5 Thermochromic Gels***

Vanadia has several important catalytic properties and is widely used in many synthetic organic schemes. Vanadia also has many other physical properties, notably thermochromic characteristics. For instance, the absorbance of vanadia particles changes depending on the temperature. The change in UV-vis absorption is irreversible. We developed an experiment to dope a 50 micron region of PDMS with vanadia and monitor the change in absorbance by applying an electric field to the channel that generates Joule heat. The Joule heat will change the absorbance characteristics of the vanadia imbedded within the PDMS. Initially we started at 0 V/cm and ramped up to 2,000 V/cm to generate significant Joule heating. The change in temperature of the channel resulted in an obvious change in the color of the vanadia matrix nearby the channel.

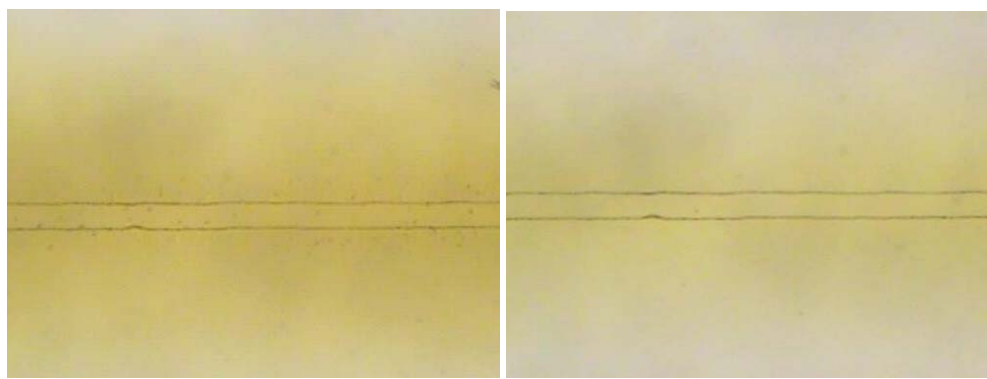


**Figure 4.9** Right: Vanadia coated channel at room temp, Left: Vanadia coated channel with 2,000 V/cm applied across the channel. The heat generated from the Joule heating converted the vandia and changed its adsorbance spectrum.

### 4.3.6 Waveguides

In addition to coatings it is also possible to generate a number of novel waveguides and laser rods using sol-gel chemistry. For instance, by diffusing a radial region near a microfluidic channel with a high refractive index material the diffused region will have a higher index of refraction than the surrounding bulk material. This generates a hollow waveguide. A dye doped waveguide can be generated by diffusing rhodamine into the side of the channel first, followed by absorption of titania to form the waveguide. The sequential processing generates a dye doped hollow waveguide. Future studies involve characterizing the loss of these waveguides and laser rod stability.

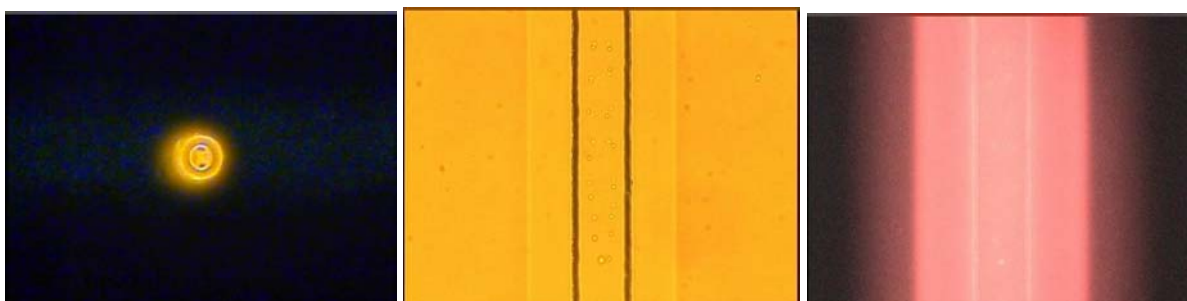


**Figure 4.10** Left: rhodamine B doped waveguide acting as a laser rod, Center: titania doped PDMS, Right: rhodamine B and titania doped PDMS.

### 4.3.7 Separations

The hydrophobic nature of PDMS tends to adsorb a number of biopolymers including proteins. Microfluidic channels fabricated from PDMS exacerbate the problem by generating a large surface area to volume ratio so the probability of a hydrophobic molecule adsorbing to the surface is significantly higher. This often can have detrimental effects for the chemical separation of proteins and hydrophobic small molecules on PDMS microfluidic devices. Several technologies have been developed to circumvent these including covalent and dynamic coatings.

We designed several coatings to try and attempt to reduce the adsorption of amino acids and proteins to the sidewall of PDMS channels. The surface derivitization chemistry using sol-gel processing, electrophoretic separations and injections was described in Chapter 3.

#### **4.3.7.1 Amino Acids**

Several amino acids were separated on PDMS and PDMS-TiO<sub>2</sub> derivitized channels to initially compare the differences in separation efficiency, resolution and migration time. After precipitating titania onto the surface of a PDMS channel we observed higher electroosmotic flows, which resulted in faster electrophoretic separations. In addition, we also observed high efficiency separations of 7 FITC derivitized amino acids in under 15 seconds on titania derivitized PDMS channels. The efficiencies of these separations ranged from 150,000 to 85,000 depending on the amino acid, and was an improvement of nearly 60,000 over native PDMS.

**Figure 4.11** shows a comparison between FITC derivitized amino acids separated both on native PDMS and the same amino acids separated on PDMS-TiO<sub>2</sub>. **Figure 4.12** shows the high efficiency FITC amino acid separation on titania modified PDMS channels.

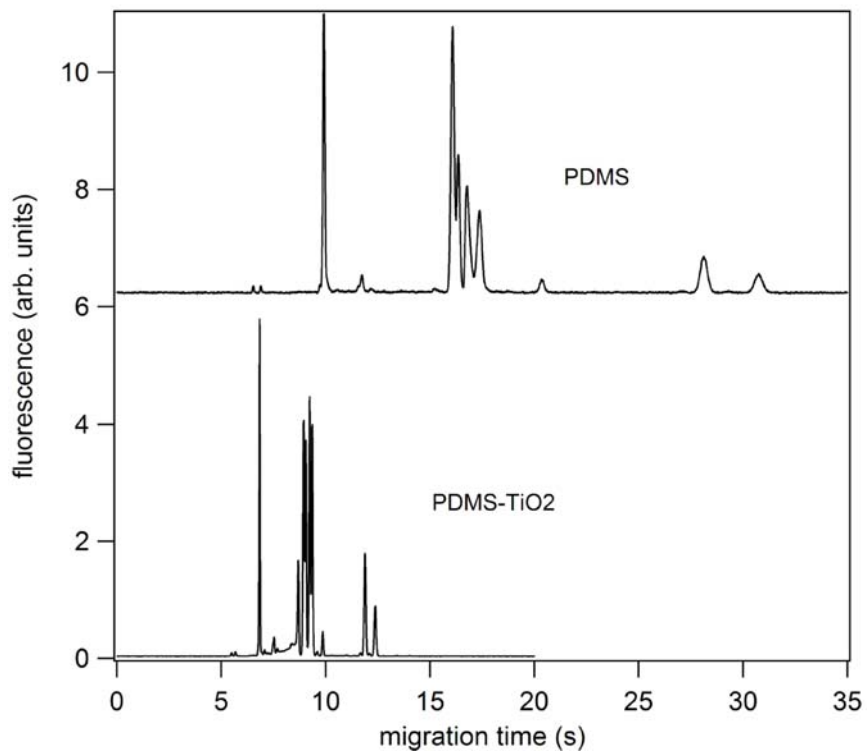


**Figure 4.11** Comparison of FITC labeled amino acids separated on PDMS and PDMS-TiO<sub>2</sub>.

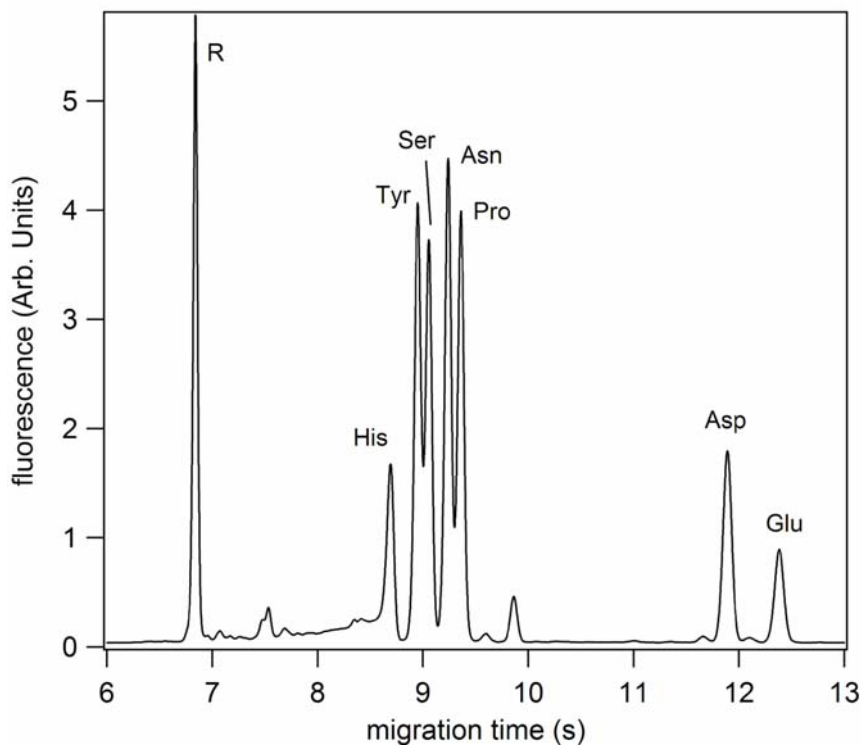


**Figure 4.12** FITC-labeled amino acids separated on PDMS-TiO<sub>2</sub> coated channels.

In addition to FITC derivitized amino acids we also investigated TRITC derivitized amino acids. In general, we discovered that TRITC derivitized amino acids have a much higher partition coefficient in PDMS than FITC derivitized amino acids. The higher partition coefficient led to band broadening and lower separation efficiencies. The reason for the difference in partition coefficients between FITC and TRITC is largely due to the side functionalities present on the chromophore. The molecular difference between both TRITC and FITC is demonstrated in **Figure 4.13**.

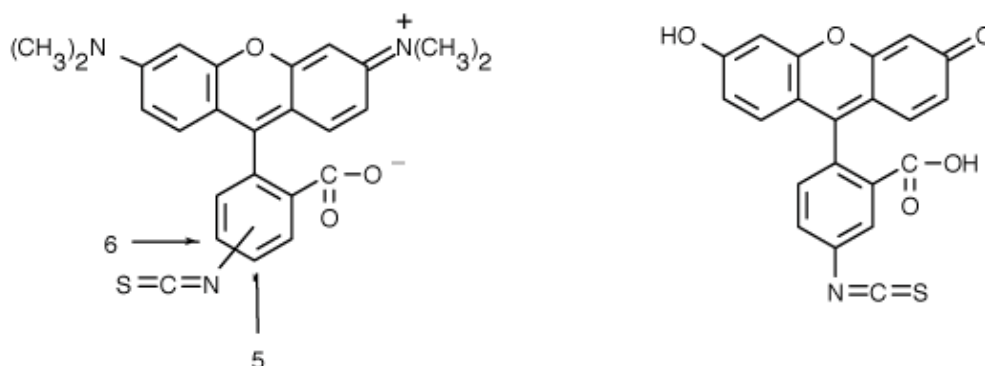


**Figure 4.13** Left: TRITC chromophore used for amine reactive labeling, Right: FITC chromophore used for amine reactive labeling.

In addition to an overall band broadening of the TRITC labeled amino acids we also observed dramatic differences between individual amino acids. For instance, we observed that Arginine labeled with TRITC had a higher partition coefficient than all of the other amino acids labeled with TRITC. The affinity of the Arg-TRITC conjugate for the PDMS yielded longer migration times and lower efficiencies.

There could be several reasons for the retention of TRITC-Arg on PDMS. First of all TRITC has a tertiary amine functionalized with two methyl groups. The methyl functionality on the fluorophore could interact through dispersion forces with the methyl functionality on the surface of the PDMS. A potentially more potent interaction would be the positively charged amine located on the right branch of the TRITC and a negative charge on the surface of the PDMS channel. The negative charge on the surface of the PDMS could originate from a charge double layer via chemisorbed ions. In addition, Arg has a similar positively charged amine for its side group. This positively charged amine could also interact with the surface to generate an additional electrostatic attraction. **Figure 4.14** demonstrates an electrophoretic separation of TAMRA labeled amino acids on a PDMS microfluidic device. Note the huge band width of arginine (R) for both PDMS and PDMS-TiO<sub>2</sub> modified channels, shown in **Figure 4.14-15**.

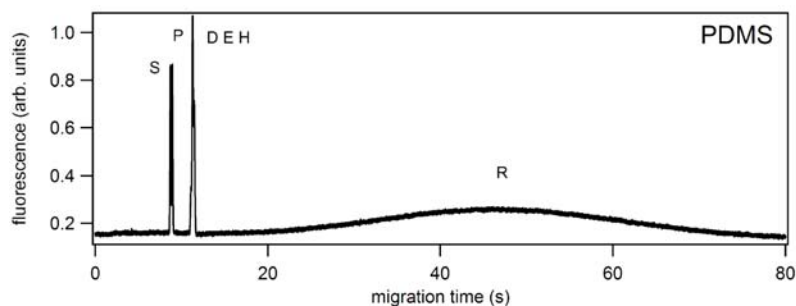


**Figure 4.14** TRITC derivitized amino acids S,P,D,E,H, and R were separated on PDMS. All amino acids exhibited fairly large band broadening due to the adsorption to the sidewall of the capillary, but arginine had the largest partition coefficient with PDMS.

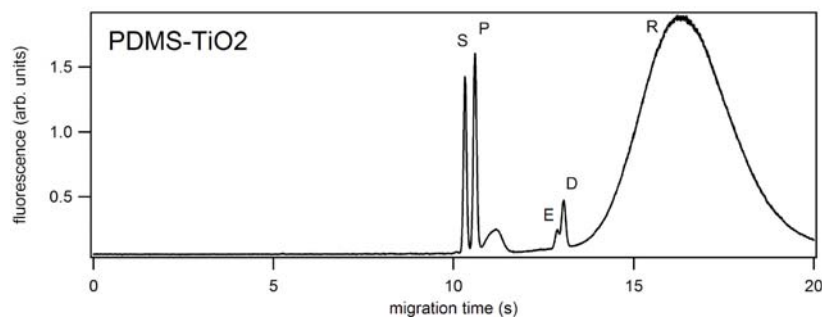


**Figure 4.15** TRITC derivitized Amino acids S,P,D,E, and R were separated on a titania modified PDMS channel. Several amino acids most notably arginine continues to adsorb to the surface.

Several groups have demonstrated that changing either the hydrophobicity of the surface or the electrostatic charge of the surface can reduce the adsorption of proteins or hydrophobic analytes. We further investigated changing both the hydrophobicity of the channel, and also changing the electrostatic charge of the channel. For instance, after derivitizing PEG to the titania surface coated channel it was possible to obtain high efficiency separations in the range of 30,000 to 50,000 theoretical plates in under 15 seconds. The increased hydrophilicity of the channel, in addition to its neutral charge dramatically reduced the adsorption of arginine labeled TRITC to the surface of the channel. This separation is illustrated in **Figure 4.16**. We also investigated the use of APTES as a surface coating. After derivitizing the surface with APTES and operating at a low pH of 4.0 we found that the EOF was reversed indicating a positively charged surface. The migration time and band broadening of arginine also indicated a minimal adsorption of this amino acid to the surface. The electrophoretic separation is shown in **Figure 4.17**. This result further suggests that the charge of the amino acid and TRITC has a significant impact on its adsorption to the sidewall.

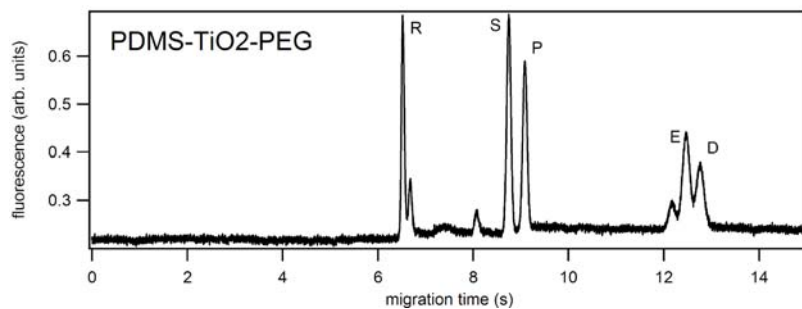


**Figure 4.16** TRITC derivitized amino acids R, S, P, E, and D separated on PEG derivitized titania.

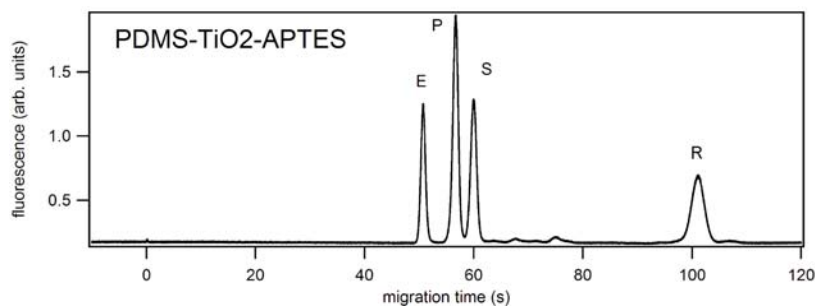


**Figure 4.17** TRITC derivitized amino acids E, P, S and R separated on APTES derivitized titania.

#### 4.3.7.2 Proteins

In addition to amino acids we were also extremely interested in analyzing the electrophoretic separation of proteins on the titania derivitized PDMS channels. Initially we separated a series of standard proteins, derivitized with AlexaFluor 488 and performed electrophoretic separations shown in **Figure 4.18**.

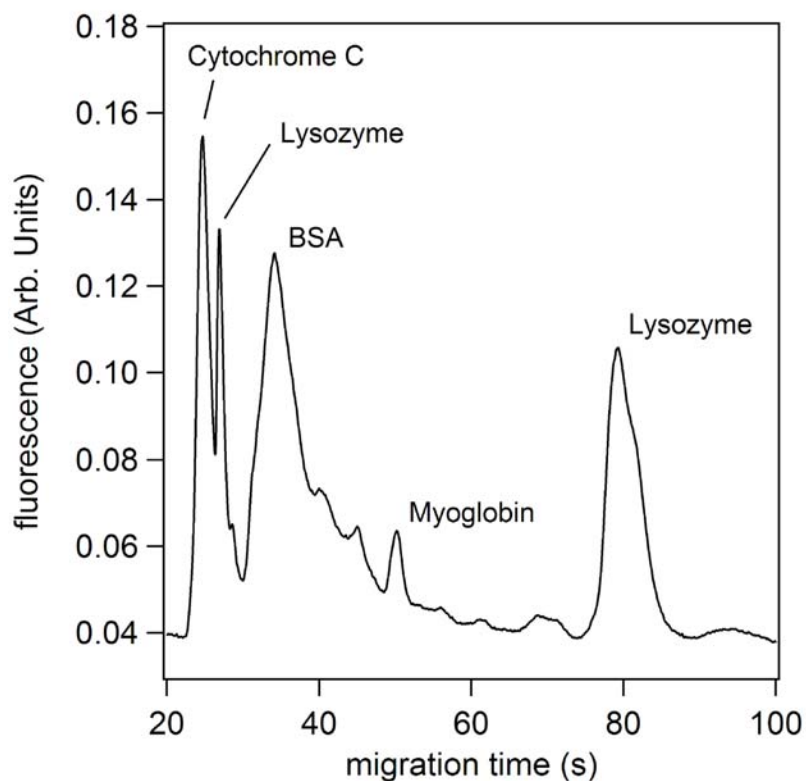


**Figure 4.18** Proteins separated on PEG-TiO<sub>2</sub> derivitized channel

We also investigated the separation of standard proteins on the APTES derivitized titania PDMS device. It was our hope to be able to use this device to further separate highly acidic proteins such as histones. We found that APTES derivitized channels was capable of generating reversed EOF's and were also capable of performing high efficiency separations of proteins at low pH's.

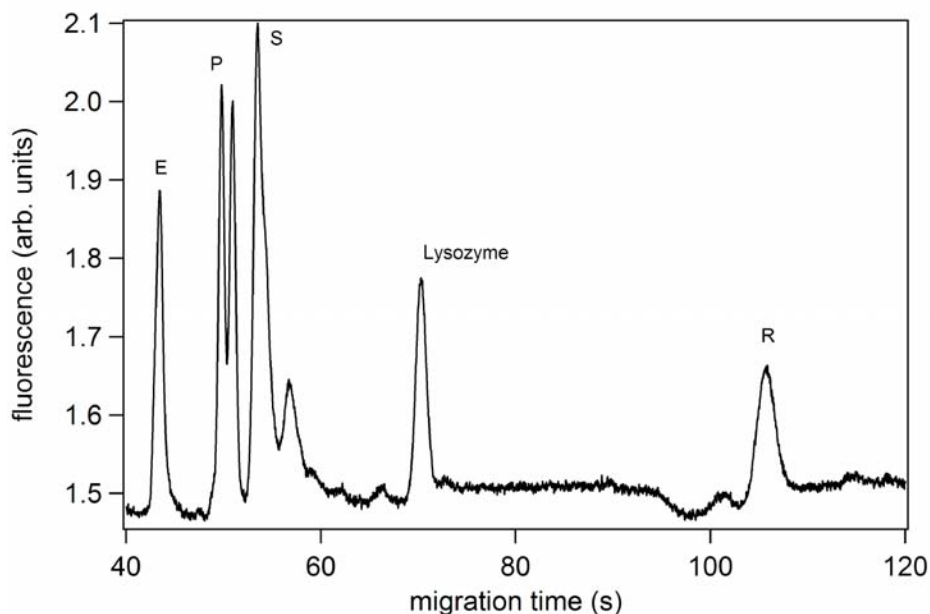


**Figure 4.19** Proteins and amino acids separated on APTES-TiO<sub>2</sub> derivitized channel.

#### 4.4 CONCLUSION

We have developed several new robust surface coatings for PDMS microchannels which are procedurally easy to apply. These procedures do not require external equipment, such as plasma cleaners, for the oxidation of the PDMS surface, and they can be performed on an enclosed channel, whereas plasma oxidation and CVD techniques must be performed on disassembled PDMS microchips. This method also retains the positive attributes of PDMS as an excellent substrate for replica micromolding, but also allows for the broad engineering of the

surface properties using common and well assessable silane based chemistries. This method has the potential for wide applicability in many different fields but especially for fabrication of PDMS-based microstructures that need specific surface chemistries, for the derivatization of PDMS surfaces for cell culturing, and potentially as waveguides given the refractive index difference between the modified annulus around the channel and the bulk PDMS. We also demonstrate a number of separations performed on these surfaces.

Future goals include the fabrication of aluminum and mixed metal oxide films along with the use of alkylsubstituted silanes to increase the physical and chemical functionality of the surfaces.

## CHAPTER 5 - MEKC of Small Molecules on PDMS

### 5.1 Introduction

This paper describes a simple method for the effective and rapid separation of hydrophobic molecules on polydimethylsiloxane (PDMS) microfluidic devices using micellar electrokinetic chromatography (MEKC). For these separations the addition of sodium dodecyl sulfate (SDS) served two critical roles – it provided a dynamic surface coating on the channel wall surfaces and generated a pseudo-stationary chromatographic phase. The dynamic SDS coating generated an EOF of  $7.1 \times 10^{-4} \text{ cm}^2/\text{Vs}$  (1.6% RSD,  $n = 5$ ), and eliminated the absorption of rhodamine B into the bulk PDMS. High efficiency separations of rhodamine B, TAMRA (6-carboxytetramethylrhodamine, succinimidyl ester) labeled amino acids, BODIPY<sup>®</sup> FL CASE (N-(4,4-difluoro-5,7-dimethyl-4-bora-3a,4a-diaza-s-indacene-3-propionyl)cysteic acid, succinimidyl ester) labeled amino acids, and AlexaFluor<sup>®</sup> labeled *Escherichia coli* bacterial homogenate on PDMS chips were performed using this method. Separations of rhodamine B and TAMRA labeled AA's using 25 mM SDS, 20% ACN, and 10 mM sodium tetraborate generated efficiencies greater than 100,000 or  $3.3 \times 10^6 \text{ N/m}$  in  $< 25 \text{ s}$  with run-to-run migration time reproducibilities  $< 1\%$  RSD over 3 hrs. The serpentine chips with 30 cm long separation channels were used to separate 17 BODIPY<sup>®</sup> labeled AA's yielding efficiencies of up to 837,000 or  $3.0 \times 10^6 \text{ N/m}$  and homogenates of *E. coli* yielding  $\sim 30$  resolved peaks with separations efficiencies of up to 600,000 or  $2.4 \times 10^6 \text{ N/m}$  and run to run reproducibilities of  $< 1\%$  RSD over 3 hrs.

We report a method for the effective and rapid separation of hydrophobic molecules in polydimethylsiloxane (PDMS) microfluidic devices through the addition of sodium dodecyl sulfate (SDS) to the running buffer. For these separations the SDS played two critical roles; first, it provided a charged, dynamic coating on the surface of the microchannel walls; and, second, it served as a pseudo-stationary phase to provide a basis for analyte separation. Because of its simplicity, effectiveness, and robustness this method should find application for the separation of a wide variety of charged and neutral molecules.

Microfluidic devices have several advantages over conventional scale chemical analysis instrumentation. These devices can integrate multiple chemical processing steps in a channel manifold so that a number of chemical manipulations can be performed either in series or parallel. Such systems are also known as micrototal analysis systems ( $\mu$ -TAS). Several different types of chemical processing and handling steps have been demonstrated using  $\mu$ -TAS including mixing, reactions, filtering, preconcentration and separations.<sup>33, 199-203</sup> Several of these processing and handling steps have been integrated to form devices capable of performing complete chemical analyses.

The microfluidic devices reported thus far have been fabricated from a variety of glasses and polymers.<sup>8, 9, 16, 17, 19, 20, 63</sup> Polymers have potential advantages over glasses as the microchip substrate material and fabrication costs are substantially lower. While several polymers have been investigated for the fabrication of microfluidic devices including poly(carbonate), poly(ester),<sup>64</sup> poly(styrene),<sup>65, 66</sup> poly(ethylene terephthalate glycol),<sup>65, 66</sup> poly(methyl methacrylate)<sup>204</sup>, poly(acrylic resins)<sup>205, 206</sup>, cellulose acetate<sup>207</sup>, and poly(olefins)<sup>208</sup>, the most popular material by far is poly(dimethylsiloxane) (PDMS)<sup>209</sup>, a durable hydrophobic elastomer. PDMS is a relatively inexpensive substrate material, and devices can be rapidly and easily

molded from the prepolymer. PDMS offers good optical transmission characteristics, high electrical resistivity, and acceptable thermal conductivity.<sup>17</sup> PDMS-based microfluidic devices, however, have some fundamental limitations stemming from the hydrophobicity of the PDMS. For example, the channels in these devices are difficult to wet and, therefore, fill. The hydrophobic surface of PDMS also nonspecifically adsorbs proteins and other hydrophobic analytes generating poor peak signals, low separation efficiencies, asymmetric peak shapes, and drifting electroosmotic flows which lead to migration time variations.<sup>49, 210</sup>

A variety of covalent and dynamic surface coatings for PDMS-based microfluidic devices have been reported to try to overcome some of the aforementioned limitations. Covalent modifications of PDMS include the formation of reactive PDMS surfaces using plasma, corona discharge or ultraviolet light. The reactive PDMS surface is then further processed by coupling it to a specific chemical functionalities either using silanization<sup>52, 53, 144</sup>, atom-transfer radical polymerization<sup>149, 211</sup>, or radiation induced graft polymerization<sup>90, 147, 212, 213</sup>. Alternative techniques for covalently modifying the PDMS surface include sol-gel coatings<sup>159</sup>, chemical vapor deposition<sup>99, 100</sup>, and radical initiators such as cerium(IV)<sup>214</sup>. Dynamic modifications of the PDMS channel wall surfaces include polyelectrolyte multilayers (PEMS)<sup>102</sup>, phospholipid bilayer coatings<sup>215</sup>, and ionic surfactant coatings<sup>49, 51, 216</sup>.

Ionic surfactant coatings on PDMS have been reported using SDS and cetyltrimmonium bromide (CTAB). Both SDS and CTAB are selectively adsorbed on PDMS surfaces.<sup>49</sup> This adsorption changes the EOF generated in the PDMS channel. PDMS capillaries coated with SDS concentrations between 0.005 to 0.1% exhibit EOFs between  $3 \times 10^{-4}$  and  $5 \times 10^{-4}$  cm<sup>2</sup>/Vs, respectively.<sup>217</sup> The addition of CTAB at concentrations between 1 to 2.3x10<sup>-4</sup>% can be used to reverse the EOF.<sup>217</sup> Hydrophobic analyte adsorption studies by Berglund et al. using optical

reflectometry have demonstrated that SDS adsorbs selectively to the surface of PDMS and significantly reduces the adsorption of hydrophobic hydroxypropyl cellulose or hydroxyethyl cellulose. Additionally, hydroxypropyl cellulose and hydroxyethyl cellulose trapped on the PDMS surface can be removed through the addition of SDS<sup>218, 219</sup>.

While MEKC has been used frequently in fused silica capillaries and in glass microchip channels there are few reports of its use on polymers with only one brief report on the precolumn labeling and separation of some biogenic amines on PDMS devices.<sup>220</sup> It is on polymers, however, especially hydrophobic polymers, like PDMS, where the use of SDS might have considerable impact due to its dual nature as both a dynamic coating agent as well as a pseudo-stationary phase. In this paper we describe the successful separations of Rhodamine B, TAMRA and BODIPY<sup>®</sup> labeled amino acids, and AlexaFluor<sup>®</sup> labeled *E. coli* homogenates in PDMS-based microchips using MEKC. To improve the initial separations, a PDMS chip with a 30 cm long serpentine separation channel incorporating tapered turns was fabricated and used for some of the separations.<sup>221</sup>

## **5.2 Experimental**

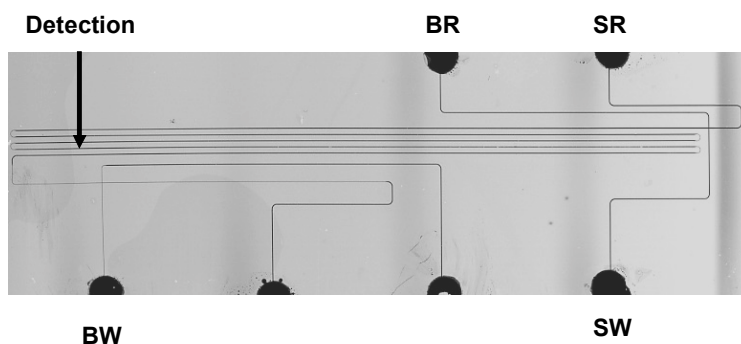
### ***5.2.1 Reagents and Solutions***

Sodium dodecyl sulfate, acetonitrile, sodium tetraborate, rhodamine B and amino acids were purchased from Acros Organics (Geel, Belgium). The polyamines 1-4 diamino butane (putrescine), 1-5 diamino pentane (cadaverine), and spermidine were purchased from Sigma Chemical Co. (St. Louis, MO). Commercial PDMS (Sylgard 184) was obtained from Dow Corning (Midland, MI). All of the chemicals were used as received. All solutions were made

using distilled, deionized water from a Barnstead Nanopure System (Dubuque, IA) and then filtered through 0.45  $\mu\text{m}$  Acrodiscs (Gelman Sciences; Ann Arbor, MI).

### 5.2.2 Microchip Fabrication

Photomasks were generated by The Photoplot Store (Colorado Springs, CO) at 40,000 dpi using a photoplotting process. The mask designs were created in AutoCAD2000LT (Thomson Learning; Albany, NY) and sent to The Photoplot Store for translation and fabrication. Two different masks were used to fabricate the chips that were used to obtain the results reported below. We used a cross microchip with a 4 cm long separation channel for the separations of Rhodamine B and fluorescently labeled hydrophobic amino acids. The dimensions of this chip are identical to that previously reported<sup>159</sup>. In addition, we used a serpentine microchip with a separation channel of 30 cm that is similar in design to what has been published previously<sup>221</sup>. The serpentine chip was used for amino acid and *E. coli* protein homogenate separations and is shown in **Figure 5.1**. The separation channel was 20  $\mu\text{m}$  deep and 75  $\mu\text{m}$  wide. The turns were tapered to minimize band-broadening. The channel dimensions in the turns were 20  $\mu\text{m}$  wide and 20  $\mu\text{m}$  deep.



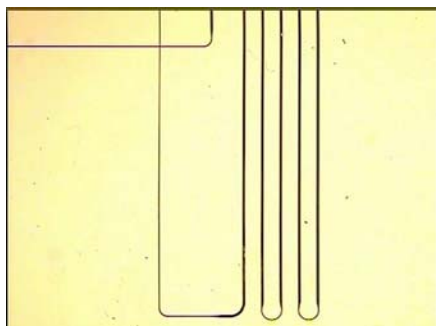


**Figure 5.1** Serpentine PDMS microfluidic chip with tapered turns and a 30 cm separation channel. The separation channel depth and width was 20 μm and 75 μm, respectively, while the tapered turns had a width of 20 μm. SR: Sample Reservoir, SW: Sample Waste, BR: Buffer Reservoir, BW: Buffer waste.

Molds were fabricated using previously reported procedures<sup>159</sup>. The Sylgard 184 elastomer was constituted and activated as specified by the manufacturer and degassed for 1 hr. Part of this mixture was poured on an SU-8 mold and another part on a clean microscope slide (the blank). After curing for 10 min at 80°C, both parts were carefully and slowly peeled off the mold and blank. The two pieces of PDMS were then conformally contacted and placed in the oven at 95°C for 2 hrs.

Reservoirs for the PDMS chips were fabricated from commercially available borosilicate glass tubing with an outer diameter of 0.8 cm and an inner diameter of 0.5 cm. Reservoirs were cut to 0.7 cm lengths and glued to 1 cm x 1 cm x 0.1 cm glass squares that had holes predrilled into them. The predrilled hole had a diameter of 0.35 cm. The glass tubing was epoxied to the glass square using EPO-TEK (Epoxy Technology; Billerica, MA) that was mixed in a ratio of 1 to 10 and cured at 90°C for 1 hr. The glass square with the predrilled hole served as a large adhesive area for anchoring the reservoir to the PDMS microchip. PDMS was mixed in a ratio of 1 to 10 and spread on the back of the glass squares. The glass squares were then placed over the small through holes in the PDMS coverplate that connected with the PDMS channels. The reservoirs were then cured for 1.5 hrs and allowed to cool at room temperature before using.

### ***5.2.3 BODIPY<sup>®</sup> Labeling Protocol***

BODIPY<sup>®</sup> FL STP ester dye was purchased from Molecular Probes (Eugene, OR). Amino acid solutions were prepared at concentrations of 5 mM in 150 mM sodium bicarbonate buffer at a pH of 8.5. The reactive BODIPY<sup>®</sup> FL STP ester dye was warmed to room temperature prior to diluting in DMSO to a concentration of 10 mM. The BODIPY<sup>®</sup>-DMSO solution was vortexed for 1 min and allowed to equilibrate for 5 min prior to adding to the amino acids for conjugation. The amino acids were labeled individually by adding 900  $\mu$ L of an amino acid solution to a microcentrifuge tube followed by the addition of 100  $\mu$ L of the reactive BODIPY<sup>®</sup> dye solution. Each tube was then vortexed for 1 min and placed in a dark box on a shaker set at 100 rpm. After 4 hrs, the labeled solutions were stored at  $< 0^{\circ}\text{C}$ .

### ***5.2.4 Amine/Protein Extraction Protocol***

The EasyLyse<sup>™</sup> bacterial protein kit from Epicenter (Madison, WI) was used to extract bacterial proteins and amines from *E. coli*. *E. coli* was harvested from an *E. coli* culture by pelleting 1 mL of the culture fluid in a microcentrifuge. *E. coli* were present at  $\sim 10^9$  cells/mL and generated  $\sim 100$ -150  $\mu$ g of cell homogenate. Once the *E. coli* were pelleted, the supernatant was removed and the pellet frozen at  $-20^{\circ}\text{C}$  for 1 hr. A solution containing 0.5 mL of distilled water, 2  $\mu$ L of 1M  $\text{MgCl}_2$ , 0.5 mL of lysis buffer and 2  $\mu$ L of enzyme mix was vortexed and allowed to equilibrate for 2 min at room temperature. The cell pellet was resuspended in 200  $\mu$ L of the above solution and incubated for 7 min at room temperature. After incubation the cellular debris were pelleted in a centrifuge for 2 min, and the supernatant was transferred to a clean tube.

### ***5.2.5 E. coli Homogenate and Polyamine Labeling***

The pH of the extracted *E. coli* homogenate was approximately neutral. Since protein/amine labeling with the AlexaFluor<sup>®</sup> 488 TFP ester is optimal around 8.5, the pH of the *E. coli* extract was adjusted. This was accomplished by adding 200  $\mu$ L of 0.1 M sodium bicarbonate to 200  $\mu$ L of the homogenate collected from the extraction described above. The pH of this solution was approximately 8.5 as measured by litmus paper. This solution was added to approximately 5 mg of TFP ester and reacted for 1 hr at room temperature. After the reaction was completed the solution was purified using the procedures described above in the experimental section.

The amine standards were diluted in a 150 mM sodium bicarbonate buffer of pH 8.5 to a final amine concentration of 5 mM. The TFP ester was added in a 4:1 mole ratio to ensure that all the amines were labeled with AlexaFluor<sup>®</sup> 488 TFP ester.

### ***5.2.6 Calculation of Diffusion Coefficient***

Diffusion coefficients were measured using the length method as previously published by Culbertson et al.<sup>122</sup> Briefly, peak variance was measured as a function of migration time to obtain the diffusion coefficient from the slope of the plot. This was achieved by collecting electropherograms at a series of different points on the separation channel and then using Igor Pro (Version 4.0.7.0; Wavemetrics; Lake Oswego, OR) to fit the Gaussian peaks and analyze the migration time and peak width.

### ***5.2.7 Separations and Detection***

The electrokinetic chromatographic separations and laser induced fluorescent detection were performed with equipment that was similar to that previously described.<sup>159</sup> Separations of TAMRA and BODIPY labeled amino acids were performed with analyte concentration of 1  $\mu$ M

unless otherwise specified. Rhodamine B separation were performed at concentration 10  $\mu\text{M}$  unless otherwise specified. The separations and gated injections<sup>117</sup> were performed using three independent and remotely programmable high voltage (0-10 kV) power sources from EMCO (Sutter Creek, CA). The proper potentials to apply at each reservoir were determined using Kirchhoff's rules and Ohm's Law.<sup>118</sup> The injection times were 0.02 s.

### ***5.2.8 Electroosmotic Flow Measurements***

EOF measurements were taken on PDMS chips using the current monitoring method.<sup>68, 222, 223</sup> Straight channels were fabricated out of PDMS and were subsequently filled with 50 mM SDS, 10 mM sodium tetraborate and 20% acetonitrile, pH = 9.5. The channel was allowed to equilibrate at room temperature for 1 hr. After this time period the reservoirs were refreshed with new buffer to assure that there were no changes in buffer composition due to evaporation. This buffer, in the anode reservoir, was replaced with 50 mM SDS, 5 mM sodium tetraborate and 20% acetonitrile, pH = 9.5. Voltage potentials of 300 V/cm were applied using a Bertan (Hauppauge, NY) custom designed 0-10 kV voltage supply resulting in the migration of the lower conductivity buffer into the channel due to electroosmotic flow. Once the lower conductivity buffer migrated to the cathodic reservoir the conductivity reached a constant value. The time that it took the lower conductivity buffer to migrate to the cathodic reservoir was used to calculate the EOM of the capillary.

### ***5.2.9 Imaging of Rhodamine B Injections***

Two rhodamine solutions were prepared, one for CZE and the other for MEKC. The MEKC solution consisted of 50 mM SDS, 10 mM sodium tetraborate and 20% acetonitrile. The CZE buffer consisted of 10 mM sodium tetraborate. Cross channel chips with separation channel

diameter, depths and lengths of 20  $\mu\text{m}$  x 10  $\mu\text{m}$  x 3.5 cm were used for the injection imaging. The gated injections<sup>117</sup> were performed using two independent and remotely programmable high voltage (0-10 kV) power sources from Bertan (Hauppauge, NY). The proper potentials to apply at each reservoir were determined using Kirchhoff's rules and Ohm's Law.<sup>118</sup> The injection times were 0.2 s. The gated injections were imaged using a Nikon Eclipse TE2000E microscope with an epi-illumination attachment and a Sony CCD color video camera (SSC-DC50A).

## 5.3 Results and Discussion

### 5.3.1 Buffer Optimization and Use

One of the primary drawbacks to the use of PDMS microchips is the difficulty of filling the channel manifolds with aqueous solutions. Small nucleation sites within the capillary produce air bubbles as the capillaries are filled with solution. Eliminating this characteristic of PDMS is extremely difficult, but also very important for the broad applicability of PDMS microchips. We found that bubble formation was greatly suppressed using SDS-MEKC buffers on PDMS microchips and that the PDMS capillaries were just as easy to fill with MEKC buffer as aqueous solutions in glass capillaries. This allowed us to fill 30 cm long PDMS capillaries with MEKC buffers without air bubble generation. We attribute this effect not only to the selective adsorption and partitioning of SDS to the surface of the PDMS capillary but also to the organic content of the solvent which helped to wet the surfaces of the channels.

The EOF of the PDMS chips using a buffer consisting of 50 mM SDS, 10 mM sodium tetraborate, and 20% acetonitrile was measured at  $7.1 \times 10^{-4} \text{ cm}^2/\text{V}\cdot\text{s}$  ( $n = 5$ , 1.6% RSD). EOF measurements for PDMS using 10 mM sodium tetraborate and 20% acetonitrile yielded an EOF

of only  $2.1 \pm 0.2 \times 10^{-4} \text{ cm}^2/\text{V}\cdot\text{s}$  (RSD = 7%, n = 10). The EOF generated on the PDMS devices with the addition of SDS was ~340% higher than the EOF generated without the SDS. The higher EOF observed for PDMS with the MEKC buffer was due to the partitioning of anionic SDS to the surface of the PDMS as was first described by Harrison's group.<sup>49</sup> This higher EOF for the MEKC buffer in PDMS microchips is useful for generating high speed MEKC separations. Typically SDS-based MEKC separations take longer to perform than CZE separations as the micelles are migrating opposite to the direction of the EOF. Increasing the EOF, decreases the migration times of the analytes and consequently increases the speed of the MEKC separations compared to the MEKC separations performed on glass chips.

### ***5.3.2 Rhodamine B Injections***

Electrokinetic gated injections were imaged using a CCD camera for both PDMS chips using CZE and MEKC. **Figure 5.2A** shows the gated injections using a PDMS chip in CZE mode. Rhodamine B is rapidly absorbed into the sidewalls of the capillary. In **Figure 5.2A**, rhodamine B can be observed diffusing into the channel wall. Upon injection of the rhodamine B into the separation channel there is significant absorption into and adsorption onto the surface yielding non Gaussian injection plugs that migrate extremely slowly with time. **Figure 5.2B** shows a gated injection using a PDMS chip in MEKC mode. The PDMS does not show any measureable absorption or adsorption to the PDMS sidewall. The injected plug is Gaussian and is transported rapidly down the channel.

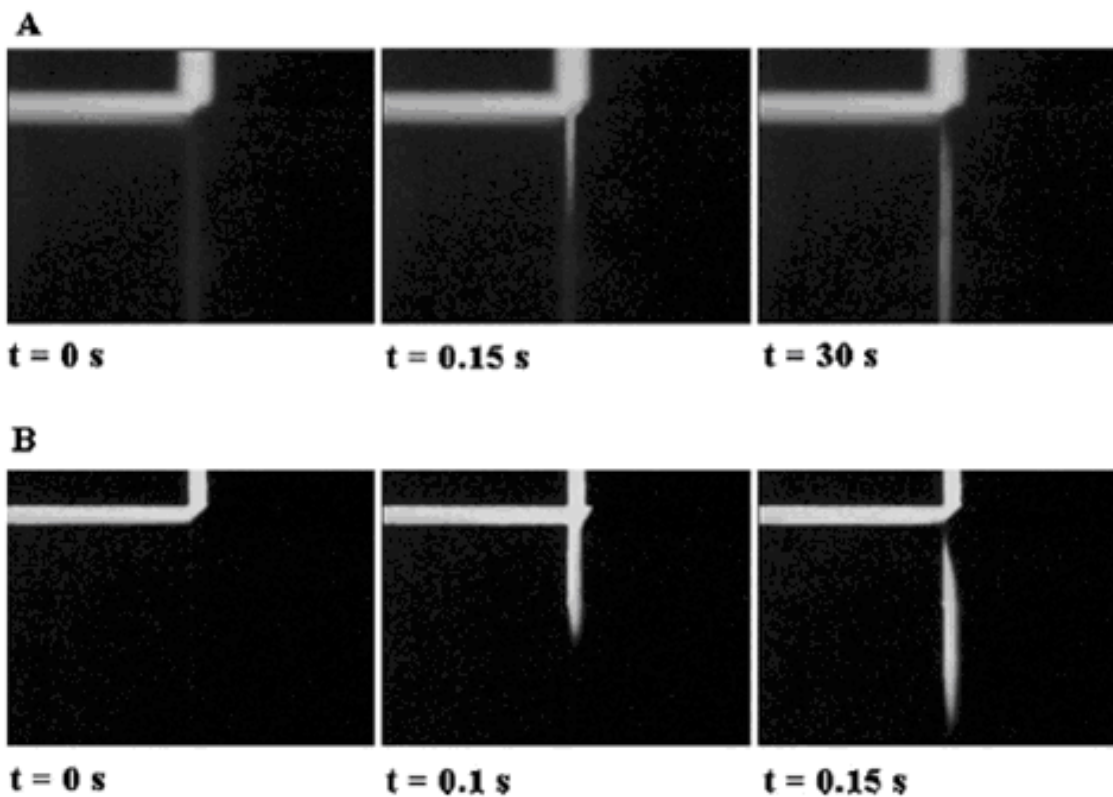


**Figure 5.2** Gated injections of rhodamine B on a PDMS chip with  $t_{inj} = 0.2$  sec and  $E = 200$  V/cm. (A) Buffer, 10 mM sodium borate; sample, 10  $\mu$ M rhodamine B. (B) Buffer, 10 mM sodium tetraborate, 50 mM SDS and 20% (v/v) acetonitrile; sample 10  $\mu$ M rhodamine B.

Both gated injections and pinched injections of RhB were examined using a high resolution CCD camera. We found minimal band broadening due to adsorption to the surface, and relatively sharp injection plugs demonstrated in **Figure 5.3**.

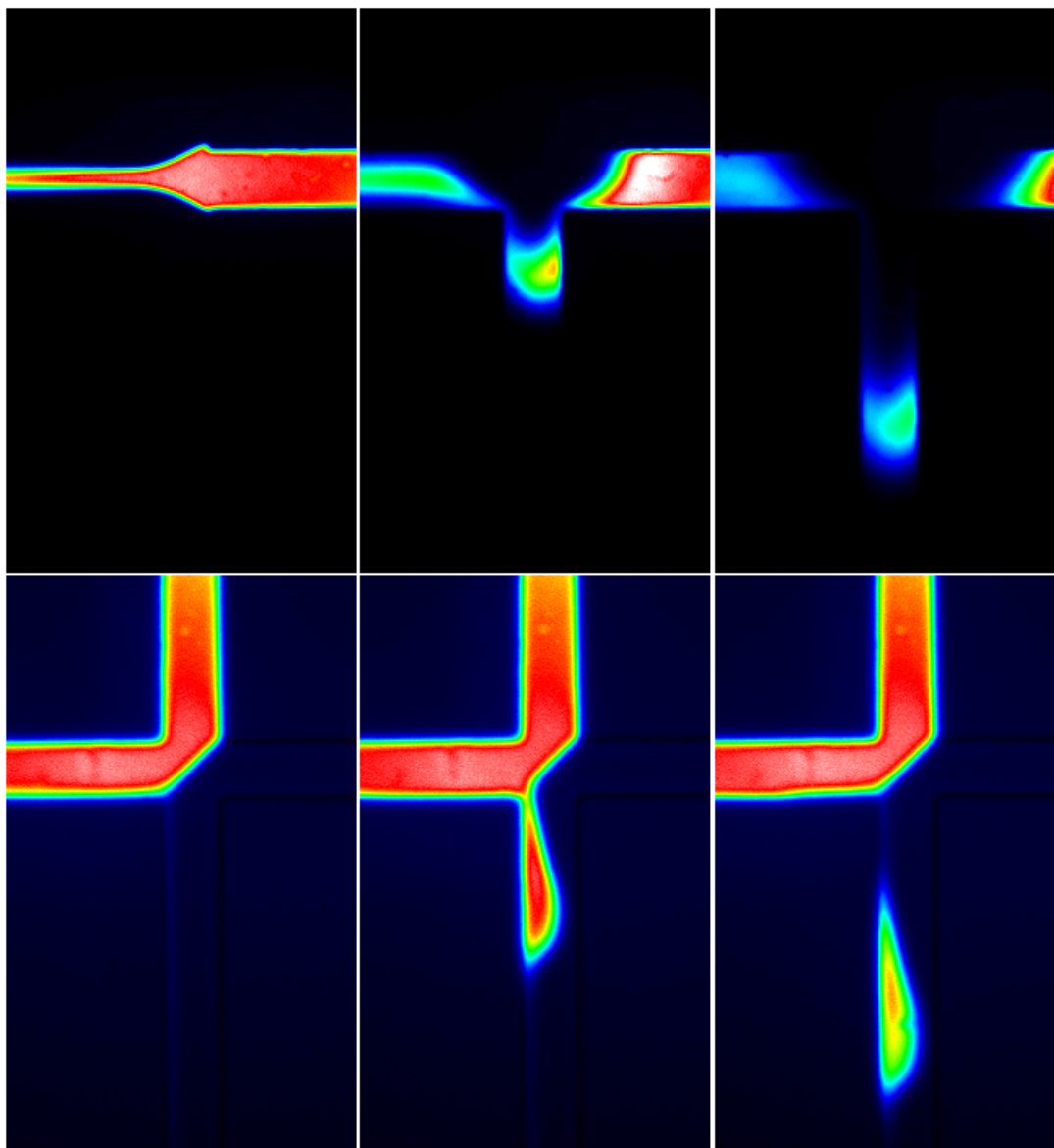


**Figure 5.3** Illustrates the injection of Rhodamine B on PDMS microfluidic devices using both pinched injections (top) and gated injections (bottom).

### ***5.3.3 Rhodamine B Separations***

Since the MEKC buffer contains acetonitrile it was critical to design reservoirs on PDMS chips that minimized the solvent evaporation as mentioned in the microchip fabrication section above. We found that uncapped reservoirs containing small volumes of fluids often contributed to large run to run percent relative standard deviations (%RSD's) as the acetonitrile would evaporate over the course of an experiment. After constructing larger, capped reservoirs, we

were able to achieve run to run reproducibilities of  $< 1\%$  RSD. As might be expected free solution separations (10 mM sodium borate buffer) of rhodamine B on PDMS microchips yielded no observable peaks on the electropherogram at a distance of 3 cm from the cross injector. This was primarily due to the absorption of the rhodamine B into the bulk PDMS. While a fluorescent signal can be observed  $\sim 0.3$  cm from the injector, this signal rapidly declines as the distance from the injector increases. Alternatively, separations of rhodamine B using the MEKC buffers generated high efficiency peaks with excellent detection limits and very reproducible run-to-run migration times and peak areas. The separations were performed on a cross channel design with a separation channel 4.0 cm long. The separation distance was 3.4 cm, and the applied electric field was 650 V/cm. Separations of rhodamine B under these conditions on PDMS chips using MEKC yielded efficiencies of  $63,000 \pm 500$  ( $n = 3$ ; RSD = 0.9%), or  $1.9 \times 10^6$  N/m. **Figure 5.4** shows electropherograms for consecutive separations of rhodamine B using MEKC on a PDMS microchip. Detection limits for this separation were 10 pM, calculated at a S/N ratio of 5. The detection volume defined by the channels ( $10\mu\text{m} \times 20\mu\text{m}$ ) and detection window ( $400\mu\text{m}$ ) was  $8 \times 10^{-8} \text{ cm}^3$  yielding a detection limit of 482 molecules. The migration time and peak area reproducibilities for these separations was 0.7% RSD ( $n = 3$ ) and 0.89% RSD ( $n = 3$ ), respectively. The diffusion coefficient of rhodamine B was measured at  $4.40 \times 10^{-6} \pm 0.2 \text{ cm}^2/\text{s}$  using the Einstein-Smoluchowski equation. The excellent detection limits for this analyte, in addition to the migration time and peak area reproducibilities, and diffusion coefficients that are within experimental error of the literature values<sup>122</sup> indicate that rhodamine B is not significantly adsorbing to the sidewall of the PDMS microfluidic device.

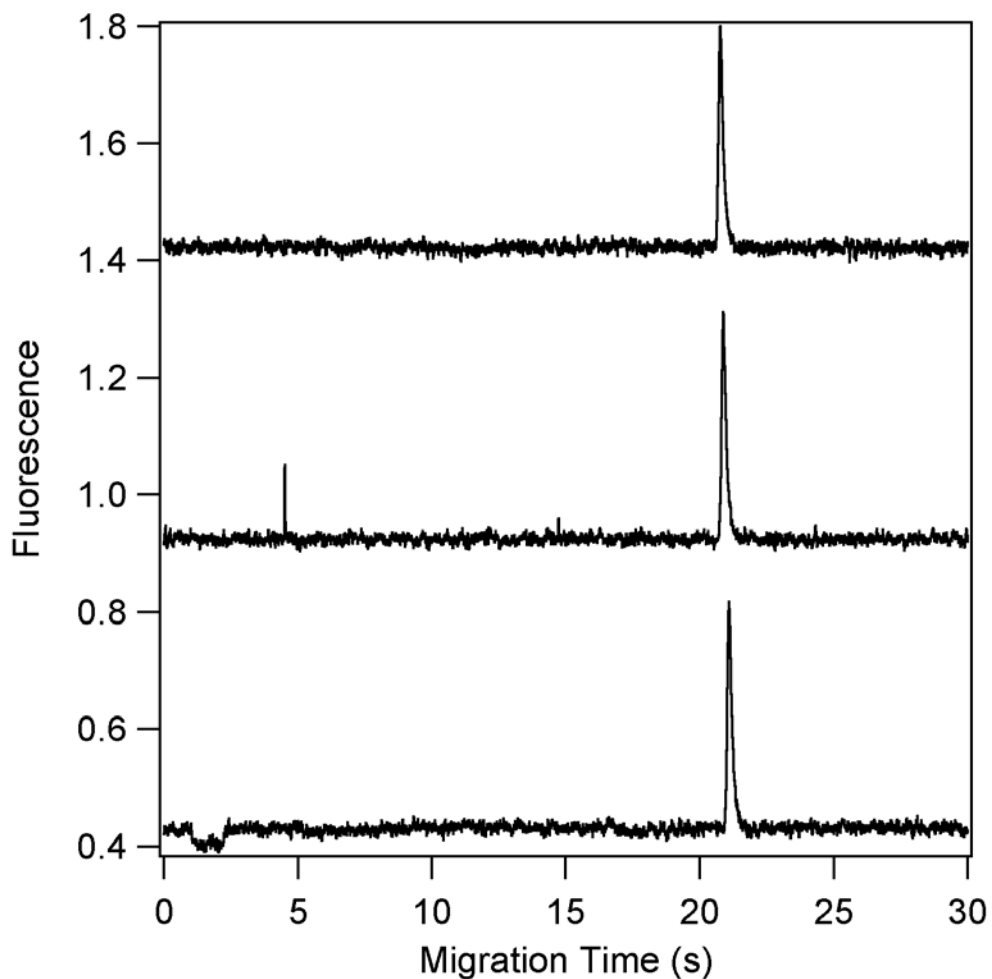


**Figure 5.4** A series of electropherograms of rhodamine B performed on PDMS microfluidic devices. Device: cross channel PDMS chip with 4.0 cm separation channel; separation distance = 3.4 cm and applied electric field = 650 V/cm; buffer: 10 mM sodium tetraborate, 50 mM SDS, 20% ACN; sample, 10  $\mu$ M rhodamine B.

### 5.3.4 Amino Acid Separations

Separations of hydrophobic TAMRA labeled amino acids performed on PDMS microchips using MEKC are shown in **Figure 5.5**. The separation parameters were identical to that of the rhodamine B separations except for a slightly longer detection distance of 3.65 cm. The microfluidic chips that we used for these studies had a longer separation channel which allowed for higher resolution among peaks. Hydrophobic amino acids such as phenylalanine and tryptophan were separated with high efficiencies. Separation efficiencies of  $136,000 \pm 3,000$  ( $n =$

5, 2.2% RSD) and  $133,000 \pm 6,000$  ( $n = 5$ , 4.5% RSD) were obtained for phenylalanine and tryptophan, respectively. These amino acid separations are significant because they demonstrate the ability to separate extremely hydrophobic amino acids on PDMS microfluidic devices. Day-to-day migration time and peak area reproducibilities of these TAMRA labeled amino acid separations averaged 5.1 %RSD and 4.4 %RSD, respectively. These separations were performed without the use of the extra volume capped reservoirs as described in the experimental. We found that it was much more difficult to control solvent evaporation from our 100  $\mu$ L uncapped reservoirs and this directly caused an increase in the reproducibility.

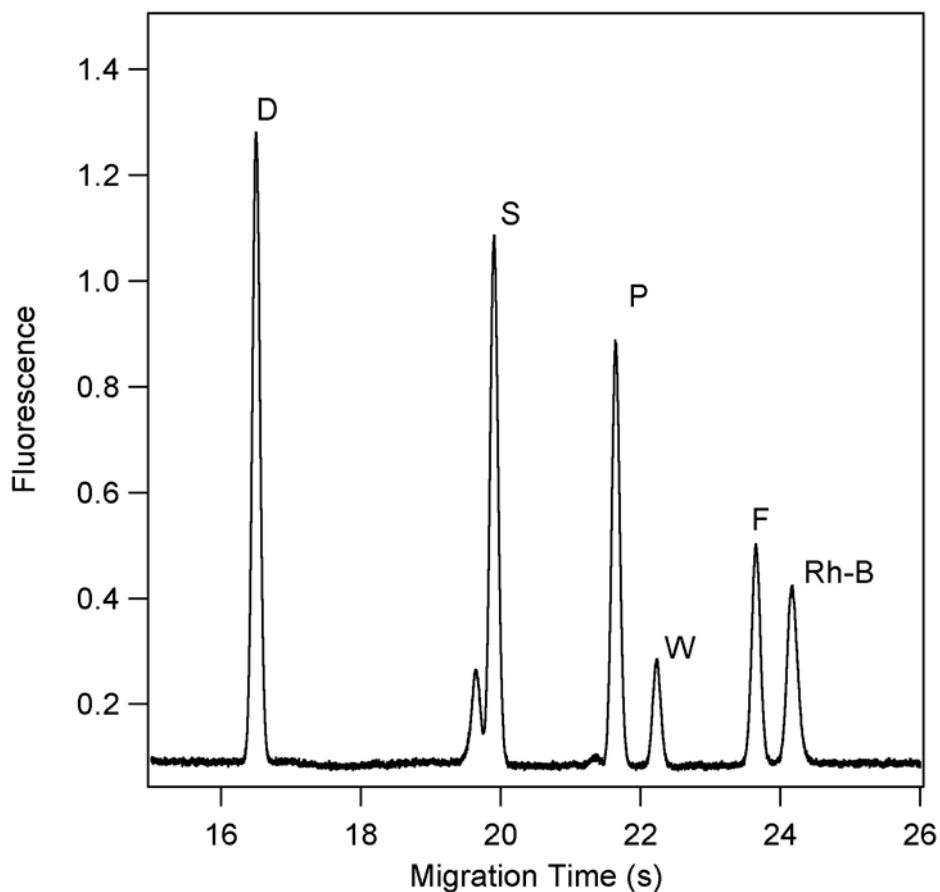


**Figure 5.5** Electropherogram of 10  $\mu$ M rhodamine B, tryptophan, phenylalanine, serine, proline, aspartic acid. Device: cross channel PDMS chip with 4.0 cm separation channel; separation distance = 3.65 cm and applied electric field = 650 V/cm; buffer, 10 mM sodium tetraborate, 50 mM SDS, 20% ACN.

To increase the separation efficiency, resolution and reproducibility of our separations we fabricated a serpentine chip shown in **Figure 5.1** that has a 30 cm separation channel with extended volume capped reservoirs. The MEKC buffer filled this PDMS channel rapidly without bubble formation. Using a Spellman high voltage power supply we applied -15 kV at the separation waste reservoir to help generate a 750 V/cm applied field strength across the separation channel.<sup>34</sup> In addition to TAMRA labeled amino acids, we also separated BODIPY labeled amino acids. **Figure 5.6** shows separations of 17 BODIPY labeled amino acids in a 50 mM SDS buffer on the PDMS serpentine chip with a 27 cm separation distance. Separation efficiencies for these amino acids ranged from  $496,000 \pm 11,000$  ( $n = 5$ , 2.3 %RSD), or  $1.8 \times 10^6$  N/m for early eluting peaks to  $837,000 \pm 24,000$  ( $n = 5$ , 2.9 %RSD), or  $3.0 \times 10^6$  N/m for later eluting peaks. Ocvirk et al. reported that BODIPY 493/503 could not be analyzed by CE in a PDMS device because it was extracted into the PDMS.<sup>49</sup> Through the application of MEKC on PDMS chips, it is now possible to separate BODIPY labeled amino acids on PDMS chips with high efficiencies.

Diffusion coefficients were also calculated for BODIPY labeled amino acids on PDMS serpentine chips to investigate whether the tapered turns introduced any effective band broadening or the BODIPY amino acids were adsorbing to the sidewall. Diffusion coefficients for BODIPY-Ser, and BODIPY-Pro were calculated to be  $3.8 \pm 0.2 \times 10^{-6}$  cm<sup>2</sup>/s and  $3.65 \pm 0.2 \times 10^{-6}$  cm<sup>2</sup>/s, respectively, and are within the experimental error of the literature values.<sup>122</sup> This suggests that neither the tapered turns nor the PDMS is appreciably affecting the band broadening of our separations as they are diffusion limited. In addition, the number of theoretical

plates as a function of migration time (i.e. separation distance) was linear, shown in **Figure 5.7** for BODIPY-aspartic acid and BODIPY-arginine.

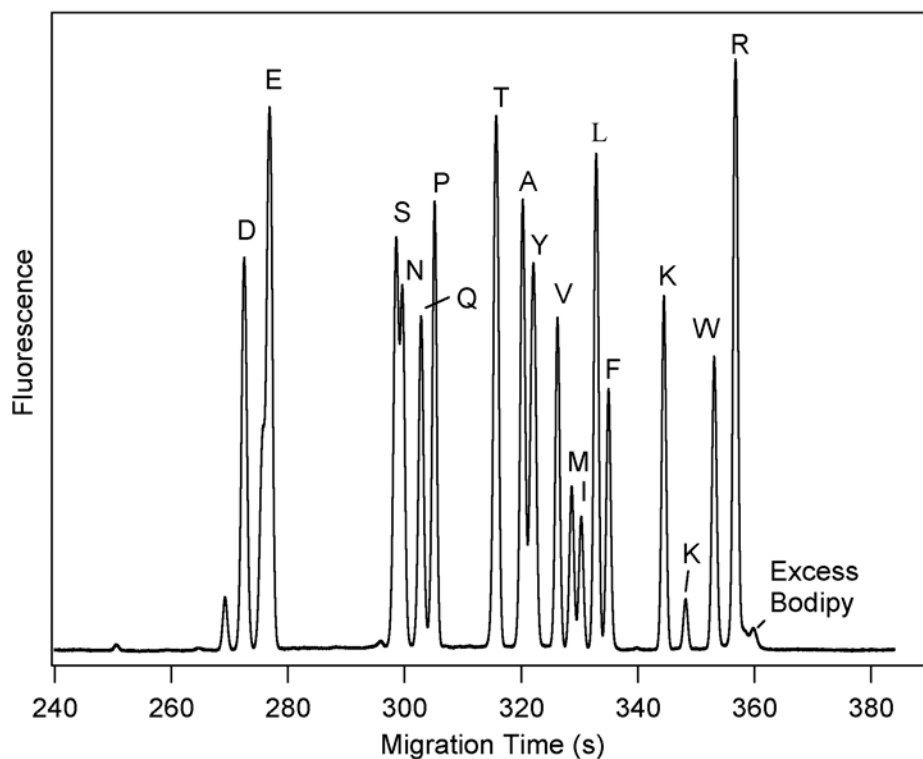


**Figure 5.6** Electropherogram of 17 labeled BODIPY amino acids; device: serpentine channel PDMS chip with 30 cm separation channel; separation distance of 27 cm and applied electric field of 750 V/cm; buffer: 10 mM sodium tetraborate, 50 mM SDS, 20% acetonitrile.

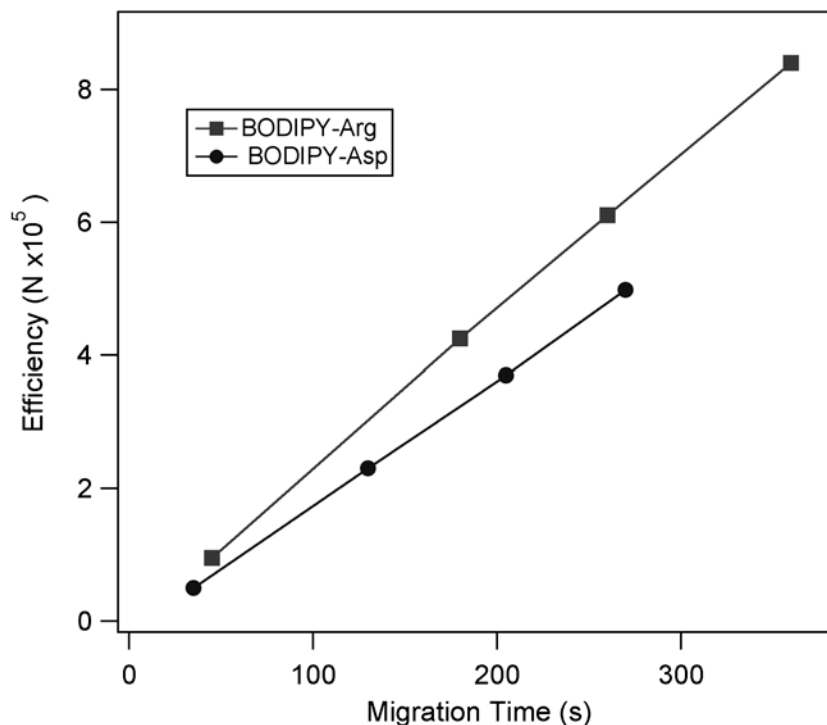


**Figure 5.7** Efficiency of glutamic acid and arginine labeled with BODIPY as a function of migration time. Electropherograms were collected using buffer of 10 mM sodium tetraborate, 50 mM SDS, and 20% acetonitrile, separation field strengths for the separation were 750 V/ cm.

### 5.3.5 Bacterial Homogenate separations

To further examine the performance of our PDMS serpentine chip we separated a *E. coli* homogenate using commercially available lysis and extraction protocols. Our primary goal for this study was to extract the proteins from the homogenate and separate them using MEKC. The results of those separations will be reported in a separate paper. As part of that analysis, the homogenate was filtered through several molecular weight cutoff filters (MWCO). The homogenate which passed through the 3,000 MWCO was used for the separations reported in this paper. This fraction is expected to contain various biogenic amines and amino acids. The separation of these amines and amino acids using MEKC is shown in **Figure 5.8**. The separation efficiencies of these peaks varied from  $320,000 \pm 3000$  for early eluting peaks to  $400,000 \pm 5000$

for later eluting peaks. Using the extended volume reservoirs run-to-run migration time and peak area reproducibilities were 1.1 %RSD, and 1.3% RSD over a 3 hr time period.

In order to tentatively identify some of the peaks in the filtered *E. coli* homogenate, AlexaFluor 488 labeled standard amines - spermidine, cadaverine and putrescene - were comigrated with the homogenate. The migration order of the polyamines increased as a function of their hydrophobicity as would be expected if the separation was primarily chromatographic in nature. The spermidine had the longest migration time followed by cadaverine (1,5 diamine pentane) and putrescene (1,4- diamine butane).

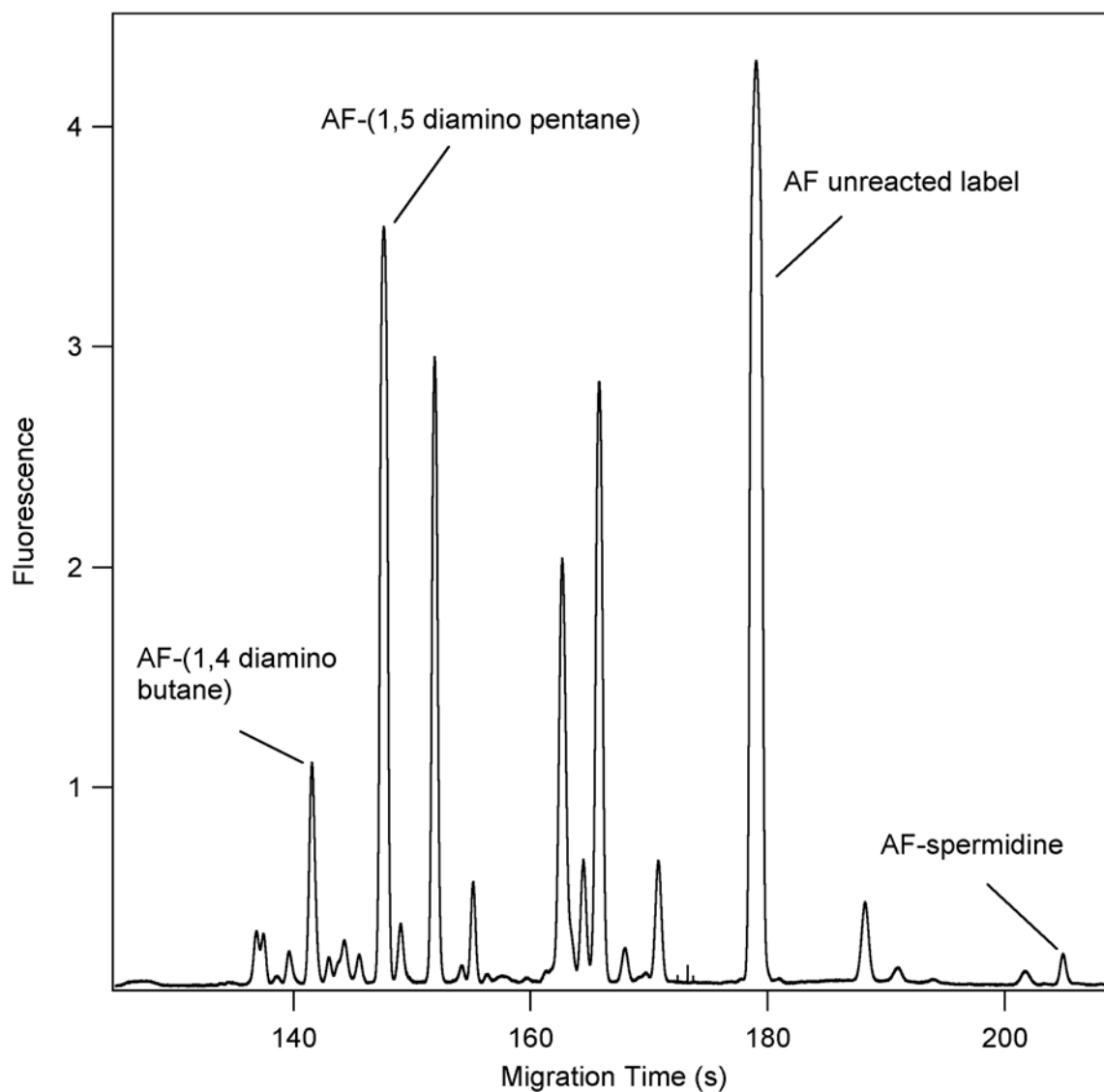


**Figure 5.8** Electropherogram of AlexaFluor 488 TFP labeled E-coli. homogenate; device: serpentine channel PDMS chip with 30 cm separation channel; separation distance of 20 cm and applied electric field of 750 V/cm; buffer: 10 mM sodium tetraborate, 50 mM SDS, 20% ACN.

### 5.4 Concluding Remarks

We have demonstrated a rapid and facile method for separating hydrophobic analytes on PDMS microchips using MEKC with very high separation efficiencies and very low detection limits. Extended separation distances were realized on these chips using a serpentine channel

pattern with tapered turns. This device was easily filled with buffer and was capable of generating diffusion limited MEKC separations. A wide variety of charged and neutral molecules were separated using this method including - rhodamine B, TAMRA and BODIPY labeled amino acids, Alexafluor labeled amines, and AlexaFluor labeled bacterial homogenates . The application of MEKC on PDMS-based microchips should significantly extend the variety of analytes that can be manipulated and analyzed. As this method takes advantage of the wide availability of soft lithography and requires no pretreatment of the PDMS either pre or post fabrication, the technology is accessible to a wide variety of research groups.

## CHAPTER 6 - MEKC of Proteins on PDMS

### 6.1 Introduction

Micellar electrokinetic chromatography (MEKC) of standard proteins was investigated on PDMS microfluidic devices. Standard proteins were labeled with AlexaFluor<sup>®</sup> 488 carboxylic acid tetrafluorophenyl ester and filtered through a size exclusion column to remove any small peptides and unreacted label. High efficiency MEKC separations of these standard proteins were performed using a buffer consisting of 10 mM sodium tetraborate, 25 mM sodium dodecyl sulfate (SDS), and 20% (v/v) acetonitrile (ACN). Separations of bovine serum albumin (BSA) using this buffer on a 3.0 cm channel generated a plate height of 0.38  $\mu\text{m}$  which correspond to  $2.6 \times 10^6$  N/m in  $< 20$  s. Additional fast separations of myoglobin,  $\alpha$ -lactalbumin, lysozyme, and cytochrome c also yielded plate heights in the range from 0.54  $\mu\text{m}$  to 0.72  $\mu\text{m}$ , which correspond to 1.3 to  $1.8 \times 10^6$  N/m. All proteins migrated with respect to their individual pI's. To improve the separations, we used a PDMS serpentine chip with tapered turns and a separation distance of 25 cm. We found that the proteins continued to migrate within a limited migration time window, thus limiting the peak capacity to  $\sim 10$ -12.

Micro total analysis systems ( $\mu$ -TAS) have the capability of integrating multiple chemical handling and analysis operations in a single channel manifold contained on a monolithic microchip. The advantages of such integration and miniaturization of chemical handling and analysis operations include: portability, automation, reduced reagent consumption, high separation efficiencies, and increased speed. Although  $\mu$ -TAS potentially has many advantages

over bulk scale analytical techniques the large surface-to-volume ratio in the channels can be a limitation in cases where analytes tend to interact with surfaces. This is particularly true for proteins. It is believed that the adsorption of proteins, either through electrostatic or hydrophobic forces to the channel walls of microfluidic devices, is the primary contributing factor to low efficiency protein separations.<sup>224</sup> Many different techniques have been developed for reducing the adsorption of proteins to the walls of the channels. Some examples include the use of pH extremes, high concentration buffers and surface coatings that are tailored for both the surface chemistry of the substrate and the proteins<sup>165, 225-231</sup>. Most of these methods have limitations that reduce their overall applicability. These limitations include increased Joule heating for high concentration buffers, electroosmotic flow (EOF) instability for buffers at extreme pH's, and coating degradation when highly basic buffers are used.

A popular substrate for the fabrication of microfluidic manifolds is poly(dimethylsiloxane) (PDMS), a durable hydrophobic elastomer that is inexpensive and into which micron scale features can be easily molded.<sup>209</sup> The hydrophobicity of PDMS causes significant problems for the transport and separation of hydrophobic analytes or analytes containing hydrophobic patches such as denatured proteins. Hydrophobic analytes adsorb onto the PDMS surface making it difficult to transport them through a microfluidic manifold.<sup>49</sup> Several solutions have been reported to improve protein separations on PDMS microfluidic devices including covalent and noncovalent surface modifications. Covalent surface modifications of PDMS channels that were subsequently used for protein separations include radiation induced graft polymerization<sup>90, 147, 212, 213</sup> and atom transfer radical polymerization<sup>149, 211</sup>. Radiation induced graft polymerization was used to graft poly(ethylene glycol) monomethoxyl acrylate – acrylic acid (PEG-AA-DIPEG) within a PDMS channel. The PEG-

AA-DIPEG coated PDMS channels were used to separate proteins F-src and F-calc to efficiencies of  $9,300 \pm 300$  and  $5,200 \pm 400$ , respectively. Another covalent modification using atom transfer radical polymerization has been demonstrated to attach poly(acrylamide) to a PDMS surface. Bovine serum albumin (BSA) separations on poly(acrylamide) coated PDMS channels yielded efficiencies of 33,000 N/m. In addition to covalent modifications, noncovalent modifications of the PDMS surface have been used to improve the separations of proteins. Ionic surfactants such as sodium dodecyl sulfate (SDS) and cetyltrimmonium bromide (CTAB) have been used to coat PDMS coated silica capillaries that were subsequently used for the separation of lysozyme, cytochrome-c, ribonuclease A and myoglobin. Separation efficiencies up to  $9.4 \times 10^5$  N/m were generated in such capillaries.<sup>49, 217</sup> Additionally, Brij35 has been used to separate glucose oxidase (GOD) and myoglobin on PDMS microfluidic devices using electrochemical detection with efficiencies of 100,100 N/m and 39,960 N/m, respectively.<sup>232</sup>

While the coating and dynamics between PDMS and ionic surfactants including SDS and CTAB have been investigated<sup>218, 219</sup>, there are only a few reports of using MEKC for separations on PDMS-based microfluidic devices. Recently, we have shown that MEKC separations using PDMS serpentine chips with a 27 cm separation channel are extremely useful for hydrophobic small molecule separations and can generate efficiencies of up to 850,000 plates or  $3.0 \times 10^6$  N/m for BODIPY labeled amino acids.<sup>159</sup> Others have applied MEKC on PDMS devices to separate biogenic amines with efficiencies of up to 21,000 plates<sup>220</sup>, but no reports have demonstrated the usefulness of MEKC on PDMS devices for the separation of proteins.

MEKC, introduced in 1984 by Terabe<sup>233</sup>, has been used primarily for small molecule analysis<sup>234</sup>, although it has also been used for the analysis of macromolecules such as proteins<sup>235-241</sup>. Successful protein separations using MEKC, however, can be tricky as completely denatured

proteins tend to adsorb a constant amount of SDS regardless of the acid-base chemistry or the hydrophobicity of the protein<sup>242</sup>. Buffers, therefore, must be carefully optimized in order to successfully separate proteins using MEKC. The selectivity of MEKC-based protein separations depends on the hydrophobic and electrostatic forces between the micelles and the surface of the protein<sup>235, 236</sup>. These forces can be modified by varying the pH, ionic strength, and surfactant concentration to optimize the separation. There are several reports of such optimizations for capillary-based separations of standard proteins<sup>217, 243-245</sup>, serum proteins<sup>241</sup>, bacterial homogenates<sup>238</sup>, plasma apolipoproteins<sup>246</sup> and urine containing imidopeptides<sup>247</sup>. The best of these separations have produced efficiencies of  $2.2 \times 10^6 \text{ N/m}^{238}$ , but they require analysis times of between 10 and 20 min.

While separation conditions and separation efficiencies have been examined previously, no reports have addressed the available migration time window and resolving power of MEKC-based protein separations, and only one report has examined the peak capacity.<sup>248</sup> These are critical parameters to understand if this method is to be used for the separation of complex, real-life protein samples. In this paper we report the first MEKC separations of fluorescently labeled standard proteins on PDMS microfluidic devices and examine analyte resolution and separation efficiency as a function of separation distance. From this data we estimate the peak capacity and discuss some of the potential limitations of MEKC when applied to protein separations.

## 6.2 Materials and Methods

### ***6.2.1 Reagents and Fluorescent Derivatization***

The standard proteins cytochrome c (equine skeletal muscle), lysozyme (egg white),  $\alpha$ -lactalbumin (bovine milk), bovine serum albumin, ribonuclease A (bovine pancreas), and myoglobin (equine skeletal muscle) were labeled with AlexaFluor<sup>®</sup> 488 tetrafluorophenyl (TFP) ester using a protein labeling kit from Molecular Probes (Eugene, OR). To prepare the standard proteins for labeling we warmed them to room temperature. Once the standard protein samples reached room temperature, 2 mg was added to 1 mL of 0.1 M sodium bicarbonate, followed by the addition of the AlexaFluor<sup>®</sup> 488 carboxylic acid tetrafluorophenyl (TFP) ester. This solution was mixed for ~1 hr at room temperature. After 1 hr had elapsed, the solution was added to the top of a Bio-Rad BioGel P-30 size exclusion purification resin. The protein-TFP conjugate was allowed to diffuse into the size exclusion purification resin for 10 min prior to adding the elution buffer. The column was eluted with a solution containing 0.1 M potassium phosphate, 1.5 M NaCl and 2 mM sodium azide at a pH of 7.2. The elution buffer was added to the column until the protein was eluted and collected. The protein standards were diluted 1:100 from their labeling cocktail into the MEKC buffer.

### ***6.2.2 Microchip Design and Fabrication***

Molds for PDMS soft polymer lithography were fabricated using SU-8 photoresist and borosilicate glass slides, as described previously.<sup>159</sup> Briefly, SU-8 2015 was spun to a thickness of 15  $\mu$ m on a borosilicate glass slide that had been thoroughly cleaned of any residue. Photomasks were aligned on the glass slide, followed by an exposure of 200 mW at 365 nm. The exposed SU-8 was then developed according to the manufacturers' instructions. Two different microchip designs were used. The first design consisted of a simple cross injector with a 4 cm long separation channel and the second consisted of a cross injector with a 30 cm long serpentine

separation channel. The serpentine design incorporated tapered turns to minimize turn induced band broadening. Both of these devices have been described previously.<sup>159</sup> PDMS was constituted and poured on the SU-8 mold using the manufacturers specifications and conformally contacted and sealed with another flat PDMS slab to form the microfluidic manifold. The PDMS used to fabricate the microfluidic device was native PDMS that had not been modified using any sol-gel methods.

After molding and conformal bonding of the PDMS chip the channel manifold was filled with SDS buffer to condition the walls. This buffer was allowed to equilibrate with the walls of the PDMS channels for 1 hr. As shown previously this treatment yielded significantly higher EOM's than native PDMS.<sup>36</sup> After conditioning the native PDMS channel walls with the SDS buffer the EOM of the chip was  $7.1 \times 10^{-4} \text{ cm}^2/\text{Vs}$  which was approximately 340% greater than the EOM of native PDMS with no SDS.<sup>36</sup> Additionally, we investigated the potential for leakage between the PDMS sheets and the potential for hydrophobic analytes to be absorbed into the bulk PDMS using epi-illumination confocal fluorescence microscopy. Briefly, a hydrophobic fluorophore, rhodamine B, was dissolved in 10 mM sodium borate, 25 mM SDS and 20% ACN. This solution was introduced into the channel manifold and monitored over a period of 4 hrs. The rhodamine B was not observed to either absorb into the sidewall of the bulk PDMS, or penetrate between the conformally bonded PDMS sheets.<sup>36</sup> It is also important to note that the swelling of the channel walls due to acetonitrile absorption was not significant. Lee et al. have demonstrated that acetonitrile has a swelling factor of 1.01, which is small compared to the swelling factor of other organic solvents.<sup>249</sup>

### ***6.2.3 Protein Detection***

After separation, the fluorescently labeled proteins were detected using laser induced fluorescence (LIF), as described previously.<sup>119</sup> In brief, laser induced fluorescence (LIF) detection of the analytes was performed using the 488 nm line of a Melles Griot Argon ion laser (35-MAP-431-208; Carlsbad, California) as the excitation source at a power of 25 mW. The 488 nm laser beam was reflected off a 500 nm long-pass dichroic mirror (500DRLP, Omega Optical; Brattleboro, VT) and focused using a 40x objective (CD-240-M40X, Creative Devices; Mechanic Station, NJ) into a small spot in the separation channel below the cross intersection. The fluorescence emission was collected with the same objective, passed through the dichroic mirror, spatially filtered with a 1 mm pinhole (Oriel, Stratford, CT), and spectrally filtered using a 545 nm bandpass filter (545AF75; Omega Optical). The signal was then detected with a photomultiplier tube (PMT, R1477; Hamamatsu Instruments, Inc.; Bridgewater, NJ) and amplified using an SR570 low noise current preamplifier (Stanford Research Systems, Inc.; Sunnyvale, CA) with a 100 Hz low pass filter. The signal from the amplifier was sampled at 500 Hz using a PCI-6036E multifunction I/O card (National Instruments, Inc.; Austin, TX) in a Dell computer (Round Rock, Texas). The data acquisition and high voltage control software was written in-house using LabVIEW (National Instruments). All data analysis was performed using Igor Pro.

## **6.3 Results and Discussion**

### ***6.3.1 MEKC Buffer Optimization***

To optimize the MEKC buffer for the separation of proteins we varied the pH, SDS concentration, and organic modifier content. The migration time, efficiency and resolution of 4

standard proteins varied significantly with SDS concentration as shown in **Figure 6.1**. These protein separations were performed using a 4.0 cm separation channel and detected at 2.5 cm. The field strength was 650 V/cm. With no SDS added to the MEKC buffer there was little to no migration of proteins through the channel as they would adsorb onto the surface of the channels. As the concentration of the SDS was increased to 5 mM a significant increase in signal was seen, although only 3 of the 4 peaks were resolved. The resolving power of the separation increased for 25 mM SDS, but began to significantly decrease for SDS concentrations of 40, 100 and 200 mM SDS. In addition to varying the ionic surfactant concentration, the effect of buffer pH and organic modifier content were also determined. Acidic pH's from 5-7 produced high efficiencies that were equal to that of basic pH's, but the acidic pH's were only capable of resolving 3 of 6 standard proteins. The addition of an organic modifier also improved the resolving power. The best resolution among the standard proteins was obtained with an acetonitrile concentration of 20%(v/v). As the organic modifier was increased to 50%(v/v) the protein peaks began to converge to a single broad peak, while as it was lowered to 0% the protein peaks migrated with high efficiencies, but again had low resolution. Changes in the analyte-micelle (i.e. stationary phase) interaction with the modification of the run buffer (i.e mobile phase) was not unexpected. This is similar to that seen in reversed phase partition chromatography where the addition of an organic modifier to the mobile phase can be used to alter the selectivities (retention ratios) of the analytes. The final optimized MEKC buffer was 25 mM SDS, 10 mM sodium borate and 20% acetonitrile with a pH of 9.5. This buffer generated the highest efficiency separations and the best resolution for the standard proteins.

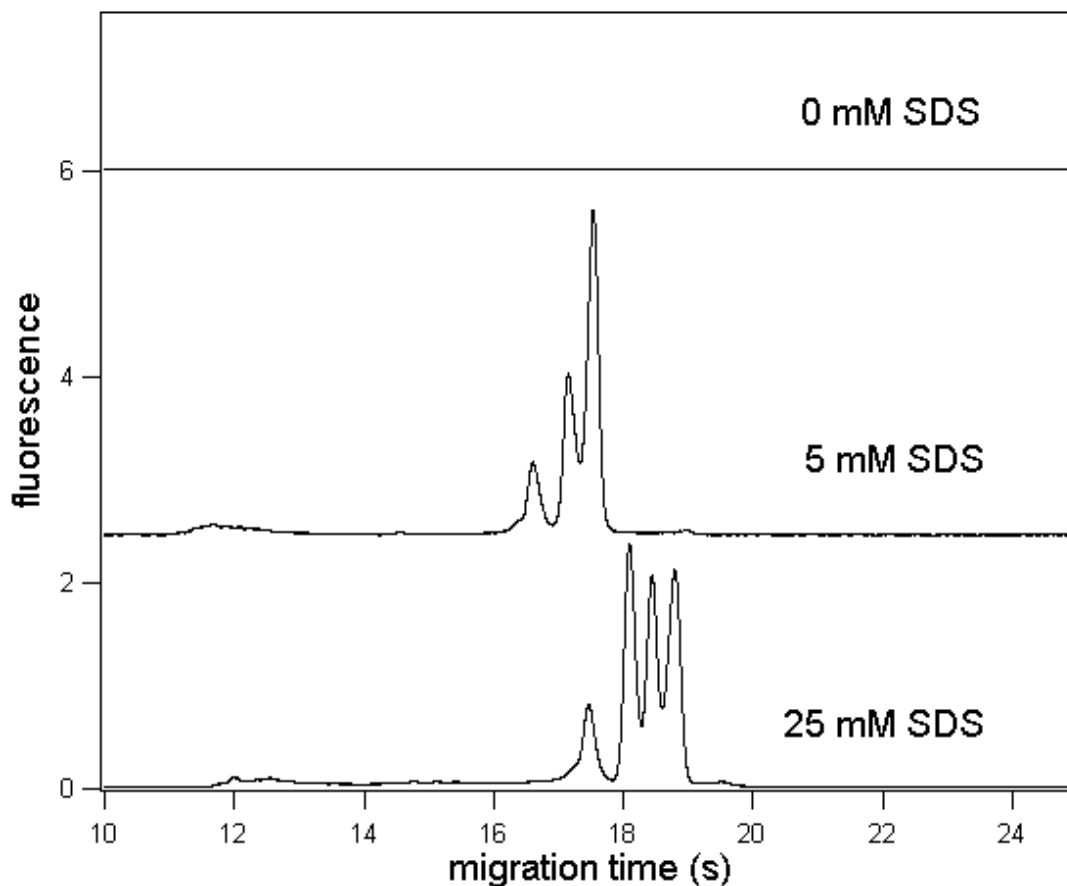


**Figure 6.1** Electropherograms of standard proteins; buffers: 0 mM SDS, 5 mM SDS, 25 mM SDS, all with 10 mM sodium borate and 20% ACN; analytes: cytochrome c, lysozyme, ribonuclease A and myoglobin in order of shortest to longest migration time, analytes diluted 1:100 from labeling cocktail; device: cross channel PDMS chip with a 4.0 cm separation channel detected at 2.5 cm, and a field strength of 650 V/cm.

In addition to the above buffer, other buffers that have been used for the successful MEKC separation of proteins in fused silica capillaries were also examined including 100 mM Tris-hydroxymethylaminoethane (TRIS) and 100 mM N-Cyclohexyl-2-aminoethanesulfonic acid (CHES) buffers.<sup>238</sup> These buffer systems provided poor separation efficiencies and resolution for the AlexaFluor labeled proteins on PDMS-based microfluidic devices. The field strength that

could be applied using these buffers was also substantially lower than the optimized MEKC buffer due to their high conductivities and resultant Joule heating.

### ***6.3.2 MEKC Separations of Proteins***

The optimized MEKC buffer described above significantly improved the protein separations on PDMS microfluidic devices and produced peak efficiencies that far exceed all reported values for protein separations produced previously in channels with native PDMS and PDMS-modified walls. For example, bovine serum albumin (BSA) is a non-selective adsorber on many materials, especially native PDMS. Using the MEKC buffer reported above BSA could be separated with a plate height of 0.38  $\mu\text{m}$ , corresponding to an efficiency of  $2.6 \times 10^6$  N/m, producing a Gaussian peak as shown in **Figure 6.2**. The run-to-run migration time reproducibility of the BSA separation was 0.9% with peak height reproducibilities of 1.5%. The high efficiency MEKC separations of BSA on PDMS are primarily the result of favorable electrostatic conditions that are established between the surface of the PDMS channel and the protein itself. These electrostatic conditions reduce any surface adsorption that may contribute to band broadening. The SDS adsorbs to the PDMS channel, as previously reported<sup>49, 216</sup>, imparting a large negative charge at the surface. In addition, SDS also adsorbs to the surface of proteins, modifying their overall charge and making them more negative. The repulsion force between the PDMS-SDS surface and the SDS-protein conjugate is likely a major contributing factor to the high efficiency separations. Other studies incorporating nonionic surfactants have been shown to be detrimental to the separation efficiency and resolution of analytes on PDMS devices.<sup>250</sup> For example, the use of Tween 20 was shown to increase the interaction of peptides with PDMS surfaces.

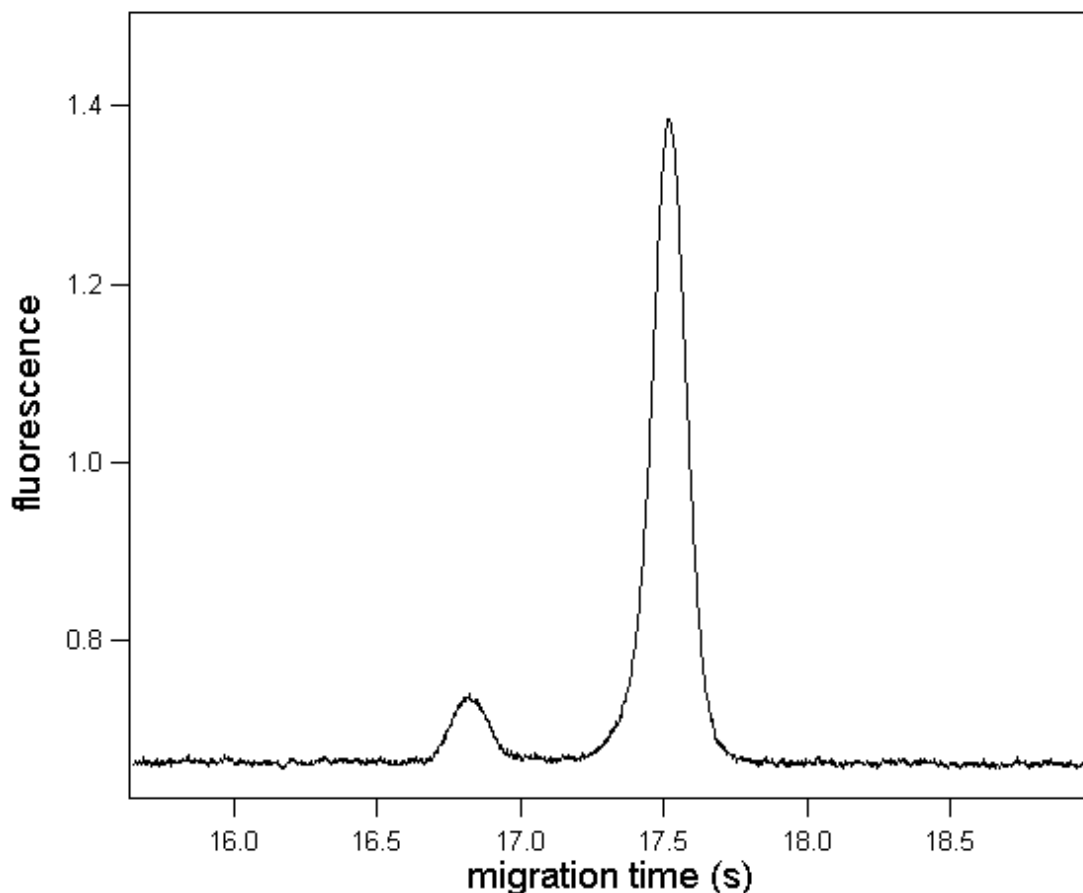


**Figure 6.2** Electropherogram of BSA-AF; buffer: 25 mM SDS, 10 mM sodium borate, 20% acetonitrile; analytes: BSA AlexaFluor 488 with 1:100 dilution from labeling cocktail; device: PDMS cross channel chip, field strength of 850 V/cm at a detection distance 3.0 cm. The minor peak located at 16.9 s is either a protein contaminate, or a result of an isomer of AlexaFluor 488.

Further electrophoretic separations of five standard proteins including cytochrome c, lysozyme, ribonuclease A, myoglobin, and  $\alpha$ -lactalbumin are shown in **Figure 6.3**. These separations used the optimized buffer with an electric field strength of 650 V/cm over a separation detection distance of 3.0 cm. Average separation efficiencies and standard deviations of the separation shown in figure 3 are listed on **Table 4**. The protein migration order was based upon the pI's of the proteins indicating that the separation mechanism was primarily charge based. Fast electrophoretic separations of six proteins, cytochrome c, lysozyme, ribonuclease A,

myoglobin, BSA, and  $\alpha$ -lactalbumin were also performed in  $< 10$  seconds as shown in **Figure 6.4**. The field strength for these separations was 1,200 V/cm and the separation distance was 2.0 cm. The separation efficiencies obtained using this method is significantly higher than any previously reported on PDMS or PDMS-modified devices.

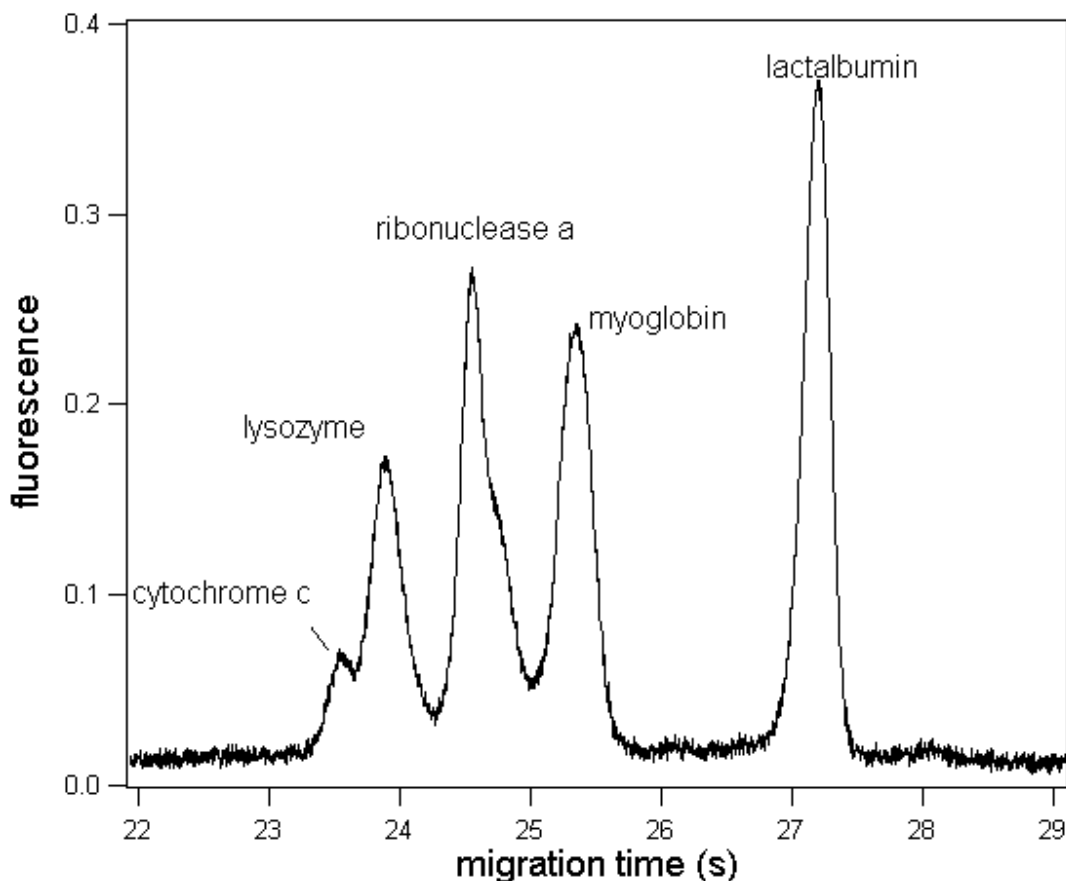


**Figure 6.3** Electropherogram of lysozyme, cytochrome c, myoglobin, ribonuclease A and  $\alpha$ -lactalbumin; buffer: 10 mM sodium borate, 25 mM SDS, and 20% acetonitrile; analytes: standard proteins diluted 1:100 from labeling cocktail; device: cross channel PDMS chip with a 4.0 cm PDMS separation channel detected at 3.0 cm with a field strength of 650 V/cm.

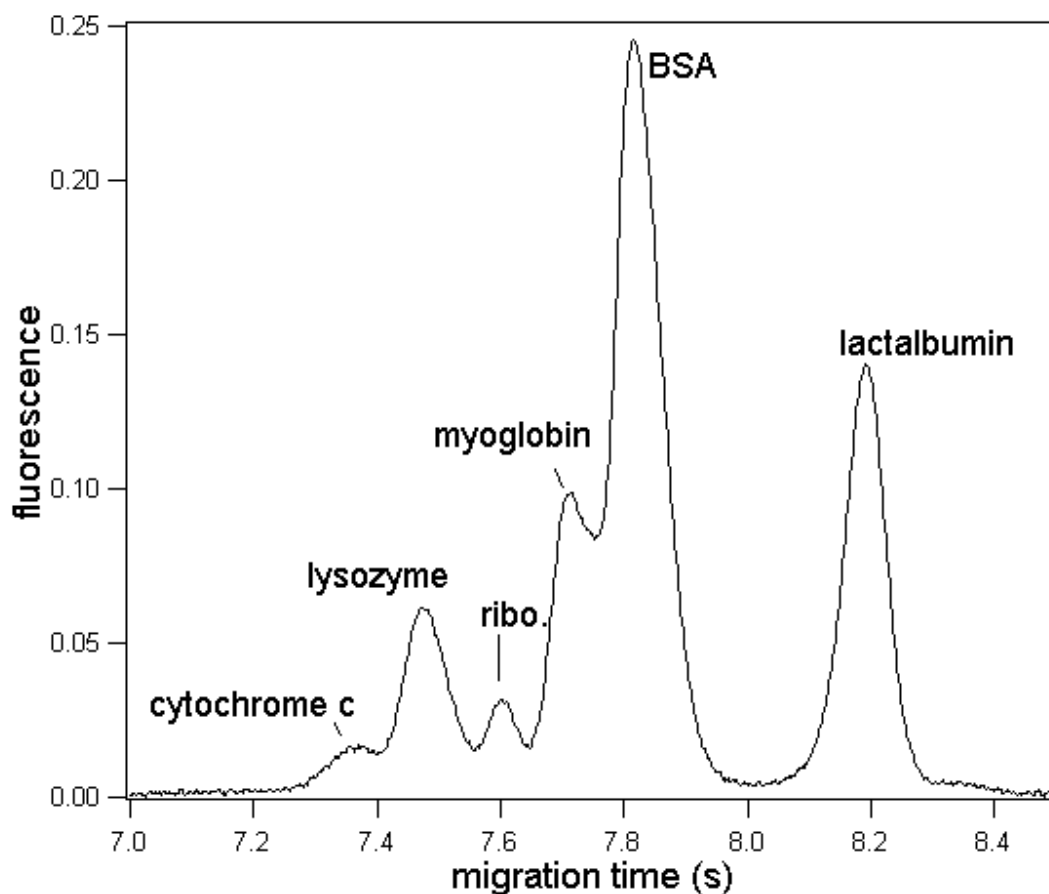


**Figure 6.4** Electropherogram of lysozyme, cytochrome c, myoglobin, ribonuclease A, BSA,  $\alpha$ -lactalbumin; buffer: 25 mM SDS, 10 mM sodium borate and 20% ACN; analytes: standard protein diluted 1:100 from labeling cocktail; device: cross channel PDMS chip with a 4.0 cm PDMS separation channel detected at 2.0 cm with a field strength of 1,200 V/cm.

Protein	N( $\pm$ Std. Dev.)	% RSD	N/s	H ( $\mu$ m)	N/m
Lysozyme	41,000 $\pm$ 800	<b>1.9</b>	2,320	<b>0.72</b>	<b>1.4 x 10<sup>6</sup></b>
Ribonuclease A	54,800 $\pm$ 500	<b>1.0</b>	3,000	<b>0.54</b>	<b>1.8 x 10<sup>6</sup></b>
Myoglobin	49,400 $\pm$ 900	<b>1.8</b>	2,655	<b>0.60</b>	<b>1.6 x 10<sup>6</sup></b>
$\alpha$ -Lactalbumin	41,900 $\pm$ 700	<b>1.7</b>	2,171	<b>0.72</b>	<b>1.3 x 10<sup>6</sup></b>
Cytochrome C	45,000 $\pm$ 800	<b>2.0</b>	2,500	<b>0.66</b>	<b>1.5 x 10<sup>6</sup></b>

**Table 4** Number of plates, standard deviation of the number of plates, plates per second, plate height, and plates per meter for proteins labeled with AlexaFluor 488 and separated on a 4.0 cm PDMS cross channel chip with a detection point of 3.0 cm using 25 mM SDS, 10 mM sodium borate and 20% ACN. The applied field strength was 650 V/cm.

### ***6.3.3 MEKC of Proteins on Serpentine Chip***

Peak capacity and resolution are important considerations for the effectiveness of MEKC separations on PDMS chips. To further improve the resolution among the standard protein mixture, a PDMS serpentine channel chip with a 30 cm separation channel was fabricated. Linear improvements were observed for the separation efficiency with increased separation distance, but no improvements were observed in resolution with increased separation distance after about 7 cm (**Figure 6.5**). This was an extremely reproducible phenomenon. The linear increase in separation efficiency with distance in **Figure 6.5** indicated that the turns of the serpentine chip did not have a detrimental effect on the separation, and therefore, should not have adversely affected the resolution. To our knowledge the effect of separation distance has never been investigated with MEKC-based protein separations. Whether the above results are a general phenomenon for MEKC-based protein separations or just confined to separations on PDMS devices remains to be seen.

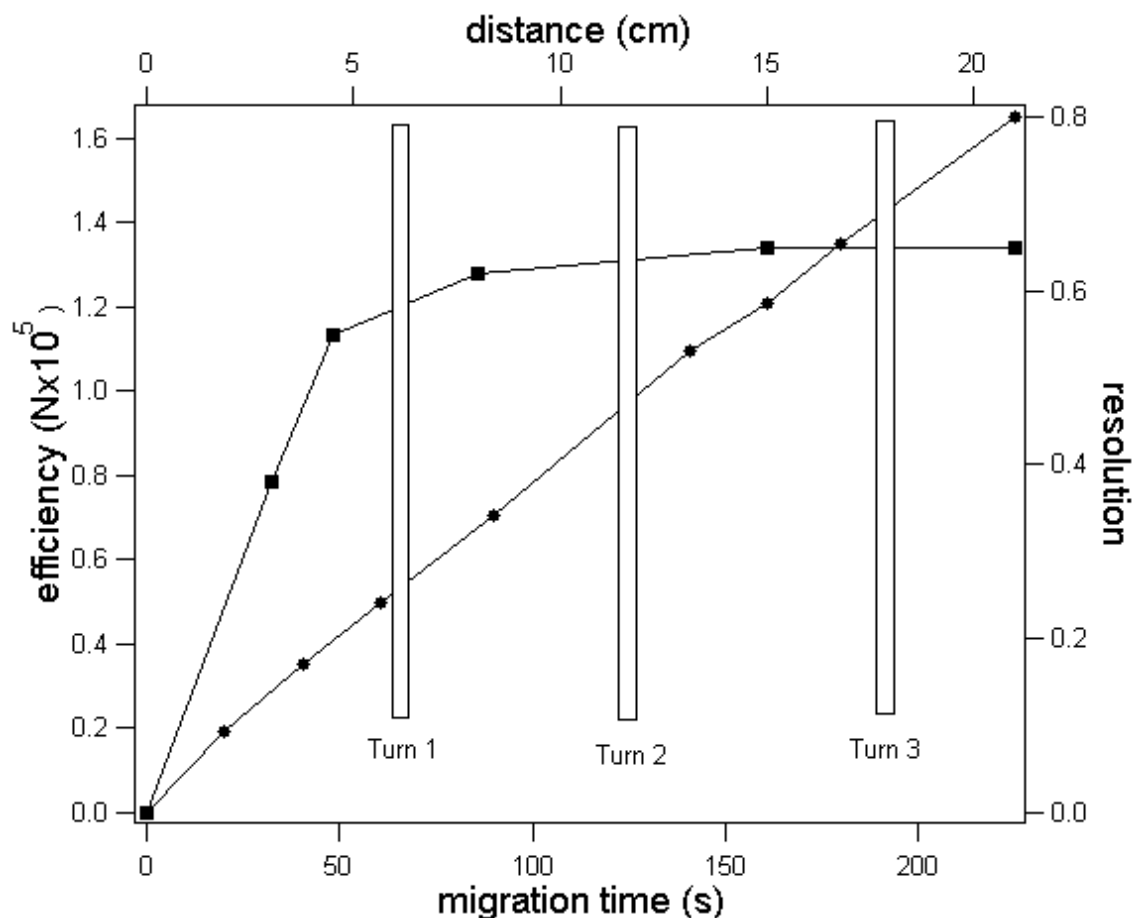


**Figure 6.5** Separation efficiency of BSA-AF and resolution between myoglobin-AF and BSA-AF as a function of both separation distance and time; buffer: 25 mM SDS, 10 mM sodium borate and 20% ACN; analytes: standard proteins diluted 1:100 from labeling cocktail; device, serpentine chip with field strength of 150 V/cm. Closed circles represent efficiency versus migration time. Closed squares represent resolution versus migration distance.

An *E. coli* metabolome homogenate consisting primarily of amines was separated using a PDMS serpentine chip. The molecular weight distribution of the homogenate was verified using molecular weight cutoff filters (MWCO). Additionally, standard diamines labeled with AlexaFluor 488 were comigrated with the *E. coli* homogenate to identify some of the peaks in the electropherogram. Efficiencies of the amines exceeded  $3.0 \times 10^6$  N/m and the resolution among the amines increased with the square root of the separation distance as expected.<sup>159</sup> The

same was seen for a variety of fluorescently labeled amino acids.<sup>159</sup> The *E. coli* metabolome homogenate was doped with lysozyme and  $\alpha$ -lactalbumin that were conjugated with AlexaFluor 488. Lysozyme and  $\alpha$ -lactalbumin were chosen because they represent the largest difference in pI values for our selection of standard proteins and would be indicative of the range in which the standard proteins would migrate. The pI difference between lysozyme and  $\alpha$ -lactalbumin is approximately 4.2 spanning from the basic lysozyme pI of 9.3 to the acidic  $\alpha$ -lactalbumin pI of 5.1. The separation efficiency of the two proteins increased linearly with separation distance, but the resolution reached a plateau after about 7 cm of separation distance. The poor resolving power of this separation method seems to be a result of the short migration time window as shown in **Figure 6.6**. This short time period limited the peak capacity to about 10-12 for the standard protein separations. These results in terms of the peak capacity are similar to previous capillary-based MEKC separations of proteins.<sup>248</sup>

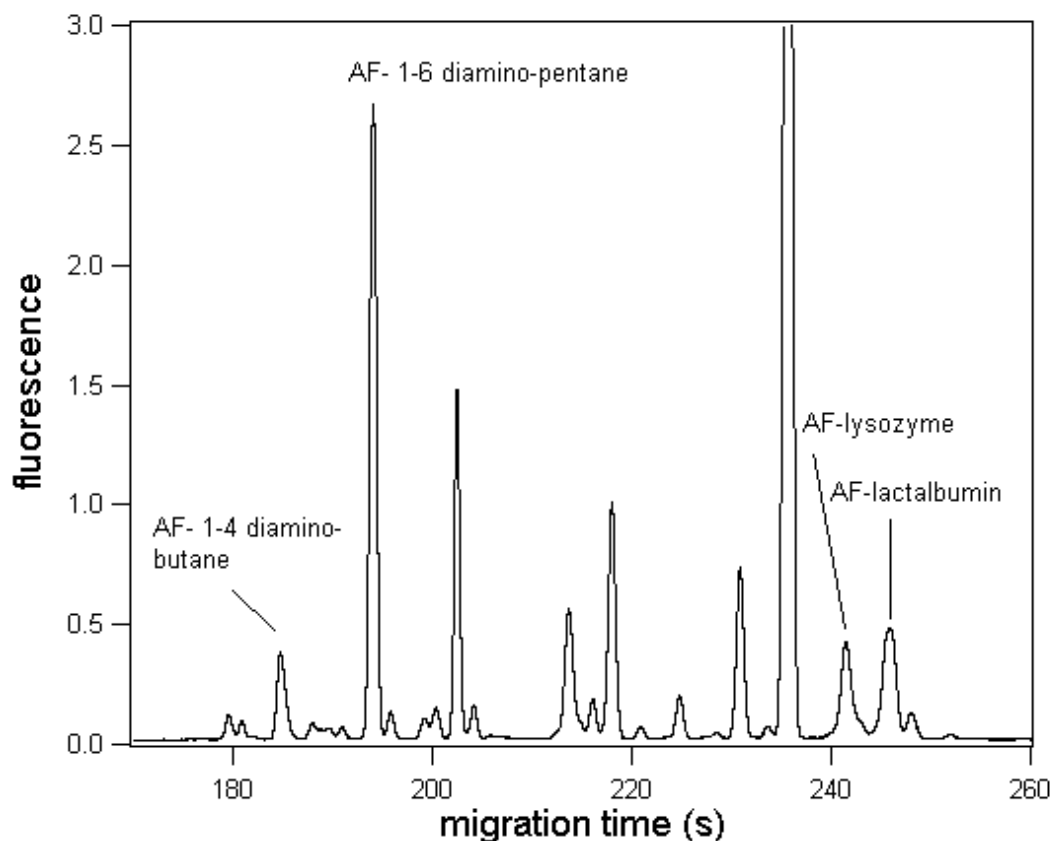


**Figure 6.6** Electropherogram of an *E. coli* homogenate of metabolic amines doped with internal protein standards of lysozyme-AF and  $\alpha$ -lactalbumin-AF that were diluted 1:100 from the labeling cocktail, device: serpentine chip with detection length of 25 cm; buffer: 25 mM SDS, 10 mM sodium borate and 20% ACN.

The late migration of the proteins in the separation window is indicative of a high retention factor for the proteins.<sup>251</sup> Attempts to lower the retention factor (i.e. the association of the SDS with the protein) by lowering the SDS concentration or increasing the organic additive resulted in lower resolution as discussed in section 3.1 above. The exact reason for this plateau in resolution after a few cm of separation is not clear at the present time, but we are further investigating this phenomenon.

## 6.4 Concluding remarks

We were successful in rapidly separating fluorescently labeled BSA, which is known to adsorb strongly to surfaces, and other fluorescently labeled standard proteins on PDMS-based microfluidic devices to efficiencies that have not been realized on native PDMS or modified PDMS microfluidic devices before. Although this method generates very fast separations and high efficiencies, improvements in the resolution among individual fluorescently labeled proteins did not increase with the square root of the separation distance as expected after the first few cm of separation.

## CHAPTER 7 - Amyloid Beta Peptide Separations

### 7.1 Introduction

Microfluidic devices using capillary electrophoresis (CE) were designed to monitor the real-time oligomerization of  $\beta$ -amyloid 1-40 (A $\beta$ 40) peptides. Glass microfluidic devices were fabricated using a simple cross channel design with a separation channel of 3.7 cm. Rapid CE separations were performed using a separation distance of 2 cm and a field strength of 200 V/cm. The separations were performed in a solution of 20% (v/v) trifluoroethanol (TFE) and 20 mM sodium phosphate at pH 7.4. CE separations performed using these conditions were capable of resolving several A $\beta$ 40 oligomers in < 80 s. The oligomeric species were identified using molecular weight cut-off filters. Time resolved CE separations demonstrate that the oligomerization from paranuclei to protofibrils increases over a 4 hr incubation period. The effects of two aggregation inhibitors, toluidine blue O and a novel synthetic product, CP2, were characterized for their efficiency to inhibit the formation of A $\beta$ 40 protofibrils.

Protein conformational abnormalities have been implicated in a wide variety of etiologically distinct diseases including Alzheimers disease, Parkinson's, Huntington's, senile systemic amyloidosis, prion encephalopathies, cystic fibrosis and type 2 diabetes.<sup>252</sup> A variety of misfolded proteins, implicated in the above diseases, have been demonstrated to oligomerize and precipitate within the extracellular or intracellular space causing cellular dysfunction and death.<sup>253</sup> In many protein conformational diseases it is still unclear whether the oligomerization that is followed by precipitation is causative or symptomatic. Nevertheless, developing methods

that reduce the oligomerization of misfolded proteins has the potential of further elucidating the pathogenesis of these diseases.<sup>254</sup>

Alzheimer's disease (AD) is a neurodegenerative disease that is characterized by the precipitation of  $\beta$ -amyloid (A $\beta$ ) peptides within the cerebral neuropil and vasculature.<sup>255</sup> A $\beta$  peptides are generated from the endoproteolysis of the amyloid precursor protein (APP). Proteolytic enzymes such as  $\alpha$ -secretase,  $\beta$ -secretase, and  $\gamma$ -secretase generate different alloforms of the  $\beta$ -amyloid peptides. The  $\alpha$ -secretase cleaves between residues 16 and 17 forming a non toxic peptide. The  $\beta$ -secretase and  $\gamma$ -secretase cleave between residues 596, 597, and 637, 638, or 639, respectively. The peptides generated from the  $\beta$  and  $\gamma$ -secretase are considered to be highly neurotoxic due to their ability to assemble into oligomers. The two primary alloforms generated by  $\beta$  and  $\gamma$ -secretase are A $\beta$ 40 and A $\beta$ 42, each consisting of 40 and 42 amino acid residues, respectively.<sup>256</sup> Both alloforms are normally found in the plasma and cerebrospinal fluid, although it has been shown that when the A $\beta$ 42/A $\beta$ 40 concentration ratio increases the likelihood of early onset AD increases.<sup>257, 258</sup> It is still unclear what physiological function, if any, the A $\beta$  peptide serves in normal cellular functions.

Structural studies of the A $\beta$  peptide have demonstrated that the physical properties of the solvent greatly affect the structure of the monomer peptide and consequently its aggregation properties.<sup>259</sup> Aqueous solvents induce primarily  $\beta$ -sheet content, whereas aqueous solvents with TFE or hexafluoroisopropanol (HFIP) induce  $\alpha$ -helix content.<sup>260</sup> Solvents that contain membrane mimicking molecules such as SDS and CTAB induce the A $\beta$  monomer to form  $\alpha$ -helices. It has been hypothesized that the oligomerization of the A $\beta$  peptide begins with an  $\alpha$ -helix seed followed by a random coil that forms  $\beta$ -sheet structures. The formation of  $\alpha$ -helix is primarily an intermolecular process, whereas the  $\beta$ -sheet formation is an intramolecular process

that is dependant upon the physical properties of the solution and the concentration of the peptide.<sup>260</sup> Changes in ionic strength and pH also change the conformation of the A $\beta$  monomer, and are thought to dramatically affect the oligomerization of the A $\beta$  peptides.

The oligomerization and assembly of A $\beta$ 40 and A $\beta$ 42 have been investigated *in vitro* using a number of techniques including: NMR<sup>261, 262</sup>, circular dichroism (CD)<sup>256, 260</sup>, fluorescence spectroscopy<sup>261</sup>, surface plasmon resonance (SPR)<sup>254</sup>, mass spectrometry<sup>263</sup>, capillary electrophoresis (CE)<sup>264</sup>, sodium dodecyl sulfate- polyacrylamide gel electrophoresis (SDS/PAGE)<sup>252, 256</sup>, size exclusion chromatography (SEC)<sup>256</sup>, dynamic light scattering (DLS)<sup>256</sup>, atomic force microscopy (AFM)<sup>252</sup> and electron microscopy<sup>264</sup>. These techniques have generated insights into the both the mechanism and kinetics of oligomerization<sup>256</sup>.

Several useful methods have been developed for monitoring the aggregation of A $\beta$  peptides in real-time including SEC, DLS, and PICUP-SDS-PAGE. Unfortunately there are several disadvantages that are associated with these techniques. SEC is useful for the real time analysis of the dimer, trimer and tetramer aggregates, but can not separate higher molecular weight oligomers quantitatively. PICUP-SDS-PAGE was demonstrated to polymerize A $\beta$  oligomers, forming covalent bonds between peptides, allowing the use of SDS-PAGE for size analysis. PICUP-SDS-PAGE is good at quantifying oligomers smaller than the pentamer, but is inefficient in polymerizing larger aggregates such as the dodecamer. DLS is capable of monitoring in real time the formation of large oligomers greater than 40 kD in size, but polydisperse solutions make quantitative analysis very difficult to impossible. In addition to the size limitations of each technique they also suffer from high detection limits, long analysis time, and low throughput.

Quantitative methods are needed that have the ability to monitor both the protofibrils with molecular weight greater than 50 kD and paranuclei with molecular weights less than 50 kD. An ideal method will combine sensitivity, high throughput, and rapid analysis. A convenient method of monitoring the oligomerization of low concentration peptides and proteins is capillary electrophoresis using laser induced fluorescence detection (CE-LIF). Detection limits for LIF have been demonstrated to be as low as 10 pM. CE-LIF can also be performed on microfluidic devices which have several advantages over conventional scale chemical instrumentation. Microfluidic devices have the capability of integrating multiple chemical processing steps within a channel manifold. The chemical manipulations can be performed in series or parallel and several different types of chemical processing and handling steps have been demonstrated including mixing, reactions, filtering, preconcentration and separations.<sup>33, 199-203</sup> Several of these processing and handling steps have been integrated to generate devices capable of performing complete chemical analyses.<sup>33, 201, 265-267</sup> Microfluidic devices have great potential for analyzing protein conformational diseases. Moreover, microfluidic platforms have the potential of combining on-chip cell culture reactors with the analysis and separation of oligomeric species, allowing for the design of experiments that have sensitivity, time-resolution and throughput that can not be performed with conventional techniques.

The first step in implementing microfluidic devices for A $\beta$  analysis is demonstrating that A $\beta$  peptides can be manipulated and analyzed on a microfluidic device. We demonstrate the ability to separate several different oligomeric species of A $\beta$  peptides on a microfluidic device using rapid CE-LIF. Separations were completed in < 80 s and were capable of monitoring in real time the oligomerization of A $\beta$  peptides from paranuclei to protofibrils. MWCO filters were used to differentiate the oligomers in the electropherogram. In addition to analyzing the real time

oligomerization of A $\beta$ 40 peptides we also examined the effect of several drugs on the inhibition of the A $\beta$ 40 oligomerization. We monitored the efficiency of these molecules to inhibit the oligomerization of the paranuclei to form protofibrils.

## **7.2 Materials and methods**

### ***7.2.1 Reagents***

Trifluoroethanol and sodium phosphate was purchased from Sigma Aldrich (St. Louis, MO). *Toluidine blue O (TBO)* was obtained from X. All of the chemicals were used as received. All solutions were made using distilled, deionized water from a Barnstead Nanopure System (Dubuque, IA) and then filtered through 0.45  $\mu$ m Acrodiscs (Gelman Sciences; Ann Arbor, MI).

### ***7.2.2 Peptide and CP2 Synthesis***

A $\beta$ 1-40 was synthesized at the Kansas State University Department of Biochemistry and was labeled with tetramethyl rhodamine (TAMRA) obtained from molecular probes (Eugene, OR). CP2 was synthesized using previously published results by Duy Hua et al.

### ***7.2.3 Microchip Fabrication***

Photomasks were generated by The Photoplot Store (Colorado Springs, CO) at 40,000 dpi using a photoplotting process. The mask designs were created in AutoCAD2000LT (Thomson Learning; Albany, NY) and sent to The Photoplot Store for translation and fabrication. The schematics of the microchips used in this study is shown in **Figure 7.1**. The fabrication of glass microfluidic devices has been described elsewhere. Briefly, microchips were fabricated from soda-lime photomask blanks (Telic Co.; Santa Monica, CA). The photomask blanks were patterned using the photomasks followed by exposure to UV light using a flood

exposure system (ThermoOriel; Stratford, CT). The exposed plate was developed using Microposit Developer (Shipley Co., Marlborough, MA) and Chrome Mask Etchant (Transene, Co.; Danvers, MA). The exposed glass was wet chemically etched using a buffered oxide etchant and the remaining photoresist was removed by immersing the plate in a stirred solution of Chrome Mask Etchant. Access holes were mechanically drilled into cover plates and cut prior to bonding. The glass slides were next bonded using previously reported procedures.X Cylindrical glass reservoirs (~140  $\mu$ L capacity) were attached using Epo-tek 353ND Epoxy (Epoxy Technologies, Inc.; Billerica, MA) where the access holes were located.

#### ***7.2.4 A $\beta$ 40 Sample Preparation:***

A $\beta$ 40 was synthesized and dissolved in 100 mM sodium bicarbonate at pH 10.5 to an A $\beta$ 40 concentration of 10  $\mu$ M. This mixture was then placed in 100  $\mu$ L aliquots in eppendorf tubes and frozen at -10°C. This step was performed to ensure no freeze-melt cycles which can cause premature peptide aggregation. The samples were then dissolved in 900  $\mu$ L of 20 mM sodium phosphate buffer and 20% (v/v) of TFE. After dissolving the peptides in the run buffer a series of sonication and centrifugation steps were performed to reduce the amount of oligomerized A $\beta$ 40 peptides. The peptides were sonicated in an ultrasonic bath for 5 min, followed by a centrifugation for 10 min at 10,000 g. The sample was immediately loaded onto the microfluidic device and separated.

#### ***7.2.5 Microchip preparation:***

The glass microchips were initially treated with methanol and 1 mM NaOH to remove any debris that may have adhered to the channels. This treatment also serves to ensure that the zeta potential is the same for each run, ensuring that the EOF and the migration times are

reproducible. We found that ensuring minimal buffer evaporation was critical for reproducible migration times of the peptides. This was accomplished by applying a 1 cm x 1 cm x 0.2 cm piece of adhesive PDMS to the reservoir. A 20 gauge needle was used to vent the top of the reservoir so no pressure heads developed.

### ***7.2.6 Separation and detection:***

The CE separations and LIF detection were performed with equipment that was similar to that previously described.<sup>159</sup> The separations and gated injections<sup>117</sup> were performed using three independent and remotely programmable high voltage (0-10 kV) power sources from EMCO (Sutter Creek, CA). The proper potentials to apply at each reservoir were determined using Kirchhoff's rules and Ohm's Law.<sup>118</sup> The injection times were 0.02 s.

## **7.3 Results and Discussion**

### ***7.3.1 A $\beta$ 40 CE Separation:***

The microfluidic device was prepared and loaded with A $\beta$ 40 peptides as described in the experimental section 2.3-2.4. The glass cleaning protocol served to remove any debris or contaminants from the glass channels that may contribute to deviations in the electroosmotic flow (EOF). This study used three microfluidic devices, shown in **Figure 7.1**, that were of identical dimensions. For all the separations an electric field of 200 V/cm and separation detection length of 2.0 cm was used. The aggregation of the A $\beta$  peptide was not affected by field strengths of up to 500 V/cm, but at elevated field strengths > 600 V/cm solvent evaporation within the channels due to Joule heating was observed. The sample was loaded into the microfluidic chip immediately after supernatant withdrawal ( $t_0$ ) and was continuously separated

over a period of 4 hrs. Over this time period we did not observe significant drifts in migration time of the monomeric peaks that could be due to adhesion of A $\beta$ 40 peptides to the capillary sidewalls. Adhesion of the peptides to the sidewalls of the capillary will cause a change in zeta potential and consequently change the EOF. Since TFE has a relatively high vapor pressure (b.p. 78°C) it was critical to minimize the solvent evaporation from the microfluidic reservoirs. Without special precautions, described in experimental section 2.4, migration times would vary 30-40% over 4 hrs primarily because of changes in the ionic strength of the buffer. Additionally, since the peptide conformation is dependent upon the ionic strength of the solution and pH it is likely that changes in conformation, and hence aggregation would occur if the solvent content were to change. Sealed reservoirs with needle vents provided migration time reproducibilities of 4.5%, as described in the experimental section 2.4.

A representative electropherogram for the CE separation of A $\beta$ 40 is shown in **Figure 7.2**. The electropherogram consists of several different oligomers ranging from the trimer and tetramer to large aggregates with MW > 50,000. The two oligomeric species that are separated to the highest resolution are the protofibrils with MW > 50,000 and paranuclei with MW < 30,000. In **Figure 7.2** the protofibrils have a migration time of 78 s, while the paranuclei with MW < 30,000 have a migration time of under 40 s.

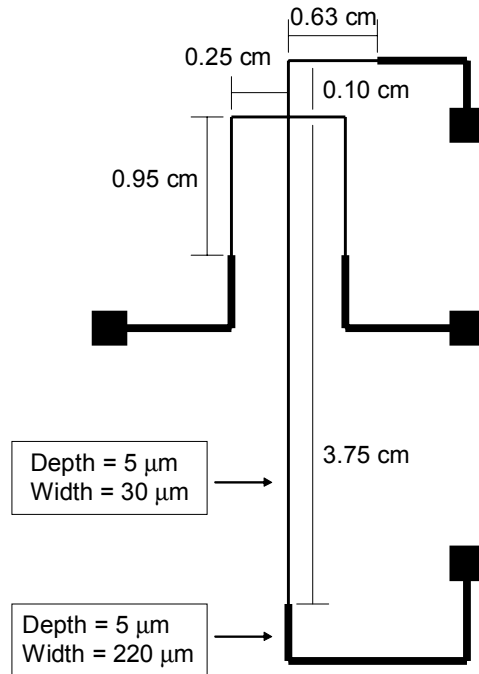


**Figure 7.1** Schematic of Cross Chip used for A $\beta$ 40 peptide separations. The chip is fabricated using the glass etching and bonding protocols listed in the experimental section.

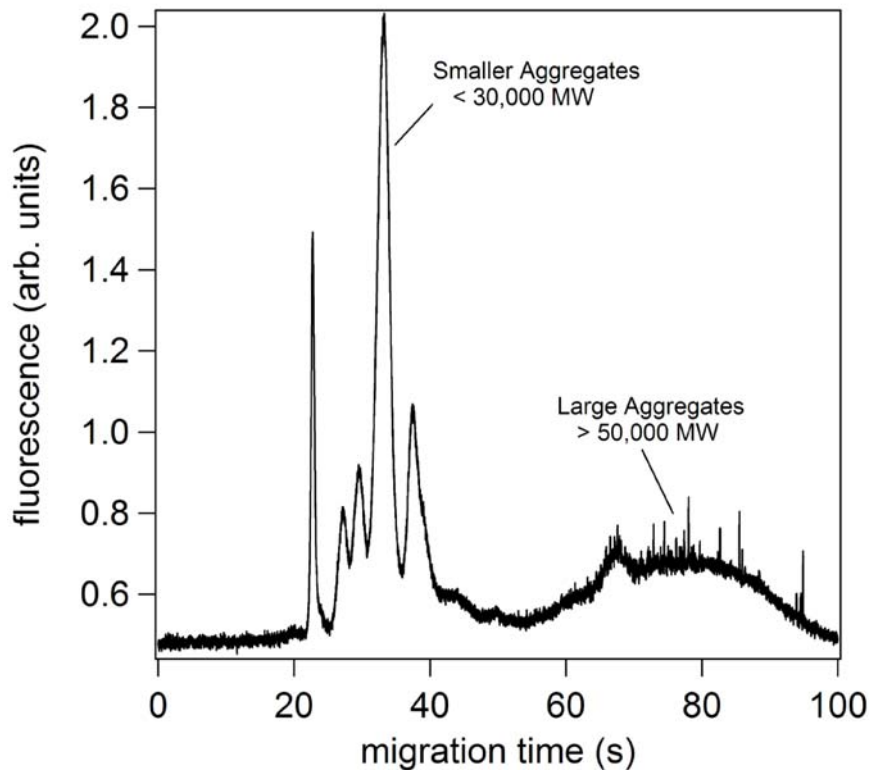


**Figure 7.2** An electropherogram of A $\beta$ 40 generated using glass microfluidic device. Device: cross channel glass chip with 2.0 cm separation distance and applied electric field of 200 V/cm; buffer: 20% TFE and 20 mM sodium phosphate buffer at pH 7.4; sample, 1  $\mu$ M A $\beta$ 40 peptides.

### ***7.3.2 Real Time monitoring of A $\beta$ 40 Aggregation:***

The oligomerization and assembly of the A $\beta$ 40 peptides to tetramers, dodecamers and protofibrils was monitored over a period of 4 hrs using microfluidic devices. Significant oligomerization of the A $\beta$ 40 peptide could be detected after 1.5 hrs. Molecular weight cut-off (MWCO) filters were used to identify the oligomeric species in the electropherogram and is shown in **Figure 7.3**. Since the TFE in solution slows the oligomerization rate the MWCO filters could be used to separate oligomers before they could react through an equilibration pathway.

Time resolved studies of the oligomerization of the A $\beta$ 40 peptides, shown in **Figure 7.4**, revealed that the protofibrils increased with time.

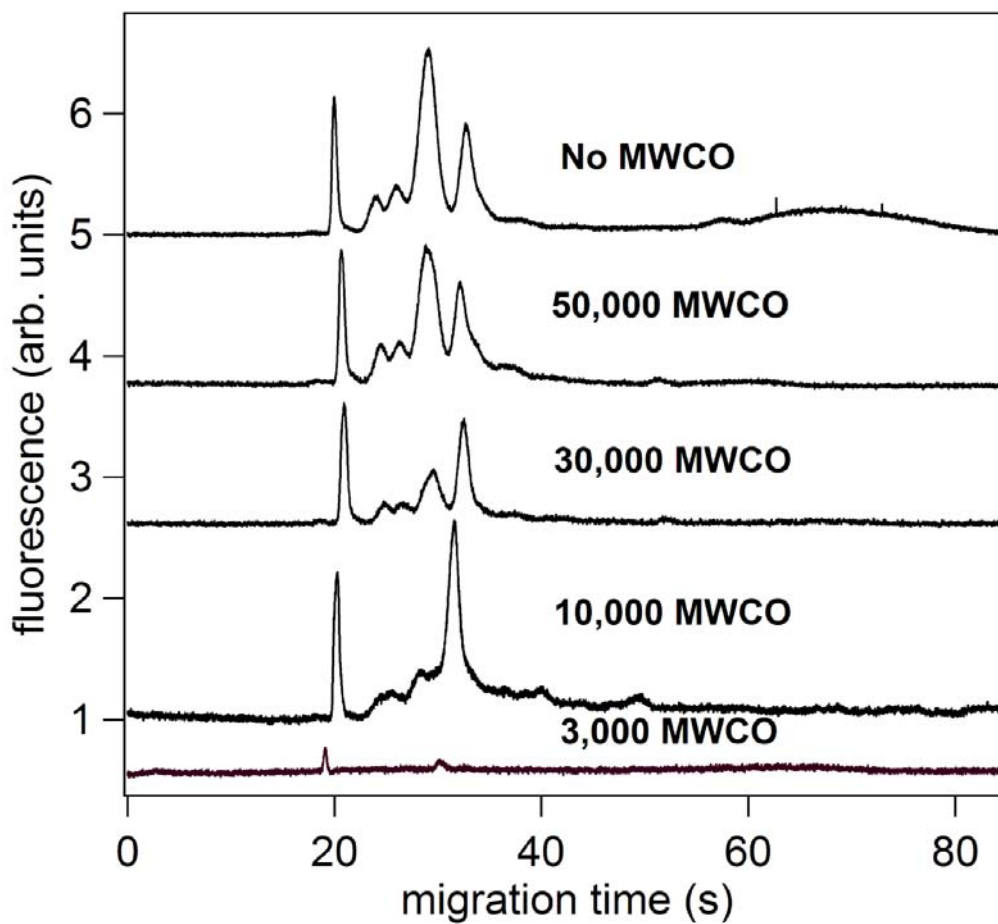


**Figure 7.3** A series of electropherograms of Aβ40 filtered with MWCO filters to isolate specific oligomers. Device: cross channel glass chip with 2.0 cm separation distance and applied electric field of 200 V/cm; buffer: 20% TFE and 20 mM sodium phosphate buffer at pH 7.4; sample, 1 μM Aβ40 peptides.

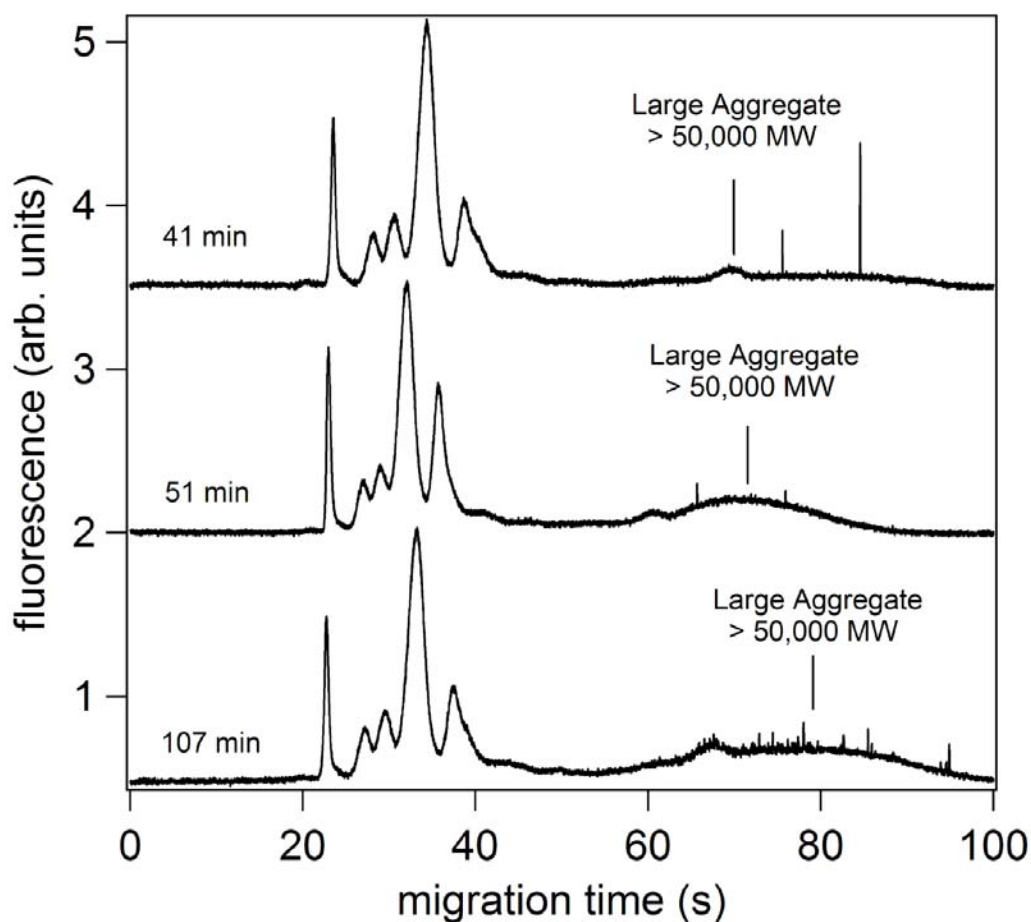


**Figure 7.4** A series of electropherograms of A $\beta$ 40 separated continuously over 3 hrs to monitor the formation of larger aggregates. Device: cross channel glass chip with 2.0 cm separation distance and applied electric field of 200 V/cm; buffer: 20% TFE and 20 mM sodium phosphate buffer at pH 7.4; sample, 1  $\mu$ M A $\beta$ 40 peptides.

### 7.3.3 Monitoring of Aggregation Inhibitors

We used two different inhibitors of A $\beta$ 40 oligomerization, Toluidine blue O and a novel synthetic product CP2. Toluidine blue O is known to inhibit the oligomerization of A $\beta$  peptides. This molecule also has an absorbance max near 488 nm, and an emission max near 520 nm, so it can be monitored with our LIF detection scheme. CP2 also has been demonstrated to reduce the aggregation of A $\beta$ 40 peptides.

**Figure 7.5** shows the reaction between Toluidine blue O and A $\beta$ 40 over a period of 300 min. Initially, the Toluidine blue O peak can be observed at 15 s. Over time this peak diminishes as it continues to react with the A $\beta$ 40 oligomers. Likewise the large aggregates slowly diminish with time.

CP2 a novel synthetic product was also analyzed for its effectiveness for reducing the aggregation of the A $\beta$ 40 aggregates. CP2 appears to be much more reactive than Toluidine blue O as initially there are no protofibrils, shown in **Figure 7.6**.

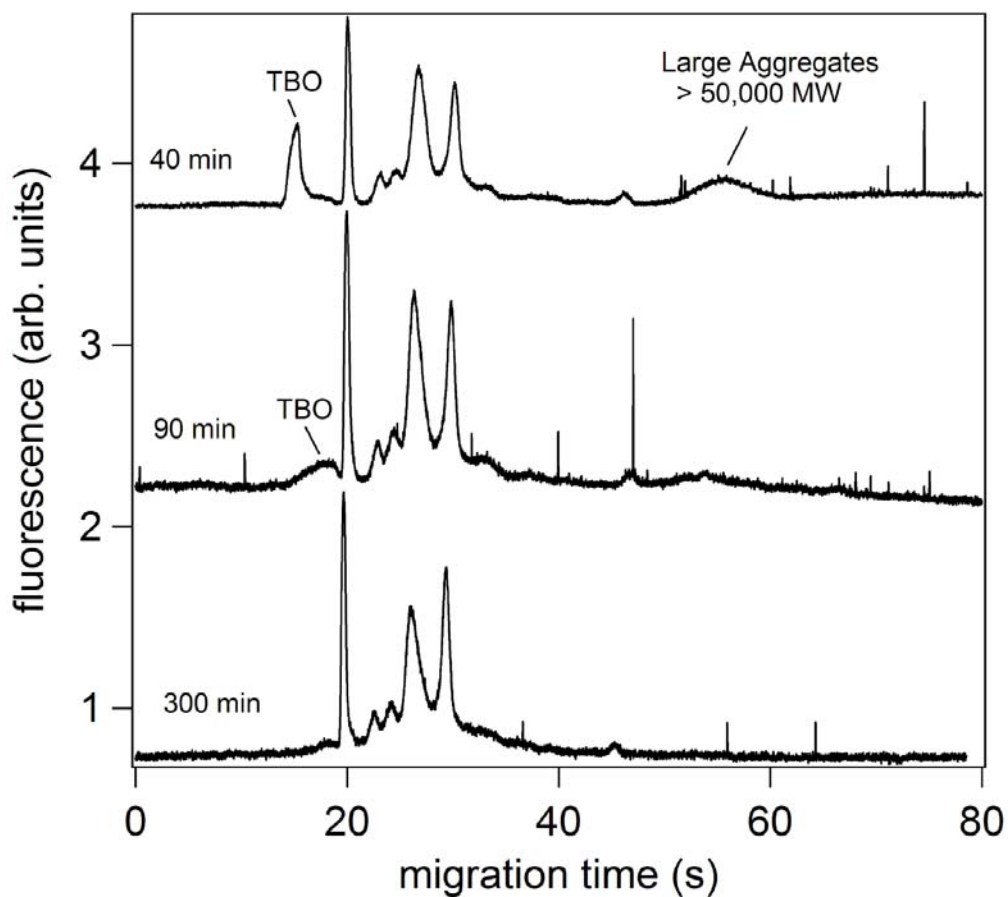


**Figure 7.5** A series of electropherograms of A $\beta$ 40 separated continuously over 3 hrs with the presence of toluidine blue O. Device: cross channel glass chip with 2.0 cm separation distance and applied electric field of 200 V/cm; buffer: 20% TFE and 20 mM sodium phosphate buffer at pH 7.4; sample, 1  $\mu$ M A $\beta$ 40 peptides and 1  $\mu$ M toluidine blue O.

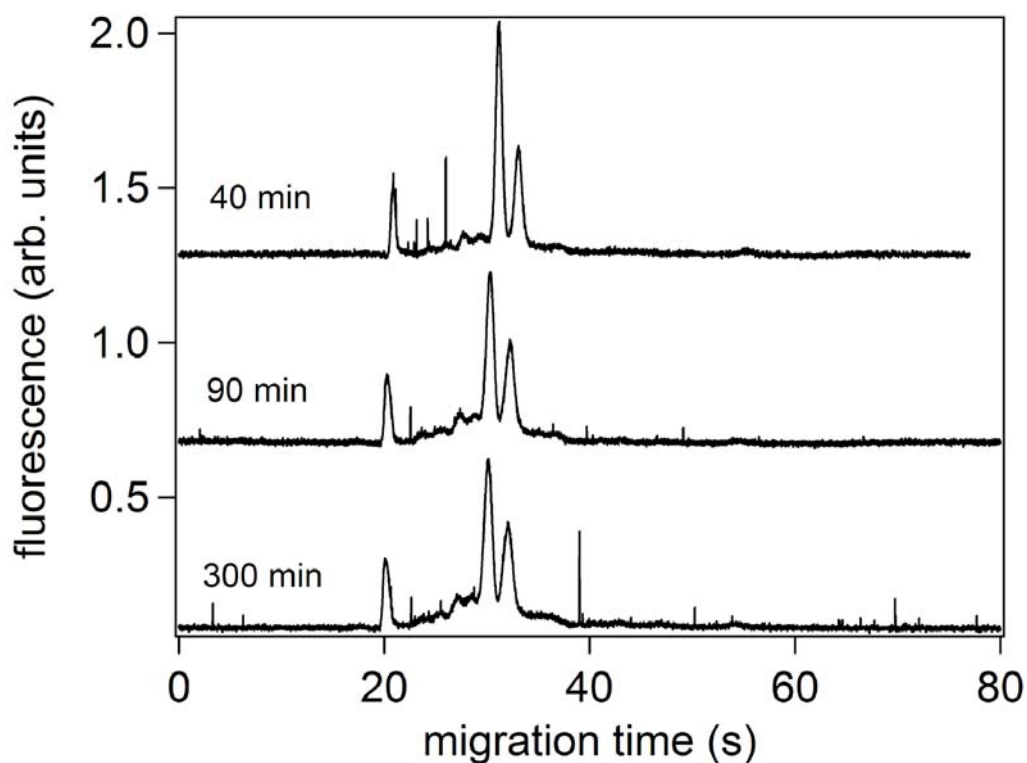


**Figure 7.6** A series of electropherograms of A $\beta$ 40 separated continuously over 3 hrs with the presence of CP2, a novel synthetic inhibitor. Device: cross channel glass chip with 2.0 cm separation distance and applied electric field of 200 V/cm; buffer: 20% TFE and 20 mM sodium phosphate buffer at pH 7.4; sample, 1  $\mu$ M A $\beta$ 40 peptides, and 1  $\mu$ M CP2.

## 7.4 Conclusion

We have demonstrated the ability to perform rapid capillary electrophoresis separations on a microfluidic device that allows for the real time analysis of the oligomerization of A $\beta$  peptides. This technique can be used to analyze the effectiveness of a wide variety of pharmaceutical drugs on the inhibition of the aggregation of A $\beta$  peptides.

# **CHAPTER 8 - Sol-Gel Membranes for Preconcentration, Separation, Purification and Novel Sensors**

## **8.1 Introduction to Sol-Gel Patterning of Membranes**

Sol-gel chemistry has proven to be extremely versatile in a number of fields including optics, electronics, catalysis, sorption, chemical sensing, and chemical separation. The versatility of sol-gel chemistry primarily stems from the wide variety of different materials that can be synthesized using different metal alkoxide precursors and the ability to impart within these materials desirable physical properties such as high surface area, low density, thermal stability, and transparency.<sup>268</sup> In this communication we demonstrate the use of sol-gel chemistry to fabricate transition metal (Ti, Zr) oxide membranes within microfluidic manifolds and their use for specific chemical manipulations on-chip. Coupling both versatile sol-gel membranes with microfluidic devices will further diversify the number of chemical and physical manipulations that can be performed on such hybrid devices.

Microfluidic devices were originally developed to sample small volumes, but over the last decade they have evolved into complex multifaceted devices that integrate multiple chemical processing steps within a single channel manifold. Several different types of chemical processing and handling steps have been demonstrated including mixing, reactions, filtering, preconcentration and separations.<sup>33, 269</sup> These processing and handling steps have been integrated with on-chip waveguides, lasers and photodiodes to generate devices capable of performing complete chemical analysis.<sup>270, 271</sup> An important chemical processing step in microfluidic devices

is the ability to perform concentration enrichment of analytes for downstream analytical detection.

Several examples of microchip concentration enrichment have been demonstrated. These examples include field amplified sample stacking (FAS), isotachopheresis (ITP), electrokinetic trapping, micellar sweeping, chromatographic preconcentration and membrane preconcentration. In previous microfluidic membrane preconcentration studies the microfluidic devices have been fabricated using multilayer lithography. This technique involves sandwiching a track etched nanoporous polycarbonate membrane between two layers of poly(dimethylsiloxane) (PDMS).<sup>272,</sup>  
<sup>273</sup> This fabrication technique suffers from some disadvantages including: a) inefficient bonding between lithographic layers that produces leaks between the two PDMS layers, b) chemical systems must be compatible with polymer microfluidics, and c) the devices are constrained to specific geometrical configurations which lead to unwanted variations in transport phenomena. Other than multilayer lithography several patterning techniques using microfluidic laminar flow have been developed which allow for the generation of structures within microfluidic devices.<sup>83</sup> Zhao et al. have demonstrated the synthesis of nylon membranes using laminar flow within microfluidic devices<sup>274</sup> and Song et al. have demonstrated a laser patterned membrane<sup>275</sup>, but to date there have been no reports demonstrating the fabrication of nanoporous membranes on microfluidic devices using sol-gel chemistry. The chemical flexibility of sol-gel processing has the potential to generate a vast number of different membranes for specific physical processes.

## **8.2 Theory of Ion Depletion and Enrichment in Nanochannels**

A number of researchers over the past five years have begun to use nanofluidics for a variety of analytical functions, some of them are just beginning to be realized such as preconcentration, injection and conduction measurements. Liu, Sweedler and Bohn have

extensively modeled and mathematically described nanofluidic channels.<sup>276,277</sup> Sharong Liu modeled the ionic flux of a nanochannel and found that both positive and negative ions are depleted from one side of the nanochannel, whereas on the opposite side of the nanochannel both positive and negative ions are enriched.<sup>278</sup> The ion enrichment and depletion effects of a nanochannel depend heavily on the double layer overlap generated when the diameter of a nanochannel is less than twice the thickness of the double layer generated at a surface. From the Gouy-Chapman model the double layer thickness depends on the concentration of the electrolyte and typically ranges from 300 nm to 3 nm for electrolyte concentrations of  $10^{-6}$  M to  $10^{-2}$  M, respectively; thus, channels with diameters less than 400 nm can demonstrate the effects of ion depletion and enrichment for low concentration electrolytes.

The question remains why both cations and anions are enriched and depleted on the same side of the membrane. The answer lies in both the electric double layer overlap and inequalities between ion fluxes. Generally when the electric double layer overlaps within a nanochannel the ionic content will be dominated by either cations or anions depending on the surface charge of the channel. For instance, consider a silica nanocapillary at pH 7. The concentration of cations will be dramatically greater than the concentration of anions within the nanocapillary. A mathematical relation for this is:  $[A^+] = \alpha[B^-]$  where  $\alpha$  is greater than 1. Next the flux of ions through the nanochannel is different for cations and anions. For instance, the flux of positive ions through the nanochannel is greater than the flux of positive ions through the microchannel. The result is an accumulation of cations near the cathode. The flux of the negative ions is faster through the microchannels, and slower through the nanochannel, the difference results in a depletion near the anode and an enrichment near the cathode. This series of ion fluxes is illustrated in **Figure 8.1**, below.

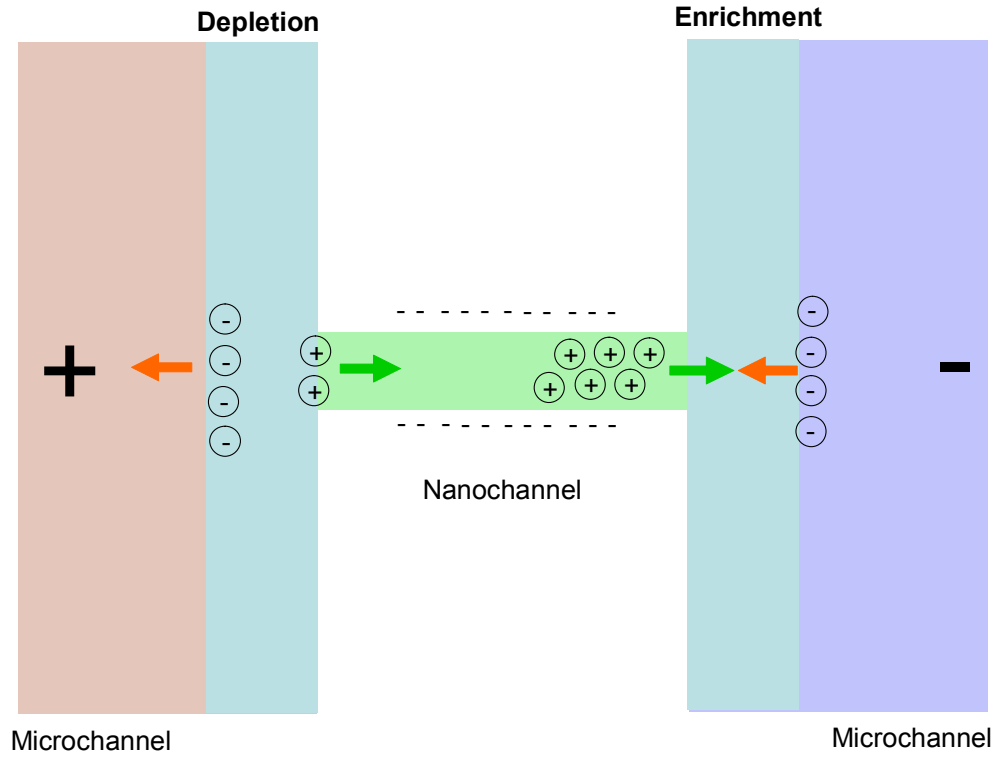


**Figure 8.1** Green arrows indicate the movement of cations, whereas orange arrows indicate the movement of anions through the nanochannel circuit.

Sharong Liu has modeled the flux of ions in a nanochannel using the following equations E.33-E.42.<sup>277, 278</sup> E.33 and E.34 describe the ion enrichment factor ( $E_F$ ) and the ion depletion factor ( $D_F$ ), where  $C_F$  and  $C_I$  are the concentration of the ions initially and finally.

$$E.33 : E_F = \frac{C_F - C_I}{C_I}$$

$$E.34 : D_F = \frac{C_I - C_F}{C_F}$$

In addition to the enrichment factors the ion flux ( $J$ ) was modeled using equations E.35 through E.38, where  $E$  is the electric field,  $S$  is the cross sectional area,  $A$  or  $B$  is the ion, and  $\mu$  is the mobility of each respective ion. The flux was modeled on each end of the nanochannel. For

instance, the depletion and enrichment of ions A and B were modeled on both sides of the nanochannel. Each side will be designated C for the cathodic end, and n for the anodic end. The derivation of these equations originates from  $v = E\mu$ .

$$E.35: J_C^A = E_C \cdot S_C \cdot \mu_A \cdot [A]_C$$

$$E.36: J_C^B = -E_C \cdot S_C \cdot \mu_B \cdot [B]_C$$

$$E.37: J_n^A = E_n \cdot S_n \cdot \mu_A \cdot [A]_n$$

$$E.38: J_n^B = -E_n \cdot S_n \cdot \mu_B \cdot [B]_n$$

As we have seen previously Kirchoff's law can be applied to the flux on either end of the channel to generate the relation in E.39.

$$E.39: J_1^A - J_1^B = J_n^A - J_n^B$$

Using E.39 and equations E.35-E.38 it is possible to model the movement of ions from one side of the channel to the other. Liu has also demonstrated that nanochannels can be used as proton pumps.<sup>277</sup>

### 8.3 Experimental

We have developed a robust and inexpensive method of patterning transition metal (Ti or Zr) oxide nanoporous membranes within microfluidic manifolds without using multilayer soft lithography. Laminar flow within microfluidic channels was used to transport transition metal alkoxides and water to a liquid-liquid interface where an interfacial sol-gel reaction was performed to fabricate a nanoporous membrane within a glass microfluidic manifold. Due to the nanoporous nature of the membrane it was possible to generate a charge depletion zone within a microfluidic channel that could consequently be used for electrokinetic trapping of small molecules, proteins and particles. This sol-gel membrane patterning method has the potential of

generating many different types of membranes that could be used for a wide variety of applications. These membranes are facile to fabricate and avoid several of the disadvantages associated with multilayer membrane microfluidic devices. In addition, the membranes can be synthesized with a wide number of chemical functionalities and physical properties due to the versatility of sol-gel processing.

High aspect ratio titania membranes with widths of 4-26  $\mu\text{m}$ , lengths of 15-500  $\mu\text{m}$  and depths of 20  $\mu\text{m}$  were fabricated in microfluidic devices using laminar flow (**Figure 8.2, 8.3**). A solution of 25% (v/v) titanium isopropoxide with isopropanol was prepared immediately prior to membrane fabrication. Depending on the desired membrane width a second solution of  $[\text{H}_2\text{O}]$  between 10-90% (v/v) isopropanol was constituted. The  $[\text{H}_2\text{O}]$  in the sol-gel reaction was the most effective method of modifying the width of the membrane. A linear range from 4-26  $\mu\text{m}$  wide membranes corresponded to  $[\text{H}_2\text{O}]$  between 10-90%. Other experimental variables included fluid velocity and reaction time which were held constant. The microchip was initially filled with neat dry isopropanol and laminar flow was established by applying an absolute pressure of 85 kPa to the microchip. Once laminar flow was established the 25% solution of titanium isopropoxide was inserted into one of the reaction reservoirs. After the titanium isopropoxide was added, the variable water-isopropanol solution was added to the second reaction reservoir. After both reactants had been added to the microchip reservoirs the interfacial sol-gel reaction was allowed to proceed for 5 min. The ambient conditions were 20% relative humidity and 23°C. After the reaction was complete the reservoirs were flushed with neat isopropanol for approximately 10 min followed by rinsing the channel with 80 mM sodium phosphate at a pH of 11.5 for approximately 10 min. The microchip was allowed to sit at room temperature for 24 hrs prior to use in preconcentration experiments. Identical conditions were used for fabricating

zirconia membranes with the exception of using zirconium isopropoxide rather than titanium isopropoxide.

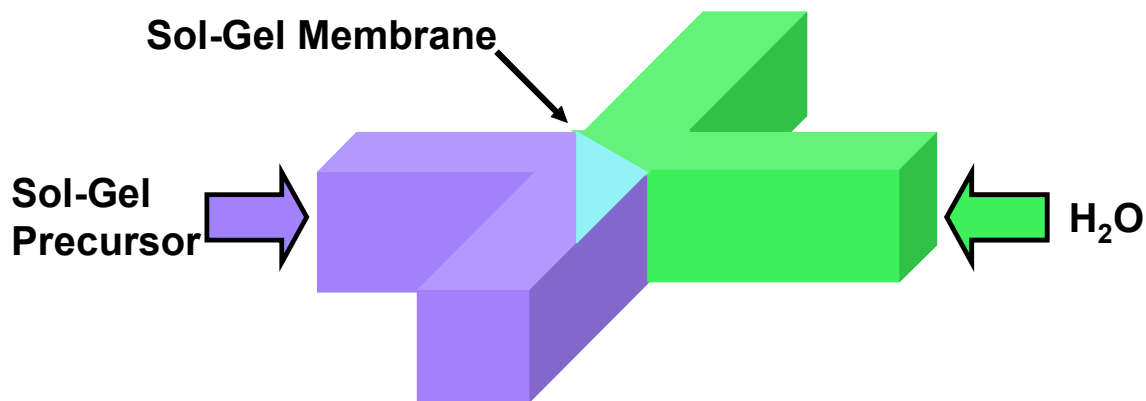


**Figure 8.2** Schematic of membrane fabrication within a microfluidic manifold.

Multiphoton microscopy was used to image the membrane over the depth of the channel and ensure that there exists an intact membrane that spans the depth of the microfluidic channel.<sup>279</sup> After the membrane was fabricated in the microfluidic channels they were filled with 1  $\mu$ M fluorescein and allowed to sit for  $\sim$  2 hrs prior to imaging. The number of fluorescein molecules within the membrane was significantly lower than the number within the bulk solution of the microfluidics. The spatial fluorescence contrast between the two areas allowed for 3D imaging of the membrane using multiphoton microscopy. Cross sections of the membrane over the depth of the channel demonstrate an intact vertical sidewall (**Figure 8.3B**).

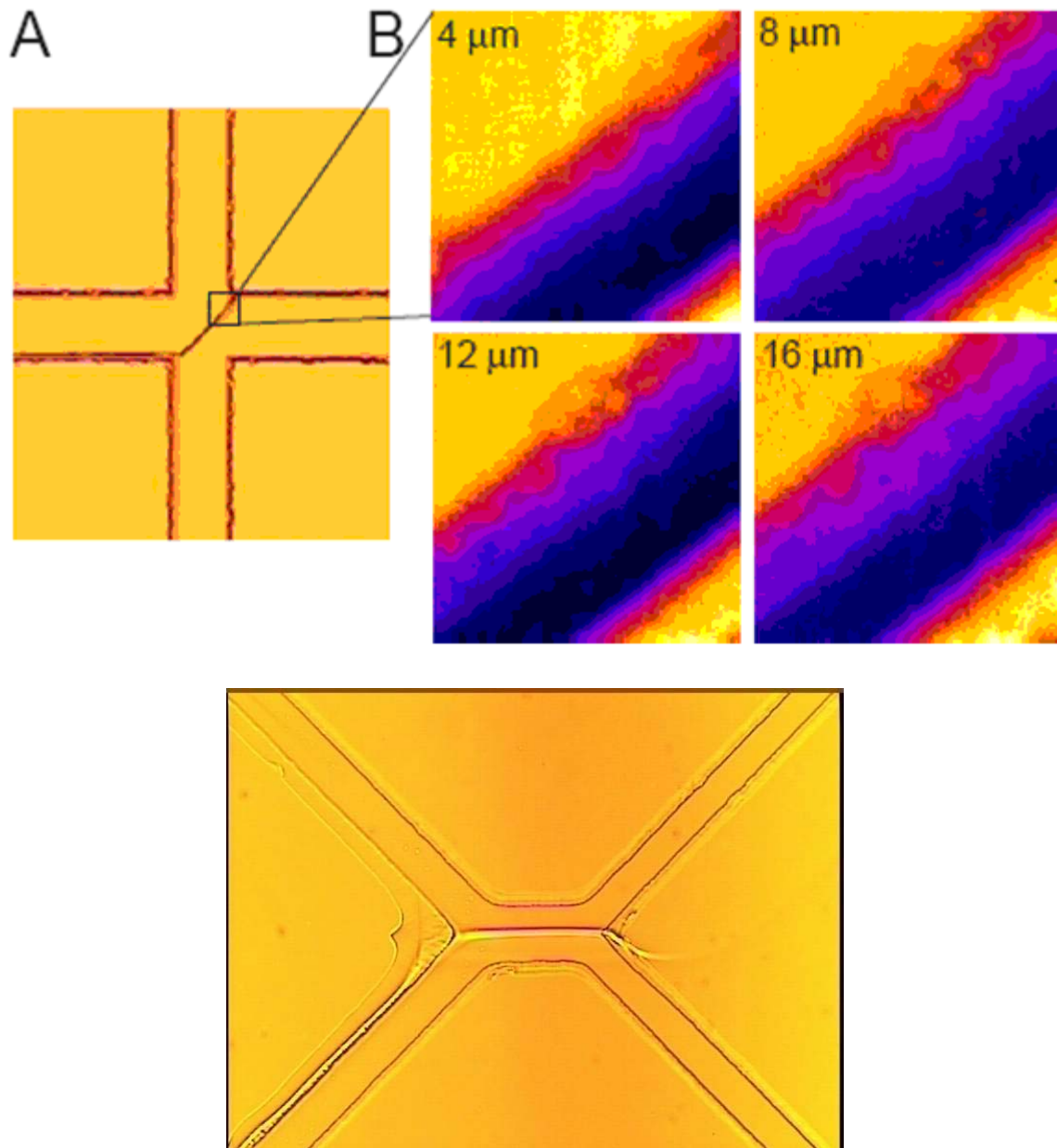


**Figure 8.3** A) Optical micrograph of a  $4\ \mu\text{m} \times 75\ \mu\text{m} \times 20\ \mu\text{m}$  titania membrane fabricated within a glass microfluidic manifold. B) Multiphoton XY scans at various depths within the glass channel ( $z = 4\ \mu\text{m}, 8\ \mu\text{m}, 12\ \mu\text{m}, 16\ \mu\text{m}$ ). C) PDMS microfluidic device with a membrane fabricated at the intersection.

#### 8.4 Ion Depletion and Enrichment Using Microfluidic Membranes

Concentration enrichment was performed using the electrical scheme diagrammed in **Figure 8.4A**. The resistance of a  $20\ \mu\text{m}$  wide titania membrane was measured at  $7.5\ \text{M}\Omega$  using  $150\ \text{mM}$  phosphate solution. An electric field of  $110\ \text{V/cm}$  was applied across the membrane that

generated an ion depletion zone which was used for ion stacking and enrichment, as previously described.<sup>272, 280, 281</sup> **Figure 8.4B** demonstrates the enrichment of Lysozyme-AlexaFluor conjugate near the titania membrane. The enrichment is spatially confined to an area of  $100 \mu\text{m}^2$ , which can be injected for CE separation and downstream analytical detection.

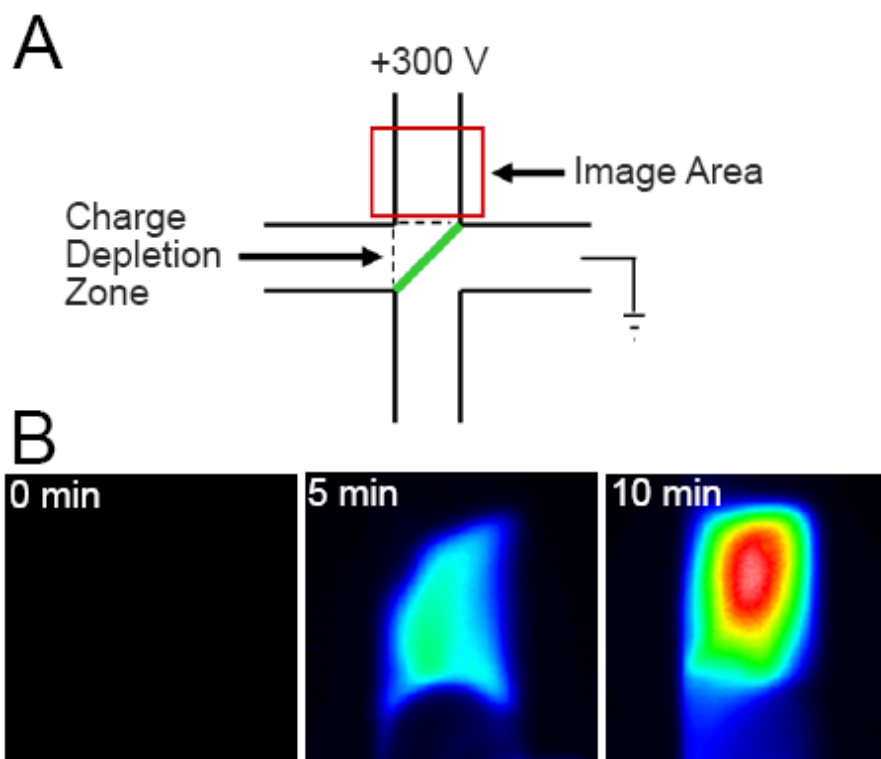


**Figure 8.4** A) Preconcentration voltage scheme for amino acids, proteins and latex particles, B) Series of CCD images of the preconcentrated plug near the charge depleted region that was formed by the titania membrane. The imaged area is illustrated in the voltage scheme above. The buffer was 80 mM sodium phosphate at pH of 11.5, 110 V/cm applied across the membrane and 150 nM lysozyme concentration. Color scale shows fluorescence, red: max, black: min.

The surface charge of the nanochannels within the membrane determines the spatial orientation of the ion depletion and enrichment with relation to the applied electric field.<sup>281</sup> In theory ion depletion for a negatively charged nanochannel should occur on the anode side of the membrane, and vice versa for a positively charged nanochannel.<sup>281</sup> Ion depletion and enrichment

regions were monitored by filling the channel manifold with fluorescein and monitoring areas of fluorescein enrichment and depletion photometrically. In **Figure 8.4B** an area of ion depletion was observed on the anode side of the membrane which was used to preconcentrate analytes. Quantitative preconcentration studies using fluorescein demonstrated over a million fold enrichment factor in under 5 min and is illustrated in **Figure 8.5**. The speed of this preconcentration is due to the high field strengths, surface area and the pore density of the titania membrane. We also performed similar concentration using amino acids, proteins and 1  $\mu\text{m}$  latex microspheres with similar efficiencies.

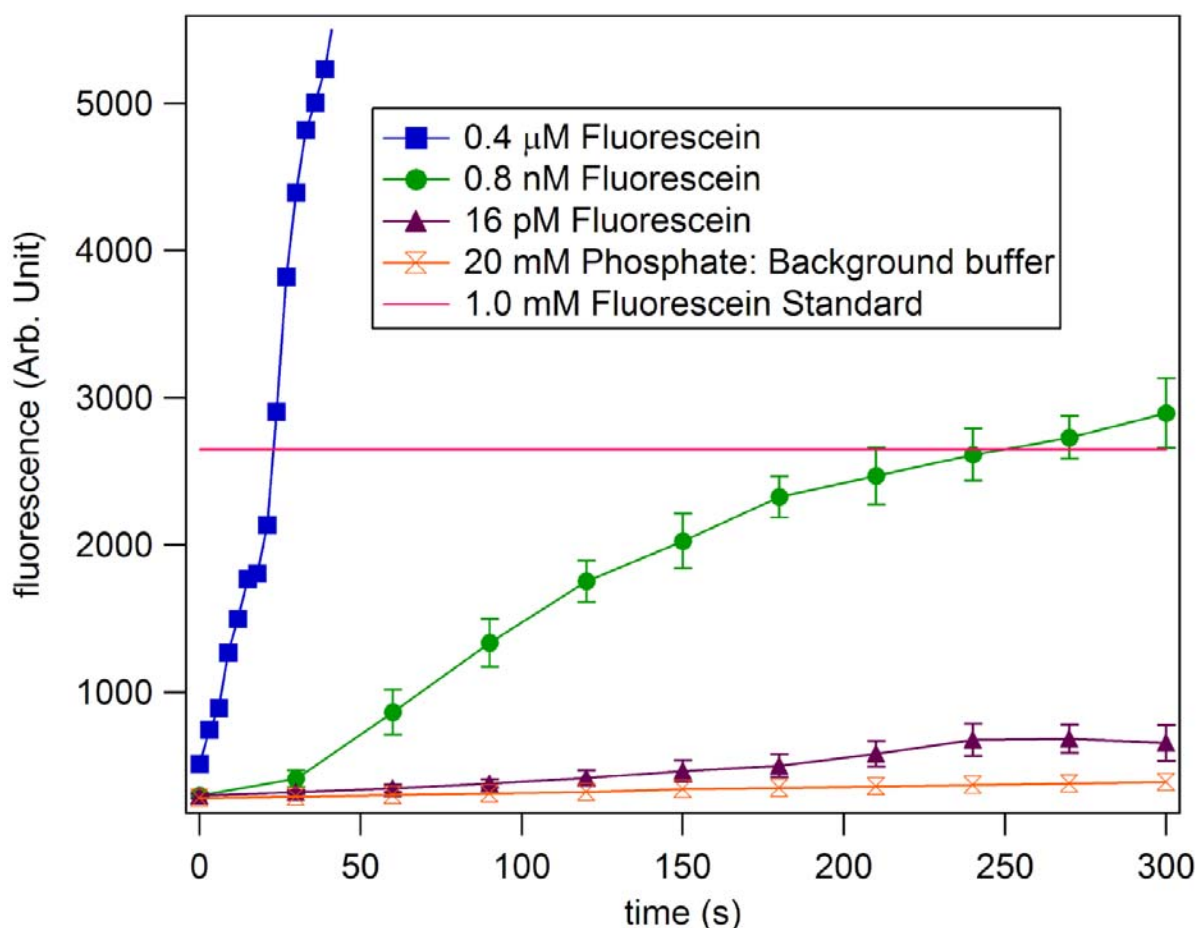


**Figure 8.5** Plot of three different fluorescein concentrations that were preconcentrated against a  $20\ \mu\text{m} \times 20\ \mu\text{m} \times 100\ \mu\text{m}$  titania membrane in a glass microfluidic manifold. The run buffer was 20 mM sodium phosphate,  $\text{pH} = 11.5$ , with an electric field of 110 V/cm applied across the membrane.

To further examine the ion depletion and enrichment zones we filled the entire channel manifold with a high concentration of fluorescein and monitored the overall intensity over time. We observed areas of fluorescence minima and maxima after applying a potential, similar to **Figure 8.4A**, across the membrane. The minima and maxima correspond to ion depletion and enrichment zones, illustrated in **Figure 8.6** below.

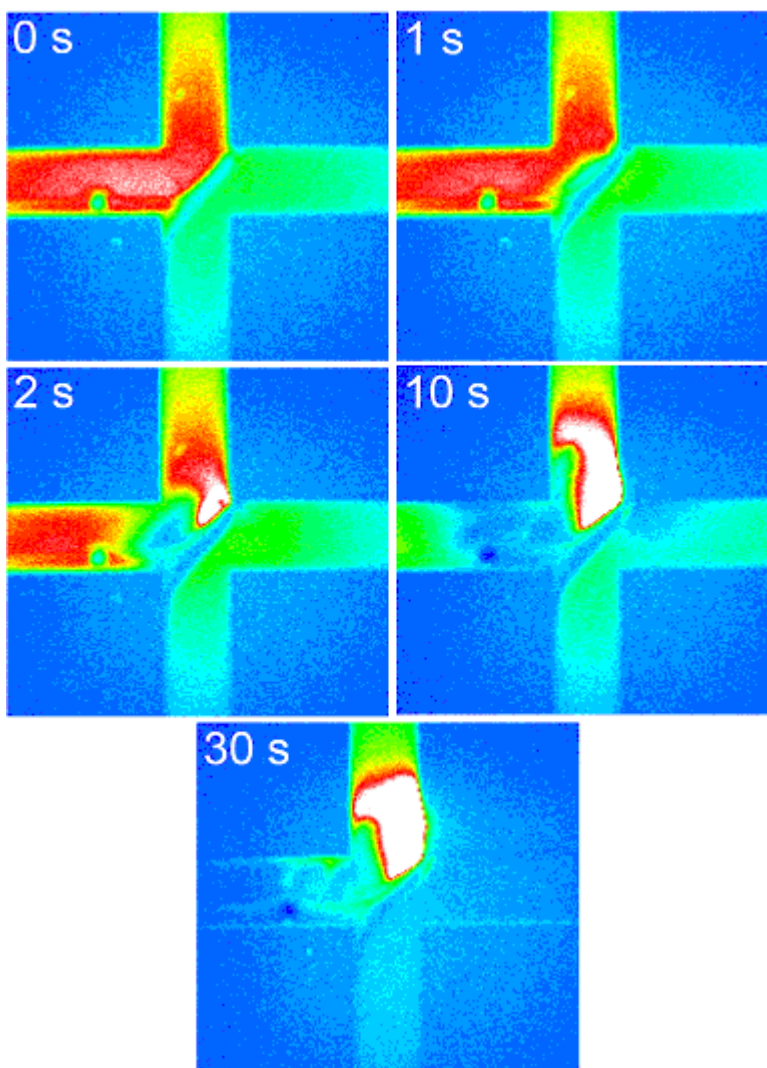


**Figure 8.6** Ion enrichment and depletion zones monitored by epi-illumination microscopy. Initially the channel manifolds were filled with 1 mM fluorescein in 80 mM sodium tetraborate at pH 11.5. The concentration enrichment and depletion was performed after applying a field

strength of 100 V/cm across the membrane while floating the other two reservoirs. Colorscale shows fluorescence, min: blue, max: white.

Ion specific enrichment has also been demonstrated to be dependent on the charge of the nanochannel, buffer characteristics and EOF of the channels. We demonstrate in **Figure 8.7** that a titania membrane is capable of performing ion enrichment on different spatial orientations relative to an applied electric field. In theory, both the charge of the nanochannel and the contents of the nanochannel will determine the flux of the ions. For instance, a negatively charged surface with a positive double layer overlap will enrich on the cathodic side, while a positively charged surface with a negative double layer overlap will enrich on the anodic side. This experiment further suggests that the ion depletion and enrichment that we are observing is based on a nanochannel phenomena, as supported by theoretical work published by Sharong Liu.

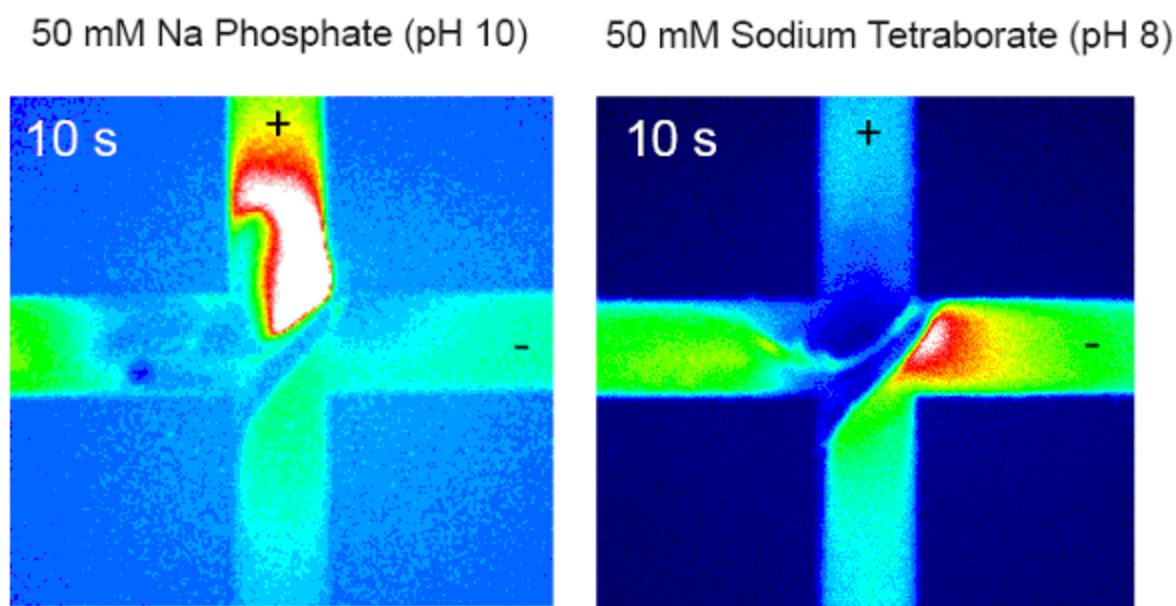


**Figure 8.7** Preconcentration studies performed using identical titania membranes with different buffer compositions. The membrane was demonstrated to preconcentrate on opposite side.

What is even more interesting is that the ion depletion zone extends the length of the channel and has the potential to be used for a number of water purification schemes. To demonstrate this effect we filled the channels with 1 mM fluorescein and monitored the ion depletion from the channels fluorometrically. Over a period of 1 min a 4 cm section of capillary was depleted of the majority of the ions and the current through this channel was in the sub micro amp range, indicating significant ion depletion. This experiment is demonstrated in **Figure 8.8**. Future experiments aim at using this technology to purify complex samples that can be used for a number of processes. Also, this device may prove to be useful for the purification of a small volume of water for other biological analysis.

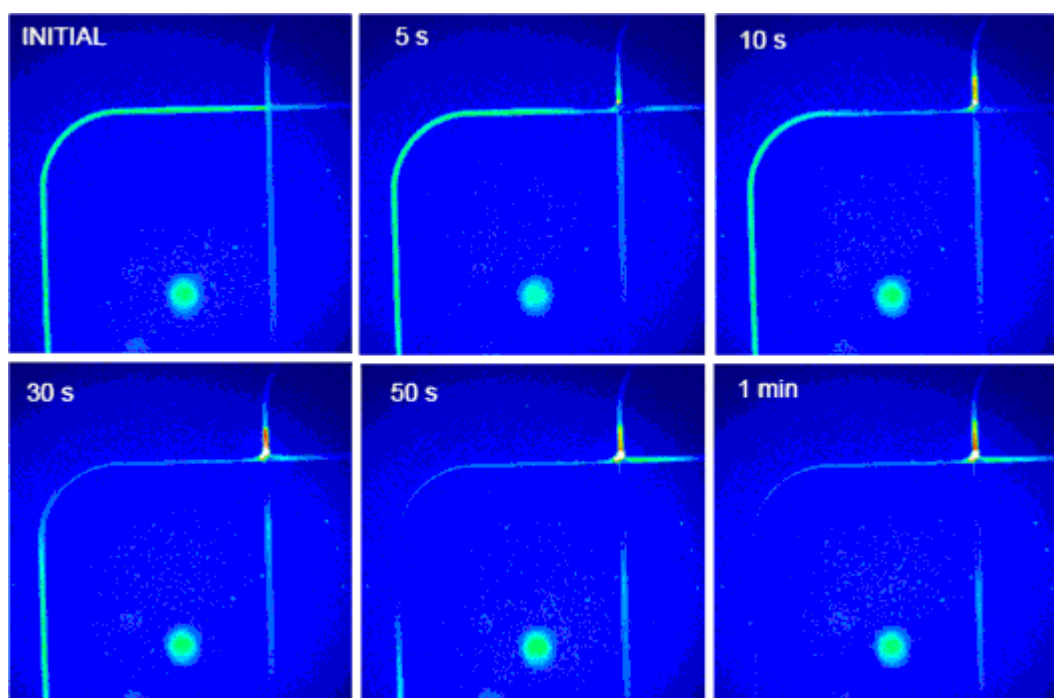


**Figure 8.8** Ion depletion of fluorescein demonstrated in the far left channel, over time the ions are depleted in this region and the sample is deionized yielding very low currents.

## 8.5 Preconcentration on Titania Membranes Coupled to Separation

Another important analytical function is the combination of concentration enrichment with a separation modality. In this case CE coupled to preconcentration works quite nicely. Since the analyte is preconcentrated in a plug near the membrane it is possible to inject this plug into the separation channel and perform a charged based separation using free solution electrophoresis. Using the electrical schematic in **Figure 8.9** we performed separations of 150 pM lysozyme, shown in **Figure 8.10**.

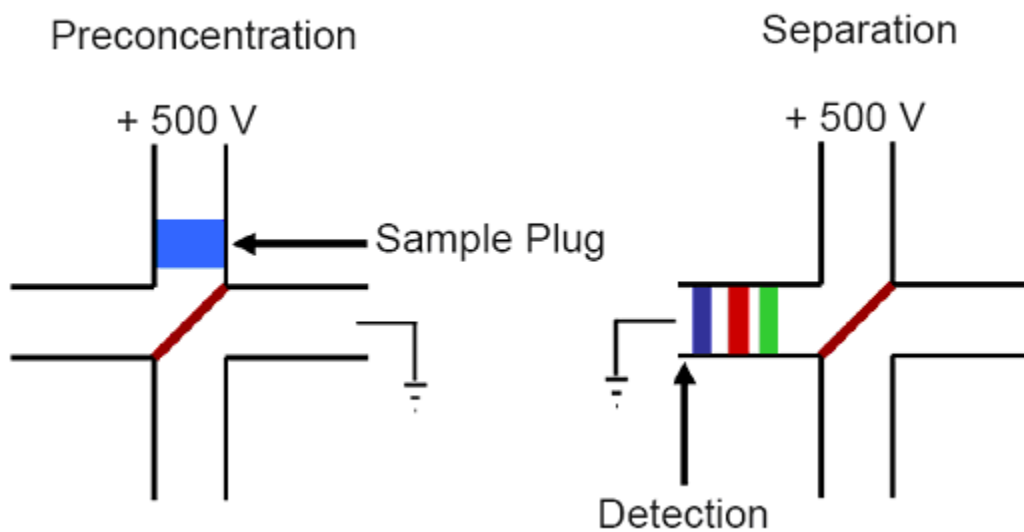


**Figure 8.9** Voltage scheme for preconcentration and electrophoretic separation.

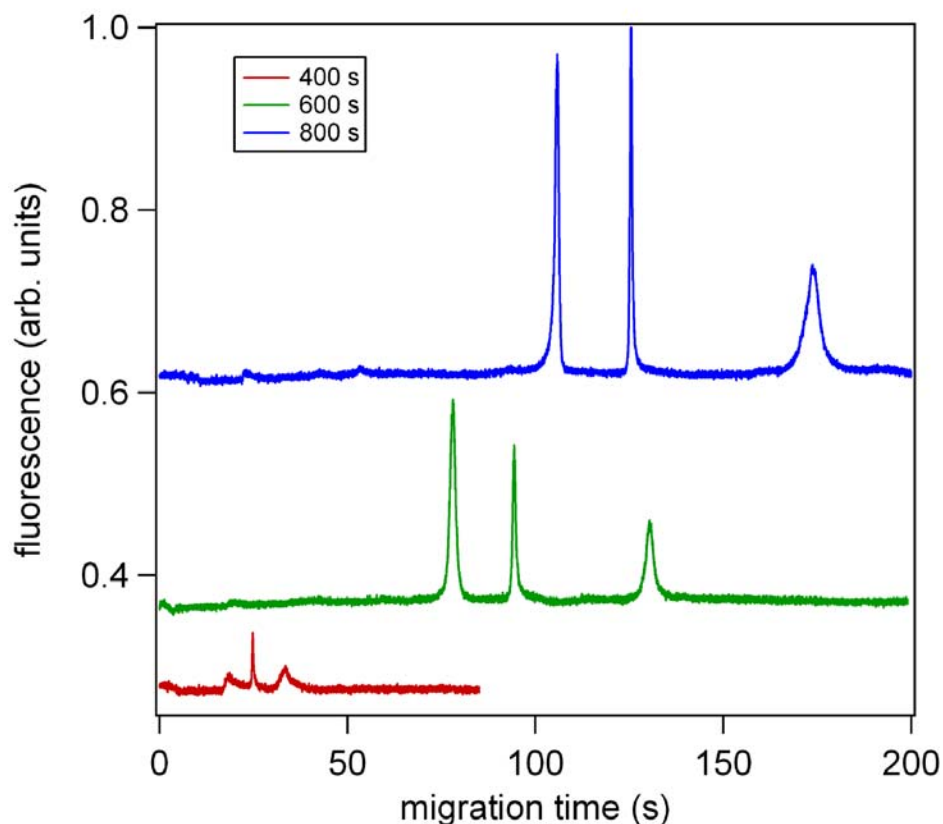


**Figure 8.10** Preconcentration of 150 pM lysozyme and separation using the voltage scheme shown in Figure 8.9. The peaks shown here indicate the hydrolysis of the protein under extremely basic conditions. The buffer used was 80 mM sodium phosphate at a pH of 11.5.

## 8.6 Titania Membrane Sensors

Titania membranes are also extremely amenable to being functionalized using common and well characterized silane chemistry. We derivitized the titania membrane using sol-gel processing with Nile Red. Since the absorptive properties of Nile Red are dramatically affected by the polarity of solvent we were capable of developing a sensor that can distinguish different solvents of varying dielectric constants. **Figure 8.11** shows a titania membrane derivitized with Nile Red in water and in hexane. The non-polar hexane gave a significantly higher fluorescent signal at 514 nm than the membrane in the water. A comparison of mean fluorescence intensity of a variety of solvents is illustrated in **Figure 8.12**. This provides a proof-of-concept for

developing fluorometric sensors for a number of different physical processes. A convenient advantage of membranes is that it is easier to flow bulk solution past a membrane than a microfluidic channel packed with beads or dots, which improves throughput.

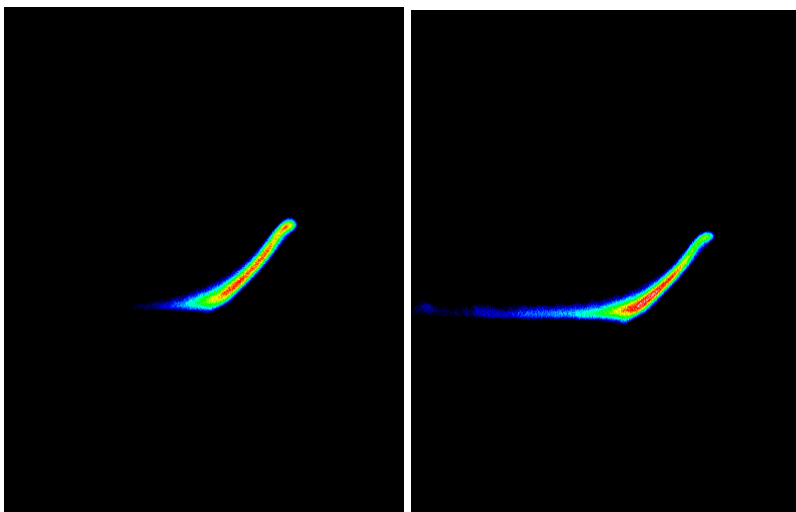


**Figure 8.11** Titania sensors functionalized with Nile red. Left: Nile-Red-Titania membrane in H<sub>2</sub>O, Right: Nile-Red-Titania membrane in hexane.

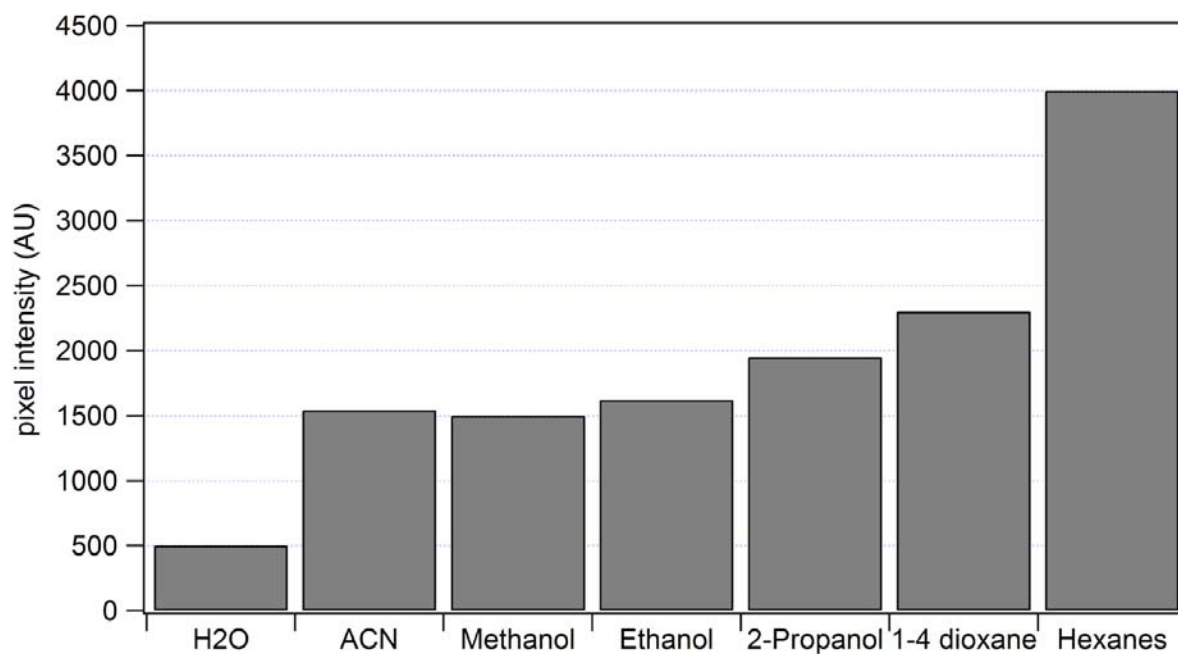


**Figure 8.12** Measurement of membrane fluorescence for a number of solvents.

## 8.7 Conclusion

In conclusion, we demonstrate a method of fabricating reproducible, robust nanoporous sol-gel metal oxide membranes within a microfluidic manifold. Titania membranes were demonstrated to perform rapid ion depletion and ion enrichment capable of million fold enrichment factors in under 5 min. In addition we have briefly demonstrated the ability to use these membranes to both perform preconcentration coupled to separation. These sol-gel nanoporous membranes have the potential of further diversifying the field of microfluidics and the physical and chemical manipulations that can be performed using such devices. Future studies will use these membranes for protein crystallization, desilicization, and biopolymer enrichment and detection.

## CHAPTER 9 - Coblock PEO-PDMS Polymers for $\mu$ fluidic Devices

### 9.1 Introduction

Silicones, specifically poly(dimethylsiloxane) (PDMS), have become very popular due to low cost and broad applicability. Besides microfluidic prototyping<sup>50</sup> and separations<sup>51</sup>, silicones can also be used for paper release agents, fiber lubricants, textile hand modifiers, corrosion inhibitors, mold release agents, antifouling materials and water repellents.<sup>149</sup> To a large extent most of these applications take advantage of the unique surface properties of silicones. The bulk surface properties of PDMS have been well characterized and include a hydrophobic surface with low surface tension. Although the bulk hydrophobicity of silicones has many advantages it

also limits the overall applicability of PDMS in biological applications. Biopolymers such as proteins and hydrophobic analytes will irreversibly adsorb to PDMS making it difficult to transport such analytes within a PDMS microfluidic manifold.

Several polymers have been investigated which attempt to reduce the biofouling of PDMS microfluidics. Cblock polymers are especially useful due to the ability to tailor the hydrophobic and hydrophilic properties of the polymer. Poly(dimethylsiloxane)-poly(ethyleneoxide) (PDMS-PEO) cblock polymers have been demonstrated to be extremely antithrombogenic allowing for utility in biomedical applications involving the analysis of hydrophobic analytes such as biopolymers and adhesive cells.<sup>282</sup>

Our overall goal was to synthesize an amphiphilic cblock polymer that retains the positive attributes of PDMS, notably its ability to serve as a good substrate for micromolding, but also eliminate disadvantages of PDMS including its hydrophobicity. To accomplish this we aimed at developing a polymer that contained block elements of both PEO and PDMS alternating blocks. An important advantage of many cblock polymers involves “block migration”, or “block reorientation”. Block reorientation occurs due to an interfacial stimulus which forces reorientation due to a favorable thermodynamic conditions. For instance, a PDMS-PEO cblock polymer will initially exhibit a PDMS moiety at a surface when exposed to air, but when exposed to water a PEO moiety is “encouraged” to migrate to the surface to yield a hydrophilic surface. This concept is illustrated in both **Figures 9.1 and 9.2**.

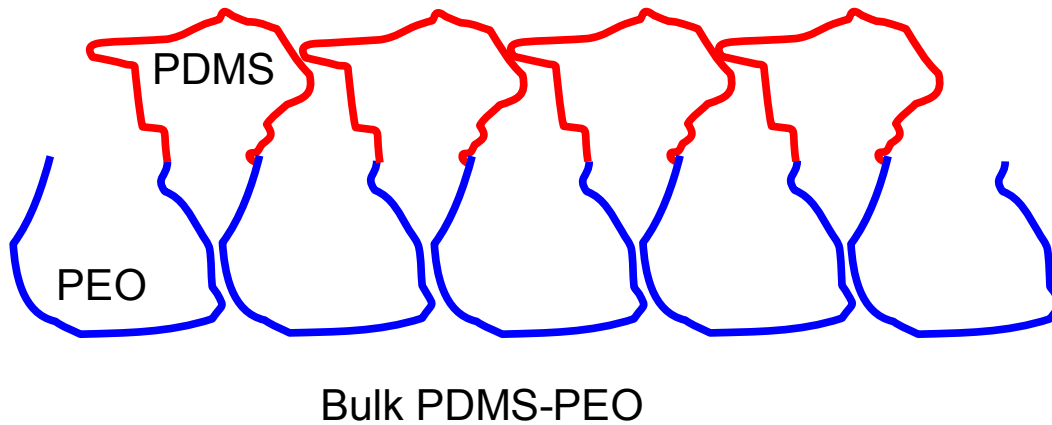


**Figure 9.1** Diagram of a PDMS surface generated under air.

### Surface under water

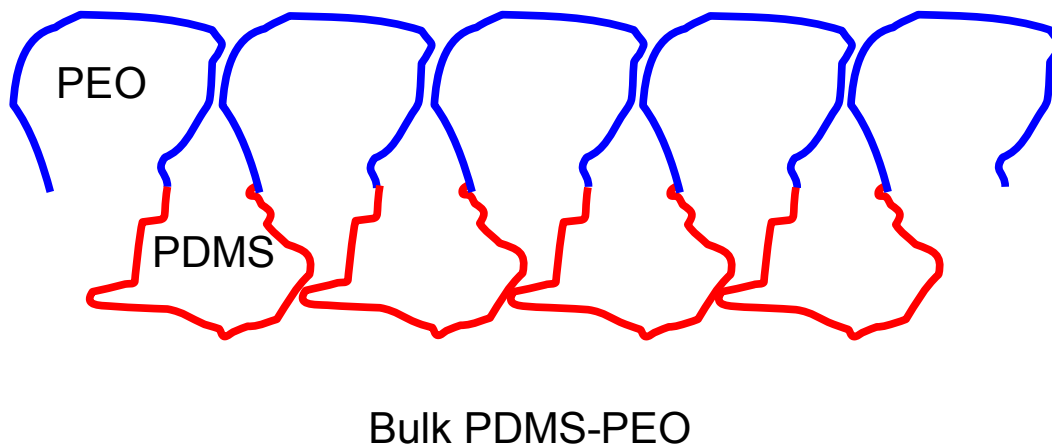


**Figure 9.2** Diagram of a PDMS-PEO surface generated under water after the PEO reorients itself at the interface.

The block migration of the PEO to the surface can be monitored using contact angle measurement. Over a period of 1 min the contact angle decreases from  $\sim 100^\circ$  to  $40^\circ$ . The time that it takes for the bulk contact angle to change from hydrophobic to hydrophilic is indicative of the microscale migration of PEO units to the bulk surface.

## 9.2 Experimental

### 9.2.1 Synthesis of PDMS-PEO Polymer

#### 9.2.1.1 The protocol for PDMS-PEO prepolymer:

Synthesis of the PDMS-PEO prepolymer was performed in a 250 mL three neck round bottom flask, with condenser, and dry air purge. After sufficiently cleaning the glassware with nitric acid and sulfuric acid (3:1) and drying glassware at 110°C for 1 hr, 19.1 g PDMS H-Term, 12 g Vinyl-Term PEO, 9.3 g of hexane, and 30 ppm platinum catalyst was added and stirred at 1 Hz. After all reagents had been added the heat was ramped to 60°C for 4 hrs. Product was rotovaped for 8 hrs. The block sizes were, PEO: 268 g/mol, PDMS-H term: 450 g/mol, The weight percents: PDMS: 63%, PEO: 37%. **Figure 9.3** shows the reaction scheme for the synthesis of the PDMS-PEO copolymer.

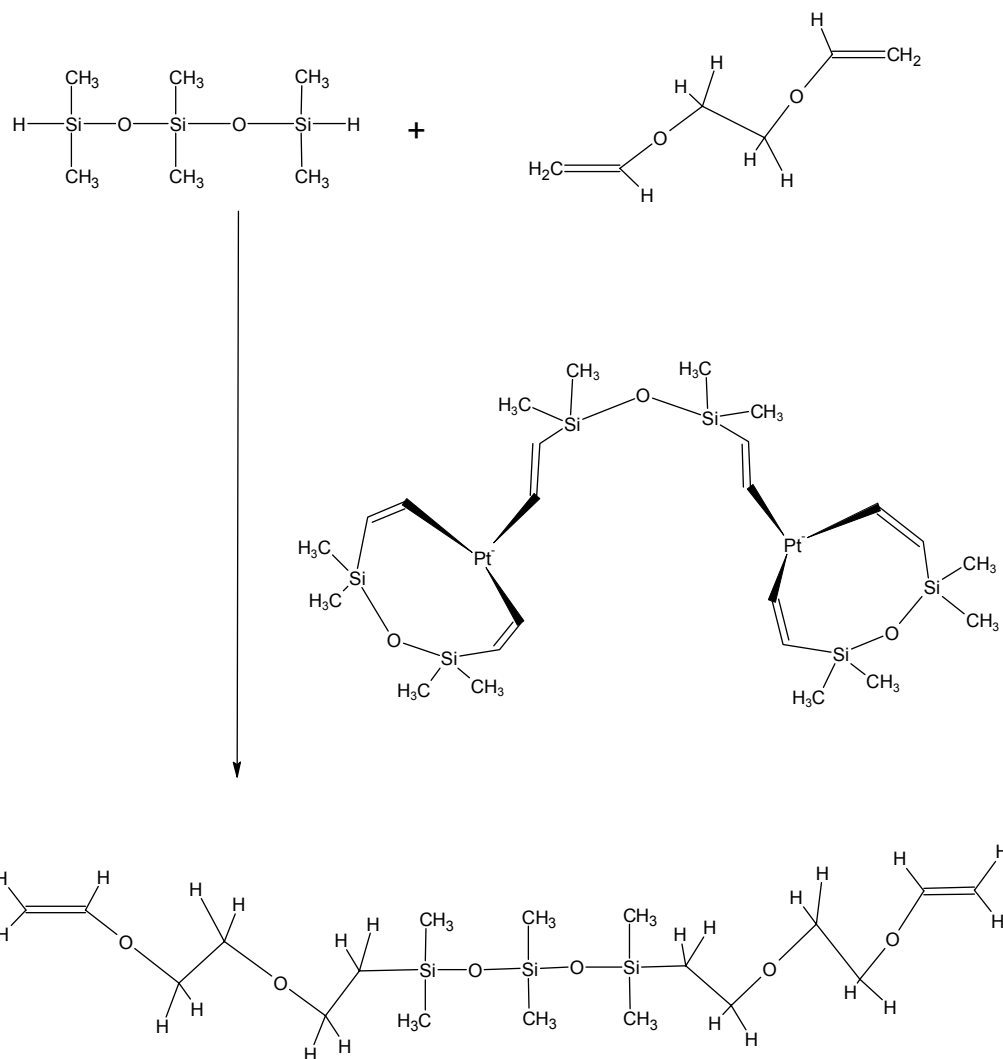


**Figure 9.3** Reaction scheme for the copolymer synthesis of PDMS-PEO

### 9.2.1.2 Reinforcement and Crosslinking:

Due to mechanical instabilities of the PDMS-PEO prepolymer we used a combination of silica precipitation and hydride terminated Q-resin to generate a mechanically stable polymer. To perform the silica precipitation 1 g TEOS was added to 5 g prepolymer and precipitated under 2.5% ethyl-amine for 8 hrs. The result was rotovaped for 8 hrs. The reinforced prepolymer was next crosslinked by adding 0.15 g HMS-301 to 1 g of prepolymer. In addition 200  $\mu\text{L}$  of Xylene with 30 ppm of platinum catalyst was added. The reaction was allowed to proceed within a

scintillation vial for 2 hrs, after about 2 hrs it had become crystal clear. This mixture was poured onto both a glass flat and an SU-8 mold to fabricate a microfluidic device. Images of features molded using this synthetic product are illustrated in **Figure 9.4**.

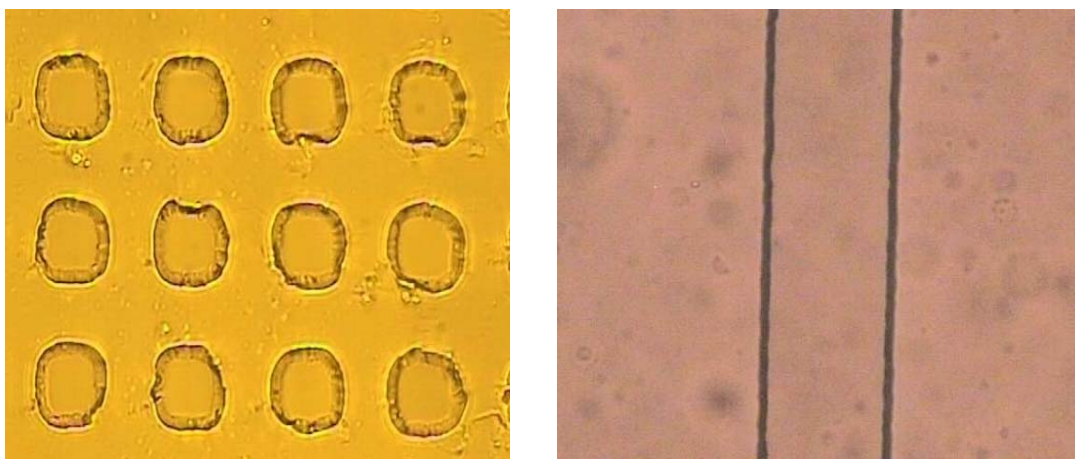


**Figure 9.4:** Left: PDMS-PEO well formed using a stamping method, Right: PDMS-PEO channels formed using SU-8 molds.

## 9.3 Results and Discussions

### *9.3.1 Contact Angle and RhB Absorption Measurements*

Contact angle measurements were recorded using procedures described previously in Chapter 3 and 4. Coblock polymers synthesized using methods described above yielded significantly more hydrophilic surfaces with lower contact angle of  $40^\circ$  to  $80^\circ$ , this compared to  $110^\circ$  for PDMS. A number of different factors affect the contact angle of the polymer. For instance, curing time and temperature, crosslinking ratio, PEO and PDMS weight content, and strengthening agents all dramatically affect the surface characteristics. **Figure 9.5** illustrates an optical micrograph comparing the contact angle of the PDMS and the contact angle of the PDMS-PEO polymer.



**Figure 9.5** Contact angles of PDMS-PEO (40°) and PDMS (110°)

In addition to bulk contact angle measurements which do not necessarily probe the molecular interactions of a bulk polymer, we were also interested in using absorption and adsorption studies of rhodamine B in PDMS-PEO channels. This experiment was similar to those described in Chapters 3 and 4, where a 10  $\mu\text{m}$  solution of rhodamine B was introduced into the channel manifold. The fluorescence profiles were measured over a period of time to examine for any absorption or adsorption. Adsorption of rhodamine B to the sidewalls of the channel is indicated by bat ears on the edges of the profile, while absorption is indicated by an increase in the full width at half max. Interestingly we saw neither increases at FWHM or bat ears suggesting no absorption or adsorption of rhodamine B over 1 hr, shown in **Figure 9.6**.

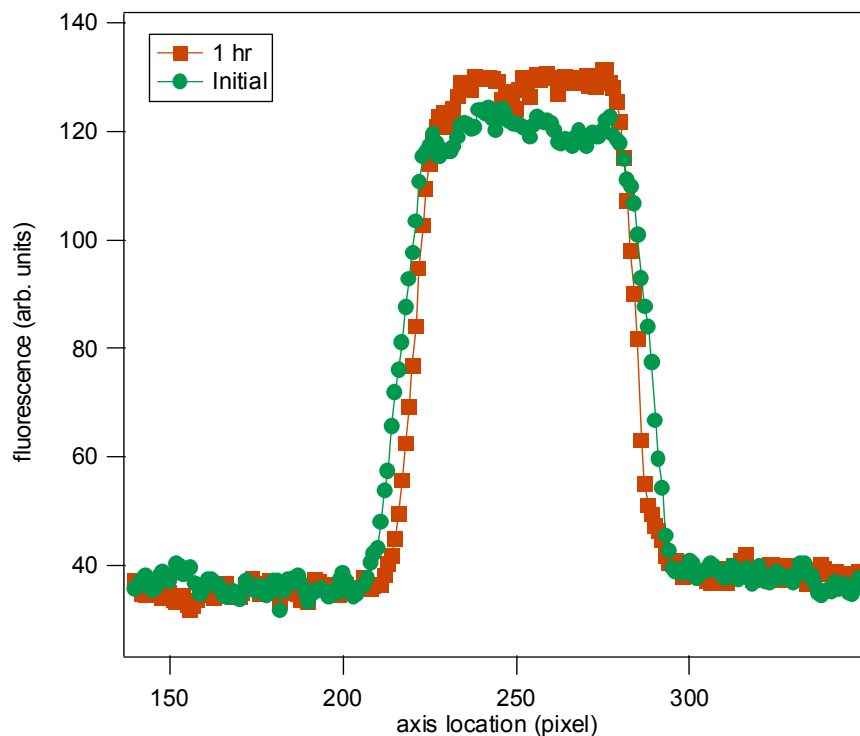


**Figure 9.6** Rhodamine B absorption profiles for PDMS-PEO microfluidics.

### 9.3.2 EOF Measurements

As mentioned in Chapter 2 the electroosmotic flow of PDMS is directed primarily by the adsorption of ions to the surface of the channel. The adsorption of ions is assisted by the hydrophobic interface formed between PDMS and water. The interface tends to adsorb less polarizable ions such as  $-OH$  or  $-Cl$ . If the hydrophobicity of the polymer is decreased the chemisorption of ions to the surface would be much less and also would tend to slow down the electroosmotic flow. Alternatively, polymer chains have the potential of reorienting and in the process have the potential of generating a significantly thick polymer entanglement near the surface. The entanglement near the surface has the potential to increase the resistance of flow and also decreasing the EOF.

The measurement of the EOM was similar to that previously described in Chapter 3-4. The electroosmotic flows were measured between  $1.0 \times 10^{-4} \text{ cm}^2/\text{Vs}$  and  $3.0 \times 10^{-5} \text{ cm}^2/\text{Vs}$  for a variety of different PEO-PDMS blends. Generally we observed that higher reinforcement with silica generated higher EOF's, but no trends with respect to crosslinker or processing parameters were apparent. The buffer that was used was 25-50 mM sodium tetraborate with an electric field strength of 300 V/cm. This EOF can be compared to  $2.3 \times 10^{-4} \text{ cm}^2/\text{Vs}$  for native PDMS using identical buffer conditions and field strengths.

### 9.3.3 Separations on PDMS-PEO Microfluidics

In addition to characterizing the potential of PDMS-PEO as a substrate for microfluidic fabrication we were also extremely interested in examining its usefulness for electrophoretic separations. Initially we examined separations of TAMRA labeled amino acids on both PDMS and PEO-PDMS. We found, much to our delight, that the separation efficiencies and resolutions were largely better or comparable in some cases. Shown below is a comparison between electropherograms of TAMRA labeled amino acids on PDMS and PEO-PDMS.

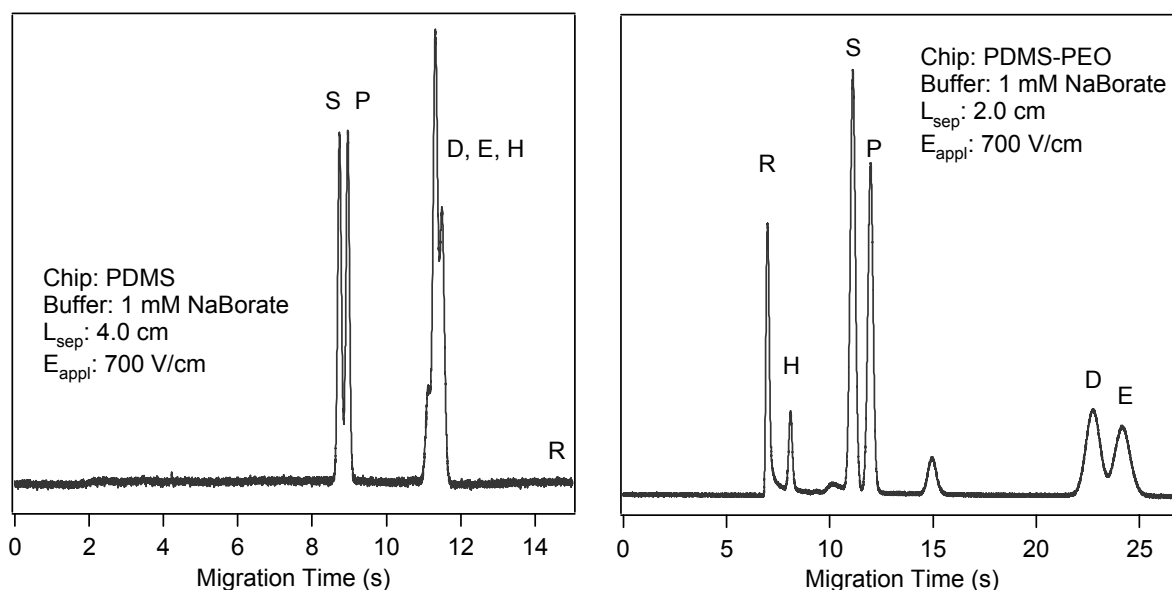


**Figure 9.7** Separations of TAMRA labeled amino acids on PDMS and PDMS-PEO

Amino Acid	N (PEO-PDMS)	N (PDMS)
	2.0 cm	4.0 cm
R	9,400	10
H	9,200	Unresolved
S	8,300	25,000
P	9,900	23,000
D	4,300	Unresolved
E	5,000	Unresolved

**Table 5** Efficiencies obtained on PDMS and PDMS-PEO for TAMRA labeled amino acids.

# CHAPTER 10 - Microfluidic Separations in Microgravity

## 10.1 Introduction

The ultimate goal of this project is to integrate microfluidic devices with NASA's space bioreactor systems. In such a system, the microfluidic device would provide real-time feedback control of the bioreactor by monitoring pH, glucose, and lactate levels in the cell media; and would provide an analytical capability to the bioreactor in extraterrestrial environments for monitoring bioengineered cell products and health changes in cells due to environmental stressors. Such integrated systems could be used as biosentinels both in space and on planet surfaces.

To demonstrate the ability of microfabricated devices to repeatedly and reproducibly sample microliter volumes from flight certified cell culture bags and perform capillary electrophoretic separations in 0, lunar, martian, and hypergravity (1.8g).

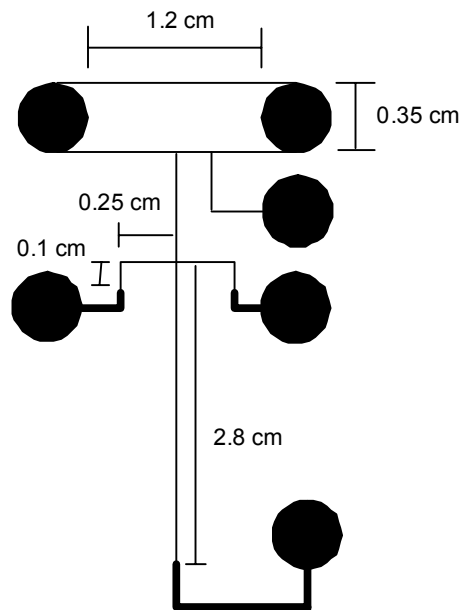


### **Figure 10.1** FTC Chip design

A “flow through” channel chip was designed, and is illustrated to the left. This chip features a large fluidic channel, located near the top of the microchip, which offers a low fluidic resistance. This channel is etched to a depth of ~ 150 microns with a width of about 0.35 cm. The low fluidic resistance of this large channel allows for the rapid flow and movement of fluid through this channel. The “flow through” channel serves as an interface between the macroscale external fluidics that will deliver sample from either a cell culture bag, or a bioreactor with the on-chip microfluidics that are designed to perform capillary electrophoresis separations of amino acids and proteins, specifically reGFP. We used differential etching techniques to fabricate the microfluidic channels with a depth of 20  $\mu\text{m}$ . This allowed for a large fluidic resistance to hydrodynamic flow through the microfluidic channels so that pressure caused by the external fluidics did not significantly affect the electrophoretic separations.

The goal of this experiment was to validate the fluidic interface between the microfluidic chip and the external fluidic network including the cell culture bag. To accomplish this goal several different samples were placed in a series of cell culture bags. Each cell culture bag contained differences not only in the number of analytes, but also in the concentration of the analytes. The different samples in each bag would allow us to characterize the fluidic interface and the time it takes for sample to reach the injector and also allow us to access the quantitative ability of the electrophoretic separations in determining differences in concentration of amino acids and proteins.

Illustrated below is a schematic of the flow through chip connected to the external fluidics. A series of CCD images were collected demonstrating the combination of

hydrodynamic fluid flow through the wide “flow through” channel, with the electrokinetic injection and separation of amino acids into the microfluidic channels. A flow rate of  $\sim 250 \mu\text{L}/\text{min}$  could be achieved through the wide “flow through” channel. This allowed for rapid real time analysis of the contents of the cell culture bag. The time it takes for the analyte to travel from the cell culture bag to the cross injector was 1-5 min depending on the flow rate from the pump.

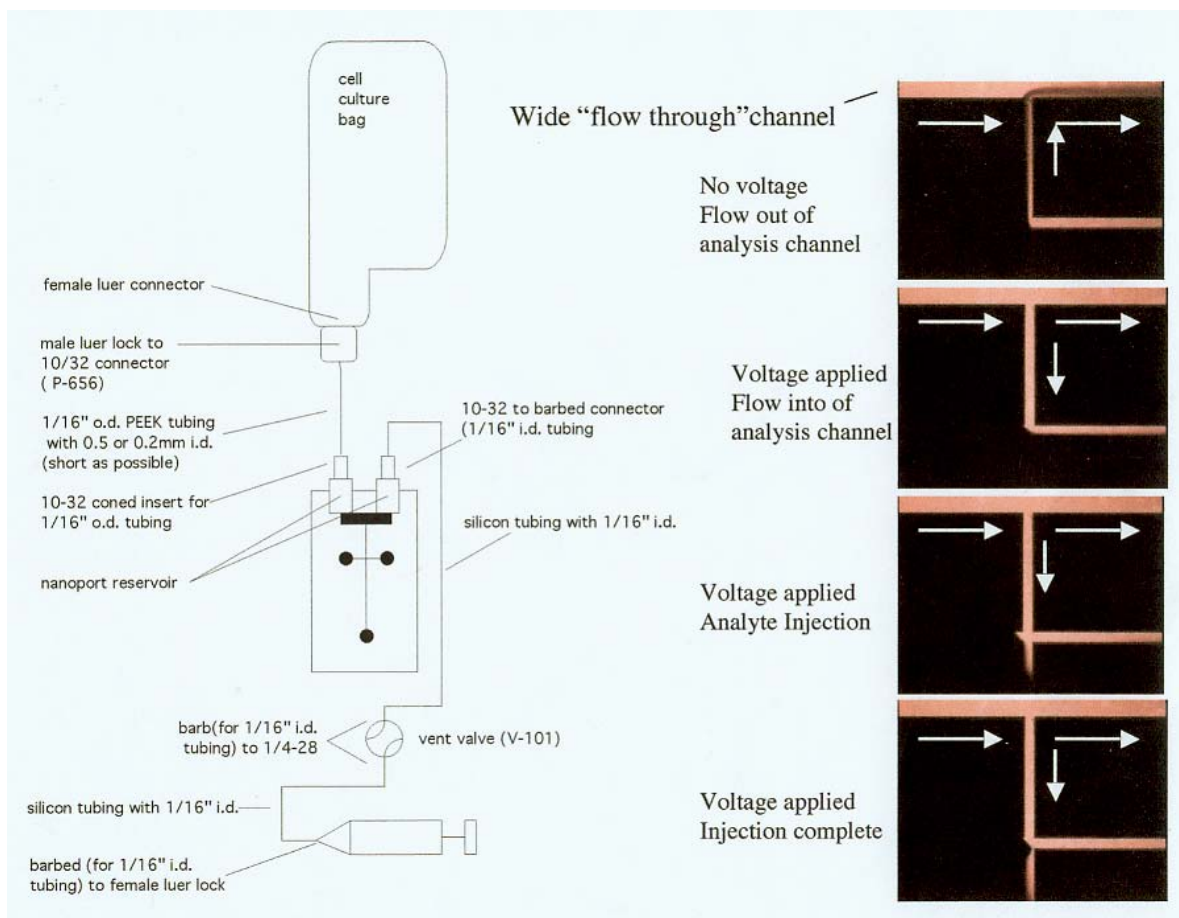


**Figure 10.2** FTC External Pumping Schematic

## 10.2 Sample Preparation

The following samples were mixed separately in three 10 mL cell culture bags using 10 mM sodium tetraborate at a pH of 9.3:

- 1  $\mu\text{M}$  Serine-FITC, 1  $\mu\text{M}$  Arginine-FITC and 1  $\mu\text{M}$  Glutamic acid-FITC
- 2  $\mu\text{M}$  of Serine-FITC, 2  $\mu\text{M}$  Arginine-FITC, 2  $\mu\text{M}$  Glutamic acid-FITC and 2  $\mu\text{M}$  Proline-FITC
- 400 nM reGFP and 500 nM reGFP

The solutions were stored at 8°C until used. A four way valve made it possible to connect these bags in parallel with the microfluidic device. Each cell culture bag was sampled for 15 min during flight before switching to another sample.

### **10.3 Chip Preparation and Operation**

Chip preparation consisted of flushing a 50/50 (v/v) 1M NaOH/methanol solution through the channels, followed by water and then run buffer. The electrophoretic separations were carried out in a pH 9.3, 10 mM sodium tetraborate buffer. Gated injections between 0.025 and 0.1 s were performed to introduce the sample into the separation channel. The separation distance was 2 cm and the field strength in the separation channel was  $\sim 1000$  V/cm. Laser light scattering off of the channel walls was used to align the device.

### **10.4 Results and discussion**

We demonstrated a reproducible interface between the cell culture bags and microfluidic channels of the microchip. The microchip was capable of performing rapid capillary electrophoresis separations of both FITC derivitized amino acids and reGFP in a reduced gravity environment.

Shown below is an example of two different sample bags being separated on the “flow through” chip in zero gravity. The first sample contained 2  $\mu\text{M}$  FITC derivitized amino acids

arginine, serine and glutamic acid. The second sample contained 1  $\mu\text{M}$  FITC derivatized amino acids arginine, proline, serine and glutamic acid. The time it takes for the sample to move from the cell culture bag to the cross injector on the microchip was approximately 3 min. The peak areas of the lower concentration analyte were decreased by 50%, in addition to the substitution of proline. A few good characteristics for this separation include the constant baseline, reproducible migration times and high efficiencies.

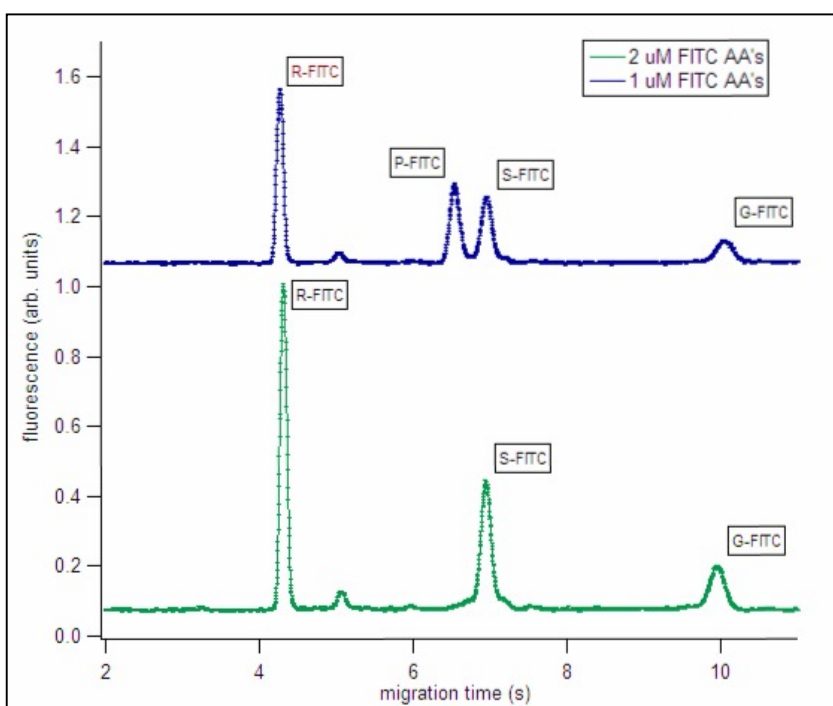
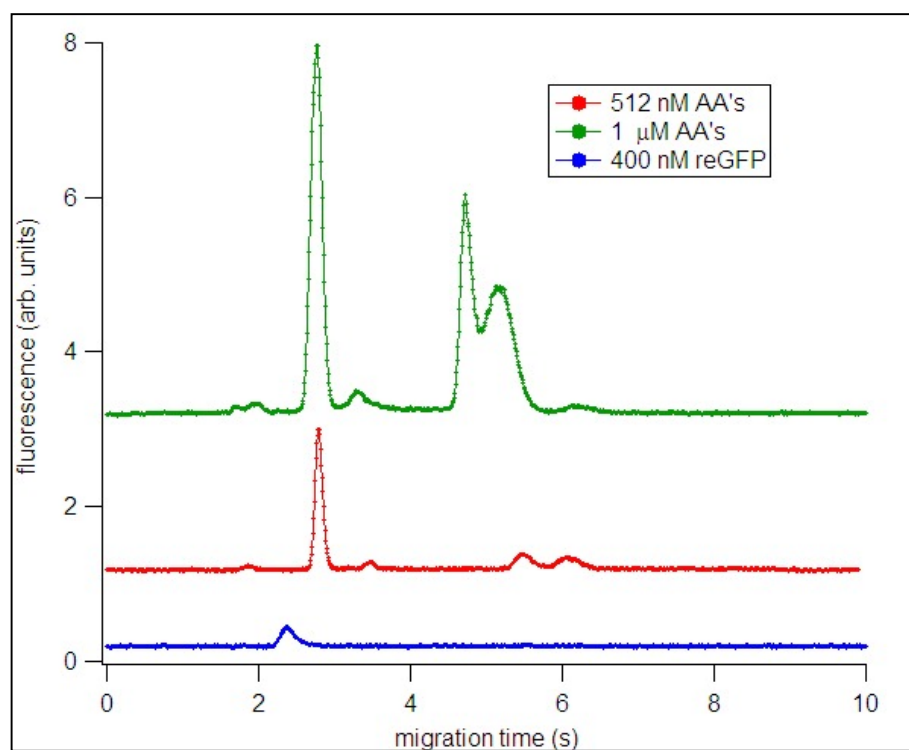


Figure 10.3 On-line sample of AA's in zero gravity.

In addition to separating amino acids we have also examined the separation of both amino acids and reGFP using the flow through chips. Shown to the left is a series of solutions containing 1) 1  $\mu\text{M}$  FITC derivatized amino acids, 2) 512 nM FITC derivatized amino acids, and 3) 400 nM reGFP. All solutions were dissolved in 10 mM sodium borate. We were able to

sample from the cell culture bags to the microfluidic chip in less than 1 min using 500  $\mu\text{L}/\text{min}$  flow rates in the flow through channel. The fast flow rate sampling caused a few peaks to broaden, but continued to allow for the separation of a series of amino acids and reGFP at reduced and hyper gravities. The green electropherogram shows arginine, proline and serine peaks in order from left to right. The red electropherogram shows a reduced concentration of the same amino acids that were present in the green electropherogram. Finally, the blue electropherogram shows the reGFP peak. Again each electropherogram represents a different sample bag connected to the chip in parallel.



**Figure 10.4** Online sampling of reGFP using the flow through chip.

Below is a series of injections of reGFP from cell culture bag containing 500 nM reGFP dissolved in sodium tetraborate. These three injections were performed in a zero g environment carried out over 1 parabola of 25 seconds. Approximate migration time of the reGFP was 2.5 s.

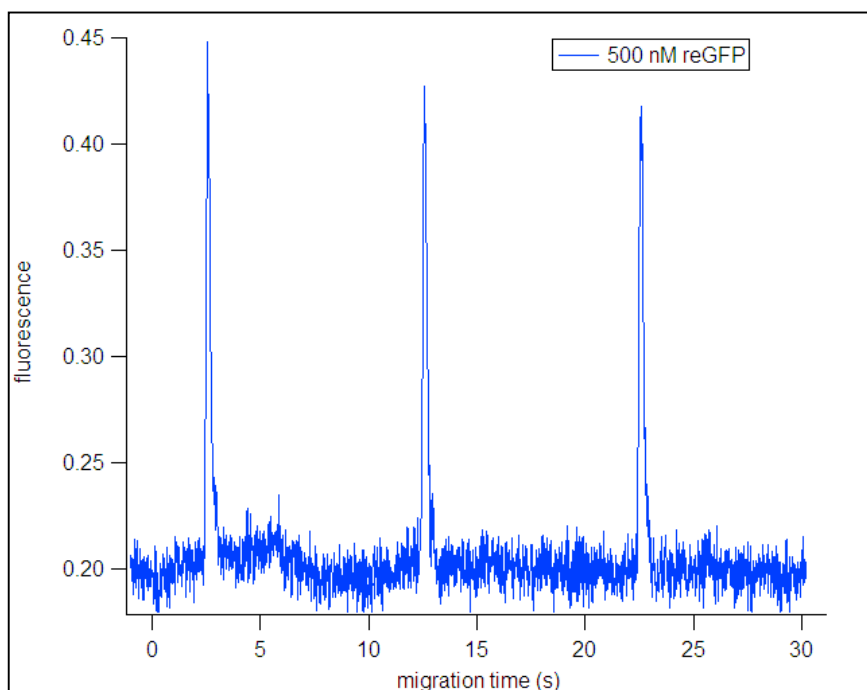


**Figure 10.5** On-line sample of reGFP and separation using the flow through chip.

### 10.5 Conclusion

We demonstrate a microchip capable of performing rapid sampling of microliter volumes that are subsequently separated and quantified using capillary electrophoresis in reduced and hyper-gravity environments. The results have validated our delivery method between the external fluidics and the on-chip microfluidics. The optimal flow rate through the flow through channel was  $\sim 250 \mu\text{L}/\text{min}$ . Using the device we have developed thus far we are ready to perform

separations of reGFP secreted in cell media in a cell culture bag and electrophoretically migrate it to a cross injector for separation and quantification.

# CHAPTER 11 - Single Cell Analysis Using PDMS Microfluidic Devices

## 11.1 Introduction

Cells are extremely complex and dynamic biochemical entities. Significant biochemical heterogeneity can exist among cells of the same type. This heterogeneity may arise via many mechanisms including localized damage, mutations, stage in the cell cycle, and differential exposure to external signals (e.g. chemical gradients) among others.<sup>283,284</sup> Understanding how and why these differences arise is critical both to a better understanding of cell biology and to the ability to detect early disease stages so that they can be treated before significant health consequences are incurred.

The analysis of single cells, however, presents a variety of challenges. Non-adherent eukaryotic cells are generally on the order of 5 to 20  $\mu\text{m}$  in diameter and, therefore, have volumes of only 0.1 to 8 pL. Many of the macromolecules of interest (mRNA and proteins) may only be present in low copy numbers; therefore, techniques which can handle such small volumes without significant dilution and which can be directly integrated with ultra-sensitive detection schemes are necessary. In addition, cells must be handled gently prior to analysis so as not to artificially perturb the biochemical pathways or molecules of interest. Finally, although one wants to only examine one cell at a time, many individual cells need to be analyzed rapidly to understand the statistical distribution of a particular analyte in the cell population so that outliers (i.e. potential disease markers) can be identified.

Microfluidic devices offer a unique platform for the rapid analysis of single cells. These devices allow the integration and automation of cell and reagent handling with cell lysis and high efficiency separations. The nonmechanical fluidic valving that can be implemented at cross intersections allows the injection of cell lysates without significant dilution. These short injection plugs along with the high separation field strengths that can be applied also enable very rapid, high efficiency separations to be performed. From a detection standpoint, microchips are generally fabricated from transparent materials with flat channel walls; therefore, high sensitivity fluorescent detection can easily be integrated into the device. The automation and integration of all of these cell handling and processing steps along with the rapid separations potentially enables the high throughput analysis of individual cells. Below we discuss several different methods that have been developed to manipulate and analyze single cells on microfluidic devices for subsequent chemical analysis.

### ***11.1.2 Microfluidic Single Cell Manipulation and Analysis***

One critical step in single cell analysis is the development of methods that can reproducibly transport cells to precise locations for further analysis. Ideally these methods should be amenable to parallel formats, have high throughput capability, limit dilution, and be robust. Reported single cell manipulation techniques include: a) hydrodynamic flow and focusing<sup>285</sup>, b) the use of on-chip valves and pumps to direct cell transport<sup>286</sup>, c) the incorporation of cells into microfluidic droplets<sup>287</sup>, d) the optical<sup>287</sup> and optoelectronic<sup>288</sup> trapping of cells, e) the dielectrophoretic trapping of cells,<sup>289</sup> and f) the geometrical trapping of cells<sup>290-293</sup> (see **Figure 11.1**).

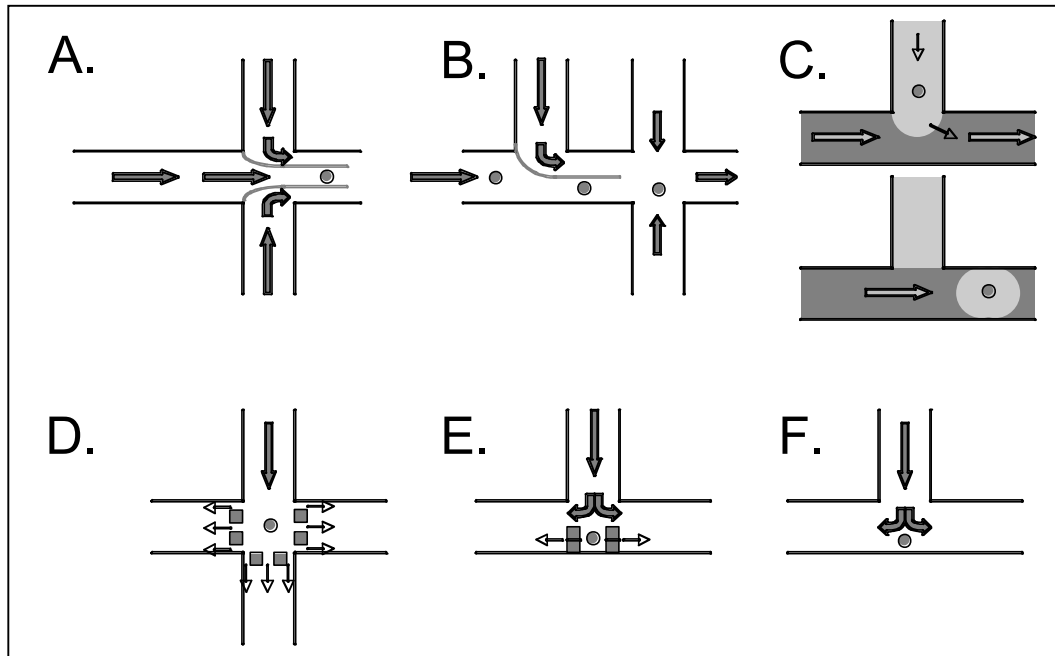


**Figure 11.1** Schematic of the various types of methods reported for transporting and manipulating cells. (A) Cells can be hydrodynamically focused at an intersection so that they all flow past an interrogation region in single file. (B) Cells can be hydrodynamically transported to an intersection where they can be lysed either electrically or chemically and the lysate injected into a separation channel. (C) Cells can be incorporated into droplets and hydrodynamically transported to an interrogation region. Cells can be trapped geometrically using pillars (D), weirs (E), or hydrodynamically balanced flows (F).

The Reynolds number for fluid flow in microfluidic devices is generally  $< 0.1$ ; therefore, the fluid flow is laminar. One can take advantage of these laminar flows to precisely transport cells throughout the microfluidic manifold. Such laminar flows have been used to perform cytometry on microfluidic devices where cells are hydrodynamically focused into a narrow stream that can be probed optically. Microchip flow cytometry has significant advantages over traditional flow cytometry as it can integrate other operations such as loading the cells with

agonists, cell lysis and separations in addition to counting.<sup>294</sup> Simple microchip flow cytometry has been used to perform cytotoxicity assays of intact cells.<sup>285</sup> Hydrodynamic transport and focusing of cells has also been used to bring cells to an intersection where they can be lysed electrically<sup>295</sup> or chemically<sup>296</sup> and the fluorescently labeled components in the lysate injected and analyzed. McClain et al. have reported the rapid electrical lysis of Jurkat cells loaded with carboxyfluorescein and Oregon green at an intersection. The lysate was immediately injected and the fluorophores separated. The analysis was performed at a rate of 12 cells/min. This was 500 times faster than a similar analysis performed using conventional capillary electrophoresis. Separation efficiencies of ~ 4,000 theoretical plates in < 2.3 s were reported.

While the above single cell analysis devices were fabricated from glass, there has been a significant movement toward poly(dimethylsiloxane) (PDMS)-based devices for performing single cell analysis. Soft lithography using PDMS has been widely adopted primarily because it is inexpensive and serves as an excellent substrate for rapid prototyping.<sup>297</sup> The elastomeric nature of PDMS has made it useful for implementing valves and peristaltic pumps on-chip for a number of different operations.<sup>298</sup> For example, microfluidic PDMS valves can be used to isolate single cells with active volumes as small as 1 pL.<sup>299</sup> We have recently incorporated PDMS-based valves and pumps for the analysis of single non-adherent eukaryotic cells. The PDMS microfluidic device was configured with an air actuated manifold located above a microfluidic liquid filled manifold. The two fluidic networks were separated by a 40  $\mu\text{m}$  deep PDMS membrane. As the actuation channels were pressurized the PDMS membrane expanded into the fluidic channel below, yielding a functional valve. **Figure 11.2a** illustrates this multilayer PDMS device with the actuation channel, fluidic channel and PDMS membrane. **Figure 11.2b** demonstrates the actuation of these channels, which can be configured to transport single cells.

PDMS valves were also located around a fluidic cross intersection for capturing single cells as they pass through the intersection **Figure 11.2c-11.2d**. After capture the cells can be lysed as reported above.<sup>295</sup>

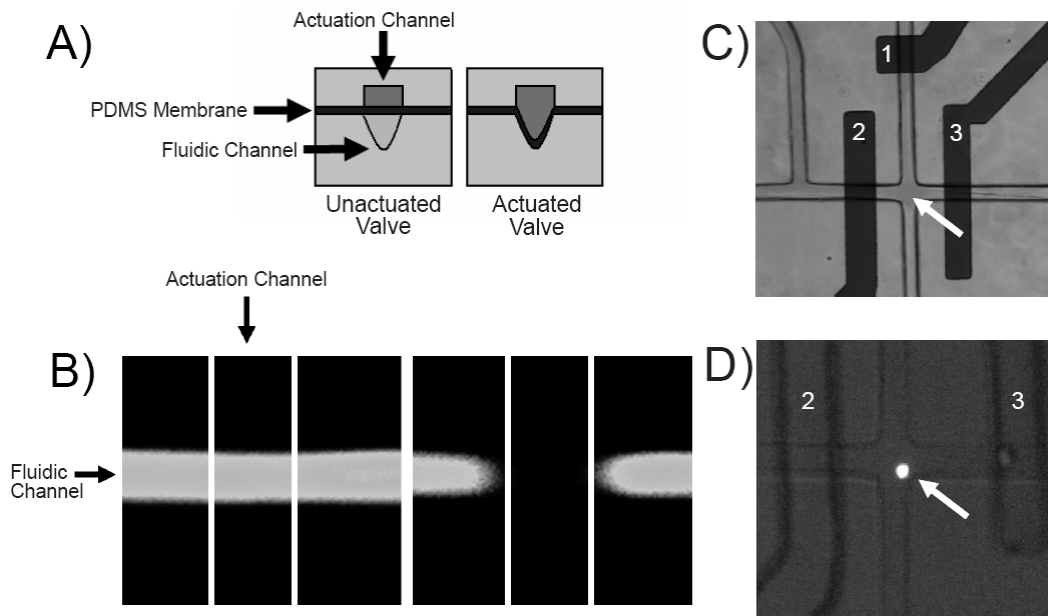


**Figure 11.2** A) Schematic illustrating a cross section of a PDMS microfluidic device designed for microfluidic elastomeric valving. Two cross sections are illustrated including an unactuated valve and an actuated valve. The actuated valve has a high pressure of  $\sim 25$  kPa applied to the actuation channel which causes the PDMS membrane to deform into the fluidic channel below. This can function as a check valve or when applied in series can be used as a peristaltic pump. B) A fluidic channel was filled with 10 mM fluorescein and imaged prior to valve actuation (left) and during valve actuation (right). After the valve is actuated the fluorescein is displaced yielding a low intensity in the areas of the membrane depression. White lines represent areas where the actuation channel is located relative to the fluidic channel. C) Three actuation valves labeled 1-3 were positioned around a fluidic cross intersection labeled with an arrow. The fluidic cross intersection allows for the transport of cells either hydrodynamically or electrokinetically. D) Trapping of a single cell is accomplished by transporting it to the intersection hydrodynamically followed by isolation by actuating check valves 1-3. A single Jurkat cell loaded with Calcein AM is shown trapped at the cross intersection.

Using PDMS, as a substrate also allows small, high-aspect-ratio features to be incorporated into the microfluidic channels. PDMS-based devices have been used to fabricate pillars in 3 channels around an intersection. Cells brought in from the fourth channel were then

captured in the intersection for chemical lysis.<sup>300</sup> While cell transport in this case was performed using optical tweezers<sup>300</sup>, the use of hydrodynamic flow can also be envisioned for transporting cells to such a trap.

The small channel dimensions and laminar flow generated in microfluidic channels has also enabled a variety of immiscible droplet based generation technologies to be developed that can also be used to confine individual cells. He et al. have demonstrated the ability to generate pL and fL aqueous monodisperse droplets on microfluidic devices.<sup>287</sup> Their device consisted of a T- intersection that was used to dispense aqueous droplets into a confluent non-aqueous stream. The droplets were used as reaction vessels for single cells. The cell containing droplets were physically transported and fused with other aqueous droplets under controlled conditions. Optical trapping facilitated the encapsulation of cells containing variable amounts of the enzyme  $\beta$ -galactosidase within the microdroplets.<sup>287</sup> These microdroplets also contained the fluorogenic substrate fluorescein di- $\beta$ -D-galactopyranoside. The cell containing droplets were transported to an interrogation region where they were lysed and a fluorescent signal was generated from the reaction between the  $\beta$ -galactosidase and fluorescein di- $\beta$ -D-galactopyranoside.

Finally, cells can also be hydrodynamically trapped between weirs (protusions that capture cells) at a T- intersection<sup>290</sup> or through the precise control of hydrodynamic flows at such intersections.<sup>292, 293, 301</sup> Reagents can then be added to the cells and reaction kinetics monitored optically. In both of these cases the cells can afterwards be released and a new cell trapped. Arrays of similar traps have also recently been reported where multiple cells can be assayed simultaneously.<sup>291</sup>

## 11.2 Outlook

Conventional analytical techniques are problematic for single cell analysis due primarily to the dilution of cellular lysates. Microfluidic technologies offer a wealth of possibilities for single cell manipulation and analysis due to the fundamental fluid dynamics that are associated with micron scale channels and a number of lithographic advancements that have been made to generate complex multifaceted devices. Single cell analysis using microfluidics holds the potential to further elucidate the complex cellular functions and malfunctions that are associated with many diseases by allowing researchers to probe the dynamic environment of the cell. In conventional techniques a large number of cells are collected and mixed together to give a statistical average of biomolecules contained within the cells. Single cell analysis allows researchers to study “outlier” cells and better understand cell physiology by comparing differences among a cell population. Moreover, microfluidic devices that are designed for high throughput single cell analysis have the potential of probing differences in cellular response to external stimuli and could provide a means of investigating a number of cellular transduction pathways.

## CHAPTER 12 - Summary and Closing Remarks

The broad goals of my research involve developing technologies that further improve the throughput and sensitivity of an analytical device. In our case the analytical device was a microfluidic platform using capillary electrophoresis (CE) and laser induced fluorescence to both separate and detect biomolecules such as amino acids, metabolites and proteins. Although microfluidic devices have many advantages they also have many technical barriers that need to be rectified before they can be used for biochemical analysis. The foremost technical barrier includes analyte substrate interactions, which are magnified in microfluidics with high surface area to volume ratios. Our goal was to modify the microfluidic substrate either through covalent or non-covalent means to generate a repulsive force between the surface of the channel and the analyte. This would ideally reduce the amount of analyte adsorption to the surface of the channel and would allow for fluidic manipulation and separation of biochemicals.

We developed several different strategies to modify the surface of PDMS. First we used sol-gel chemistry to modify the surface of PDMS by precipitating a durable inorganic coating on the channel surface, described in Chapters 2-4. The inorganic coatings that we investigated include silica, titania, vanadia and zirconia. These durable inorganic coatings had characteristic EOF's and were overall more hydrophilic than native PDMS. The inorganic coatings also proved useful for a variety of separations yielding diffusion limited separations of amino acids and other small molecules. We further derivitized these surfaces with a number of functionalities including PEG, APTES, thiol and perfluoro. The derivitized metal oxide surfaces were useful for free solution separation of proteins. Second, we developed a dynamic SDS coating method on PDMS devices, described in Chapters 5-6. This method was capable of manipulating extremely

hydrophobic analytes on PDMS devices while simultaneously using a pseudostationary phase capable of adding a dimension of selectivity to the separation mode. Electrokinetic separations of Rhodamine B generated efficiencies of  $\sim 100,000$  plates using this MEKC method.

Unfortunately proteins could be manipulated on-chip using this method, but electrophoretic separations had reduced resolutions.

Additional experiments using CE also examined the separation of A $\beta$  peptides and reGFP proteins described in Chapter 7 and 10. We demonstrate the ability to use microfluidic devices to monitor the aggregation of the A $\beta$  peptides and the disaggregation of these devices using novel inhibitors. In addition to surface coatings we also employed membranes for the preconcentration of analytes described in Chapter 8. The membranes were capable of million fold concentration enrichment of fluorescein in under 300 seconds. Finally we used coblock polymers for the separation of hydrophobic compounds in Chapter 9 and a review on single cell manipulation and chemical analysis in chapter 11.

## CHAPTER 13 - REFERENCES

1. Manz, A.; Graber, N.; Widmer, H. M., Miniaturized total chemical-analysis systems: a novel concept for chemical sensing. *Sensors Actuators B* **1990**, 1, 244-248.
2. Atencia, J.; Beebe, D. J., Controlled Interfaces. *Nature* **2005**, 437, 648.
3. McClain, M. A.; Culbertson, C. T.; Jacobson, S. C.; Allbritton, N. L.; Sims, C.; Ramsey, J. D., Microfluidic Devices for the High-Throughput Chemical Analysis of Cells. *Anal. Chem.* **2003**, 75, (21), 5646-5655.
4. Carlo, D. D.; Aghdam, N.; Lee, L. P., Single-Cell Enzyme Concentrations, Kinetics, and Inhibition Analysis Using High-Density Hydrodynamic Cell Isolation Arrays. *Anal. Chem.* **2006**, 78, (14), 4925-4930.
5. Irimia, D.; Geba, D. A.; Toner, M., Universal Microfluidic Gradient Generator. *Anal. Chem.* **2006**, 78, (10), 3472-3477.
6. Lion, N.; Reymond, F.; Girault, H. H.; Rossier, J. S., Why the move to microfluidics for protein analysis? *Current Opinion in Biotechnology* **2003**, 15, (1), 31-37.
7. Lion, N.; Rohner, T.; Dayon, L.; Arnaud, I. L.; Damoc, E.; Youhnovski, N.; Wu, Z.-Y.; Roussel, C.; Jossierand, J.; Jensen, H.; Rossier, J. S.; Przybylski, M.; Girault, H. H., Microfluidic Systems in Proteomics. *Electrophoresis* **2003**, 24, 3533-3562.
8. Sia, S. K.; Whitesides, G. M., Microfluidic devices fabricated in poly(dimethylsiloxane) for biological studies. *Electrophoresis* **2003**, 24, (21), 3563-3576.
9. Makamba, H.; Kim, J. H.; Lim, K.; Park, N.; Hahn, J. H., Surface modification of poly(dimethylsiloxane) microchannels. *Electrophoresis* **2003**, 24, (21), 3607-3619.
10. Marko-Varga, G.; Nilsson, J.; Laurell, T., New directions of Miniaturization within the Proteomics Research Area. *Electrophoresis* **2003**, 24, 3521-3532.
11. Belder, D.; Ludwig, M., Surface modification in microchip electrophoresis. *Electrophoresis* **2003**, 24, (21), 3595-3606.
12. Vilkner, T.; Janasek, D.; Manz, A., Micro Total Analysis Systems. Recent Developments. *Anal. Chem.* **2004**, 76, (12), 3373-3386.
13. Reyes, D. R.; Iossifidis, D.; Auroux, P.-A.; Manz, A., Micro Total Analysis Systems. 1. Introduction, Theory, and Technology. *Anal. Chem.* **2002**, 74, (12), 2623-2636.
14. Auroux, P.-A.; Iossifidis, D.; Reyes, D. R.; Manz, A., Micro Total Analysis Systems. 2. Analytical Standard Operations and Applications. *Anal. Chem.* **2002**, 74, (12), 2637-2652.
15. Khandurina, J.; Guttman, A., Bioanalysis in microfluidic devices. *Journal of Chromatography A* **2002**, 943, 159-183.
16. Becker, H.; Locascio, L. E., Polymer Microfluidic Devices. *Talanta* **2002**, 56, (2), 267-287.
17. McDonald, J. C.; Whitesides, G. M., Poly(dimethylsiloxane) as a material for fabricating microfluidic devices. *Accounts of Chemical Research* **2002**, 35, (7), 491-499.
18. Harrison, D. J.; Oleschuk, R. D.; Thibault, P., Microfluidic systems for analysis of the proteome with mass spectrometry. *Lab-on-a-Chip* **2003**, 249-270.

19. Binyamin, G.; Boone, T. D.; Lackritz, H. S.; Ricco, A. J.; Sassi, A. P.; Williams, S. J., Plastic microfluidic devices: electrokinetic manipulations, life science applications, and production technologies. *Lab-on-a-Chip* **2003**, 83-112.
20. Locascio, L. E.; Henry, A. C.; Johnson, T. J.; Ross, D., Surface chemistry in polymer microfluidic systems. *Lab-on-a-Chip* **2003**, 65-82.
21. Hecht, E., *Optics*. Addison Wesley: San Francisco, CA, 2004.
22. Xia, Y.; Whitesides, G. M., *Angew. Chem., Int. Ed. Engl.* **1998**, 37, 550-575.
23. Christenson, A. M.; Corder, G. W.; DeVore, T. C.; Augustine, B. H., A Photolithography Laboratory Experiment for General Chemistry Students. *J. Chem. Ed.* **2003**, 80, (2), 183.
24. Bowden, M. J., *Materials for Microlithography*. American Chemical Society: Washington, DC, 1984; Vol. 266.
25. Quirk, M.; Serda, J., *Semiconductor Manufacturing Technology*. Prentice Hall: Upper Saddle, River, NJ, 2001.
26. Microchem, *Nano SU-8 2000*. MicroChem: Newton, MA, 2003.
27. Xia, Y.; Rogers, J. A.; Paul, K. E.; Whitesides, G. M., Unconventional Methods for Fabricating and Patterning Nanostructures. *Chem. Rev.* **1999**, 99, 1823-1843.
28. Madou, M. J., *Fundamentals of Microfabrication*. CRC: New York, NY, 2002.
29. Xia, Y.; Whitesides, G. M., Soft Lithography. *Ann. Rev. Mater. Sci.* **1998**, 28, 153-184.
30. Beebe, D. J.; Mensing, G. A.; Walker, G. M., Physics and Applications of Microfluidics in Biology. *Annu. Rev. Biomed. Eng* **2002**, 4, 261-286.
31. Attiya, S.; Jemere, A. B.; Thompson, T.; G., F.; Seiler, K.; Chiem, N.; Harrison, D. J., Design of an interface to allow microfluidic electrophoresis chips to drink from the fire hose of the external environment. *Electrophoresis* **2001**, 22, 318-327.
32. Gottschlich, N.; Jacobson, S. C.; Culbertson, C. T.; Michael Ramsey, J. M., Two-Dimensional Electrochromatography/Capillary Electrophoresis on a Microchip. *Anal. Chem.* **2001**, 73, (11), 2669-2674.
33. Roper, M. G.; Shackman, J. G.; Dahlgren, G. M.; Kennedy, R. T., Microfluidic Chip for continuous monitoring of hormone secretion from live cells using an electrophoresis-based immunoassay. *Anal. Chem.* **2003**, 75, 4711-4717.
34. Culbertson, C. T.; Jacobson, S. C.; Ramsey, J. D., Microchip Devices for High-Efficiency Separations. *Anal. Chem.* **2000**, 72, 5814-5819.
35. Meagher, R. J.; Seong, J.; Laibinis, P. E.; Barron, A. E., A very thin coating for capillary zone electrophoresis of proteins based on a tri(ethylene glycol)-terminated alkyltrichlorosilane. *Electrophoresis* **2004**, 25, (3), 405-414.
36. Roman, G. T.; McDaniel, K.; Culbertson, C. T., *Analyst* **2005**, Submitted.
37. Siegman, A. E., *Lasers*. University Science Books: Sausalito, CA, 1986.
38. Bruckhalter, J.; Seiwald, R. Isothiocyanate Compounds and Means of Producing the Same Isothiocyanate Compounds". 1960.
39. Heim, R.; Tsien, R. Y., Engineering Green Fluorescent Protein. *Curr. Biol.* **1996**, 6, (2), 178-182.
40. [www.probes.com](http://www.probes.com), Technical Resources. In Molecular Probes: Eugene, OR, 2006.
41. Chen, Y. F.; Dovichi, N. J., Subattomole amino acid analysis by capillary zone electrophoresis and laser- induced fluorescence. *Science* **1988**, 242, 562-564.
42. Tiselius, A.; Pedersen, K. O.; Eriksson-Quensel, I. B., *Nature* **1937**, 139, 546.
43. Hjerten, S., *Biochim. Biophys. Acta* **1961**, 53, 514-517.
44. Jorgenson, J. W., Electrophoresis. *Anal. Chem.* **1986**, 58, (2), 293-298.

45. Heiger, D. N., *High Performance Capillary Electrophoresis*. Hewlet Packard: Paris, 1992.
46. Gas, B.; Kenndler, E., Peak Broadening in microchip electrophoresis: A discussion of the theoretical background. *Electrophoresis* **2002**, 23, 3817-3826.
47. Huang, X.; Gordon, J. J.; Zare, R. N., Current-monitoring method for measuring the electroosmotic flow rate in capillary zone electrophoresis. *Anal. Chem.* **1988**, 60, (17), 1837-1838.
48. Cheng, S.; Blanchard, W. C.; Chin Tiao, W., Direct control of the electroosmosis in capillary zone electrophoresis by using an external electric field. *Anal. Chem.* **1990**, 62, (14), 1550-1552.
49. Ocvirk, G.; Munroe, M.; Tang, T.; Oleschuk, R.; Westra, K.; Harrison, D. J., Electrokinetic Control of Fluid Flow in Native Poly(dimethylsiloxane) Capillary Electrophoresis Devices. *Electrophoresis* **2000**, 21, (1), 107-115.
50. Effenhauser, C. S.; Bruin, G. J.; Paulus, A.; Ehrat, M., Integrated Capillary Electrophoresis on Flexible Silicone Microdevices: Analysis of DNA Restriction Fragments and Detection of Single DNA Molecules on Microchips. *Anal. Chem.* **1997**, 69, (17), 3451-3457.
51. Duffy, D. C.; McDonald, J. C.; Schueller, J. A.; Whitesides, G. M., Rapid Prototyping of Microfluidic systems in poly(dimethylsiloxane). *Anal. Chem.* **1998**, 70, (23), 4974-4984.
52. Wang, B.; Chen, L.; Abdulali-Kanji, Z.; Horton, J. H.; Oleschuk, R. D., Aging Effects on Oxidized and Amine-Modified Poly(dimethylsiloxane) Surfaces Studied with Chemical Force Titrations: Effects on Electroosmotic Flow Rate in Microfluidic Channels. *Langmuir* **2003**, 19, (23), 9792-9798.
53. Wang, B.; Abdulali-Kanji, Z.; Dodwell, E.; Horton, J. H.; Oleschuk, R. D., Surface characterization using chemical force microscopy and the flow performance of modified polydimethylsiloxane for microfluidic device applications. *Electrophoresis* **2003**, 24, (9), 1442-1450.
54. Launer, P. J., Infrared analysis of organosilicon compounds: spectra-structure correlations. *Silicon Compounds Register and Review* **1987**, 100.
55. Lucovsky, G.; Manitini, M. J.; Srivastava, J. K.; Irene, E. A., Low-temperature growth of silicon dioxide films: A study of chemical bonding by ellipsometry and infrared spectroscopy. *J. Vac. Sci. Technol. B* **1987**, 5, (2), 530-537.
56. Pai, P. G.; Chao, S. S.; Takagi, Y., Infrared spectroscopic study of SiO<sub>x</sub> films produced by plasma enhanced chemical vapor deposition. *J. Vac. Sci. Technol. A* **1985**, 4, (3), 689-694.
57. Kim, Y.-H.; Hawang, M. S.; Kim, H. J.; Kim, J. Y.; Lee, Y., Infrared spectroscopy study of low-dielectric-constant fluorine-incorporated and carbon-incorporated silicon oxide films. *Journal of Applied Physics* **2001**, 90, (7), 3367-3370.
58. Ebelmen, J. J., *Ann.* **1846**, 57, 331.
59. Geffcken, W.; Berger, E., *German Patent* **1939**, 736411 (May 1939).
60. Collinson, M. M., Structure, Chemistry, and Applications of Sol-Gel Derived Materials. In *Handbook of Advanced Electronic and Photonic Materials and Devices*, Nalwa, H. S., Ed. Academic Press: New York, 2001; Vol. Volume 5: Chalcogenide Glasses and Sol-Gel Materials, pp 163-194.
61. Collinson, M. M., Analytical Applications of Organically Modified Silicates. *Mikrochimica Acta* **1998**, 129, 149-165.

62. Locascio, L. E.; Perso, C. E.; Lee, C. S., Measurement of electroosmotic flow in plastic imprinted microfluidic devices and the effect of protein adsorption on flow rate. *J. Chrom. A* **1999**, 857, 275-284.
63. Boone, T. D.; Fan, Z. H.; Hooper, H. H.; Ricco, A. J.; Tan, H.; Williams, S. J., Plastic advances microfluidic devices. *Analytical Chemistry* **2002**, 74, (3), 78A-86A.
64. Xu, W.; Uchiyama, K.; Shimosaka, T.; Hobo, T., Fabrication of polyester microchannels and their applications to capillary electrophoresis. *J. Chromatogr. A* **2001**, 907, 279-289.
65. Barker, S. L. R.; Ross, D.; Tarlov, M. J.; Gaitan, M.; Locascio, L. E., Control of Flow Direction in Microfluidic Devices with Polyelectrolyte Multilayers. *Anal. Chem.* **2000**, 72, (24), 5925-5929.
66. Barker, S. L. R.; Tarlov, M. J.; Canavan, H.; Hickman, J. J.; Locascio, L. E., Plastic microfluidic devices modified with polyelectrolyte multilayers. *Anal. Chem.* **2000**, 72, (20), 4899-4903.
67. Speher, A.-M.; Koster, S.; Linder, V.; Kulmala, S.; de Rooij, N. F.; Verpoorte, E.; Sigrist, H.; Thormann, W., Electrokinetic characterization of poly(dimethylsiloxane) microchannels. *Electrophoresis* **2003**, 24, 3674-3678.
68. Ocvirk, G.; Munroe, M.; Tang, T.; Oleschuk, R.; Westra, K.; Harrison, D. J., Electrokinetic Control of Fluid Flow in Native Poly(dimethylsiloxane) Capillary Electrophoresis Devices. *Electrophoresis* **2000**, 21, 107-115.
69. Lacher, N. A.; de Rooij, N. F.; Verpoorte, E.; Lunte, S. M., Comparison of the performance characteristics of poly (dimethylsiloxane) and Pyrex microchip electrophoresis devices for peptide separations. *Journal of Chromatography A* **2003**, 1004, 225-235.
70. Fu, A. Y.; Spence, C.; Scherer, A.; Arnold, F. H.; Quake, S. R., A microfabricated fluorescence-activated cell sorter. *Nature Biotech.* **1999**, 17, 1109-1111.
71. Unger, M. A.; Chou, H.-P.; Thorsen, T.; Scherer, A.; Quake, S. C., Monolithic Microfabricated Valves and Pumps by Multilayer Soft Lithography. *Science* **2000**, 288, 113-116.
72. Fu, A. Y.; Chou, H.-P.; Spence, C.; Arnold, F. H.; Quake, S. C., An Integrated Microfabricated Cell Sorter. *Anal. Chem.* **2002**, 74, 2451-2457.
73. Groisman, A.; Enzelberger, M.; Quake, S. C., Microfluidic Memory and Control Devices. *Science* **2003**, 300, 955-958.
74. Thorsen, T.; Maerkl, S. J.; Quake, S. C., Microfluidic Large-Scale Integration. *Science* **2002**, 298, 580-584.
75. Chou, H.-P.; Unger, M. A.; Quake, S. R., A Microfabricated Rotary Pump. *Biomedical Devices* **2001**, 3, (4), 323-330.
76. Quake, S. C.; Scherer, A., From Micro- to Nanofabrication with Soft Materials. *Science* **2000**, 290, 1536-1540.
77. Jiang, X.; Whitesides, G. M., Engineering microtools in polymers to study cell biology. *Engineering in Life Sciences* **2003**, 3, (12), 475-480.
78. Chen, X.; Wu, H.; Mao, C.; Whitesides, G. M., A prototype two-dimensional capillary electrophoresis system fabricated in poly(dimethylsiloxane). *Analytical Chemistry* **2002**, 74, (8), 1772-1778.
79. Stroock, A. D.; Dertinger, S. K. W.; Ajdari, A.; Mezic, I.; Stone, H. A.; Whitesides, G. M., Chaotic Mixer for Microchannels. *Science* **2002**, 295, 647-651.
80. Chabinye, M. L.; Chiu, D. T.; McDonald, J. C.; Stroock, A. D.; Christian, J. F.; Karger, A. M.; Whitesides, G. M., An integrated fluorescence detection system in

- poly(dimethylsiloxane) for microfluidic applications. *Analytical Chemistry* **2001**, 73, (18), 4491-4498.
81. McDonald, J. C.; Metallo, S. J.; Whitesides, G. M., Fabrication of a Configurable, Single-Use Microfluidic Devices. *Anal. Chem.* **2001**, 73, 5645-5650.
  82. Yang, P.; Wirnsberger, G.; Huang, H. C.; Cordero, S. R.; McGehee, M. D.; Scott, B.; Deng, T.; Whitesides, G. M.; Chmelka, B. F.; Buratto, S. K.; Stucky, G. D., Mirrorless Lasing from Mesostuctured Waveguides Patterned by Soft Lithography. *Science* **2000**, 287, 465-467.
  83. Kenis, P. J. A.; Ismagilov, R. F.; Whitesides, G. M., Microfabrication Inside Capillaries Using Multiphase Laminar Flow Patterning. *Science* **1999**, 285, 83-85.
  84. Jackman, R. J.; Brittain, S. T.; Adams, A.; Prentiss, M. G.; Whitesides, G. M., Design and Fabrication of Topologically Complex, Three-Dimensional Microstructures. *Science* **1998**, 280, 2089-2091.
  85. Duffy, D. C.; McDonald, J. C.; Schueller, O. J. A.; Whitesides, G. M., Rapidprototyping of Microfluidic systems in poly(dimethylsiloxane). *Anal. Chem.* **1998**, 70, (23), 4974-4984.
  86. Kim, J.; Chaudhury, M. K.; Owen, M. J., Hydrophobic Recovery of Polydimethylsiloxane Surfaces. *J. Colloid and Interface Science* **2000**, 226, 231-236.
  87. Morra, M.; Occhielo, E.; Marola, R.; Garbassi, F.; Humphrey, P.; Johnson, D., On the aging of Oxygen Plasma-Treated Polydimethylsiloxane Surfaces. *J. Colloid and Interface Science* **1990**, 137, 11-24.
  88. Hillborg, H.; Gedde, U. W., Hydrophobicity recovery of polydimethylsiloxane after exposure to corona discharge. *Polymer* **1998**, 39, 484-489.
  89. Lee, J. N.; Park, C.; Whitesides, G. M., Solvent Compatibility of Poly(dimethylsiloxane)-Based Microfluidic Devices. *Analytical Chemistry* **2003**, 75, (23), 6544-6554.
  90. Hu, S.; Ren, X.; Bachman, M.; Sims, C. E.; Li, G. P.; Allbritton, N. L., Tailoring the Surface Properties of Poly(dimethylsiloxane) Microfluidic Devices. *Langmuir* **2004**, 20, (13), 5569-5574.
  91. Hu, S.; Ren, X.; Bachman, M.; Sims, C. E.; Li, G. P.; Allbritton, N. L., Surface-Directed, Graft Polymerization within Microfluidic Channels. *Analytical Chemistry* **2004**, 76, (7), 1865-1870.
  92. Hu, S.; Ren, X.; Bachman, M.; Sims, C. E.; Li, G. P.; Allbritton, N., Surface Modification of Poly(dimethylsiloxane) Microfluidic Devices by Ultraviolet Polymer Grafting. *Analytical Chemistry* **2002**, 74, (16), 4117-4123.
  93. Xiao, D.; Van Le, T.; Wirth, M. J., Surface Modification of the Channels of Poly(dimethylsiloxane) Microfluidic Chips with Polyacrylamide for Fast Electrophoretic Separations of Proteins. *Analytical Chemistry* **2004**, 76, (7), 2055-2061.
  94. Xiao, D.; Zhang, H.; Wirth, M., Chemical Modification of the Surface of Poly(dimethylsiloxane) by atom-transfer radical polymerization of acrylamide. *Langmuir* **2002**, 18, 9971-9976.
  95. Chen, L.; Ren, J.; Bi, R.; Chen, D., Ultraviolet sealing and poly(dimethylacrylamide) modification for poly(dimethylsiloxane)/glass microchips. *Electrophoresis* **2004**, 25, (6), 914-921.
  96. Hu, S.; Ren, X.; Bachman, M.; Sims, C. E.; Li, G. P.; Allbritton, N. L., Cross-linked Coating for Electrophoretic Separations in Poly(dimethylsiloxane) Microchannels. *Electrophoresis* **2003**, 24, 3679-3699.

97. Slentz, B., E.; Penner, N., A.; Regnier, F., E., Capillary electrochromatography of peptides on microfabricated poly(dimethylsiloxane) chips modified by cerium(IV)-catalyzed polymerization. *Journal of chromatography. A* **2002**, 948, (1-2), 225-33.
98. Sung, W.-c.; Huang, S.-y.; Liao, P.-c.; Lee, G.-b.; Li, C.-w.; Chen, S.-h., Poly(dimethylsiloxane)-based microfluidic device with electrospray ionization-mass spectrometry interface for protein identification. *Electrophoresis* **2003**, 24, (21), 3648-3654.
99. Lahann, J.; Balcells, M.; Rodon, T.; Lee, J.; Choi, I. S.; Jensen, K. F.; Langer, R., Reactive polymer coatings: A platform for patterning proteins and mammalian cells onto a broad range of materials. *Langmuir* **2002**, 18, (9), 3632-3638.
100. Lahann, J.; Balcells, M.; Lu, H.; Rodon, T.; Jensen, K. F.; Langer, R., Reactive Polymer coatings: A first step toward surface engineering of microfluidic devices. *Analytical Chemistry* **2003**, 75, (9), 2117-2122.
101. Badal, M. Y.; Wong, M.; Chiem, N.; Salimi-Moosavi, H.; Harrison, D. J., Protein Separation and Surfactant Control of Electroosmotic Flow on Poly(dimethylsiloxane)-coated Capillaries and Microchips. *J. Chromatogr. A* **2002**, 947, 277-286.
102. Liu, Y.; Fanguy, J. C.; Bledsoe, J. M.; Henry, C. S., Dynamic coating using polyelectrolyte multilayers for chemical control of electroosmotic flow in capillary electrophoresis microchips. *Anal. Chem.* **2000**, 72, 5939-5944.
103. Collinson, M. M., Sol-gel Strategies for the Preparation of Selective Materials for Chemical Analysis. *Critical Reviews in Analytical Chemistry* **1999**, 29, (4), 289-311.
104. Collinson, M. M., Recent trends in analytical applications of organically modified silicate materials. *Trends in Analytical Chemistry* **2002**, 21, (1), 30-37.
105. Mark, J. E.; Pan, S.-J., Reinforcement of Polydimethylsiloxane Networks by in-situ Precipitation of Silica: A New Method for Preparation of Filled Elastomers. *Makromolekulare Chemie* **1982**, 3, 681-685.
106. Jiang, C.-Y.; Mark, J. E., The effects of various catalysts in the in-situ precipitation of reinforcing silica in polydimethylsiloxane networks. *Makromolekulare Chemie* **1984**, 185, 2609-2617.
107. Mark, J. E.; Jiang, C.-Y.; Tang, M.-Y., Simultaneous Curing and Filling of Elastomers. *Macromolecules* **1984**, 17, 2613-2616.
108. Mark, J. E.; Ning, Y.-P., Effects of Ethylamine Catalyst Concentration in the Precipitation of Reinforcing Silica Filler in an Elastomeric Network. *Polymer Bulletin* **1984**, 12, 413-417.
109. Ning, Y.-P.; Tang, M.-Y.; Jiang, C.-Y.; Mark, J. E.; Roth, W. C., Particle Sizes of Reinforcing Silica Precipitated into Elastomeric Networks. *J. Appl. Polymer Sci.* **1984**, 29, 3209-3212.
110. Tang, M.-Y.; Mark, J. E., Effect of Composition and Cross-Link Functionality on the Elastomeric Properties of Bimodal Networks. *Macromolecules* **1984**, 17, 2616-2619.
111. Mark, J. E.; Ning, Y.-P.; Jiang, C.-Y.; Tang, M.-Y., Electron microscopy of elastomers containing in-situ precipitated silica. *Polymer* **1985**, 26, (December), 2069-2072.
112. Ning, Y.-P.; Mark, J. E., Precipitation of reinforcing filler into polydimethylsiloxane prior to its end linking into elastomeric networks. *Journal of Applied Polymer Science* **1985**, 30, 3519-3522.
113. Mark, J. E., Generate reinforcing particles in place. *Chemtech* **1989**, 19, 230-233.
114. Sylgard 184 Silicone Elastomer - Material Safety Data Sheet. In Dow Corning Corporation: Midland, MI, 2000.

115. Arkles, B., Look What You Can Make with Silicones. *CHEMTECH* **1983**, 13, 542-555.
116. Haugland, R. P., *Handbook of Fluorescent Probes and Research Chemicals*. 6th ed.; Molecular Probes: Eugene, OR, 1996.
117. Jacobson, S. C.; Koutny, L. B.; Hergenröder, R.; Moore, A. W., Jr.; Ramsey, J. M., Microchip Capillary Electrophoresis with an Integrated Postcolumn Reactor. *Anal. Chem.* **1994**, 66, (20), 3472-3476.
118. Seiler, K.; Fan, Z. H.; Fluri, K.; Harrison, D. J., Electroosmotic Pumping and Valveless Control of Fluid Flow within a Manifold of Capillaries on a Glass Chip. *Anal. Chem.* **1994**, 66, 3485-3491.
119. Jacobson, S. C.; Ramsey, J. M., Integrated microdevice for DNA restriction fragment analysis. *Anal. Chem.* **1996**, 68, (5), 720-723.
120. Stevens, M. P., *Polymer Chemistry: An Introduction*. Oxford University Press: New York, 1999.
121. Culbertson, C. T.; Jacobson, S. C.; Ramsey, J. M., Dispersion sources for compact geometries on microchips. *Anal. Chem.* **1998**, 70, (18), 3781-3789.
122. Culbertson, C. T.; Jacobson, S. C.; Ramsey, J. M., Diffusion coefficient measurements in microfluidic devices. *Talanta* **2002**, 56, 365-373.
123. Jiang, C.-Y.; Mark, J. E., The effects of various catalysts in the in-situ precipitation of reinforcing silica in polydimethylsiloxane networks. *Makromol. Chemie* **1984**, 185, 2609-2617.
124. Kresge, C. T.; Leonowicz, M. E.; Roth, W. J.; Vartuli, J. C.; Beck, J. S., Ordered mesoporous molecular sieves synthesized by a liquid crystal template mechanism. *Nature* **1992**, 359, (6397), 710-712.
125. Mark, J. E.; Jiang, C.-Y.; Tang, M.-Y., Simultaneous Curing and Filling of Elastomers. *Macromol.* **1984**, 17, 2613-2616.
126. Mark, J. E.; Ning, Y.-P., Effects of Ethylamine Catalyst Concentration in the Precipitation of Reinforcing Silica Filler in an Elastomeric Network. *Polymer Bull.* **1984**, 12, 413-417.
127. Mark, J. E.; Pan, S.-J., Reinforcement of Polydimethylsiloxane Networks by in-situ Precipitation of Silica: A New Method for Preparation of Filled Elastomers. *Makromol. Chemie* **1982**, 3, 681-685.
128. Yang, T.; Jung, S.; Mao, H.; Cremer, P. S., Fabrication of Phospholipid Bilayer-Coated Microchannels for On-Chip Immunoassay. *Anal. Chem.* **2001**, 73, (2), 165-169.
129. Special Issue on "Organic-Inorganic Nanocomposite Materials, *Chem. Mater.* **2001**, 13, (1-2), 1.
130. Dawson, A.; Kamat, P. V., Semiconductor-Metal Nanocomposites. Photoinduced Fusion and Photocatalysis of Gold-Capped TiO<sub>2</sub> (TiO<sub>2</sub>/Gold) Nanoparticles. *J. Phys. Chem. B* **2001**, 105, (5), 960-966.
131. Fox, M.; Chen, c.-C., Mechanistic Features of the Semiconductor Photocatalyzed Olefin-to-Carbonyl Oxidative Cleavage. *J. Am. Chem. Soc.* **1981**, 103, (22), 6757-6759.
132. Kamat, P. V.; Huehn, R.; Nicolaescu, R., A "Sense and Shoot" Approach for Photocatalytic Degradation of Organic Contaminants in Water. *J. Phys. Chem. B* **2002**, 106, (4), 788-794.
133. Obare, S. O.; Ito, T.; Balfour, M. H.; Meyer, G. J., Ferrous Hemin Oxidation by Organic Halides at Nanocrystalline TiO<sub>2</sub> Interfaces. *Nano Lett.* **2003**, 3, (8), 1151-1153.

134. Yu, J. C.; Zhang, L.; Zheng, Z.; Zhao, J., Synthesis and Characterization of Phosphated Mesoporous Titanium Dioxide with High Photocatalytic Activity. *Chem. Mater.* **2003**, *15*, (11), 2280-2286.
135. Bechinger, C.; Ferrere; Zaban, A.; Sprague, J.; Gregg, B. A., Photoelectrochromic windows and displays. *Nature* **1996**, *383*, (6601), 608.
136. Hagfeldt, A.; Gratzel, M., Light-Induced Redox Reactions in Nanocrystalline Systems. *Chem. Rev.* **1995**, *95*, (1), 49-68.
137. Mills, A.; Le Hunte, S., An Overview of Semiconductor Photocatalysis. *J. Photochem. Photobio. A* **1997**, *108*, 1-35.
138. Breiner, J. M.; Mark, J. E., Preparation, structure, growth mechanisms and properties of siloxane composites containing silica, titania or mixed silica-titania phases. *Polymer* **1998**, *39*, (22), 5483-5493.
139. Auroux, P. A.; Iossifidis, D.; Reyes, D. R.; Manz, A., Micro Total Analysis Systems. 2. Analytical Standard Operations and Applications. *Anal. Chem.* **2002**, *74*, (12), 2637-2652.
140. Leach, A. M.; Wheeler, A. R.; Zare, R. N., *Anal. Chem.* **2003**, *75*, (4), 967-972.
141. McDonald, J. C.; Duffy, D. C.; Anderson, J. R.; Chiu, D. T.; Wu, H.; Schueller, O. J. A.; Whitesides, G. M., *Electrophoresis* **2000**, *21*, (1), 27-40.
142. Ren, X. Q.; Bachman, M.; Sims, C.; Li, G. P.; Allbritton, N. L., *J. Chrom. B* **2001**, *762*, 117-125.
143. He, B.; Tait, N.; Regnier, F., Fabrication of Nanocolumns for Liquid Chromatography. *Anal. Chem.* **1998**, *70*, (18), 3790-3797.
144. Wang, B.; Oleschuk, R. D.; Horton, J. H., Chemical Force Titrations of Amine- and Sulfonic Acid-Modified Poly(dimethylsiloxane). *Langmuir* **2005**, *21*, (4), 1290-1298.
145. Hu, S.; Ren, X.; Bachman, M.; Sims, C. E.; Li, G. P., Surface-Directed, Graft Polymerization within Microfluidic Channels. *Anal. Chem.* **2004**, *76*, (7), 1865-1870.
146. Hu, S.; Ren, X.; Bachman, M.; Sims, C. E.; Li, G. P.; Allbritton, N. L., Surface Modification of Poly(dimethylsiloxane) Microfluidic Devices by Ultraviolet Polymer Grafting. *Anal. Chem.* **2002**, *74*, (16), 4117-4123.
147. Hu, S.; Ren, X.; Bachman, M.; Sims, C. E.; Li, G. P.; Allbritton, N. L., Cross-linked Coating for Electrophoretic Separations in Poly(dimethylsiloxane). *Electrophoresis* **2003**, *24*, (21), 3679-3699.
148. Xiao, D.; Van Le, T.; Wirth, M. J., Surface Modification of the Channels of Poly(dimethylsiloxane) Microfluidic Chips with Polyacrylamide for Fast Electrophoretic Separations of Proteins. *Anal. Chem.* **2004**, *76*, (7), 2055-2061.
149. Xiao, D.; Zhang, H.; Wirth, M., Chemical Modification of the Surface of Poly(dimethylsiloxane) by Atom-Transfer Radical Polymerization of Acrylamide. *Langmuir* **2002**, *18*, (25), 9971-9976.
150. Slentz, B. E.; Penner, N. A.; Regnier, F. E., Capillary electrochromatography of peptides on microfabricated poly(dimethylsiloxane) chips modified by cerium(IV)-catalyzed polymerization. *J. Chrom. A* **2002**, *948*, (1-2), 225-33.
151. Sung, W.-c.; Liao, P.-c.; Lee, G.-b.; Li, C.-w.; Chen, S.-h., Poly(dimethylsiloxane)- based microfluidic device with electrospray ionization-mass spectrometry interface for protein identification. *Electrophoresis* **2003**, *24*, (21), 3648-3654.
152. Lahann, J.; Balcells, M.; Lu, H.; Rodon, T.; Jensen, K. F.; Langer, R., Reactive Polymer coatings: A first step toward surface engineering of microfluidic devices. *Anal. Chem.* **2003**, *75*, (9), 2117-2122.

153. Badal, M. Y.; Wong, M.; Chiem, N.; Salimi-Moosavi, H.; Harrison, D. J., Protein Separation and Surfactant Control of electroosmotic flow on poly(dimethylsiloxane) coated capillaries and microchips. *J. Chrom. A* **2002**, 277-286.
154. Barker, S. L.; Tarlov, M. J.; Canavan, H.; Hickman, J. J.; Locascio, L. E., Plastic Microfluidic Devices Modified with Polyelectrolyte Multilayers. *Anal. Chem.* **2000**, 72, (20), 4899-4903.
155. Linder, V.; Verpoorte, E.; Thormann, W.; de Rooij, N. F.; Sigrist, H., *Anal. Chem.* **2001**, 73, (17), 4181-4189.
156. Ning, Y.-P.; Mark, J. E., Precipitation of reinforcing filler into polydimethylsiloxane prior to its end linking into elastomeric networks. *J. Appl. Polymer Sci.* **1985**, 30, 3519-3522.
157. Tang, M.-Y.; Mark, J. E., Effect of Composition and Cross-Link Functionality on the Elastomeric Properties of Biomodal Networks. *Macromol.* **1984**, 17, 2616-2619.
158. Brennan, D. P.; Doble, A.; Sideris, P. J.; Oliver, S. R., Swollen Poly(dimethylsiloxane) (PDMS) as a Template for Inorganic Morphologies. *Langmuir* **2005**, ASAP article.
159. Roman, G. T.; Hlaus, T.; Bass, K. J.; Seelhammer, T. G.; Culbertson, C. T., Sol-Gel Modified Poly(dimethylsiloxane) Microfluidic Devices with High Electroosmotic Mobilities and Hydrophilic Channel Wall Characteristics. *Anal. Chem.* **2005**, 77, (5), 1414-1422.
160. Parks, G. A., The Isoelectric Points of Solid Oxides, Solid Hydroxides, and Aqueous Hydroxo Complex Systems. *Chem. Rev.* **1964**, 65, (2), 177-198.
161. Churaev, N. V.; Sergeeva, I. P.; Sobolev, V. D.; Derjaguin, B. V., *J. Colloid Interface Sci.* **1981**, 84, 451.
162. Jorgenson, J. W.; Lukacs, K. D., *Clin. Chem.* **1981**, 84, 1551.
163. Lukacs, K. D.; Jorgenson, J. W., *J. High Resolut. Chromatogr. Chromatogr. Commun.* **1985**, 8, 407.
164. Honda, S.; Yamamoto, K.; Suzuki, S.; Ueda, M.; Kakehi, K., *J. Chrom. A* **1991**, 588, 327.
165. McCormick, R. M., Capillary Zone Electrophoretic Separation of Peptides and Proteins Using Low pH Buffers in Modified Silica Capillaries. *Anal. Chem.* **1988**, 60, (21), 2322-2328.
166. Towns, J. K.; Regnier, F. E., *J. Chrom. A* **1990**, 516, 69.
167. Fujimoto, C., Titanium dioxide coated surfaces for capillary electrophoresis and capillary electrochromatography. *Electrophoresis* **2002**, 23, (17), 2929-2937.
168. Tsai, P.; Wu, C.-T.; Lee, C. S., Electrokinetic studies of inorganic coated capillaries. *J. Chrom. B.* **1994**, 657, 285-290.
169. Xu, L.; Feng, Y.-Q.; Shi, Z.-G.; Da, S.-L.; Ren, Y.-Y., Nonaqueous capillary electrophoresis using a titania-coated capillary. *J. Chrom. A.* **2004**, 1028, 165-170.
170. Bellaistre, M. C. d.; Mathieu, O.; Randon, J.; Rocca, J. L., Control of electroosmotic flow in zirconia-coated capillaries. *J. Chrom. A.* **2002**, 971, 199-205.
171. Xie, M.-J.; Feng, Y.-Q.; Da, S.-L., Capillary electrophoresis using zirconia coated fused silica capillaries. *J. Sep. Sci.* **2001**, 24, 62-66.
172. Xie, M.-J.; Feng, Y.-Q.; Da, S.-L.; Meng, D.-Y.; Ren, L.-W., Capillary electrophoresis and open tubular capillary electrochromatography using a magnesia-zirconia coated capillary. *Anal. Chim. Acta* **2001**, 428, 255-263.
173. Sagiv, J., Organized monolayers by adsorption. 1. Formation and structure of oleophobic mixed monolayers on solid surfaces. *J. Am. Chem. Soc.* **1980**, 102, (1), 92-98.
174. Silberzan, P.; Leger, L.; Ausserre, D.; Benattar, J. J., Silanation of silica surfaces. A new method of constructing pure or mixed monolayers. *Langmuir* **1991**, 7, (8), 1647-1651.

175. Wirth, M. J.; Fairbank, R. W. P.; Fatunmbi, H. O., *Science* **1997**, 275, (5296), 44-48.
176. Thorsteinsdottir, M.; Isaksson, R.; Westerflund, D., *Electrophoresis* **1995**, 16, 557-563.
177. Figeys, D.; van Oostveen, I.; Ducret, A.; Aebersold, R., *Anal. Chem.* **1996**, 68, (11), 1822-1828.
178. Shao, X. W.; Shen, Y. F.; O'Neill, K.; Lee, M. L., *J. Chrom. A* **1999**, 830, 415-422.
179. Chapman, R. G.; Ostuni, E.; Liang, M. N.; Meluleni, F.; Kim, E.; Yan, L.; Pier, G.; Warren, H. S.; Whitesides, G. M., Polymeric Thin Films That Resist the Adsorption of Proteins and the Adhesion of Bacteria. *Langmuir* **2001**, 17, (4), 1225-1233.
180. Ostuni, E.; Chapman, R. G.; Holmlin, R. E.; Takayama, S.; Whitesides, G. M., A Survey of Structure-Property Relationships of Surfaces that Resist the Adsorption of Protein. *Langmuir* **2001**, 17, (18), 5605-5620.
181. Clark, J. D. T., *Electron. Spectrosc. Relat. Phenom.* **1997**, 10, 455.
182. Seah, M. P.; Gilmore, I. S.; Beamson, G., *Surf. Interface Anal.* **1998**, 26, 642.
183. Seahand, M. P.; Dench, W. A., *Surf. Interface Anal.* **1979**, 1, 2.
184. Sherwood, P. M. A., *J. Vac. Sci. Technol.* **1996**, A14, 1424.
185. Proctorand, A.; Sherwood, P. M. A., *Anal. Chem.* **1982**, 54, 13.
186. Lee, C. S.; Blanchard, W. C.; Wu, C.-T., Direct Control of the electroosmosis in capillary zone electrophoresis by using an external electric field. *Anal. Chem.* **1990**, 62, (14), 1550-1552.
187. Lee, C. S.; McManigill, D.; Wu, C. T.; Patel, B., Factors affecting direct control of electroosmosis using an external electric field in capillary electrophoresis. *Anal. Chem.* **1991**, 63, (15), 1519-1523.
188. Striova, J.; Higgins, D. A.; Collinson, M. M., Phase Separation in Class II Organically Modified Silicate Films As Probed by Phase-Imaging Atomic Force Microscopy. *Langmuir* **2005**, 21, 6137-6141.
189. Chang-Yen, D. A.; Eich, R. K.; Gale, B. K., A monolithic PDMS waveguide system fabricated using soft-lithography techniques. *J. Lightwave Tech.* **2005**, 23, (6), 2088-2093.
190. Surnev, S.; Ramsey, M. G.; Netzer, F. P., Vanadium oxide surface studies. *Prog. Surf. Sci.* **2003**, 73, 117-165.
191. Vaidya, A. A.; Norton, M. L., DNA Attachment Chemistry at the Flexible Silicone Elastomer Surface: Toward Disposable Microarrays. *Langmuir* **2004**, 20, (25), 11100-11107.
192. Hiroshi, H.; Kazumi, S., Structure and physical properties of vanadium (V<sub>2</sub>O<sub>5</sub>) gels containing germanium oxide (GeO<sub>2</sub>). *J. Non-Cryst. Solids* **1990**, 121, (1-3), 68-71.
193. Vissers, D. R., A kinetic study of orthophosphate sorption on metal oxides. *J. Phys. Chem.* **1969**, 73, (6), 1953-1955.
194. Frauchiger, L.; Taborelli, M.; Aronsson, B.-O.; Descouts, P., Ion adsorption on titanium surfaces exposed to a physiological solution. *App. Surf. Sci.* **1999**, 143, 67-77.
195. Kekker, R. J.; De Bruijn, J. D.; Van Den Brink, I.; Bovell, Y. P.; Layrolle, P.; Van Blitterswijk, C. A., Bone tissue engineering on calcium phosphate-coated titanium plates utilizing cultured rat bone marrow cells: a preliminary study. *J. Mat. Sci.: Mat. Med.* **1998**, 9, 859-863.
196. Stoch, A.; Jastrzebski, W.; Brozek, A.; Stock, J.; Szaraniec, J.; Trybalska, B.; Kmita, G., FTIR absorption-reflection study of biomimetic growth of phosphates on titanium implants. *J. Mol. Struct.* **2000**, 555, 375-382.
197. Wu, W.; Nancollas, G. H., Nucleation and Crystal Growth of Octacalcium Phosphate on Titanium Oxide Surfaces. *Langmuir* **1997**, 13, (4), 861-865.

198. Zhang, Q.; Chen, X. L. J.; Zhang, X., Fabrication of Porous Titanium and Biomimetic Deposition of Calcium Phosphate. *Key Enginer. Mat.* **2003**, 240-242, 89-92.
199. Vreeland, W. N.; Locascio, L. E., Using Bioinspired Thermally Triggered Liposomes for High Efficiency Mixing on Microfluidic Devices. *Anal. Chem.* **2003**, 75, 6906-6911.
200. He, B.; Burke, B. J.; Zhang, X.; Zhang, R.; Regnier, F. E., A Picoliter-Volume Mixer for Microfluidic Analytical Systems. *Anal. Chem.* **2001**, 73, 1942-1947.
201. Gottschlich, N.; Culbertson, C. T.; McKnight, T. E.; Jacobson, S. C.; Ramsey, J. M., Integrated Microchip-Device for the Digestion, Separation and Postcolumn Labeling of Proteins and Peptides. *J. Chrom. B.* **2000**, 745, 243.
202. Hadd, A. G.; Jacobson, S. C.; Ramsey, J. M., Microfluidic Assays of Acetylcholinesterase Inhibitors. *Anal. Chem.* **1999**, 71, 5206.
203. Foote, R. S.; Khandurina, J.; Jacobson, S. C.; Ramsey, J. M., Preconcentration of Proteins on Microfluidic Devices Using Porous Silica Membranes. *Anal. Chem.* **2005**, 77, (1), 57-63.
204. Liu, J.; Pan, T.; Woolley, A. T.; Lee, M. L., Surface modified poly(methyl methacrylate) Capillary Electrophoretic Microchips for Protein Analysis. *Anal. Chem.* **2004**, 76, (23), 6948-6955.
205. Martynova, L.; Locascio, L. E.; Gaitan, M.; Kramer, G. K.; Christensen, R. G.; MacCrehan, W. A., *Anal. Chem.* **1997**, 69, 2626-2630.
206. McCormick, R. M.; Nelson, R. J.; Goretty Alonso-Amigo, M.; Benvegno, D. J.; Hooper, H. H., *Anal. Chem.* **1997**, 69, 2626-2630.
207. Roberts, M. A.; Rossier, J. S.; Berier, P.; Girault, H., *Anal. Chem.* **1997**, 69, 2035-2042.
208. Gaudioso, J.; Craighead, H. G., Characterizing electroosmotic flow in microfluidic devices. *J. Chrom. A.* **2002**, 971, (1-2), 249-253.
209. McDonald, J. C.; Duffy, D. C.; Anderson, J. R.; Chiu, D. T.; Wu, H. S.; Olivier, J. A.; Whitesides, G. M., Fabrication of microfluidic systems in poly(dimethylsiloxane). *Electrophoresis* **2000**, 21, (1), 27-40.
210. Towns, J. K.; Reignier, F. E., *Anal. Chem.* **1992**, 64, 2473-2478.
211. Xiao, D.; Van Le, T.; Wirth, M. J., Surface Modification of the Channels of Poly(dimethylsiloxane) Microfluidic Chips with Polyacrylamide for Fast Electrophoretic Separations of Proteins. *Analytical Chemistry* **2004**, 76, (7), 2055-2061.
212. Hu, S.; Ren, X.; Bachman, M.; Sims, C. E.; Li, G. P., Surface-Directed, Graft Polymerization within Microfluidic Channels. *Analytical Chemistry* **2004**, 76, (7), 1865-1870.
213. Hu, S.; Ren, X.; Bachman, M.; Sims, C. E.; Li, G. P.; Allbritton, N. L., Surface Modification of Poly(dimethylsiloxane) Microfluidic Devices by Ultraviolet Polymer Grafting. *Analytical Chemistry* **2002**, 74, (16), 4117-4123.
214. Slentz, B. E.; Penner, N. A.; Regnier, F. E., Capillary electrochromatography of peptides on microfabricated poly(dimethylsiloxane) chips modified by cerium(IV)-catalyzed polymerization. *Journal of Chromatography A.* **2002**, 948, (1-2), 225-33.
215. Tinglu, Y.; Jung, S.-y.; Hanbin, M.; Cremer, P. S., Fabrication of Phospholipid Bilayer-Coated Microchannels for On-Chip Immunoassay. *Anal. Chem.* **2001**, 73, 165-169.
216. Badal, M. Y.; Wong, M.; Chiem, N.; Salimi-Moosavi, H.; Harrison, D. J., Protein Separation and Surfactant Control of electroosmotic flow on poly(dimethylsiloxane) coated capillaries and microchips. *J. Chromatogr. A* **2002**, 277-286.
217. Badal, M. Y.; Wong, M.; Chiem, N.; Salimi-Moosavi, H.; Harrison, D. J., Protein Separation and surfactant control of electroosmotic flow in poly(dimethylsiloxane)- coated capillaries and microchips. *Journal of Chromatography A.* **2002**, 947, 277-286.

218. Berglund, K. D.; Przybycien, T. M.; Tilton, R. D., Coadsorption of Sodium Dodecyl Sulfate with Hydrophobically Modified Nonionic Cellulose Polymers. 2. Role of Surface Selectivity in Adsorption Hysteresis. *Langmuir* **2003**, *19*, 2714-2721.
219. Berglund, K. D.; Przybycien, T. M.; Tilton, R. D., Coadsorption of Sodium Dodecyl Sulfate with Hydrophobically Modified Nonionic Cellulose Polymers. 1. Role of Polymer Hydrophobic Modification. *Langmuir* **2003**, *19*, 2705-2713.
220. Ro, K. W.; Lim, K.; Kim, H.; Hahn, J. H., Poly(dimethylsiloxane) microchip for precolumn reaction and micellar electrokinetic chromatography of biogenic amines. *Electrophoresis* **2002**, *23*, 1129-1137.
221. Ramsey, J. D.; Jacobson, S. C.; Culbertson, C. T.; Ramsey, J. M., High Efficiency, Two-Dimensional Separations of Protein Digests on Microfluidic Devices. *Anal. Chem.* **2003**, *75*, (15), 3758-3764.
222. Lee, C. S.; Blanchard, W. C.; Wu, C. T., Direct control of the electroosmosis in capillary zone electrophoresis by using an external electric field. *Anal. Chem.* **1990**, *62*, (14), 1550-2.
223. Lee, C. S.; McManigill, D.; Wu, C. T.; Patel, B., Factors affecting direct control of electroosmosis using an external electric field in capillary electrophoresis. *Anal. Chem.* **1991**, *63*, (15), 1519-23.
224. Lauer, H. H.; McManigill, D., *Anal. Chem.* **1986**, *58*, 166.
225. Walbroehl, Y.; Jorgenson, J. W., *J. Microcolumn Separations* **1989**, *1*, 41.
226. Zhao, Z.; Malik, A.; Lee, M., *Anal. Chem.* **1993**, *65*, 2747.
227. Dolnik, V.; Novotny, M., *J. Microcolumn Separations* **1992**, *4*, 515.
228. Giles, M.; Kleemiss, M. H.; Schomberg, G., *Anal. Chem.* **1994**, *66*, 2038.
229. Hjerten, S., *J. Chromatography* **1985**, *347*, 191.
230. Jorgenson, J. S.; Lukacs, K. D., *Science* **1983**, *222*, 266.
231. Zhu, M.; Rodriguez, R.; Hansen, D.; Wehr, T., *J. Chromatography* **1990**, *516*, 123.
232. Dou, Y.-H.; Bao, N.; Xu, J.-J.; Meng, F.; Chen, H.-Y., Separation of proteins on surface-modified poly(dimethylsiloxane) microfluidic devices. *Electrophoresis* **2004**, *25*, 3024-3031.
233. Terabe, S.; Otsuka, K.; Ichikawa, K.; Tsuchiya, A.; Ando, T., *Anal. Chem.* **1984**, *56*, 111-113.
234. Yashima, T.; Tsuchiya, A.; Morita, O., Separation of Closely Related Large Peptides by Micellar Electrokinetic Chromatography with Organic Modifiers. *Anal. Chem.* **1992**, *64*, (23), 2981-2984.
235. Strege, M. A.; Lagu, A. L., Capillary electrophoretic protein separations in polyacrylamide-coated silica capillaries and buffers containing ionic surfactants. *Journal of Chromatography* **1993**, *630*, 337-344.
236. Strege, M. A.; Lagu, A. L., Micellar electrokinetic chromatography of proteins. *Journal of Chromatography A* **1997**, *780*, 285-296.
237. Strege, M. A.; Lagu, A. L., Capillary Electrophoresis of biotechnology derived proteins. *Electrophoresis* **1997**, *18*, 2343-2352.
238. Michels, D. A.; Hu, S.; Dambrowitz, K. A.; Eggertson, M. J.; Lauterbach, K.; Dovichi, N. J., Capillary sieving electrophoresis-micellar electrokinetic chromatography fully automated two-dimensional capillary electrophoresis analysis of *Deinococcus radiodurans* protein homogenate. *Electrophoresis* **2004**, *25*, (18-19), 3098-3105.
239. Wang, C.; Lucy, C. A., Mixed cationic/anionic surfactants for semipermanent wall coatings in capillary electrophoresis. *Electrophoresis* **2004**, *25*, (1), 825-832.

240. Szoko, E., Protein and peptide analysis by capillary zone electrophoresis and micellar electrokinetic chromatography. *Electrophoresis* **1997**, 18, 74-81.
241. Andrieux, K.; Olivier, J. C.; Taverna, M.; Vauthier, C.; Couvreur, P.; Ferrier, D., Analysis of serum proteins by micellar electrokinetic capillary chromatography. Application to a drug carrier evaluation. *J. Liq. Chrom. and Rel. Technol.* **1996**, 19, (20), 3333-3353.
242. Weber, K.; Osborn, M., The Reliability of Molecular Weight Determinations by Dodecyl Sulfate Polyacrylamide Gel Electrophoresis. *J. Biol. Chem.* **1969**, 244, 4406-4412.
243. Jing, P.; Kaneta, T.; Imasaka, T., Micellar electrokinetic chromatography with diode laser-induced fluorescence detection as a tool for investigating the fluorescence labeling of proteins. *Electrophoresis* **2002**, 23, 550-555.
244. Mistry, K.; Krull, I.; Grinberg, N., Capillary electrochromatography. *Journal of Separation Science* **2002**, 25, 935-958.
245. Jing, P.; Kaneta, T.; Imasaka, T., Band Broadening Caused by Multilabeling of Proteins. *J. Chromatogr. A* **2002**, 959, 281-287.
246. Tadey, T.; Purdy, W. C., *J. Chromatography A* **1993**, 652, 131-138.
247. Grimm, R.; Zanaboni, G.; Viglio, S.; Dyne, K.; Valli, M.; Cetta, G.; Iradarola, P., *J. Chromatography A* **1997**, 768, 57-66.
248. Hu, S.; Michels, D. A.; Fazal, M. A.; Ratisoontorn, C.; Cunningham, M. L.; Dovichi, N. J., Capillary Sieving Electrophoresis/Micellar Electrokinetic Capillary Chromatography for Two-Dimensional Protein Fingerprinting of Single Mammalian Cells. *Anal. Chem.* **2004**, 76, (14), 4044-4049.
249. Lee, J. N.; Park, C.; Whitesides, G. M., Solvent Compatibility of Poly(dimethylsiloxane)-Based Microfluidic Devices. *Anal. Chem.* **2003**, 75, (23), 6544-6554.
250. Lacher, N. A.; Rooij, N. F. d.; EVerpoorte, E.; Lunte, S. M., Comparison of the performance characteristics of poly(dimethylsiloxane) and Pyrex microchip electrophoresis devices for peptide separations. *J. Chrom. A.* **2003**, 1004, 225-235.
251. Watzig, H.; Degenhardt, M.; Kunkel, A., Strategies for capillary electrophoresis: Method development and validation for pharmaceutical and biological applications. *Electrophoresis* **1998**, 19, 2695-2752.
252. Quist, A.; Doudevski, I.; Hai, L.; Azimova, R.; Ng, D.; Frangione, B.; Kagan, B.; Ghiso, J.; Lal, R., Amyloid ion channels: A common structural link for protein-misfolding disease. *Proc. Nat. Acad. Sci.* **2005**, 102, (30), 10427-10432.
253. Selko, D. J., Folding proteins in fatal ways. *Nature* **2003**, 426, 900-904.
254. Cairo, C. W.; Strzelec, A.; Murphy, R. M.; Kiessling, L. L., Affinity-Based Inhibition of B-Amyloid Toxicity. *Biochemistry* **2002**, 41, 8620-8629.
255. Selko, D. J., *Neuron* **1991**, 6, 487-498.
256. Bitan, G.; Kirkitadze, M. D.; Lomakin, A.; Vollers, S. S.; Benedek, G. B.; Teplow, D. B., Amyloid b-protein (Ab) assembly: Ab40 and Ab42 oligomerize through distinct pathways. *Proc. Nat. Acad. Sci.* **2003**, 100, (1), 330-335.
257. Scheuner, D.; Eckman, C.; Jensen, M.; Song, X.; Citron, M.; Suzuki, N.; Bird, T. D.; Hardy, J.; Hutton, M.; Kukull, W., *Nat. Med.* **1996**, 2, 864-870.
258. Golde, T. E.; Eckman, C. B.; Younkin, S. G., *Biochim. Biophys. Acta Mol. Basis Dis.* **2000**, 1502, 172-187.
259. Cruz, L.; Urbanc, B.; Borreguero, J. M.; Lazo, N. D.; Teplow, D. B.; Stanley, H. E., Solvent and mutation effects on the nucleation of amyloid b-protein folding. *Proc. Nat. Acad. Sci.* **2005**, 102, 18258-18263.

260. Barrow, C. J.; Yasuda, A.; Kenny, P. T. M.; Zagorski, M. G., Solution conformations and aggregational properties of Ab peptides. *J. Mol. Bio.* **1992**, 225, (4), 1075-1093.
261. Mansfield, S. L.; Gotch, A. J.; Harms, G. S.; Johnson, C. K.; Larive, C. K., Complementary Analysis of Peptide Aggregation by NMR and Time-Resolved Laser Spectroscopy. *J. Phys. Chem. B* **1999**, 103, 2262-2269.
262. Luhrs, T.; Ritter, C.; Adrian, M.; Riek-Loher, D.; Bohrmann, B.; Dobeli, H., 3D structure of Alzheimers amyloid-b1-42 fibrils. *Proc. Nat. Acad. Sci.* **2005**, 102, 17342-17347.
263. Cheng, X.; van Breemen, R. B., Mass Spectrometry-Based Screening for Inhibitors of b-Amyloid Protein Aggregation. *Anal. Chem.* **2005**, 77, 7012-7015.
264. Sabella, S.; Quaglia, M.; Lanni, C.; Racchi, M.; Govoni, S.; Caccialanza, G.; Calligaro, A.; Bellotti, V.; Lorenzi, E. D., Capillary Electrophoresis studies on the aggregation process of b-amyloid 1-42 and 1-40 peptides. *Electrophoresis* **2004**, 25, 3186-3194.
265. Emrich, C. A.; Tian, H.; Medintz, I. L.; Mathies, R. A., Microfabricated 384-Lane Capillary Array Electrophoresis Bioanalyzer for Ultrahigh-Throughput Genetic Analysis. *Anal. Chem.* **2002**, 74, 5076-5083.
266. Karlinsey, J. M.; Monahan, J.; Marchiarullo, D. J.; Ferrance, J. P.; Landers, J. P., Pressure injection on a valved microdevice for electrophoretic analysis of submicroliter samples. *Anal. Chem.* **2005**, 77, 3637-3643.
267. Tang, T.; Badal, M. Y.; Ocvirk, G.; Lee, W. E.; Bader, D. E.; Bekkaoui, F.; Harrison, D. J., Integrated microfluidic electrophoresis system for analysis of genetic materials using signal amplification methods. *Anal. Chem.* **2002**, 74, 725-733.
268. Collinson, M. M., Analytical Applications of Organically Modified Silicates. *Mikrochim. Acta* **1998**, 129, 149-165.
269. Broyles, B. S.; Jacobson, S. C.; Ramsey, J. M., Sample Filtration, Concentration, and Separation Integrated on Microfluidic Devices. *Anal. Chem.* **2003**, 75, 2761-2767.
270. Mogensen, K. B.; Kwok, Y. C.; Eijkel, J. C. T.; Petersen, N. J.; Manz, A.; Kutter, J. P., A Microfluidic Device with an Integrated Waveguide Beam Splitter for Velocity Measurements of Flowing Particles by Fourier Transformation. *Anal. Chem.* **2003**, 75, 4931-4936.
271. Vezenov, D. V.; Mayers, B. T.; Conroy, R. S.; Whitesides, G. M.; Snee, P. T.; Chan, Y.; Nocera, D. G.; Bawendi, M. G., A Low-Threshold, High-High Efficiency Microfluidic Laser. *J. Am. Chem. Soc.* **2005**, 127, 8952-8953.
272. Dai, J.; Ito, T.; Sun, L.; Crooks, R. M., Electrokinetic Trapping and Concentration Enrichment of DNA in a Microfluidic Channel. *J. Am. Chem. Soc.* **2003**, 125, 13026-13027.
273. Cannon, D. M.; Kuo, T. C.; Bohn, P. W.; Sweedler, J. V., Nanocapillary Array Interconnects for Gated Analyte Injections and Electrophoretic Separations in Multilayer Microfluidic Architectures. *Anal. Chem.* **2003**, 75, 2224-2230.
274. Zhao, B.; Viernes, N. O. L.; Moore, J. S.; Beebe, D. J., Control and Applications of Immiscible Liquids in Microchannels. *J. Am. Chem. Soc.* **2002**, 124, 5284-5285.
275. Song, S.; Singh, A. K.; Kirby, B. J., Electrophoretic Concentration of Proteins at Laser-Patterned Nanoporous Membranes in Microchips. *Anal. Chem.* **2004**, 76, 4589-4592.
276. Cannon, D. M.; Kuo, T. C.; Bohn, P. W.; Sweedler, J. V., Nanocapillary Array Interconnects for Gated Analyte Injections and Electrophoretic Separations in Multilayer Microfluidic Architectures. *Anal. Chem.* **2003**, 75, (10), 2224-2230.
277. Liu, S.; Pu, Q.; Gao, L.; Korzeniewski, C.; Matzke, C., From Nanochannel-Induced Proton Conduction Enhancement to a Nanochannel-Based Fuel Cell. *Nano Lett.* **2005**, 5, (7), 1389-1393.

278. Pu, Q.; Yun, J.; Temkin, H.; Liu, S., Ion-Enrichment and Ion-Depletion Effect of Nanochannel Structures. *Nano Lett.* **2004**, 4, (6), 1099-1103.
279. Higgins, D. A.; Luther, B. J., *J. Chem. Physics* **2003**, 119, 3935.
280. Wang, Y.-C.; Stevens, A. L.; Han, J., Million-fold Preconcentration of Proteins and Peptides by Nanofluidic Filter. *Anal. Chem.* **2005**, 77, 4293-4299.
281. Pu, S.; Yun, J.; Temkin, H.; Liu, S., Ion-Enrichment and Ion-Depletion Effect of Nanochannel Structures. *Nano Lett.* **2004**, 4, (6), 1099-1103.
282. Grainger, D. W.; Knutson, K.; Kim, S. W.; Feijen, J., Poly(dimethylsiloxane)-poly(ethylene oxide)-heparin block copolymers II: Surface characterization and in vitro assessments. *J. Biomed. Mat. Res.* **1990**, 24, 403-431.
283. Xiong, W.; Ferrell, J. E., A positive-feedback-based bistable 'memory module' that governs a cell fate decision. *Nature* **2003**, 426, 460-465.
284. Brandman, O.; Ferrell, J. E.; Li, R.; Meyer, T., Interlinked Fast and Slow Positive Feedback Loops Drive Reliable Cell Decisions. *Science* **2005**, 310, 496-498.
285. Poulsen, C. R.; Culbertson, C. T.; Jacobson, S. C.; Ramsey, J. M., Static and Dynamic Acute Cytotoxicity Assays on Microfluidic Devices. *Anal. Chem.* **2005**, 77, (22), 667-672.
286. Balagadde, F. K.; You, L.; Hansen, C. L.; Arnold, F. H.; Quake, S. R., Long-Term Monitoring of Bacteria Undergoing Programmed Population Control in a Chemostat. *Science* **2005**, 309, 137-140.
287. He, M.; Edgar, J. S.; Jeffries, G. D. M.; Lorenz, R. M.; Shelby, J. P.; Chiu, D. T., Selective Encapsulation of Single Cells and Subcellular Organelles into Picoliter- and Femtoliter-Volume Droplets. *Anal. Chem.* **2005**, 77, 1539-1544.
288. Chiou, P. Y.; Ohta, A. T.; Wu, M. C., Massively Parallel Manipulation of Single Cells and Microparticles Using Optical Images. *Nature* **2005**, 436, 370-372.
289. Taff, B. M.; Voldman, J., A Scalable Addressable Positive-Dielectrophoretic Cell-Sorting Array. *Anal. Chem.* **2005**, 77, 7976-7983.
290. Wheeler, A. R.; Thronset, W. R.; Whelan, R. J.; Leach, A. M.; Zare, R. N.; Liao, Y. H.; Farrell, K.; Manger, I. D.; Daridon, A., Microfluidic Device for Single Cell Analysis. *Anal. Chem.* **2003**, 75, 3581-3586.
291. Di Carlo, D.; Aghdam, N.; Lee, L. P., Single-Cell Enzyme Concentrations, Kinetics, and Inhibition analysis Using High-Density Hydrodynamic Cell isolation arrays. *Anal. Chem.* **2006**, 78, ASAP.
292. Peng, X. Y.; Li, P. C. H., A Three-Dimensional Flow Control Concept for Single-Cell Experiments on a Microchip. 1. Cell Selection, Cell Retention, Cell Culture, Cell Balancing, and Cell Scanning. *Analytical Chemistry* **2004**, 76, (18), 5273-5281.
293. Peng, X. Y.; Li, P. C. H., A Three-Dimensional Flow Control Concept for Single-Cell Experiments on a Microchip. 2. Fluorescein Diacetate Metabolism and Calcium Mobilization in a Single Yeast Cell As Stimulated by Glucose and pH Changes. *Analytical Chemistry* **2004**, 76, (18), 5282-5292.
294. Schrum, D. P.; Culbertson, C. T.; Jacobson, S. C.; Ramsey, J. M., Microchip Flow Cytometry Using Electrokinetic Focusing. *Anal. Chem.* **1999**, 71, 4173-4177.
295. McClain, M. A.; Culbertson, C. T.; Jacobson, S. C.; Allbritton, N. L.; Sims, C. E.; Ramsey, J. M., Single Cell Analysis Using Microfluidics. *Anal. Chem.* **2003**, 75, (21), 5646-5655.
296. Li, P. C. H.; Harrison, D. J., Transport, Manipulation, and reaction of Biological Cells On-chip Using Electrokinetic Effects. *Anal. Chem.* **1997**, 69, 1564-1568.

297. Gates, B. D.; Xu, Q.; Stewart, M.; Ryan, D.; Wilson, C. G.; Whitesides, G. M., New Approaches to Nanofabrication: Molding, Printing, and Other Techniques. *Chem. Rev.* **2005**, 105, 1171-1196.
298. Lee, C.-C.; Sui, G.; Elizarov, A.; Shu, C. J.; Shin, Y.-S.; Dooley, A. N.; Huang, J.; Daridon, A.; Wyatt, P.; Stout, D.; Kolb, H. C.; Witte, O. N.; Satyamurthy, N.; Heath, J. R.; Phelps, M. E.; Quake, S. R.; Tseng, H. R., Multistep Synthesis of a Radiolabeled Imaging Probe Using Integrated Microfluidics. *Science* **2005**, 310, 1793-1796.
299. Marcus, J. S.; Anderson, W. F.; Quake, S. R., Parallel Picoliter RT-PCR Assays Using Microfluidics. *Anal. Chem.* **2006**, 78, 956-958.
300. Hellmich, W.; Pelargus, C.; Leffhalm, K.; Ros, A.; Anselmetti, D., Single cell manipulation, analytics, and label-free protein detection in microfluidic devices for systems nanobiology. *Electrophoresis* **2005**, 26, 3689-3696.
301. Peng, X. Y.; Li, P. C. H., A three-dimensional flow control concept for single-cell experiments on a microchip. 2. Fluorescein diacetate metabolism and calcium mobilization in a single yeast cell as stimulated by glucose and pH changes. [Erratum to document cited in CA141:291680]. *Analytical Chemistry* **2004**, 76, (24), 7400.



